HIGGS PAIR PRODUCTION SEARCHES WITH THE ATLAS EXPERIMENT AT THE LHC AND THE HL-LHC

A DISSERTATION
SUBMITTED TO THE DEPARTMENT OF PHYSICS
AND THE COMMITTEE ON GRADUATE STUDIES
OF STANFORD UNIVERSITY
IN PARTIAL FULFILLMENT OF THE REQUIREMENTS
FOR THE DEGREE OF
DOCTOR OF PHILOSOPHY

JANNICKE PEARKES
DECEMBER 2022

CERN-THESIS-2022-262
01/12/2022

Abstract

Searches for HH production ask the seemingly simple question: "If we can produce one Higgs boson during an LHC collision, can we produce two?". A decade after the Higgs discovery, we are getting tantalizing close to answering that question, but for now, it remains unanswered. This thesis aims to motivate why this is an interesting question, document our efforts toward answering it, and provide insight into when we expect to be able to claim evidence for HH production in the future.

Chapter 1 will discuss why HH searches are interesting from a theoretical standpoint, building up from the Standard Model of particle physics. Chapter 2 will explain the experimental apparatus, the ATLAS experiment at the Large Hadron Collider (LHC). Chapter 3 will discuss how we use ATLAS to reconstruct the particle collisions at the LHC. Chapter 4 will discuss how we can improve the reconstruction of bottom quark jets. Chapter 5 will dive into the HH to $b\bar{b}\gamma\gamma$ search and present the latest results in this channel. Chapter 6 will discuss future analysis improvements in the $b\bar{b}\gamma\gamma$ search channel. Chapter 7 will show how $b\bar{b}\gamma\gamma$ fits into the landscape of HH searches at the LHC and will present the latest HH combined results with the $b\bar{b}b\bar{b}$ and $b\bar{b}\tau^+\tau^-$ channels. Chapter 8 will project the expected HH search results at the High Luminosity LHC. Finally, Chapter 9 will discuss the ATLAS Inner Tracker upgrade for the High Luminosity LHC, which will be required for continued exploration of HH production in the future.

Acknowledgments

You rarely get to explicitly thank everyone for their role in your life, big or small. The acknowledgments are my favourite part of reading any thesis, so I went ahead and made them extra long.

First, I want to thank my constellation of advisors. Caterina, thank you for having me as your first PhD student and for growing with me during this process. Thank you for having excellent taste in exciting and meaningful physics and providing me with a strong research direction. I have learned so much from you, and seeing you continuously and ambitiously push the forefront of science is incredibly inspiring. Thank you for the rapid and constructive feedback on this thesis, which made writing it a surprisingly enjoyable process. Thank you, Su Dong, for your laid-back attitude and your enthusiasm for all things pixel-related. And thank you, Charlie, although never formally an advisor, for all the wisdom, advice, and encouragement over these years.

I want to thank my thesis committee members, Giorgio, Tim, Natalia, and Dustin, for making my defense lively and fun and making submitting this thesis possible.

The $b\bar{b}\gamma\gamma$ search was my first major analysis, and I am incredibly grateful to have worked on it with such a talented team. Thank you to Valentina for being an amazing analysis contact, superhuman post-doc, and the best vampire ever. Thank you, Elisabeth, Adele, and Louis, for your team leadership. Thank you to Alex for being a great office mate, for the one-on-one statistics and spurious signal tutorials, analysis strategy discussions, INT note editing, and, of course, the dancing monkeys. Alkaid, thank you for all of the hard work you put into the software and the physics, and for being one of the friendliest and most responsive people to boot. Thank you also to Mohamed, Elena, Zihang, Raphael, Tyler, Laura, and Ivan for working alongside me and astounding me with your work ethic and creativity.

Thank you to Stefano and Rui for bringing me along on the HH combination (and prospects) ride. Stefano, thank you for always answering my questions thoughtfully and patiently, and for my favourite quote: "We may not have become better physicists here, but we have definitely become better graphic designers.". Rui, thank you for teaching me the hh_combination_framework, the art of running fits, and for the many cowboy emojis. Thank you to Tulin and Xiaohu for leading the HH MC validation efforts. Max, Marco, and Chris G. for all things EFT and $b\bar{b}b\bar{b}$. Christina, for being my go-to $b\bar{b}\tau^+\tau^-$ person. Katharine, Liza, Alessandra, and Jason, thank you for making the

HH subgroup an excellent and fun place to grow up as a scientist. Liza, thank you for both the design and life consulting. Katharine, thank you for being the role model opposite me behind the SLAC/SMU office wall. Thank you to everyone else in the HH subgroup who has participated in pub quizzes, helped me with a JIRA ticket, submitted a comment on CDS (did I say that?), and contributed to my experience here.

I am also grateful for my time working with the pixel modules group. Thank you, Susanne, for providing the wonderful lab, guidance, and mentoring during my qualification task. Matthias H., Sascha, Bora, Lingxin, and Steffen for bringing me into the module testing fold and holding meetings in German with me. Thank you, Richard B., and Marek, for the pixel module QA/QC support. Zijun, thank you for your deep knowledge of all things RCE/RD53A/PulsarIIb-related and Dodo's songs on zoom. Matthias W. for the linux and networking wizardry. Gerhardt for helping set up RCE and trying to eat a styrofoam packing peanut that one time.

A PhD is nothing without peers, so thank you to all of the students in the SLAC ATLAS group for the dinners, hikes, and general camaraderie. Nicole, thank you for being my PhD sibling. Thank you for comparing notes on everything, HH/b-tagging/ML/you-name-it, often in the middle of the night, and riding through all of the ups and downs of a PhD with me. Thank you, Rachel S., for the art, Murtaza, for the turtlenecks, Aviv, for the chuckles, and, Sanha, for the can-do attitude. Thank you Sam, Aidan, and Chris M., for the friendship, but most importantly, the karaoke. And thank you to all the summer students I have had the pleasure of working with.

Thank you also to the post-docs and other senior members in the SLAC ATLAS group and beyond. Thank you, Rachel H., for the train facts. Thank you, Hannah, for the many cupcakes. Rafael, for flavour tagging advice. Zhi, for the hugs. Brendon, for the most chipper of attitudes. Rebecca, for the encouragement. Adrienne, for always making sure I got my forms in on time. Catrin for being a friendly face at CERN. Michael K. for the machine learning and my addiction to pottery Instagram. Eric for fun design sessions. Philippe, for your ITk leadership. Ariel for the never-ending fountain of ideas. Rainer for the chats from across the hall. And Michael P., (honorary ATLAS member) for the enthusiasm. Thank you also to the friendly faces in B84, Cam for the homemade beer and the best Higgsdependance day party, and Sander for being a source of encouragement in physics and climbing.

Thank you to all of the people who supported me in pursuing a PhD in the first place. Thank you, Alison, Colin, and Wojtek, for your support at UBC. Thank you, Alison, for always knowing exactly what I was thinking. Thank you, Wojtek, for listening to me, questioning me, and pushing so incredibly hard to make our projects successful. Thank you to the entire UBC crew, Tal, Alex, Sebastien, Steffen, Nicky, Robin H., Robin N., Felix, Elham, Matt, Vincent, and Matthias. It has been a joy seeing your careers blossom and meeting up with you around the globe, whether in Vancouver, at CERN, or in California. Thank you to the UVic ATLAS group, Bob, Michel, and Richard, for letting me join in on your lunches, and Tony, Alison, Kayla, Claire, Justin, Ryan,

and Danika, for making my summer at UVic so much fun. Thank you to the CMS μTCA group at DESY: Isabel, Ulf, and especially Özgür for teaching me how to mentor students by being a fantastic mentor to me. Thank you, Brad, Jens, and the TITAN group, for making my first research position as an undergrad such a positive experience. Thank you, Jason, for starting this adventure with me and for holding my hand throughout the PhD application process.

I also would like to thank all of the friends I have made through CERN during this PhD experience. Kathryn, thank you for your feisty personality, that bottle of wine after my flight back to Geneva that one time, and the many long tram-rides home. Danny, thank you for the Yaris adventures and for tolerating Kathryn and I's atrocious singing. Thank you, Sean, for all the particooles and the "cool, cool, cool"s. Thank you, Jennet, for the slime, and Lesya and Audrey for the R1 menu translation pictures. Thank you, Melissa, Alex, Konstantin, Naomi, Giacomo, Matthew, and so many others, for the fun times skiing, brunching, and hanging out at CERN.

Thank you to all of my Stanford friends. Thank you, Cyndia and Ben, for the hikes and hotpot, and Cyndia especially, for the cookies, gossip, and sharing all of the existential angst. Thank you, Ryan and Kelly, for the DC trips. Thank you, Kate and Claire, Alana, Saarik, and Nick, for TJs snacks, climbing, and BBQs. Thank you also to Alex, Matt, and Megan for keeping Fizz alive at Stanford and for all the international tax advice.

Sameen, and Jessica, thank you for being the best pandemic roommates ever - thank you both for indulging me in the trashiest of mid-covid TV shows. Sameen, I couldn't have gotten through that first period of the shelter-in-place when it was just the two of us without you. Thank you for BBG and your endless amount of hobbies. Thank you, Jessica, for the sourdough and blazingly fast Gen Z internet skills. I'm excited for the day when we can all call ourselves doctors.

Thank you also to the Snailbours for being a fabulous neighbourhood community. Jacob for teaching me the kindness in driving people to airports and making people art. Mel, Alan, Julie, and Marty, for always welcoming us at the Bunhouse for dinner and the wild and wonderfully-themed parties. Aurora, Nate, and Gabriel, for the speed record on Cathedral peak, skiing Becker, and making fresh pasta from scratch while camping in the desert. Thank you also to Matt, Emily, Kathy, and Blaire, for leading me up big and scary rocks outdoors despite my fear of heights, and racing around Woodside in the cold.

Thank you to the Canadian hiking crew, Alei, Charlotte, Krissy, Florina, and Emma. Our yearly backpacking trips have been a much appreciated break from the grind of the PhD. I can't believe we have pulled off trips five years in a row! Broken collarbones, bears, cougars, coyotes, couloirs, and pandemics have nothing on us, and I'm already looking forward to Tour de Mont Blanc next year.

Thank you to my grandparents and extended family for your support. Thank you for never letting me take myself too seriously and for teasing me about being unable to find large things like my skis, even though I have spent my entire PhD looking for very small things.

Thank you, Joey, for these past two years. Thank you for teaching me spontaneity and how to

look up at the sky. Thank you for bringing me tea in the mornings. Thank you for our backcountry laps in Tahoe, for taking me flying through fireworks, and waking up with me beside the ocean or next to stampeding cows. I am so excited for this next adventure with you.

Thank you, Krissy, for being the most precious baby sister. I am so lucky to have someone who understands me so completely. Thank you for our long phone calls while running, even just to commiserate about bugs in our code, or to chat about what we are going to eat for dinner. Thank you for dancing on the chairlifts, lighting all the campfires, and never failing to take a picture of me whenever I fall down. Thank you to Sean for falling in love with Krissy and making her happy.

Thank you to my parents, Kiera and Tony, for encouraging me to follow my dreams and letting me fail. For raising me across countries and continents and making every place feel like home. Thank you, Mum, for encouraging me to have a life that is interesting rather than perfect. And thank you, Papa, for teaching me that time is worth money, so you better be doing something worthwhile with it. I am so grateful to both of you for the decades of love and support.

And finally, thank you to California for the glorious sunshine, beautiful landscape, and the people you have brought together for this period of my life.

Contents

List of Tables

List of Figures

Chapter 1

Motivation for HH Searches

In 2012 the ATLAS and CMS experiments at the Large Hadron Collider (LHC) announced the discovery of the Higgs boson [1, 2]. Since then, major efforts have been dedicated to studying the properties of the Higgs, such as its mass, spin, parity, and couplings to other particles. To date, all reported results have been consistent with the Standard Model (SM) predictions [3, 4, 5, 6]. This chapter will introduce the Standard Model Higgs boson and its properties. In particular, one of its properties, the Higgs boson self-coupling, is still largely unconstrained. In this chapter, we will discuss how to probe the Higgs self-coupling through Higgs boson pair production (HH) searches and how a deviation of the HH production rate from the Standard Model prediction would point to new physics beyond the Standard Model.

1.1 The Standard Model of particle physics

The Standard Model of particle physics is currently our best theoretical framework describing the fundamental particles in our universe and their interactions. A fundamental particle is not composed of any other particles. In other words, it is a particle that, as far as we can tell, contains no internal structure. As shown in Figure 1.1, 17 fundamental particles make up the Standard Model. These 17 particles can be split into two categories fermions and bosons.

The fermions all have the property of half-integer spin. Fermions can be further subdivided into quarks and leptons. Quarks carry fractional electric charge and colour charge, which allows them to interact via the strong, electromagnetic, and weak forces. Up-type quarks carry a charge of $+2/3$, and down-type quarks carry a charge of $-1/3$. Leptons have integer electric charge and no colour charge. Because they are colourless, leptons do not interact via the strong force and only interact via the electromagnetic and weak forces. Charged leptons have a charge of -1 and include the electrons, muons, and tau leptons. Each charged lepton is paired with a neutrino of the same flavour. As the name suggests, neutrinos are electrically neutral. Three generations of fermions

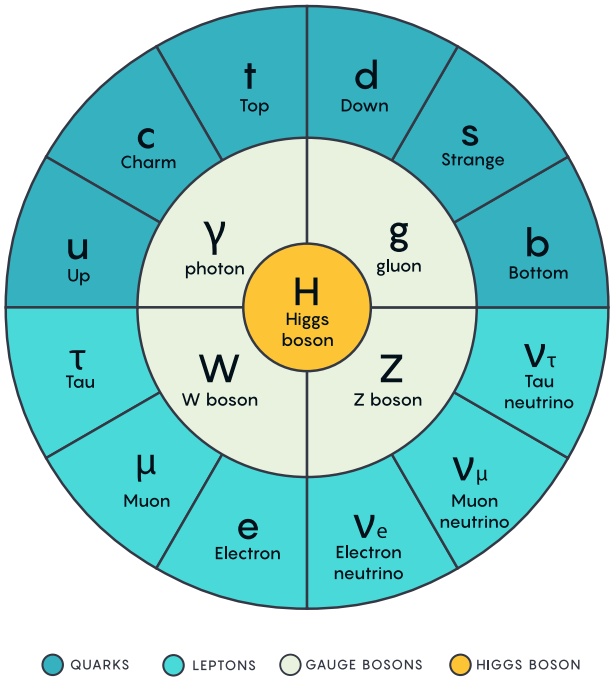

Figure 1.1: The fundamental particles of the Standard Model. Figure adapted from Ref. [7]

exist, each generation heavier than the first. The first generation consists of the $u, d, e, \& \nu_e$, the second consists of the $c, s, \mu, \& \nu_\mu$ and the third consists of the $t, d, \tau, \& \nu_\tau$. These generations all share similar properties except for their masses, which vary by many orders of magnitude as shown in Table 1.1. As the heavier particles decay into lighter ones, the matter we see around us is primarily composed of the first generation of leptons. Up and down quarks make up protons and neutrons, and electrons, when combined with protons and neutrons, make up our atoms. However, the reason why we have three generations of fermions is still a mystery.

The bosons have integer spin. The spin-1 bosons, the photon, the W & Z bosons, and the gluon are each affiliated with a different force. The photon mediates the electromagnetic force, the W & Z bosons mediate the weak force, and the gluon mediates the strong force. As we will see in the next section, the electromagnetic and weak forces are low-energy manifestations of the electroweak force. Electroweak symmetry breaking describes how the electroweak force breaks into the electromagnetic and weak forces. The Higgs boson plays a key role in electroweak symmetry breaking. It is also unique as it is the only known spin-0 particle in the Standard Model. The Higgs mass is a free parameter in the SM. The latest results from ATLAS and CMS place the mass at 125.09±0.24 GeV as shown in Figure 1.2.

Particle Name	Symbol	Mass	Electric Charge	Spin
Quarks				
Up	u	2.16 MeV	+2/3	+1/2
Charm	c	1.27 GeV	+2/3	+1/2
Top	t	173 GeV	+2/3	+1/2
Down	d	4.67 MeV	-1/3	+1/2
Strange	s	93.4 MeV	-1/3	+1/2
Bottom	b	4.18 GeV	-1/3	+1/2
Leptons				
Electron	e	0.51 MeV	-1	+1/2
Muon	μ	105 MeV	-1	+1/2
Tau	τ	1.77 GeV	-1	+1/2
Electron neutrino	ν_e	< 1.1 eV	0	+1/2
Muon neutrino	ν_μ	< 1.1 eV	0	+1/2
Tau neutrino	ν_τ	< 1.1 eV	0	+1/2
Bosons				
Photon	γ	0	0	1
Gluon	g	0	0	1
Z	Z	91.2 GeV	0	1
W	W	80.4 GeV	$\pm$ 1	1
Higgs	H	125.09 GeV	0	0

Table 1.1: Table of fundamental particles and their measured masses [8]. Note that while SM neutrinos are technically massless, the SM can be extended to include Dirac or Majorana neutrinos.

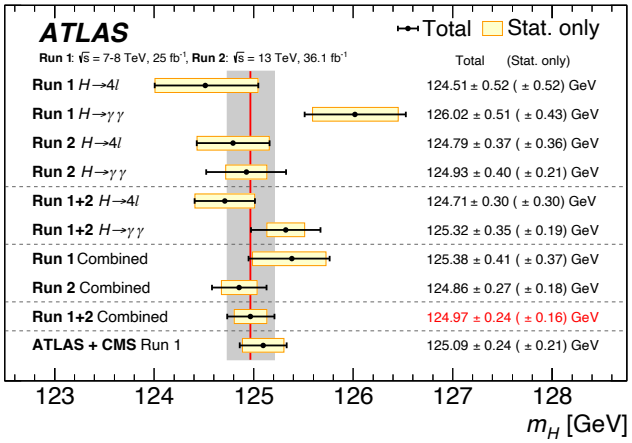

Figure 1.2: Higgs boson mass as measured by the ATLAS and CMS experiments during Run 1 and Run 2 [9].

1.2 Symmetries of the Standard Model

The way particles within the Standard Model interact can be described by a quantum field theory with the following gauge symmetry:

$$SU_C(3) \times SU_L(2) \times U_Y(1)$$

The first term, $SU_C(3)$, describes quantum chromodynamics, e.g. the strong interaction between coloured particles. The $SU_C(3)$ group has 8 generators consisting of the 8 3x3 Gell-Mann matrices corresponding to the 8 massless gluon colours. The second two terms $SU_L(2) \times U_Y(1)$ correspond to the Electroweak interaction, the four generators of which give rise to the physics $W^{\pm}$, Z, and γ bosons. The $SU_L(2)$ symmetry conserves handedness because it can only couple with left-handed particles (or right-handed anti-particles). The $U(1)$ symmetry conserves hypercharge, Y, where $Y = 2(Q - I_3)$, and Q is charge, and I_3 is the third component of isospin.

Following these symmetries, the Standard Model Lagrangian can compactly be written as:

$$\mathcal{L} = -\frac{1}{4}F^a_{\mu\nu}F_a^{\mu\nu} + i\bar{\psi}\not{D}\psi + (y_{ij}\bar{\psi}_i\bar{\psi}_j + h.c.) + |D_\mu\phi|^2 - V(\phi)$$

Where ψ are the fermion fields, ϕ is the Higgs (scalar) field, $F^a_{\mu\nu}$ is the field strength tensor of the A_μ gauge fields, $F^a_{\mu\nu} = \partial_\mu A^a_\nu - \partial_\nu A^a_\mu + g f^{abc} A^b_\mu A^c_\nu$, D_μ is the gauge covariant derivative, $D_\mu = \partial_\mu - igA^a_\mu t_a$, and t_a is a group generator. The field strength tensor and covariant derivative ensure gauge invariance.

However, there are no explicit mass terms in the SM Lagrangian. This is a problem as we know that fermions have mass, and massive bosons such as the W and Z exist. To solve this problem, the Brout-Englert-Higgs mechanism was posed as a solution [10, 11, 12, 13, 14, 15]. This mechanism introduces a self-interacting complex scalar field (the Higgs field) which breaks the $SU_L(2) \times U_Y(1)$ symmetry.

1.3 The Higgs field and Electroweak Symmetry Breaking

The Higgs field is a weak isospin doublet with four components:

$$\phi = \begin{pmatrix} \phi^+ \\ \phi^0 \end{pmatrix} = \frac{1}{\sqrt{2}} \begin{pmatrix} \phi_1 + i\phi_2 \\ \phi_3 + i\phi_4 \end{pmatrix} \tag{1.1}$$

Where ϕ^+ is a positively charged field and ϕ^0 is a neutral field.

The portion of the SM Lagrangian from Eq. 1.2 associated with the Higgs field is:

$$\mathcal{L} = |D_\mu\phi|^2 - V(\phi) \tag{1.2}$$

The first term is the kinetic term, where D_μ is chosen to ensure invariance under $SU_L(2) \times U_Y(1)$ symmetry.

$$D_\mu = \partial_\mu + igT \cdot W_\mu + \frac{ig'}{2} Y B_\mu \tag{1.3}$$

Here g and g' are the strengths of the $SU_L(2)$ and $U_Y(1)$ gauge couplings. The Higgs potential $V(\phi)$ is described by:

$$V(\phi) = -\mu^2 \phi^2 + \lambda \phi^4 \tag{1.4}$$

Differentiating with respect to ϕ^2, we can find the minimum of the potential is the vacuum expectation value. For $\mu^2 \leq 0$ this minimum is at 0, but for $\mu^2 > 0$ the minimum is at:

$$\phi^\dagger \phi = \frac{-\mu^2}{2\lambda} = \frac{v^2}{2}, \qquad v = \sqrt{\frac{-\mu^2}{\lambda}} = \frac{2m_W}{g} = 246 \text{ GeV}$$

I.e., there are infinite minima in the complex ϕ^+, ϕ^0 plane at the vacuum expectation value v. A projection of this potential in two dimensions is shown in Figure 1.3.

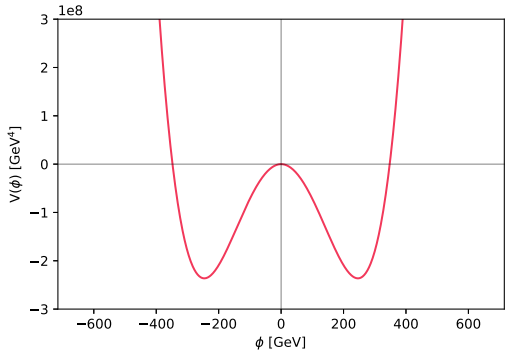

Figure 1.3: The Standard Model Higgs potential

We can arbitrarily choose a direction for ϕ (spontaneous symmetry breaking):

$$\langle \phi \rangle = \frac{1}{\sqrt{2}} \begin{pmatrix} 0 \\ v \end{pmatrix} \tag{1.5}$$

E.g., $\phi_1 = \phi_2 = \phi_4 = 0$ and $\phi_3 = v$, this choice of vacuum state breaks the local gauge symmetry, although the potential itself is still symmetric. This particular choice of gauge is known as the unitarity gauge. Perturbing about this vacuum state, we can rewrite $\phi(x)$ as a function of the mass scalar Higgs field:

$$\langle \phi \rangle = \frac{1}{\sqrt{2}} \begin{pmatrix} 0 \\ v + h(x) \end{pmatrix} \tag{1.6}$$

and substituting into the part of SM Lagrangian from Equation 1.2 corresponding to the Higgs we get:

$$\begin{aligned} \mathcal{L} = & \frac{1}{2}(\partial_\mu h)(\partial_\mu h) \\ & + \frac{1}{8} g^2 W_\mu W^\mu (v+h)^2 + \frac{g'^2 + g^2}{8} Z_\mu Z^\mu (v+h)^2 \\ & + \frac{\mu^2}{2}(v+h)^2 - \frac{\lambda}{16}(v+h)^4 \end{aligned} \tag{1.7}$$

In this expansion, the W, Z, and Higgs bosons have subsequently acquired masses corresponding to the quadratic terms associated with their respective gauge fields:

$$m_W = \frac{gv}{2}, \; m_Z = \frac{\sqrt{g'^2 + g^2}v}{2}, \; m_H = \sqrt{2\mu^2}$$

The Higgs field interacts with fermions via the Yukawa interaction and fermions also acquire masses via their interaction with the Higgs [8]. This will not be derived in this thesis, but can be written as:

$$m_f = \frac{h_f v}{\sqrt{2}}$$

Where h_f is the Higgs-fermion interaction. It is interesting to note that Higgs couplings to fermions are linearly proportional to their masses, while the couplings to bosons are proportional to the square of the boson masses. As a result, the dominant mechanisms for Higgs boson production and decay involve the coupling of the Higgs to $W^\pm$ and Z bosons, and the heavier third-generation fermions (top and bottom quarks and the τ leptons). Figure 1.4 shows the measured Higgs boson couplings to SM particles with respect to both the fermion and boson masses as measured by ATLAS. These couplings are measured by measuring the cross-sections for the experimentally accessible Higgs boson production and decay modes. Within the experimental uncertainties, they all agree remarkably well with the SM prediction. The couplings to electrons and light quarks have not yet been measured, since the Higgs boson couples less strongly to lighter particles.

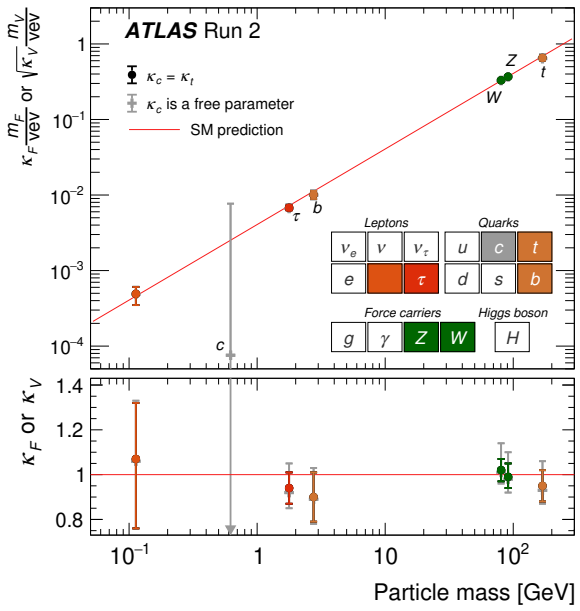

Figure 1.4: Measured Higgs boson coupling strength modifiers and their uncertainties, defined as $\kappa_F m_F/v$ for fermions and $\sqrt{\kappa_V} m_V/v$ for vector bosons. [16]

1.4 The Higgs self-coupling

At this point we have talked about the Higgs mass and its couplings to other particles, but one term we have yet to examine is the Higgs self-coupling. This is described by the λ term in the SM Higgs potential.

$$V(\phi) = -\mu^2\phi^2 + \lambda\phi^4 \tag{1.8}$$

In the SM, the Higgs self-coupling at the minimum of the Higgs potential is expected to be:

$$\lambda_{\text{SM}} = \frac{m_h^2}{2v^2} = 0.129 \tag{1.9}$$

Taking this last term and once again choosing the unitarity gauge and perturbing by $h(x)$ about the minimum of the Higgs potential (v) we can write:

$$\begin{aligned} \lambda\phi^4 =& \lambda\left(\frac{(v+h(x))}{\sqrt{2}}\right)^4 \\ \approx& \frac{1}{4}(\lambda h^4 + 4\lambda v h^3 + 6\lambda v^2 h^2 + ...) \end{aligned} \tag{1.10}$$

This first term is the quartic interaction, but the second term shows that the triple Higgs interaction (h^3) is also sensitive to the Higgs self-coupling. This is important because it provides a way to probe the Higgs self-coupling through any interactions that involve such vertices. These triple Higgs and quartic interactions are illustrated in Figure 1.5.

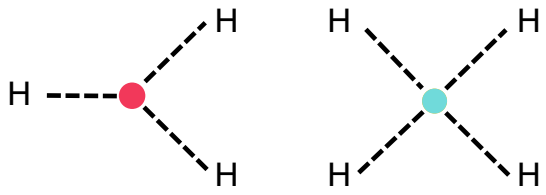

Figure 1.5: Illustration of triple and quartic Higgs self-interactions

In particular, the ratio of the measured Higgs self-coupling to its expected Standard Model value can be defined as κ_λ:

$$\kappa_\lambda = \frac{\lambda}{\lambda_{\text{SM}}} \tag{1.11}$$

HH and single Higgs production processes are sensitive to variations of κ_λ. Precise measurements of their inclusive and differential cross-sections can be used to set constraints on κ_λ. However, as we will see in Sections 1.8 and 1.9, this is an extremely challenging measurement due to the low HH production cross-section, and the relatively small effects of κ_λ on the single Higgs processes. Because of these challenges, a precise measurement of κ_λ may take decades or more to establish. For example, in Chapter 8 we will explore the prospects for measuring κ_λ with ATLAS and 4000fb^{-1} of High Luminosity LHC data. From these studies, κ_λ is expected to be constrained to 50% uncertainty if the Higgs potential is SM-like. By measuring κ_λ we will be able to thoroughly test our understanding of electroweak symmetry breaking. Measuring κ_λ will allow us to understand the Higgs interactions with itself and probe the shape of the Higgs potential in an entirely new way. This is a worthwhile endeavor in itself and will be an achievement to celebrate. That said, part of the reason why measuring the Higgs self-coupling is interesting is because many reasons could cause κ_λ to stray from its Standard Model value of 1. As we will discuss in Section 1.9, deviations in κ_λ would also increase the HH production rate. The next section will discuss how new physics could cause deviations in κ_λ, and the remainder of the thesis will be dedicated to our efforts in measuring κ_λ.

1.5 The Higgs and physics beyond the Standard Model

Although the Standard Model is our best theory of the particles we can detect on earth, there are numerous questions it does not answer. Some of the most pressing of these questions surround the nature of dark matter, dark energy, and the matter/anti-matter asymmetry in our universe.

Extensions to the Standard Model, through the addition of new particles and fields, attempt to address these questions, but we have yet to find any evidence for them on earth. The Higgs sector could provide us with key insights towards solving these mysteries as it contains both the most recently discovered particle and is the sector with the largest number of free parameters in the Standard Model.

For example, the Higgs boson could have exotic decay modes to light dark matter particles. Alternatively, heavy particles, such as a spin-0 Z', spin-2 Randall-Sundrum graviton, or other scalar particles generated in many super-symmetry theories, such as two Higgs doublet models, could decay to Higgs pairs. Searches for these resonant signatures are important for constraining the space of possible dark matter models. In addition to the resonant signatures, new particles, such as light, colored scalars could result in non-resonant enhancements to the HH cross-section through loop corrections [17].

New physics signatures can also be probed through measurements of the Higgs couplings to other Standard Model particles, as illustrated earlier in Figure 1.4. The Higgs self-coupling, in particular, allows us to probe the shape of the Higgs potential. A broad class of new physics models that alter the Higgs field, such as the Minimal Super-symmetric Standard Model, the Next-to-Minimal Super-symmetric Standard Model, and Little Higgs models, could change the shape of the Higgs potential [18]. For illustration, Figure 1.6 shows three examples of BSM models that would alter the Higgs potential alongside the SM Landau-Ginzburg Higgs potential.

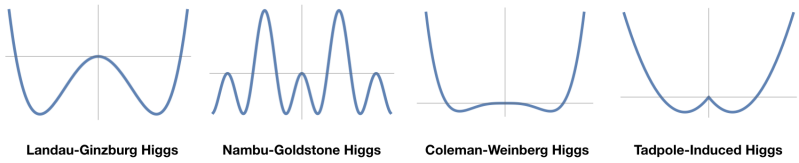

Figure 1.6: Examples of different Higgs potentials associated with different models [19]

Some of the most popular classes of models that make the Higgs potential interesting are those that could be a solution to the matter/anti-matter asymmetry in our universe. These models are known as electroweak baryogenesis models and point to the electroweak phase transition as a possible source of the asymmetry we see today. The electroweak phase transition occurred as the universe expanded and cooled, and the electroweak force decoupled into electromagnetism and the weak force. During this transition, the Higgs potential went from being perfectly symmetric to being spontaneously broken. As illustrated in Figure 1.7a, in the Standard Model this transition was smooth and is not expected to be a source of baryogenesis. However, if the phase transition was a first-order transition, it could produce a double minimum at some critical temperature, as illustrated in Figure 1.7b. This would create a meta-stable state where the Higgs field could be broken in some places in the universe and symmetric in other places. Bubbles of the symmetry-broken phase could

nucleate and expand within the surrounding symmetric phase. If CP violation can occur in the underlying electroweak theory, baryon asymmetries could be created along the bubble walls and be a source of baryogenesis [20]. A first-order phase transition in the early universe could result in O(1) deviations to the Higgs potential seen today [18]. Precise measurements of the Higgs self-coupling could help rule out many models that are candidates for electroweak baryogenesis today.

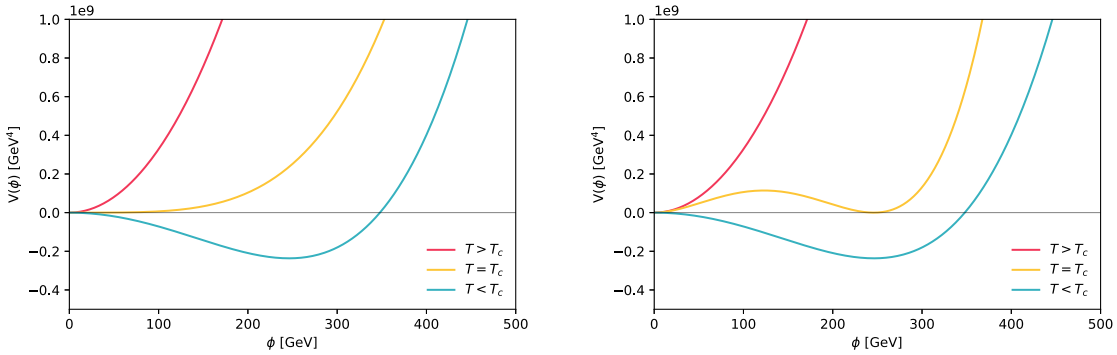

(a) (b)

Figure 1.7: (a) First and (b) second-order phase transitions of the Higgs potential as a function of temperature (T)

1.6 Higgs production mechanisms at the LHC

Higgs production at the LHC occurs primarily through gluon-gluon fusion (ggF), vector boson fusion (VBF), Higgs-strahlung (WH, ZH) and associated production with a $t\bar{t}$ pair ($t\bar{t}H$). The leading order Feynman diagrams for each of these processes is shown in Figure 1.8. The predicted cross-sections of these main production processes and their associated uncertainties are listed in Table 1.2. Gluon–gluon fusion is the dominant production mode with a total cross-section of 48.6 pb.

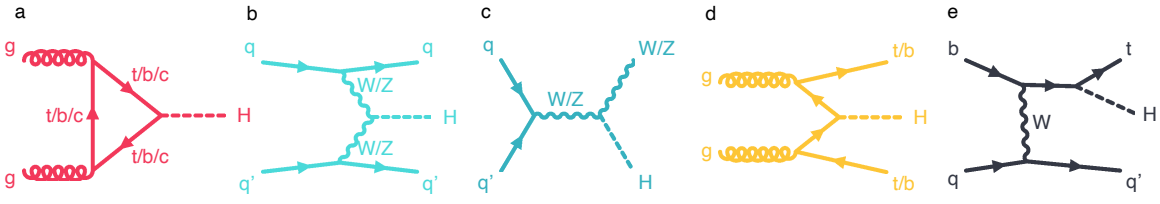

Figure 1.8: Examples of Feynman diagrams for Higgs boson production. The Higgs boson is produced via gluon–gluon fusion (a), vector-boson fusion (VBF; b), and associated production with vector bosons (c), top- or b-quark pairs (d), or a single top quark (e). Figure adapted from Ref. [16]

Production Mode	Cross-section (pb)
ggF	$48.6^{+4.6}_{-6.7}$
VBF	$3.78^{+2.2}_{-2.2}$
WH	$1.37^{+2.6}_{-2.6}$
ZH	$0.88^{+4.1}_{-3.5}$
$t\bar{t}H$	$0.50^{+6.8}_{-9.9}$
Total	55.1

Table 1.2: Table of expected Higgs production cross-sections for an SM Higgs boson with $m_H = 125$ GeV at $\sqrt{s}$ =13 TeV [8]

Single Higgs cross-section uncertainties

The uncertainties on the ggF Higgs cross-sections come from a variety of different sources as illustrated in Figure 1.9. The dominant uncertainty, $\delta(\text{PDF} + \alpha_s)$, comes from uncertainties around the Parton Distribution Functions (PDFs) and running of the strong coupling constant (α_s). Uncertainties surrounding QCD corrections at higher orders beyond N^{3}LO are accounted for by the δ(scale) uncertainty. Higher order effects due to electroweak corrections are included in the δ(EW) uncertainty. The δ(PDF-TH) uncertainty attempts to account for the fact that the PDFs are evaluated at NNLO, where the full QCD cross-sections are evaluated at N^{3}LO. δ(t,b,c) accounts for the finite quark masses which are neglected in QCD correction beyond NLO. $\delta(1/m_t)$ is an uncertainty that comes from the top-quark mass scheme [21, 22, 23]. The same types of uncertainties are also applicable to HH production, although ggF HH production is calculated at NNLO, therefore the exact size and ratios of the uncertainties are slightly different.

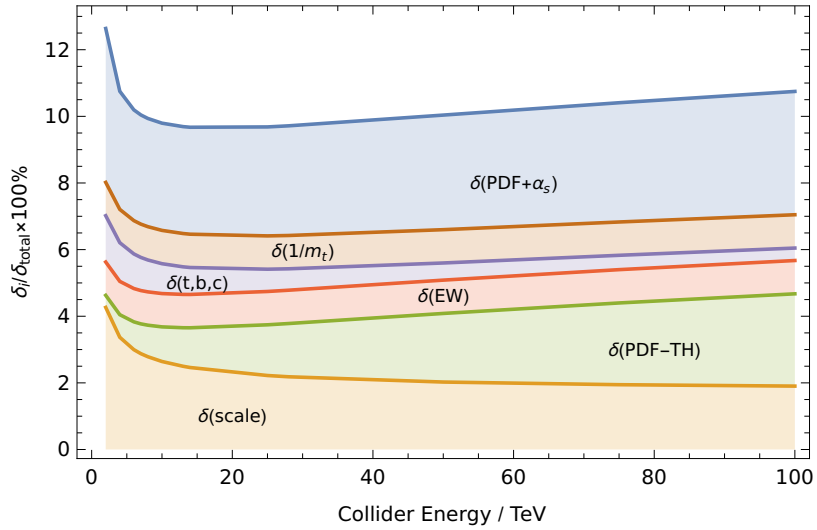

Figure 1.9: ggF Higgs cross-section uncertainty breakdown [21]

1.7 Higgs decay modes

Due to its large mass of 125 GeV, the Higgs can decay to almost all of the SM particles, with the exception of the top quark which has a mass of 173 GeV. As discussed in Section 1.4, the Higgs interacts most strongly with heavy particles. The expected branching ratios for each Higgs decay mode are shown in Table 1.3. The dominant Higgs decay mode is $H \to b\bar{b}$ with a branching fraction of 58%. It is worth noting that because photons are not massive particles, $H \to \gamma\gamma$ is highly suppressed and has a small branching ratio of 0.227%. The $H \to \gamma\gamma$ decay proceeds either through a W or fermion loop as illustrated in Figure 1.10. The primary contribution in the fermion loop is through the top quark due to the large top-Yukawa interaction. Despite this very small branching fraction, $H \to \gamma\gamma$ is a very clean signature at the LHC and was one of the leading channels in the Higgs discovery.

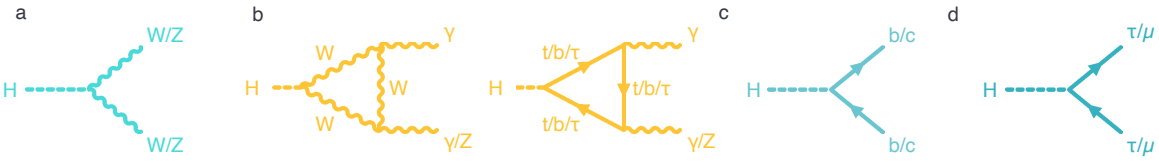

Figure 1.10: Examples of Feynman diagrams for Higgs boson decays. The Higgs boson decays into a pair of vector bosons (a), a pair of photons or a Z boson and a photon (b), a pair of quarks (c), and a pair of charged leptons (d). Figure adapted from Ref. [16]

Decay channel	Branching Ratio (%)	Relative Uncertainty (%)
$H \to b\bar{b}$	58.2	$^{+1.2}_{-1.3}$
$H \to W^+W^-$	21.4	$\pm$ 1.5
$H \to \tau^+\tau^-$	6.27	$\pm$ 1.6
$H \to c\bar{c}$	2.89	$^{+5.5}_{-2.0}$
$H \to ZZ$	2.62	$\pm$ 1.5
$H \to \gamma\gamma$	0.227	$\pm$ 2.1
$H \to Z\gamma$	0.153	$\pm$ 5.8
$H \to \mu^+\mu^-$	0.0218	$\pm$ 1.7

Table 1.3: Table of expected Higgs decay branching ratios for an SM Higgs boson with $m_H = 125$ GeV at $\sqrt{s}$ =13 TeV[8]

1.8 Single Higgs sensitivity to κ_λ

Although single Higgs boson processes are not sensitive to the Higgs self-coupling at leading order, the self-coupling contributes to the next to leading order electroweak corrections. The Feynman diagrams for the self-coupling's contribution to both the Higgs self-energy and through additional

corrections are shown in Figure 1.11. As shown in Figure 1.12, changes in κ_λ can result in changes to the overall Higgs cross-sections and branching ratios, as well as the overall kinematics. Although these effects are relatively small compared to those that we will see in HH production, κ_λ can be constrained by comparing precise measurements of single Higgs measurements to predictions that involve these corrections as suggested by Ref. [24, 25, 26, 27, 28, 29].

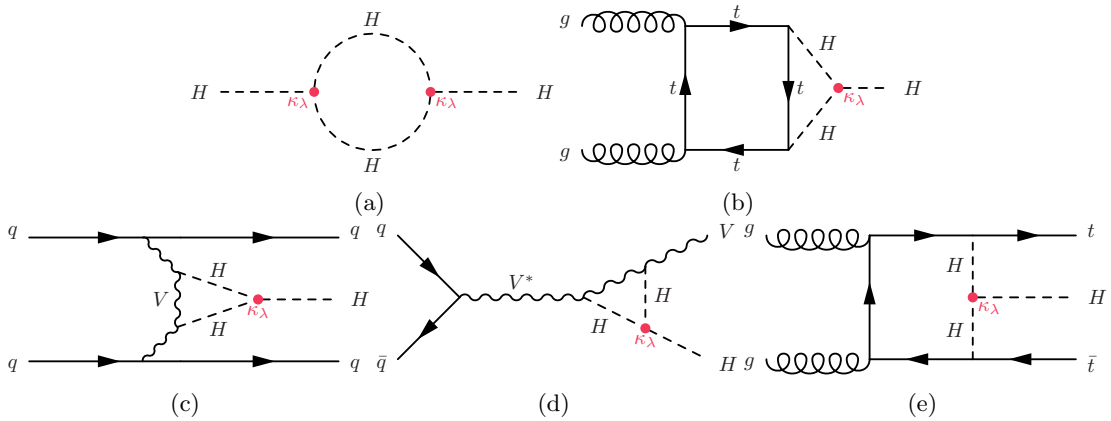

Figure 1.11: Examples of one-loop κ_λ dependent single Higgs diagrams for (a) the Higgs boson self-energy, and for single Higgs production in the (b) ggF, (c) VBF, (d) VH, and (e) $t\bar{t}H$ modes [30].

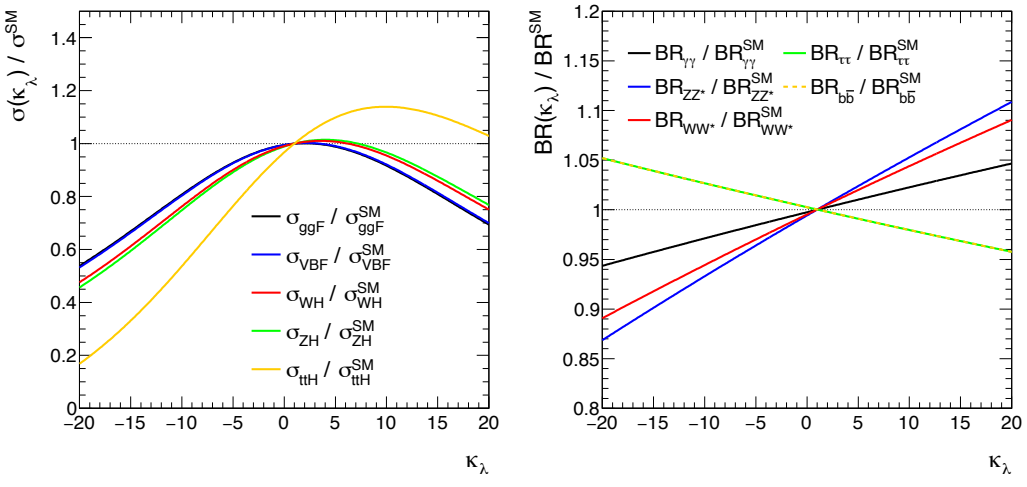

Figure 1.12: Changes to the single Higgs (a) cross-sections and (b) branching ratios as a function of κ_λ [31].

1.9 HH production mechanisms

Like single Higgs production, Higgs pairs can be produced through several different production mechanisms at the LHC. Figure 1.13 shows the most common production modes as a function of the center of mass energy. Similar to the single Higgs production modes, at $\sqrt{s}$ =13 TeV these include ggFHH production, VBF HH production, double Higgs bremsstrahlung from top quarks ($t\bar{t}\,HH$), and double Higgs-strahlung (WHH/ZHH). In this thesis, we will focus on the dominant ggF and VBF HH production modes with cross-sections of 31.02 and 1.72 fb respectively. Future colliders may be able to measure the other production modes ($t\bar{t}\,HH$, WHH, ZHH, and tjHH), but as they have much lower SM cross-sections, they are neglected for now.

HH production rates vary as a function of the Higgs self-coupling as discussed in Refs. [32, 33, 34]. Figure 1.13 shows the predicted cross-sections as a function of κ_λ. For all production modes, the HH cross-section increases as κ_λ deviates far from the SM.

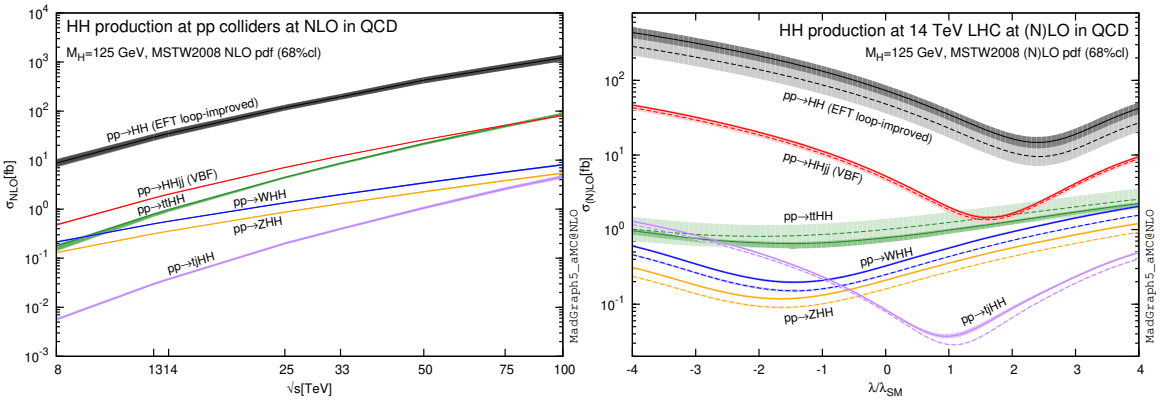

(a) (b)

Figure 1.13: Predicted HH cross-sections as a function of (a) production mechanism and (b) κ_λ [32]

HH production through gluon–gluon fusion

For 13 TeV pp collisions and a Higgs boson mass $m_H = 125.09$ GeV [35], the ggF cross-section, calculated at next-to-next-to-leading-order (NNLO) accuracy in the finite top-quark mass approximation (FTapprox), is $\sigma_{HH}(\text{ggF}) = 31.02^{+2.2\%}_{-5.0\%}\,(\text{Scale})\,^{+4\%}_{-18\%}\,(m_{\text{top}}) \pm 3.0\%\,(\alpha_s\text{+PDF})$ fb [36, 37, 38, 22]. A detailed description of these uncertainties can be found in Section 1.6.

At leading order ggFHH production can be described by the box and triangle Feynman diagrams shown in Figure 1.14. The triangle diagram is sensitive to the Higgs self-coupling (κ_λ) through its triple Higgs vertex. The box diagram does not contain a triple Higgs vertex and therefore is insensitive to κ_λ at leading order. In addition to κ_λ, both the triangle and box diagrams are sensitive to the top-quark Yukawa coupling k_t. For the majority of this thesis, k_t will be set to its

SM value of 1. However, joint measurements of single Higgs and HH production can be combined to constrain both coupling modifiers simultaneously.

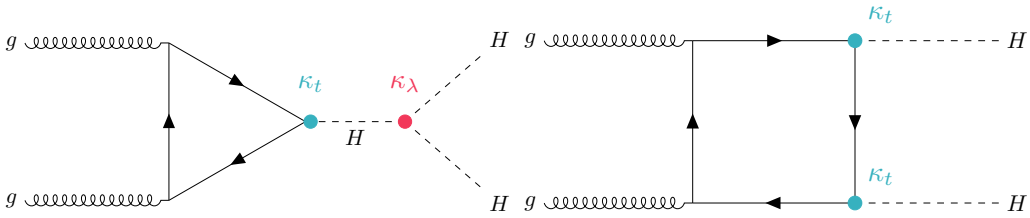

(a) Triangle diagram (b) Box diagram

Figure 1.14: The Feynman diagrams for the dominant gluon–gluon fusion production processes. The quark content in the diagrams is dominated by the top-quark contribution due to the large top-quark Yukawa coupling to the Higgs boson.

The two leading order HH production diagrams interfere destructively, leading to a very small HH production cross-section of 31fb^{-1} at 13 TeV [39, 40, 41]. Because of these strong interference effects, the HH production cross-section is especially sensitive to κ_λ. Figure 1.15 shows the HH and single Higgs cross-sections as a function of κ_λ. Although the HH production cross-section is very small close to the SM, at large absolute values of κ_λ the cross-section grows rapidly. As described in Section 1.4, non-SM values of κ_λ could come from BSM physics models of electroweak baryogenesis. Large deviations in κ_λ would lead to HH cross-sections that could be detected with our Run 2 dataset and are the key motivation for searches for HH production in this thesis.

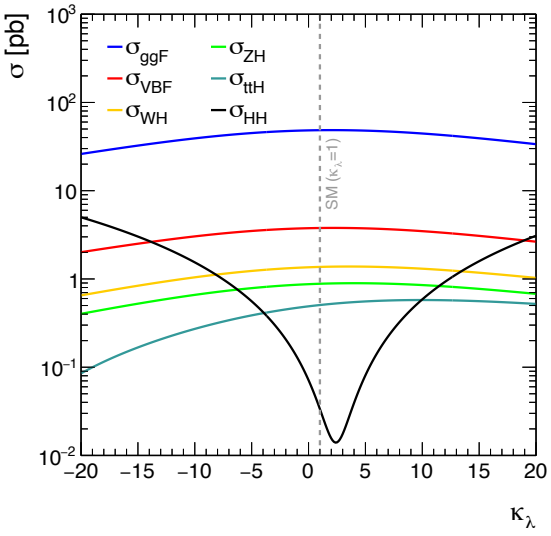

Figure 1.15: HH cross-section as a function of κ_λ relative to single Higgs processes [42]

In addition to increasing the cross-section, changing κ_λ also changes differential m_{HH} distributions. This means that both the overall HH cross-section and the shape of the m_{HH} distribution are sensitive to κ_λ. Figure 1.16 shows the differential cross-sections as a function of m_{HH} for the box and triangle diagrams, their interference, and the overall amplitude. The overall amplitude can be written as a sum of the box and triangle diagrams and their interference terms as follows:

$$\begin{aligned}\frac{d\sigma}{dm_{HH}} &= |A(\kappa_\lambda)|^2 = |\kappa_\lambda M_\triangle(m_{HH}) + M_\square(m_{HH})|^2 \\ &= \kappa_\lambda^2 M_\triangle(m_{HH})^2 + \kappa_\lambda M_\triangle^* M_\square(m_{HH}) + \kappa_\lambda M_\triangle M_\square^*(m_{HH}) + M_\square(m_{HH})^2\end{aligned} \tag{1.12}$$

When κ_λ^2 is very large, the triangle diagram contributes more, and this leads to a shift in the overall m_{HH} spectrum towards lower m_{HH} values. If $\kappa_\lambda = 2.2$, maximum interference occurs and the spectrum shifts towards very high m_{HH} values. When $\kappa_\lambda = 0$, the contribution from the triangle diagram is 0, and therefore the spectrum is entirely dominated by the box diagram and peaks roughly at $2m_{\text{top}}$ due to resonant effects in the virtual top quark loop.

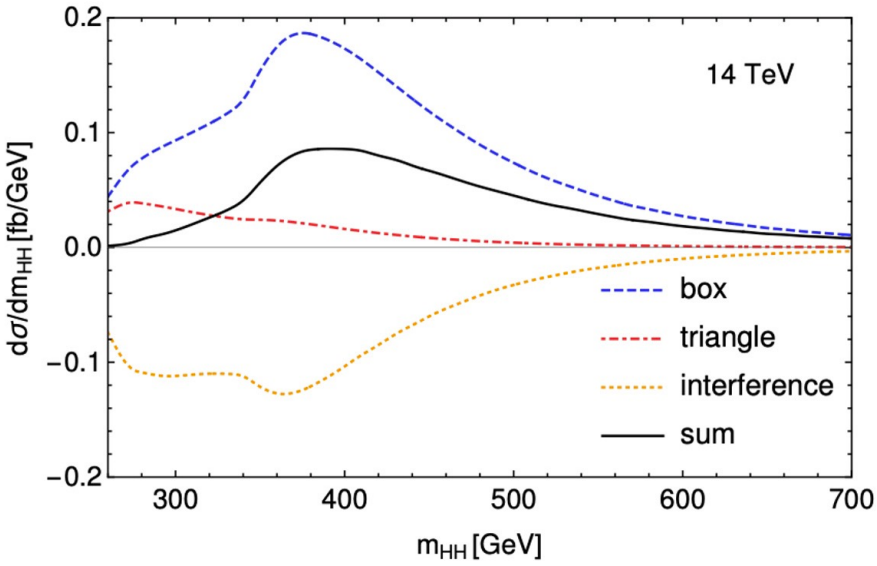

Figure 1.16: Relative contributions of box and triangle diagrams and their interference as a function of m_{HH} [43]

HH production through vector boson fusion

The di-Higgs vector-boson fusion (VBF) production cross-section, calculated at next-to-next-to-next-to-leading order (N3LO) for $m_H = 125.09$ GeV, is $\sigma_{HH}(\text{VBF}) = 1.72^{+0.03\%}_{-0.04\%}\,(\text{Scale})\,\pm 2.1\%\,(\alpha_s\text{+PDF})$ fb [36],

which is one order of magnitude lower than the cross-section of the ggF process. The VBF production mode provides the analysis with additional sensitivity to the Higgs trilinear coupling, as shown in Figure 1.17. In addition to κ_λ sensitivity, VBF HH production is also sensitive to κ_{2V} and κ_V. κ_{2V}, in particular, cannot be probed at leading order through any other process.

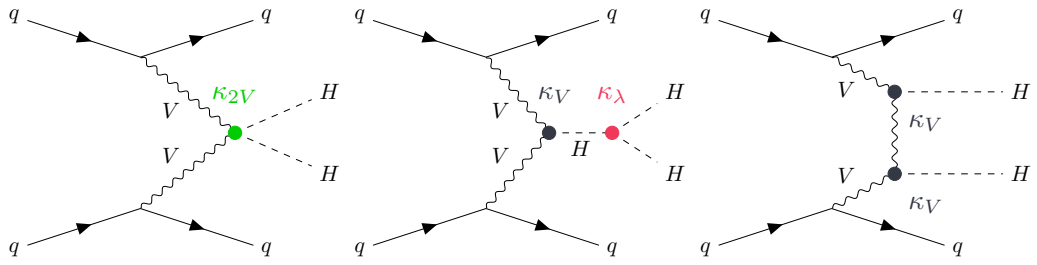

Figure 1.17: The VBF production of Higgs boson pairs via (a) the $HHVV$ vertex, (b) the trilinear coupling, and (c) the VVH production mode.

1.10 HH decay channels

As we saw in Table 1.3 there are many possible final states for Higgs decays. HH searches, by construction, have double the number of possible final states. The branching ratios for some of the most popular search channels are shown in Table 1.18. As the HH production cross-section is very small, the current leading search channels typically make use of at least one Higgs decaying to $b\bar{b}$ in the final state. Three channels dominate the HH sensitivity. $HH \to b\bar{b}b\bar{b}$, $HH \to b\bar{b}\tau^+\tau^-$, and $HH \to b\bar{b}\gamma\gamma$. These channels have a large range in branching ratios going from $b\bar{b}b\bar{b}$ at 33% to $b\bar{b}\gamma\gamma$ at 0.26%. While having a large branching ratio allows for better HH signal statistics, reaching strong analysis sensitivity relies on a combination of high statistics and low background rates. The strengths of the different HH final states will be discussed in more detail in Chapter 7.

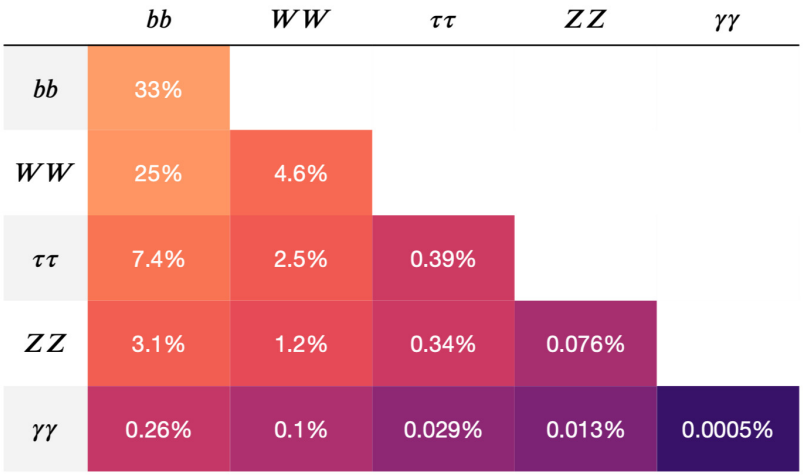

Figure 1.18: Branching ratios for the most popular HH search channels. The columns indicate the final state of one of the Higgs bosons and the rows indicate the final state of the other.

Chapter 2

The ATLAS Experiment

The Large Hadron Collider is a 27 km long particle collider that collides protons at the highest human-made energies of 13 TeV. It sits at the border between Switzerland and France and houses four large general-purpose experiments, ALICE, LHCb, ATLAS, and CMS, as illustrated in Figure 2.1. The goal of these experiments is to understand the properties of fundamental particles to further our understanding of the universe we live in. By colliding protons at sufficiently high energies, new particles can be created. The ATLAS detector uses several carefully designed subsystems to measure the properties of the newly created particles and their interactions. This chapter provides an overview of the LHC and describes the geometry and key design concepts behind the ATLAS experiment.

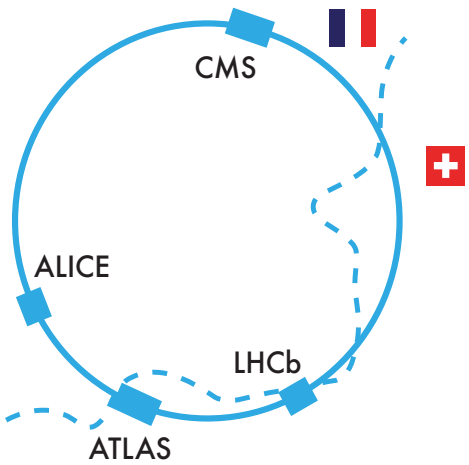

Figure 2.1: Location of the Large Hadron Collider on the border between Switzerland and France

2.1 The Large Hadron Collider

The CERN accelerator complex accelerates protons in several stages, as illustrated in Figure 2.2. First, hydrogen is passed through a duoplasmotron to strip it of its electron, producing a bare proton [44]. These protons are then accelerated by a linear accelerator (LINAC 2) to 50 MeV. These are then passed to the proton synchrotron booster (BOOSTER), where they are accelerated to 1.4 GeV. Next, they pass into the proton synchrotron (PS) where they are accelerated to 25 GeV. Next, they are accelerated by the super proton synchrotron (SPS) to 450 GeV. Finally, they are injected into the Large Hadron Collider (LHC) where they are accelerated in opposite directions, each with an energy of 6.5 TeV [45].

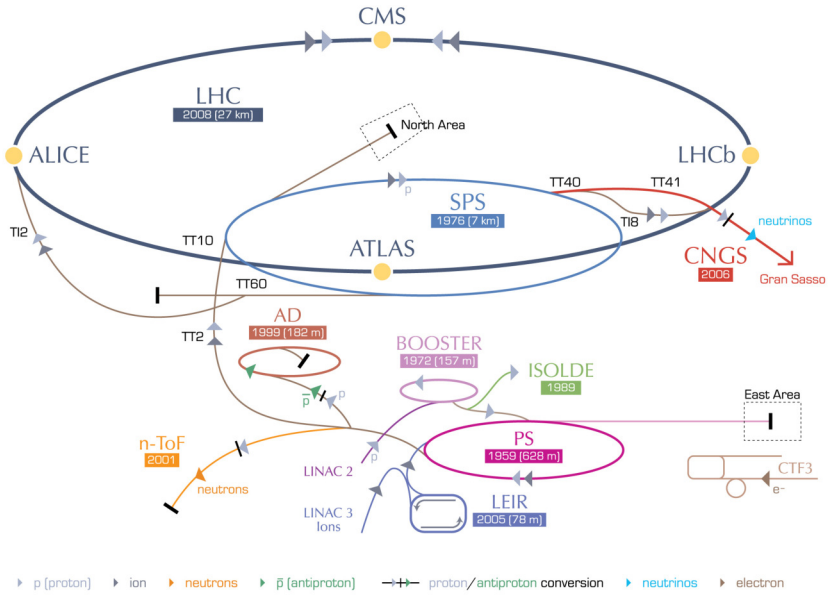

Figure 2.2: CERN Accelerator Complex [46]

After injection, bunches of protons typically circulate in the LHC for about 8 hours before the beam is dumped due to deteriorating beam conditions. The beam circulates in bunch trains of 2808 bunches at a time, 24.95 ns (7 m) apart. Each bunch contains about 1.15×10^11 protons [47]. At the ATLAS interaction point, the beam is focused and is measured to be about $\sigma_{x,y} = 7\,\mu\text{m}$ and $\sigma_z = 30\text{mm}$ in size [48]. Despite the strong focus at the interaction point, only about 30 protons interact during any given bunch crossing. To collect enough data to measure rare processes like HH production, a high instantaneous luminosity is desirable.

The instantaneous luminosity is defined as:

$$L = \frac{N_b^2 n_b f_{\text{rev}} \gamma}{4\pi\sigma_x\sigma_y} F = \frac{N_b^2 n_b f_{\text{rev}} \gamma}{4\pi\sqrt{\epsilon_x \epsilon_y \beta_x \beta_y}} F$$

N_b is number of particles per bunch, n_b number of bunches per beam, f_{rev} frequency of revolution, $\gamma_r = 1/\sqrt{1 - v^2/c^2}$ is the relativistic gamma factor. $\epsilon_{x,y}$ is normalized transverse beam emittance, and $\beta x, y$ is the beta function, which both are related to the shape of the beams and how they are focused. F is the geometric luminosity reduction factor which is an artifact of the beams not colliding head-on.

$$F = \left[1 + \left(\frac{\theta_c \sigma_z}{2\sigma_{x,y}}\right)^2\right]^{-1/2}$$

For a given process the total number of collisions involving the process, known as events, can be calculated by multiplying the cross-section (σ) by the total integrated luminosity $\mathcal{L} = \int L dt$ as shown in Equation 2.1.

$$N_{\text{event}} = \sigma_{\text{event}} \mathcal{L} = \sigma_{\text{event}} \int L dt$$

This means that more events can be collected by running the collider for more time, (t), or increasing the instantaneous luminosity, L.

To put these equations into context, during Run 2, ATLAS has collected 139 fb^{-1}of data. For Higgs production with a total cross-section around 57 pb [49] this means that the number of Higgs events produced during Run 2 has approximately been 8.5 million. For HH production with a cross-section of 31 fb [36] this means that the total number of Higgs events produced has approximately been 4,600. Given that the LHC has an operating budget of ∼$1.2 billion per year, this puts the cost of an individual Higgs boson in ATLAS at $600 and a Higgs pair at $1 million.

The average number of interactions per bunch crossing is defined as pile-up (PU) where:

$$\langle PU \rangle = \frac{L \sigma_{pp}^{\text{inelastic}}}{n_b f_{\text{rev}}}$$

Figure 2.3 shows the distributions of pile-up during the Run 2 data-taking periods where ATLAS collected 139fb^{-1}at 13 TeV during 2015-2018. The pile-up profile is different every year as the beam conditions are continuously optimized. Run 3 of the LHC started in 2022 and is expected to collect 150fb^{-1}at 13.6 TeV. Around 2030 the LHC will be upgraded from an average pile-up of 30 interactions per bunch crossing to 200 at 14 TeV. This upgrade is known as the High-Luminosity LHC. The impact of this upgrade on HH searches is discussed in Chapter 8. To cope with this increased luminosity, the ATLAS detectors will also be upgraded. One of these upgrades, the ATLAS Inner Tracker (ITk), will be discussed in more detail in Chapter 9.

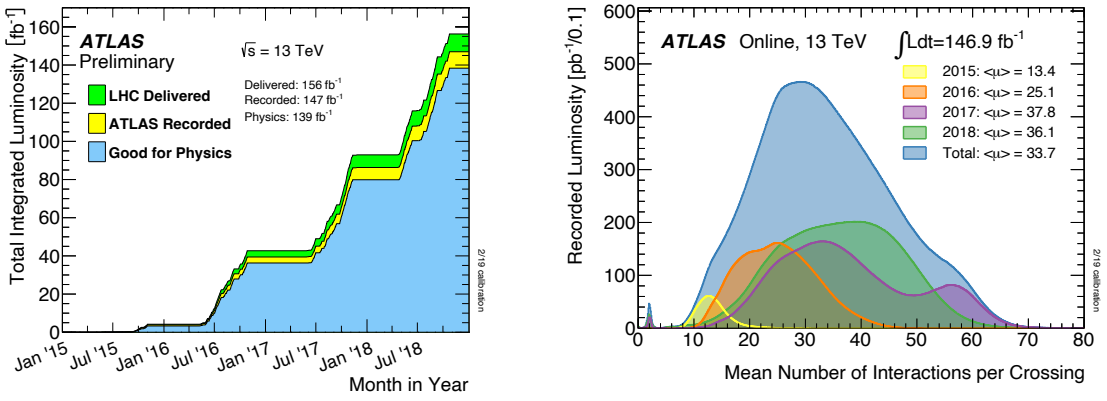

(a) (b)

Figure 2.3: ATLAS integrated luminosity and pile-up during the Run 2 data-taking [50]

2.2 The ATLAS Detector

The ATLAS Detector is the largest of the four general-purpose particle detectors at the Large Hadron Collider. It is over 6 stories tall, as illustrated in Figure 2.4. The majority of the detector volume in ATLAS comes from the toroidal magnets for the muon spectrometer described in Section 2.2.4.

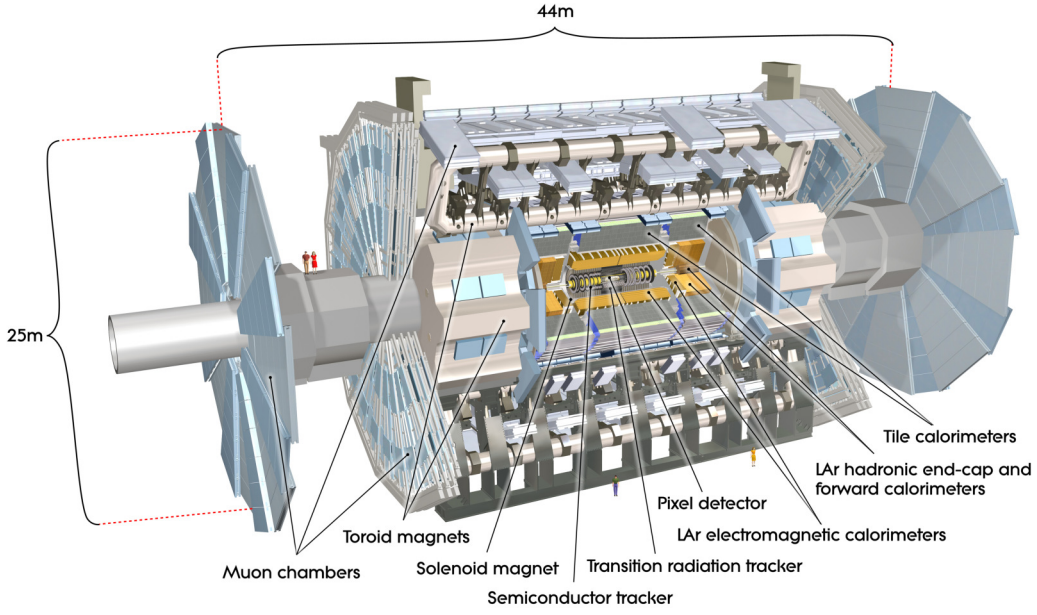

Figure 2.4: The ATLAS detector [51]

Each section of the detector specializes in detecting different types of outgoing particles produced during a collision. The layout of the ATLAS detector subsystems is visualized in Figure 2.5. Tracking detectors are closest to the interaction point and measure the momenta of charged particles. Next, the electromagnetic (EM) and hadronic calorimeter (HCal) systems aim to measure the particle energies and directions by stopping the particles in their volume. Muons are the only charged particles that do not typically lose enough energy to stop in the calorimeter system. The outermost region of the detector, the muon spectrometer, consists of additional tracking layers and is dedicated to identifying muons and measuring their momenta. Neutrinos do not interact with the detectors and therefore escape ATLAS without being directly detected.

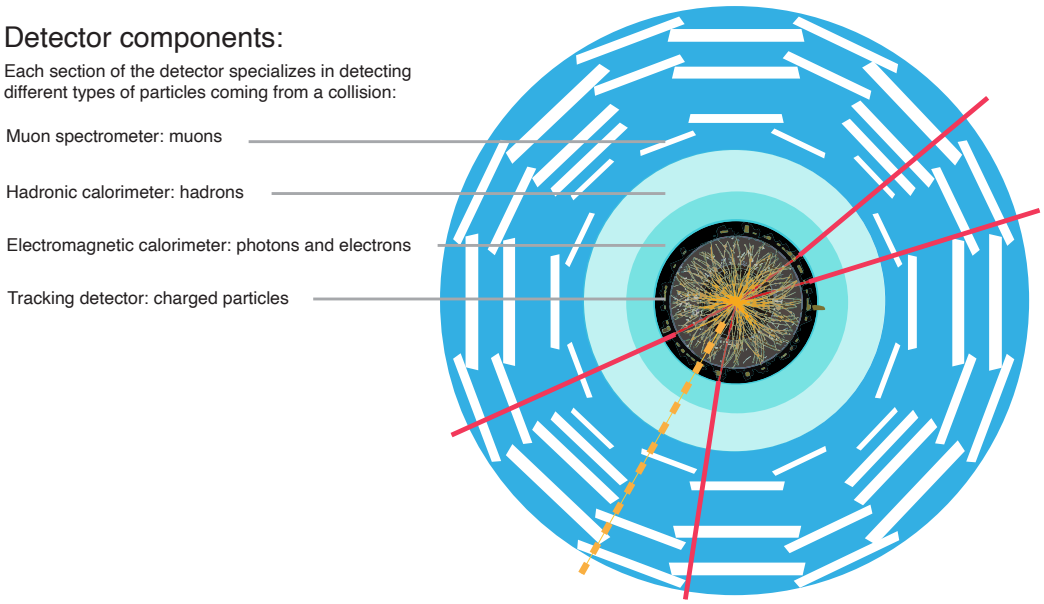

Figure 2.5: An illustration of the different ATLAS detector subsystems with the tracking detector in the center, the electromagnetic and hadronic calorimeters in the next two layers, and the muon spectrometer system surrounding them.

2.2.1 Detector coordinates and observables

The ATLAS detector uses a cylindrical coordinate system for describing its geometry. The geometry is centered about the interaction point. The z direction runs along the length of the cylinder, and the x and y directions run in the transverse plane, as illustrated in Figure 2.6. The azimuthal angle direction, ϕ, is the angle about the z direction.

At hadron colliders, the angle from the transverse plane, θ is often described in terms of pseudo-rapidity η shown in equation 2.1. Where $\eta = 0$ corresponds to the direction along the transverse plane and $\eta = \infty$ corresponds to the direction along the beampipe (z).

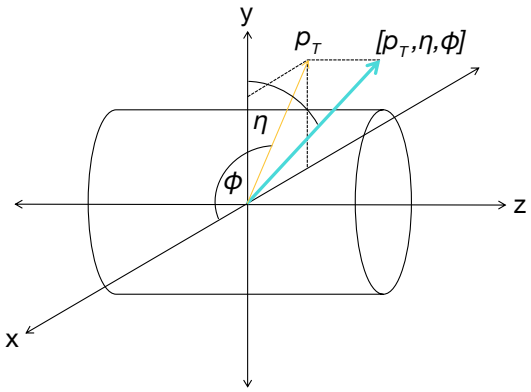

Figure 2.6: ATLAS detector coordinate system

$$\eta = -\ln\left(\tan\left(\frac{\theta}{2}\right)\right) \tag{2.1}$$

Pseudo-rapidity is equivalent to the rapidity, y defined in equation 2.2, when particles are massless. Particle production at a hadron collider is more or less constant in rapidity. Rapidity is Lorentz invariant to boosts along z, meaning that shifts in rapidity ($\pm\Delta y$) are Lorentz invariant.

$$y = \frac{1}{2}\ln\frac{E + p_z}{E - p_z} \tag{2.2}$$

The angular distance between two objects ΔR is measured in terms of distances in $\eta - \phi$ or $y - \phi$. Typically at the LHC, the particle masses are so small relative to their energies that ΔR is a reasonable approximation.

$$\Delta R = \sqrt{(\Delta\eta)^2 + (\Delta\phi)^2} \tag{2.3}$$

$$\Delta R_y = \sqrt{(\Delta y)^2 + (\Delta\phi)^2} \tag{2.4}$$

The momentum in the transverse plane, p_T, shown in equation 2.5 is a very useful observable during a particle collision. This is because while the total initial momentum in the z axis of the proton constituents is unknown, the total initial momentum in the transverse plane is zero.

$$p_T = \sqrt{p_x^2 + p_y^2} \tag{2.5}$$

As $E^2 = p^2 + m^2$, the four-vector of any particle can be described by its three momentum vectors and mass or energy. In detector coordinates this looks like: (p_T, η, ϕ, m) or (p_T, η, ϕ, E).

The invariant mass of a system of many particles can be calculated by summing the 4-vectors of the constituent particles. $m = (\vec{P_1} + \vec{P_2}$. For massless particles, such as photons where $E = pc$ and

setting $c = 1$, the invariant mass of the two-particle system can be calculated as:

$$m_{\gamma\gamma} = \sqrt{(E_1 + E_2)^2 - (\vec{p_1} + \vec{p_2})^2} = \sqrt{(E_1 + E_2)^2 - (p_1^2 + p_2^2 + \vec{p_1} \cdot \vec{p_2})} = \sqrt{2E_1E_2(1 - \cos\alpha)}$$

where α is the opening angle between the two photons and $E_{1,2}$ are their respective energies. This quantity will be very important in Chapter 5 when discussing the $HH \to b\bar{b}\gamma\gamma$ analysis as it is the primary variable used to extract the signal.

2.2.2 Inner detector

The inner detector sits in the heart of the ATLAS experiment closest to the collision point. The layers of sensors in the ATLAS inner detector record when and where a charged particle passes through them. By combining signals across multiple layers, we can reconstruct "tracks" signaling where charged particles traversed our detector. The algorithms for reconstructing these tracks are discussed in Section 3.1 and are important inputs for flavour-tagging discussed in Section 3.8.

The inner detector consists of three types of tracking detectors, the pixels, strips, and transition radiation tracker, as illustrated in Figure 2.7. The four pixel layers sit closest to the beam pipe, between $r = 33.25 - 122.5$mm. The Semiconductor Tracker consists of 4 layers of strip detectors between $299 - 514$mm. The transition radiation tracker is made of straw drift tubes and sits between $r = 563 - 1066$mm. The ATLAS tracker covers the area of $|\eta| < 2.5$, e.g. down to 10° from the beam pipe.

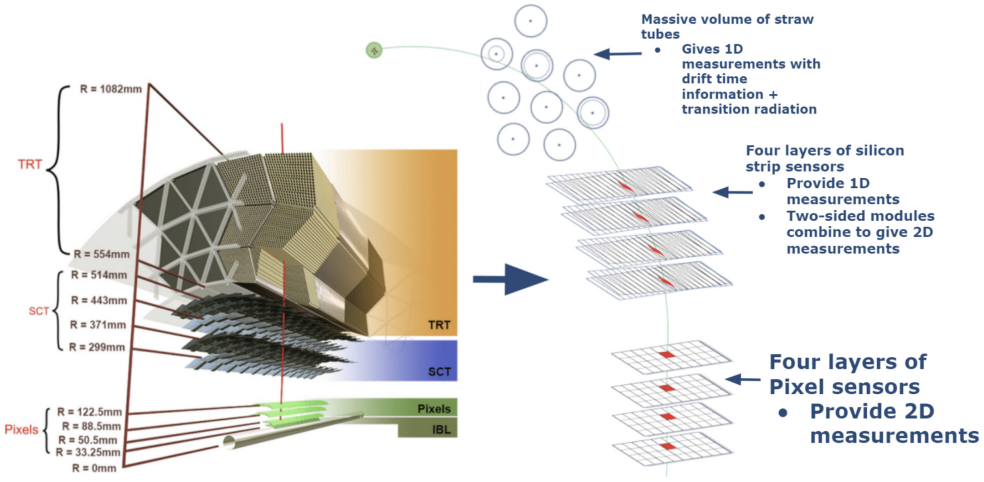

Figure 2.7: An illustration of the different tracking subsystems in ATLAS [52]

The tracker is encased in a solenoid which creates a 2T magnetic field. We can use the curvature

of the tracks in the magnetic field to learn about the particle's properties as illustrated in Figure 2.8. By examining the Lorentz force equation for a charged particle in a magnetic field, we can see that the force on the particle in a magnetic field is:

$$\vec{F} = m\frac{d\vec{v}}{dt} = q(\vec{v} \times \vec{B})$$

And for a particle traversing perpendicular to a uniform magnetic field.

$$\frac{mv^2}{R} = qvB$$

$$R = \frac{mv}{qB}$$

Charged particles in a magnetic field bend more strongly depending on their charge, mass, and momentum. A particle with higher momentum $p = mv$ will bend less than a particle with low momentum. A larger charge over mass ratio and magnetic field will increase the curvature of the track. A negatively charged particle will curve in the opposite direction from a positively charged particle.

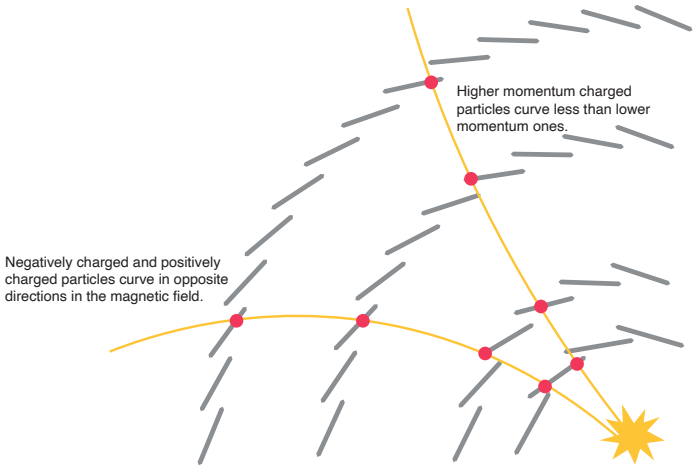

Figure 2.8: Illustration of particle trajectories within the ATLAS pixel detector

The momentum resolution of an idealized barrel-shaped tracker can be approximated analytically [53], [54] to be:

$$\frac{\sigma_{p_T}}{p_T} \approx \left(\frac{\sigma_{r\phi} p_T}{BL^2}\sqrt{\frac{5}{N+5}}\right) \oplus \left(\frac{0.0136 \text{ GeV/c}}{0.3\beta BL}\sqrt{d_{tot}/X_0}\right) \cosh^{\frac{1}{2}} \eta$$

Where $\sigma_{r\phi}$ is the position resolution in the $r-\phi$ plane, B is the magnetic field, L is the distance between the inner and outer layer, N is the number of layers, d_{tot} is the thickness of the layers

and X_0 is the radiation length of the material. The first term describes the geometrical detector resolution, and the second term captures the effects of multiple scattering. From this equation we can see that very high p_T tracks have more uncertainty, as do tracks at high η.

In an idealized world, momentum resolution improves when B and L are large, i.e. the largest tracker in the largest magnetic field. Additional tracking layers can improve the momentum resolution, but add to the material budget with a trade-off due to multiple scattering.

2.2.3 Calorimeters

Where trackers are designed to measure momentum, the ATLAS calorimeter system, shown in Figure 2.9, is designed to measure the energies of particles produced in a particle collision. The ATLAS calorimeter system consists of two main components, the Electromagnetic Calorimeter (ECal), designed to measure photons and electrons, and the Hadronic Calorimeter (HCal), designed to measure hadrons.

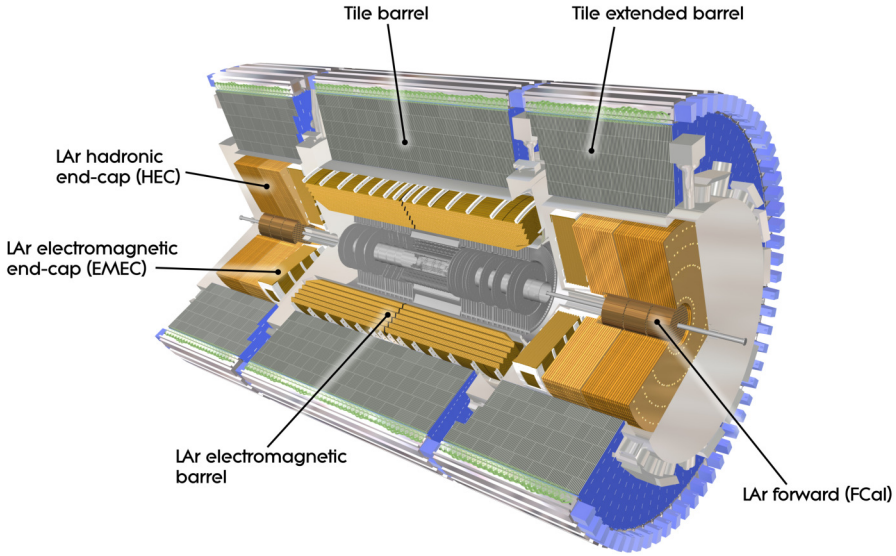

Figure 2.9: The ATLAS calorimeter system [55]

When a particle travels through a calorimeter, it ionizes or excites the calorimeter medium, producing ionization electrons or visible photons via scintillation. These are then collected through photo-detectors or readout electrodes.

Electrons primarily lose energy through bremsstrahlung above 10 MeV.

$$\langle E(x) \rangle = E_0 \exp^{-\frac{x}{X_0}}$$

where E_0 is the initial energy for the electron, x is the distance traveled and X_0 is the radiation length.

Photons primarily lose energy through e^+e^- pair production.

$$I(x) = I_0 \exp^{-\frac{7}{9}\frac{x}{X_0}}$$

where I_0 is the initial photon intensity.

Hadrons interact with the nuclei in the material via the strong force rather than the electromagnetic force. This means that hadronic showers are governed by the nuclear interaction length λ.

$$\lambda = \frac{A}{N_A \sigma \rho}$$

where A is the atomic weight of the target, N_A is Avogadro's number and σ is the inelastic nuclear cross-section (which depends on the target and incoming particle), and ρ is the density of the material.

The energy resolution of a calorimeter is governed by the following equation:

$$\frac{\sigma_E}{E} = \frac{S}{\sqrt{E}} \oplus \frac{N}{E} \oplus C$$

S is the stochastic term that accounts for statistical fluctuations in the signal-generating process, such as the number of photons generated in the detector, N is the electronic noise term, and C is a constant term that comes from detector inhomogeneities. Unlike in tracking detectors where the resolution deteriorates at higher particle energies, in calorimeters, the resolution improves as the energy of the incident particle increases. Table 2.1 compares the resolutions for the different ATLAS subsystems.

Electromagnetic Calorimeter

Electromagnetic showers consist of showers of electrons and photons. These showers are typically more collimated and lose energy more quickly than hadronic showers. The ATLAS electromagnetic (EM) calorimeter is a sampling calorimeter made of interleaved accordion-style layers of liquid argon for the sampling medium and lead and stainless steel to induce showers. The accordion geometry is shown in Figure 2.11(a), the EM calorimeter is finely segmented especially in the first layer to allow for precision measurements of $H \to \gamma\gamma$, and the rejection of $\pi_0 \to \gamma\gamma$ decays. The EM calorimeter is dominated by sampling fluctuations. The barrel region is $|\eta| < 1.475$, end-caps cover $1.375 < |\eta| < 3.2$. The number of radiation lengths for the ECal is $\approx 2.3X_0$ at $\eta = 0$

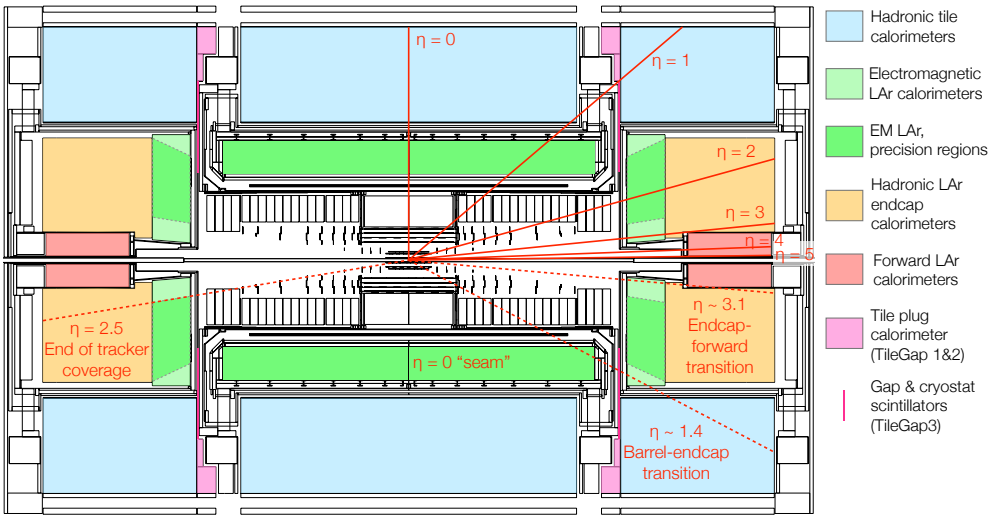

Figure 2.10: Layout of the ATLAS calorimeters with pseudorapitidy (η) values marked for reference. Figure from [56].

Hadronic Calorimeter

The ATLAS Hadronic calorimeter system is designed to measure hadrons. It consists of the Tile Calorimeter (TileCal) covering $|\eta| < 1.7$, and the Hadronic End-cap Calorimeter (HEC) covering $1.5 < |\eta| < 3.2$. The TileCal is made up of 420,000 plastic scintillator tiles interspersed with steel as an absorbing medium, illustrated in Figure 2.11(b). The TileCal extends from r=2.28m to r=4.25m corresponding to 9.7 nuclear interaction lengths (λ) at η=0. The Hadronic End Cap calorimeter uses liquid argon for its scintillating material, but copper instead of steel (as in the EM calorimeter) to dissipate heat better.

Forward Calorimeter

The Forward Calorimeter (FCal) covers the forward regions between $3.1 < |\eta| < 4.9$. To sustain the radiation damage expected at high η, the FCal also uses liquid argon as its active material and a combination of copper and tungsten as the absorber.

2.2.4 Muon spectrometer

While most other particles stop in the EM and Hadronic calorimeters, muons above 3 GeV typically continue through. The muon spectrometer tracks muons as they move through the ATLAS toroidal magnets (0.5-1T) and are deflected in the $\pm z$ direction [59]. The muon spectrometer has a trigger

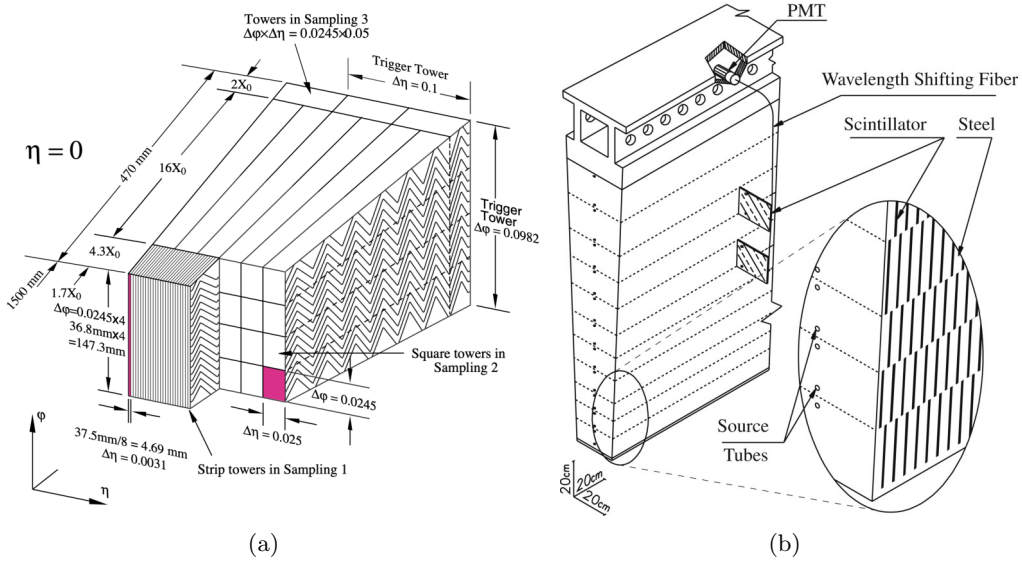

Figure 2.11: (a) LAr EM Calorimeter [57] (b) Hadronic calorimeter [58]

system that is coarsely segmented and consists of resistive plate chambers in the barrel and thin gap chambers in the forward regions. The precision tracking system consists of monitored drift tubes and cathode strip chambers that are used to precisely reconstruct the muon tracks. The measurements in the muon spectrometer are largely independent of those in the inner tracker. This means that the two measurements can be combined to create an even more precise measurement.

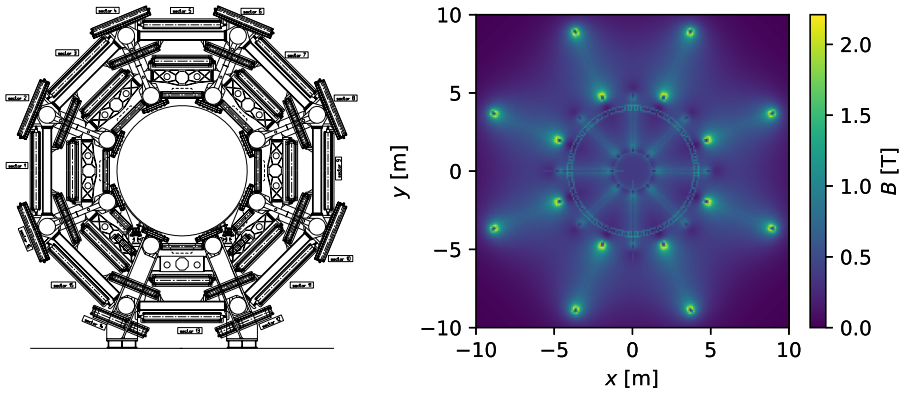

Figure 2.12: (a) Muon spectrometer barrel layout with 8 coils [59] (b) B-Field in muon system in transverse plane [60]

The momentum resolution of the muon spectrometer is governed by the following equation:

$$\frac{\sigma(p_T)}{p_T} = \frac{r_0}{p_T} \oplus r_1 \oplus r_2 \cdot p_T$$

The first term accounts for fluctuations of the energy loss in the material, and the second term accounts for multiple scatters, magnetic field inhomogeneities, and misalignment in the radial direction. The third term describes spatial resolution effects and residual misalignments. Both r_0 and r_1 are much smaller than r_2 which dominates at 0.17% when $|\eta| < 1.05$, 0.34% when $1.05 < |\eta| < 2.0$,and 0.05% where $|\eta| > 2.0$ [61]. Table 2.1 compares the coverage, trigger capabilities and resolutions of each of the ATLAS detector subsystems.

Detector Subsystem	$\lvert\eta\rvert$	Trigger	Resolution
Inner Detector			
Pixel	< 2.5	No	
SCT	< 2.5	No	$\sigma_{p_T}/p_T = 0.05\%\ p_T \oplus 1\%$
TRT	< 2.0	No	
Calorimeters			
EM	< 3.2	Yes, ($\lvert\eta\rvert < 2.5$)	$\sigma_E/E = 10\%/\sqrt{E} \oplus 0.7\%$
Tile	< 1.7	Yes	$\sigma_E/E = 50\%/\sqrt{E} \oplus 3\%$
HEC	[1.5, 3.2]	Yes	$\sigma_E/E = 50\%/\sqrt{E} \oplus 3\%$
FCal	[3.1, 4.9]	Yes	$\sigma_E/E = 100\%/\sqrt{E} \oplus 10\%$
Muon Systems			
RPC	< 1.05	Yes	
TGC	[1.05, 2.4]	Yes	
MDT	< 2.7	No	$\sigma_{p_T}/p_T = 0.05\%$-$0.17\%\ p_T$
CSC	[2.0, 2.7]	No	

Table 2.1: A comparison of the subsystems in the ATLAS detector

2.2.5 Trigger

With collisions occurring every 25 ns (40 MHz) and over 100 million readout channels and an average event size of 1.6 MB, the amount of data coming off of the ATLAS detector is 1 TB/s. This would be challenging to store, so the ATLAS trigger system uses a tiered approach to reduce the amount of data to a more reasonable rate of $\approx$ 1 kHz for permanent storage. The trigger's two stages consist of the hardware-based level 1 (L1) trigger and the software-based High Level Trigger (HLT).

In the L1 trigger, coarse measurements of various objects (leptons, photons, and jets) are used to select events of interest. Calorimeter towers with a segmentation of 0.1×0.1 in the $\eta - \phi$ plane are used for jet triggers. Muon triggers look for co-incidences within the muon spectrometer trigger

chambers which have a low resolution but a high readout rate. The L1 accept rate is 100 kHz.

The High Level trigger consists of two systems, the level-2 (L2) trigger and the event filter (EF). Both of these have much finer granularity than the L1 trigger. L2 is similar to L1, but performs finer granularity measurements. The event filter does a software-based full event reconstruction with ATLAS's Athena software framework to do full event reconstruction. The HLT accept rate is around 1 kHz.

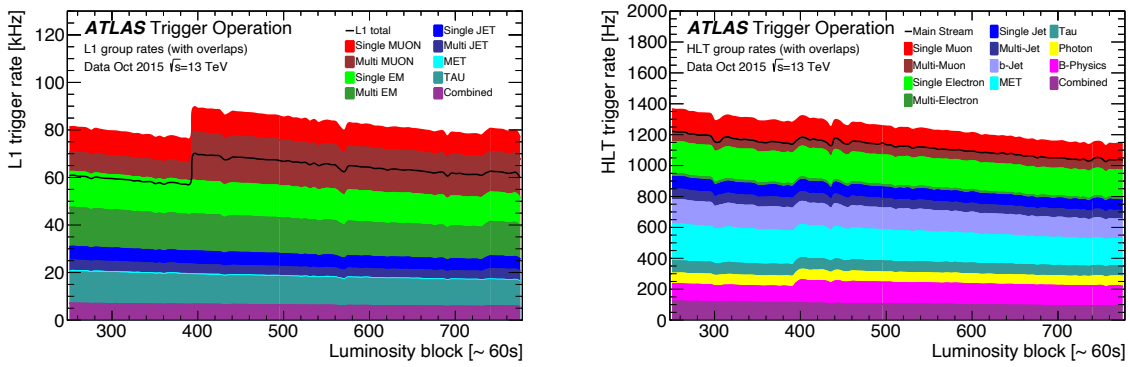

(a) (b)

Figure 2.13: (a) L1 and (b) HLT trigger rates during an LHC fill in 2015. The total rate in black is less than the sum of the individual groups due to overlaps between triggers. Here the di-photon triggers used in the $b\bar{b}\gamma\gamma$ analysis fall under the MultiEM category in (a) and the Photon category in (b). The rate increase around luminosity block 400 is due to the removal of prescaling of the B-physics triggers [62]

.

Chapter 3

Object Reconstruction

After particles have left their signatures in the different layers of the ATLAS detector, it is up to the reconstruction algorithms to correlate the signatures across subsystems to interpret them as "physics objects". In this chapter, we will first focus on the low-level objects - tracks and topoclusters - which are then combined into higher-level objects like photons or electrons. Tracks reconstruct the trajectory of charged particles, and topoclusters aim to represent single-particle energy deposits within the calorimeters. These primary inputs are combined to identify the primary vertex and different signatures in each event. This chapter will focus on photons, b-jets, and tau leptons - the physics objects used in the $HH \to b\bar{b}\gamma\gamma$ analysis and the HH combination with the $b\bar{b}b\bar{b}$ and $b\bar{b}\tau^+\tau^-$ channels.

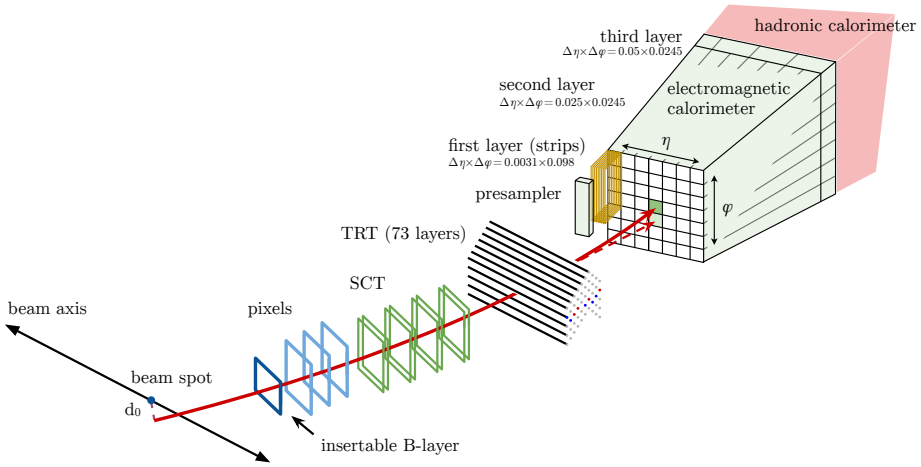

Figure 3.1: An illustration of how low-level features such as a track and energy deposits in the calorimeter can be combined to identify a physics object such as an electron in the ATLAS detector [63].

3.1 Tracks

Charged particles leave signals in the different layers of the inner tracker as they traverse it. These signals, known as hits, tell us where charged particles have passed through the sensors. By combining the hits across many layers, we can reconstruct the helical particle trajectories known as tracks. A track in ATLAS can be described by the following five global track parameters, as illustrated in Figure 3.2.:

$$(d_0, z_0, \phi, \theta, \frac{q}{p})$$

d_0 is the transverse impact parameter - the distance of closest approach to the primary vertex in the transverse plane. z_0 is the longitudinal impact parameter - the distance to the primary vertex along the z-axis at the point of closest approach in the transverse plane. ϕ and θ describe the angle of the track at the point of closest approach relative to the x-axis and z-axis respectively. The charge over momentum ratio $\frac{q}{p}$ is determined from the curvature of the track in the magnetic field.

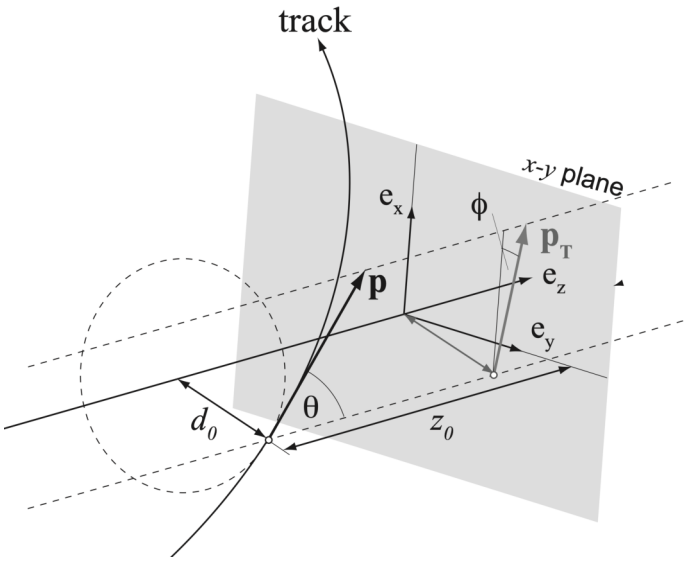

Figure 3.2: An illustration of the d_0, z_0, ϕ, and θ track parameters [64]

Two approaches are combined to form tracks in ATLAS, the inside-out approach, and the outside-in approach. The majority of tracks are reconstructed with the inside-out approach illustrated in Figure 3.3. In this approach, hits come from space points within the pixels and semiconductor tracker. Track seeds are formed by three hits that match coarsely-grained pre-built templates. Next, these seeds are extrapolated to "roads", ranges in η and ϕ, to be searched for additional hits to add to the track. The next stage of track finding involves iteratively adding hits via a Kalman filter. The Kalman filter alternates between fitting a track and adding new hits. First, it uses the

available hits in the track seed to estimate track parameters and uncertainties. Next, it predicts where the next hit might be. If a potential fit is found, it is added to the track. The track is refit to update the track parameters and a prediction is made for the next hit location. This continues until all layers in the silicon detector have been exhausted. After this, the track is refit with a detailed detector geometry to account for multiple scattering. This produces a "track candidate". Multiple track candidates can have overlapping hits, so the next stage involves ambiguity solving Figure 3.6 provides an appreciation of the combinatorial complexity of resolving ambiguities. Track candidates are ranked based on the track score, which combines the quality of the track fit (χ^2/N_{DOF}), the number of hits (more hits result in a better score), the precision of the hits, and the number of "holes" (missing hits)t. The ambiguous hits go to track candidates with the higher track score, and this process is repeated until no hits are shared between track candidates. Finally, the track is extrapolated and refitted with information from the transition radiation tracker. An outside-in tracking algorithm is run in a second pass on any hits that are not already used in the inside-out algorithm. This outside-in algorithm extrapolates tracks from the TRT to the silicon trackers. More details on track reconstruction can be found in References [64], and [65].

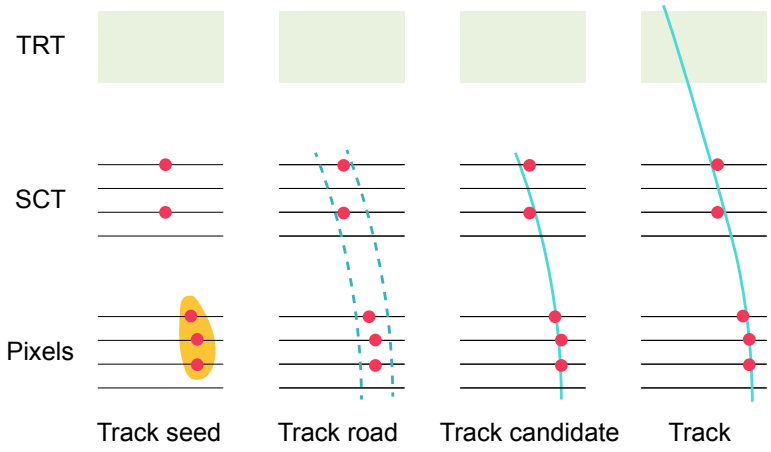

Figure 3.3: An illustration of the inside-out track finding algorithm. Illustration inspired by [66]

Tracks in ATLAS are required to pass either the "loose" or "tight" quality requirements to reject tracks coming from very low energy particles and fake tracks produced due to noise and combinatorics. "Loose" tracks require p_{T} >500 MeV, $|\eta| < 2.5$, the number of silicon hits ≥ 7, no shared hits, 2 or fewer "holes" in the pixel and semiconductor tracker, 1 or fewer pixel "holes". "Holes" are layers of the tracker that the track traverses that do not pick up any hits along the track path. "Tight" tracks make the additional requirements of 9 or more silicon hits if $|\eta| < 1.65$ (barrel region) and 11 or more hits if $|\eta| > 1.65$ (endcap region) and at least one hit in one of the two innermost pixel layers, and 0 holes in the pixel detector. The expected track reconstruction

efficiencies in ATLAS are shown in Figure 3.4.

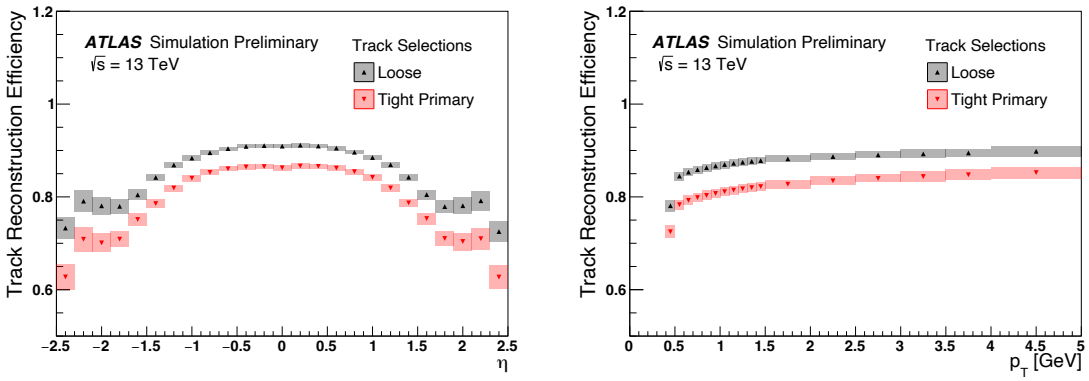

Figure 3.4: Track reconstruction efficiency in (a) η and (b) p_T evaluated with simulated minimum bias events [67].

3.2 Topoclusters

Similar to how tracks describe particle trajectories by combining signals in the inner detector, topological clusters (topoclusters) describe the energy deposited by individual particles in the calorimeters by combining signals across calorimeter cells. As a particle interacts with the calorimeters, it typically deposits energy across many calorimeter cells. Topoclusters are introduced to combine the energy deposited across many cells into a single object. Topoclusters are seeded when enough energy has been deposited to exceed the local cell level thresholds for electronic noise and pile-up by 4 standard deviations. $\zeta = E/\sigma_{\text{noise}} > 4$ where $\sigma_{noise} = \sigma_{\text{noise}}^{\text{electronic}} \oplus \sigma_{\text{noise}}^{\text{pile-up}}$ [68]. Different parts of the calorimeter have different expected values of electronic noise and pile-up depending on the size of the cell and the location within the detector. After seeding, all cells neighbouring the topocluster seed are added to the topocluster if the energy exceeds two standard deviations of the expected noise. Finally, all cells neighbouring any of the cells already in the topocluster are included. If the topocluster has two distinct maxima, an algorithm splits the topoclusters in two. After creating the topocluster, an event-by-event origin correction with respect to the primary vertex is applied to every topocluster, based on its depth within the calorimeter and η [56]. Topoclusters are calibrated to give the same response for electromagnetic showers from electrons or photons [68].

3.3 Photons

Photons are among some of the most accurately measured particles in ATLAS. Their excellent energy resolution contributed significantly to the $H \to \gamma\gamma$channel being used in the Higgs discovery [1] and

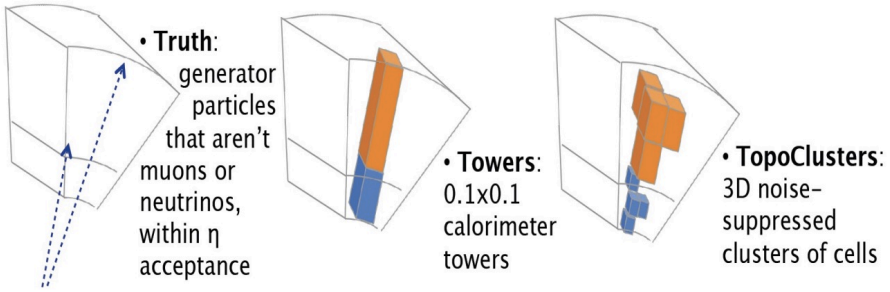

Figure 3.5: An illustration of topoclusters in ATLAS Calorimeter

is a key reason for the high sensitivity in the $HH \rightarrow b\bar{b}\gamma\gamma$ analysis.

Photons are initially seeded from topoclusters that have at least 400 MeV deposited in the EM calorimeter and where more than 50% of the total topocluster energy is deposited in the EM calorimeter. Photon candidates are designated as being either unconverted or converted. The signature for an unconverted photon is a topocluster in the electromagnetic calorimeter that can not be associated with a track as photons are electrically neutral. Converted photons are where the photon has undergone $\gamma \rightarrow e^+e^-$ pair production in the inner detector, producing two reconstructed tracks leading into a topocluster. Due to material interactions, about 20% of photons convert in the inner detector at low $|\eta|$ and about 65% convert by $|\eta| \approx 2.3$ [69]. Topoclusters that are associated with a single track are immediately vetoed, but considered for electron identification discussed in Section 3.5.1.

After seeding, photons are identified through their shower shapes in the first and second layers of the EM calorimeter, and the energy leakage into the hadronic calorimeter. Photons coming from the primary interaction point deposit energy in a single-pronged structure (compared to $\pi_0 \rightarrow \gamma\gamma$ which produces two prongs), and typically do not deposit energy in the hadronic calorimeter. The identification efficiency for unconverted and converted photons ranges from 84% to 98% for photons p_{T} between 30 GeV and 250 GeV [69]. Reconstructed photons are only defined for $|\eta| < 2.37$ due to the coverage of the EM calorimeters.

To reject background photons, which often are accompanied by nearby activity in the hadronic calorimeter, photons are also required to be isolated. This means that the sum of the energies or momenta within a radius of $\Delta R < 0.2$ must be smaller than a certain threshold. Energy-based isolation is calculated from topoclusters in the calorimeter:

$$E_{iso} = \sum_{c \in \Delta R} E_T^{\text{cluster,c}} - E_T^{\gamma,\text{clusters}} - E_T^{\text{pile-up}}$$

Momentum-based isolation is calculated using tracks with $p_{\mathrm{T}} > 1$ GeV.

$$p_{iso} = \sum_{t \in \Delta R} p_T^t - p_T^{\gamma,\text{tracks}}$$

Isolated photons must have a transverse energy E_T satisfying:

$$E_{iso} < 0.065 \cdot E_T \text{ and } p_{iso} < 0.05 \cdot E_T$$

Isolated photons with transverse momenta between 30 GeV and 250 GeV, have an identification efficiency for unconverted and converted photons that ranges from 84% to 98% [69].

Photons are calibrated based on a multivariate regression algorithm trained with MC samples, where the input variables are corrected with data-driven techniques. The calibrated energy is finally corrected by applying scale factors derived from $Z \to ee$ events.

3.4 Primary vertex selection

Primary vertex reconstruction aims to determine which of the many proton-proton interactions resulted in a hard-scatter. Vertex reconstruction starts with using "tight" tracks. Vertex reconstruction requires at least two "tight" tracks crossing to be considered as a candidate vertex. For vertex reconstruction along the beamline, the longitudinal resolution is about 30 µm and transverse resolution is about 10-12 µm depending on the LHC running conditions [70]. As events with high pile-up can have many candidate vertices, the vertex with the highest squared transverse momentum of associated tracks, $\sum p_{T,\text{track}}^2$, is typically selected as the primary vertex. All physics objects are subsequently derived with respect to the selected vertex.

3.4.1 Primary vertex selection for diphoton events

As gluon–gluon fusion $H \to \gamma\gamma$ events only have photons in the final state, they have low charged particle multiplicity, which makes primary vertex selection using tracks more difficult. To combat this, $H \to \gamma\gamma$ analyses have developed a primary vertex selection that incorporates information on the pointing direction of the photons [72].

This technique uses a neural network that combines the following information: the z-position where the photon trajectories intersect the beam axis, the $\sum p_T$ and $\sum p_T^2$ of the tracks in the primary vertex, the $\Delta\phi$ between the vector sum of the primary vertex tracks and the diphoton system, and the position of photon conversion vertices. The diphoton pointing position resolution along the z-aixs is about 15mm [72] using the calorimeter alone. In ggF $H \to \gamma\gamma$ searches this technique improves the primary vertex selection by $\sim 20\%$ and improves the diphoton mass resolution by 8% relative to the default primary vertex reconstruction [72]. This technique is also used in $b\bar{b}\gamma\gamma$, but because there are b-jets which produce tracks in the final state, it only improves the reconstruction efficiency by about 2% relative to the $\sum p_T^2$ method.

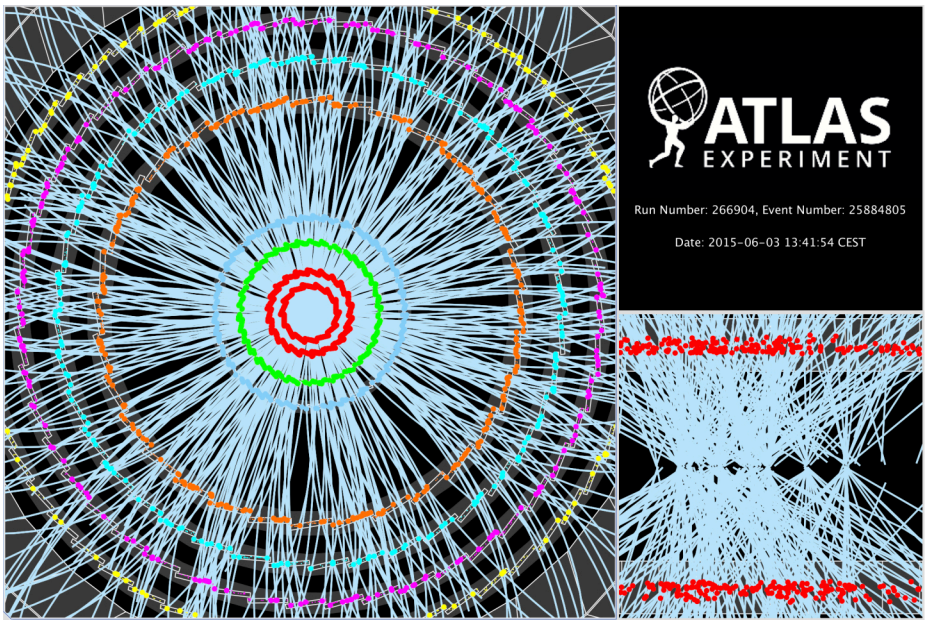

Figure 3.6: Actual reconstructed tracks from an event in the ATLAS tracker. The inlay on the bottom right displays 17 reconstructed vertices [71].

3.5 Electrons and muons

In this thesis, leptons play an important role in b-hadron decays, where their presence within a jet suggests that the b-hadron decayed semi-leptonically. This has implications for the b-jet energy corrections discussed in Chapter 4. In the $b\bar{b}\gamma\gamma$ analysis, isolated leptons are used to reject backgrounds and HH signals from other channels via a lepton veto.

3.5.1 Electrons

Electrons are reconstructed from energy deposits measured in the electromagnetic calorimeter ($|\eta| < 2.47$), which are matched to tracks in the inner detector. Electron identification proceeds in a similar way to the methods used for photons. Shower shapes in the EM calorimeter are used to see if the EM shower development matches that of an electron, and track-cluster matching is used to see if an electron track can be associated to the shower. The electrons used in the lepton veto are required to pass the loose isolation: $E_{iso} < 0.20 \cdot E_T$ and $p_{iso} < 0.15 \cdot E_T$.

3.5.2 Muons

Muons are initially reconstructed from high-quality tracks found in the muon spectrometer. The muon track candidates are then combined with tracks in the inner detector through a global fit. Muons can be identified and measured with good accuracy across the range in p_{T} from 3 GeV to

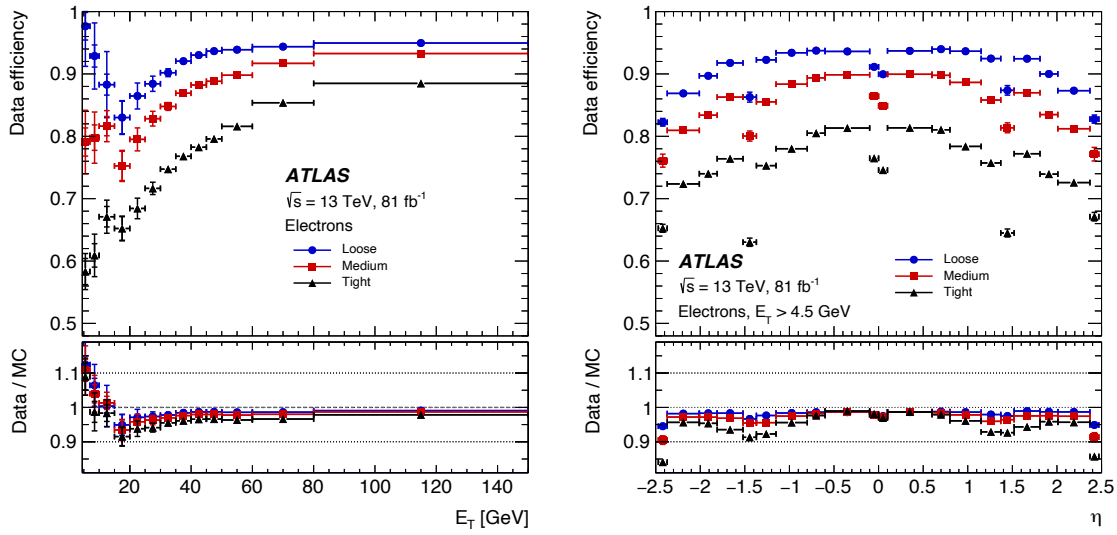

Figure 3.7: The electron identification efficiency in $Z \to ee$ events in data as a function of E_T (left) and as a function of η (right) for the Loose, Medium, and Tight operating points. The efficiencies are obtained by applying data-to-simulation efficiency ratios measured in $J/\psi \to ee$ and $Z \to ee$ events to $Z \to ee$ simulation. For both plots, the bottom panel shows the data-to-simulation ratios. [69].

several hundred GeV [73] as shown in Figure 3.8. Muons passing the medium quality working point will be considered in this thesis. The muons used in the lepton veto are required to pass the loose isolation: $E_{iso} < 0.30 \cdot E_T$ and $p_{iso} < 0.15 \cdot E_T$.

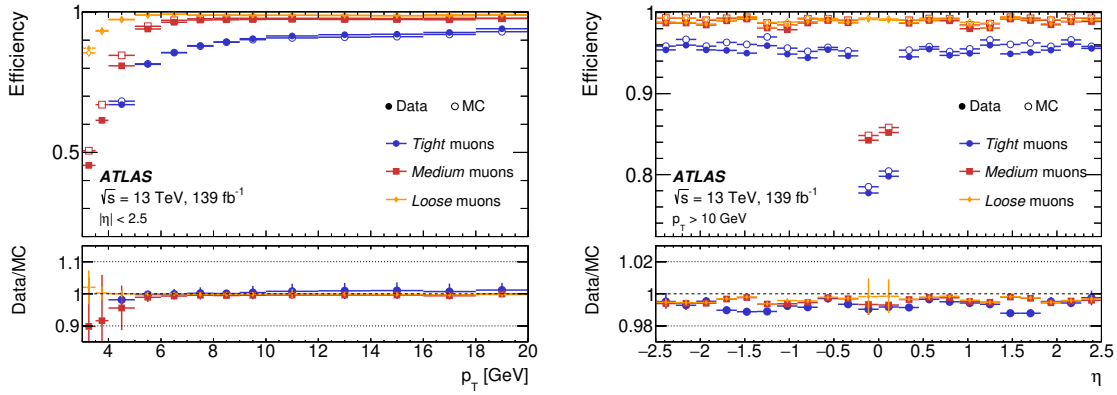

Figure 3.8: Muon reconstruction and identification efficiencies for the loose, medium, and tight criteria. The left plot shows the efficiencies measured in $J/\psi \to \mu\mu$ events as a function of p_{T}. The right plot displays the efficiencies measured in $Z \to \mu\mu$ events as a function of η, for muons with $p_{\mathrm{T}} > 10$ GeV. [73].

3.6 Jets

Jets attempt to reconstruct the showers of particles produced by quarks and gluons as they hadronize. Jets are formed by clustering a combination of topoclusters and tracks, known as "particle flow objects". Particle flow objects combine the excellent energy resolution for charged particles measured by the inner detector with the energies measured in the topoclusters. The inner detector has a better energy resolution for lower energy charged particles, whereas the calorimeter has a better energy resolution for high energy (>100 GeV) and neutral particles. To create particle flow objects, topoclusters are matched to individual tracks in the calorimeter. If the track p_{T} exceeds a parameterized threshold, the track p_{T} is subtracted from the topocluster energy. If the track p_{T} is greater than the topocluster energy, the topocluster is removed entirely, but if it is less than the topocluster energy, the energy is subtracted on a cell-by-cell basis. [68], [56].

Jet clustering on the particle flow objects is based on the anti-k_t algorithm using the following distance measure between two input objects [74], [75]:

$$d_{ij} = \min(p_{T,i}^{-2}, p_{T,j}^{-2}) \frac{\Delta R_{ij}}{R}$$

$$d_{iB} = p_{T,i}^{-2}$$

The algorithm searches the set of all topoclusters for the combination that minimizes d_{ij} or d_{iB}. If the minimum is d_{iB}, the topocluster is considered a finished jet and removed from the list. Otherwise, the two topoclusters i and j, which minimize d_{ij} are removed from the set and replaced by the combination of their 4-vectors. These steps are repeated until there are no more particles left in the set. The fact that objects with the smallest d_{ij} are iteratively combined favours clustering the high p_{T} objects that are close to each other first. R sets the angular scale of the clustering. In ATLAS, two common jet definitions are used; small radius jets have an R=0.4, and large radius jets have an R=1.0. Figure 3.9 illustrates topoclusters in the $\eta - \phi$ plane and the location of their corresponding $R = 1.0$ jets.

To suppress jets produced in concurrent pp interactions, each jet within the tracking acceptance of $|\eta| < 2.4$, and with $p_{\mathrm{T}} < 60$ GeV, is required to satisfy the "tight" jet-vertex tagger [77] criteria used to identify the jet as originating from the selected primary vertex of the event.

After jet clustering, the jets must be calibrated to create an energy response that is as close to the true particle energy as possible. This is done in a multi-step process, illustrated in Figure 3.10, which uses both simulation and data-driven techniques to account for pile-up, biases introduced through the jet clustering algorithm, detector geometry effects, and differences between data and simulation. As shown Figure 3.11, the jet response is highly variable across detector regions and energy regimes. The Jet Energy Scale (JES) is defined as the mean of a Gaussian core fit of the ratio between the reconstructed jet energy and the true jet energy, $E_{\mathrm{reco}}/E_{\mathrm{truth}}$, and after calibration it ideally is 1 [78]. The width of the fitted jet response distribution is known as the Jet Energy Resolution (JER), is

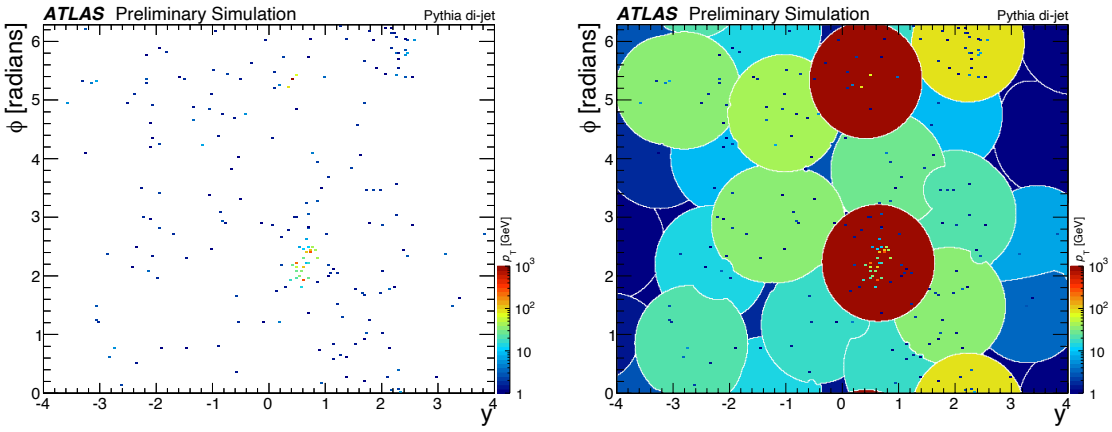

(a) (b)

Figure 3.9: Topoclusters and corresponding $R = 1.0$ jets from an event displayed in the $\eta - \phi$ plane of the ATLAS detector. Figures reproduced from [76]

ideally as small as possible. The systematic uncertainties in the jet energy scale for central, $R = 0.4$ jets ($|\eta| < 1.2$) vary from 1-5% with the uncertainty being high at low p_{T} (5%), decreasing to (1%) for jets in the range of (250-2500 GeV), and then increasing to 3.5% at high p_{T}, as illustrated in Figure 3.12. The relative jet energy resolution is measured and ranges from $(24 \pm 1.5)\%$ at 20 GeV to $(6 \pm 0.5)\%$ at 300 GeV [56].

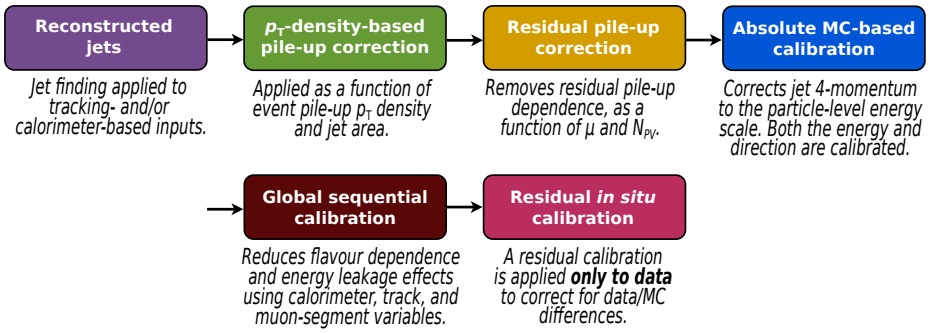

Figure 3.10: Stages of jet energy scale calibrations. Each one is applied to the four-momentum of the jet. Figure from [56]

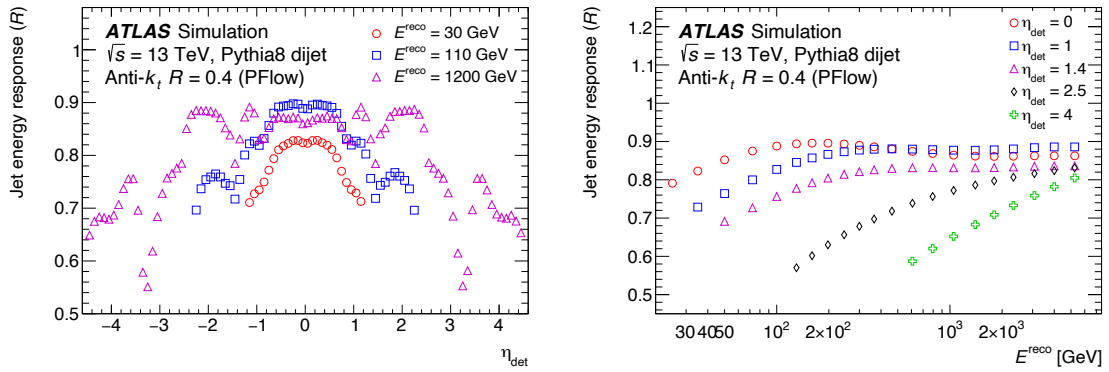

(a) (b)

Figure 3.11: The average energy response as a function of reconstructed jet a η and b energy E_{reco}. Each value is obtained from the corresponding parameterized function derived with the Pythia 8 MC sample and only jets satisfying $p_{\text{T}} > 20$ GeV are shown. [56]

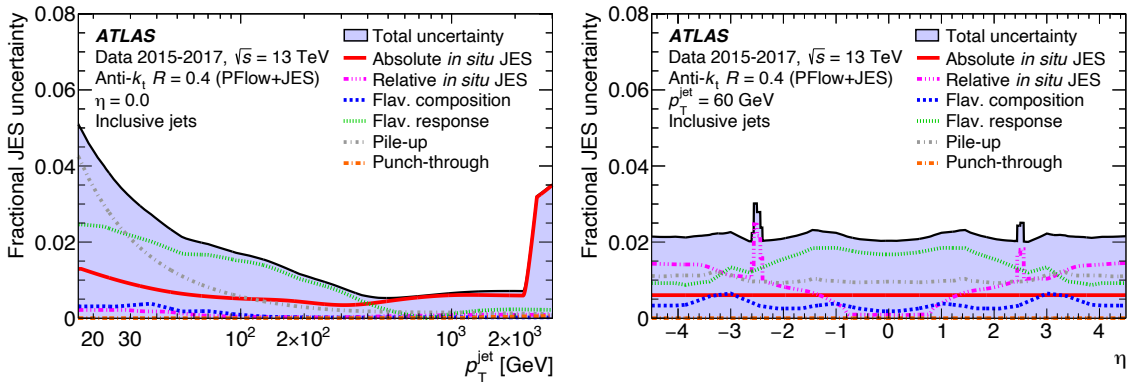

(a) (b)

Figure 3.12: Fractional jet energy scale systematic uncertainty components for anti-k_t $R = 0.4$ jets a as a function of jet p_{T} at $\eta = 0$ and b as a function of η at $p_{\text{T}} = 60$ GeV, reconstructed from particle-flow objects. The total uncertainty, determined as the quadrature sum of all components, is shown as a filled region topped by a solid black line. Flavour-dependent components shown here assume a dijet flavour composition. [56]

3.7 Missing transverse energy

The missing transverse energy relies on the fact that the momentum in the transverse plane is approximately 0 before a collision. The missing transverse energy estimates the amount of energy that has escaped the detector by calculating the negative vector sum of all reconstructed objects: $E_T^{\text{miss}} = -\sum_i p_{T,i}$

3.8 Flavour tagging

Identifying jets that come from b decays is particularly important in HH searches, which often search for at least one Higgs decaying into a $\bar{b}$ pair, as this decay has the largest branching ratio. Flavour tagging is the process of identifying jets that come from the hadronization of a heavy-flavour quark, such as b and c-quarks, or light-flavour quarks such as u,d, and s.

b-tagging relies on the fact that the average lifetime for hadrons containing b quarks is longer than that of a hadron that involves lighter quarks. Thus, b-hadrons typically travel a longer distance in the inner detector, producing a displaced secondary vertex as illustrated in Figure 3.13.

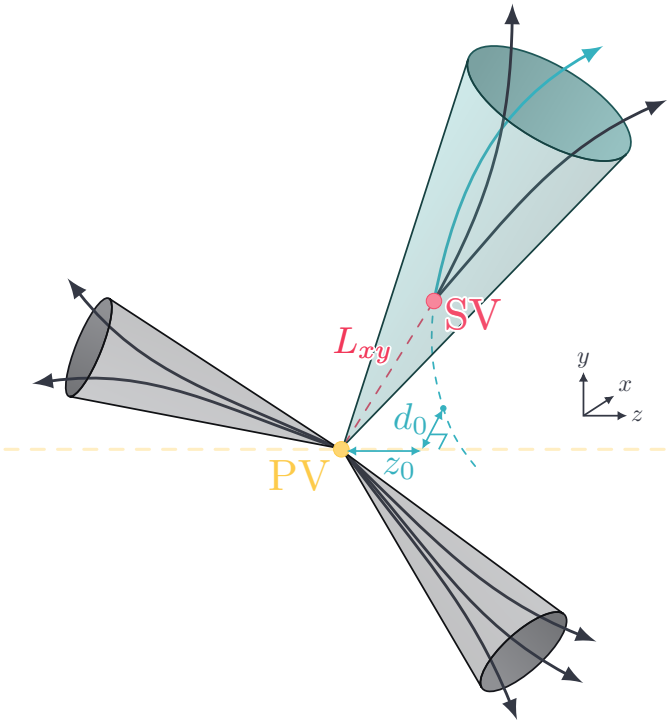

Figure 3.13: b-jet illustration. Image adapted from [79]

The reason for this long lifetime is because the b-hadron decay relies on a flavour change from a $b \to c$, which occurs through a W-boson exchange. Because b-hadrons are relatively light (~ 5 GeV) relative to W bosons (80 GeV), the energy available for this process is small, the W is virtual, and the process is suppressed, which results in a longer lifetime. For example, for a B^0 b-hadron ($\bar{b}$), one of the most commonly produced b-hadrons at the LHC, the lifetime (τ) is 1.519ps and the mass (m) is 5.28 GeV [80]. The average decay length $\langle l \rangle$ is given by:

$$\langle l \rangle = \beta\gamma c\tau$$

Where $\gamma = \frac{1}{\sqrt{1-\beta^2}}$ and $\beta = \frac{v}{c}$ [81]. This is a linear relationship as a function of the relativistic momentum. Particles with a larger momentum/mass ratio will travel longer distances before decaying. In Figure 3.14, we can see that the decay length for a 50 GeV b-hadron is on the order of 5mm (see Figure 4.3 for the distributions of an average b-jet in a $t\bar{t}$ sample peaking around 50 GeV). Note that in equation 3.8 τ is the mean particle lifetime. However, particle decay is a Poisson process and therefore the particle lifetimes follow an exponential distribution e.g. the most probable lifetimes for any unstable particle are much closer to 0.

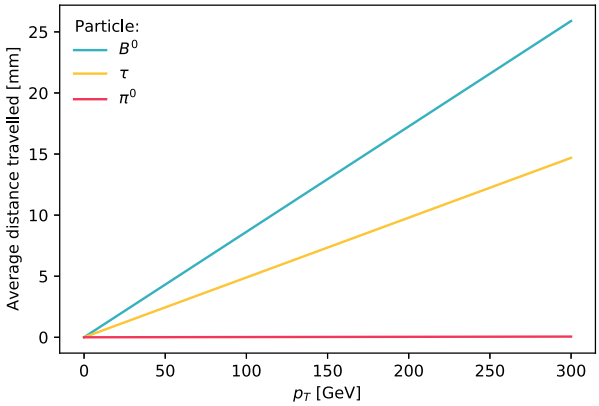

Figure 3.14: Average flight length as a function of momentum for a B^0 b-hadron, a τ lepton and a π^0 with lifetimes of 1.5×10^{-12}, 2.9×10^{-13} and 8.5×10^{-17}s, and masses of 5.3, 1.8 and 0.14 GeV respectively [80].

In addition to having a long lifetime, in b-jets are high in momentum as around 70% of the initial b-quark energy is transferred to the final b-hadron. Because b-hadrons are also some of the heaviest pseudo-stable particles in the SM, their lighter decay products typically are high momentum too. Relative to light jets, which have an average of 3.7 associated tracks per jet, b-jets have slightly more, 5.5, associated tracks [82].

Flavour tagging is typically performed on $R = 0.4$ jets and combines the jets with tracks from the inner detector, and therefore is only defined for $|\eta| < 2.4$. Tracks are associated to jets within a p_{T}-dependent cone that goes from 0.45 for a jet with $p_{\mathrm{T}} = 20$ GeV to 0.24 at a jet $p_{\mathrm{T}} \geq 2$ TeV [81]. Most flavour tagging algorithms fall into one of two categories: vertexing-based algorithms, which attempt to reconstruct secondary vertices, and impact-parameter-based algorithms, which examine the displacement of reconstructed tracks within the jet relative to the primary vertex. The different approaches are complementary and therefore they are combined into a set of high-level taggers illustrated in Figure 3.15.

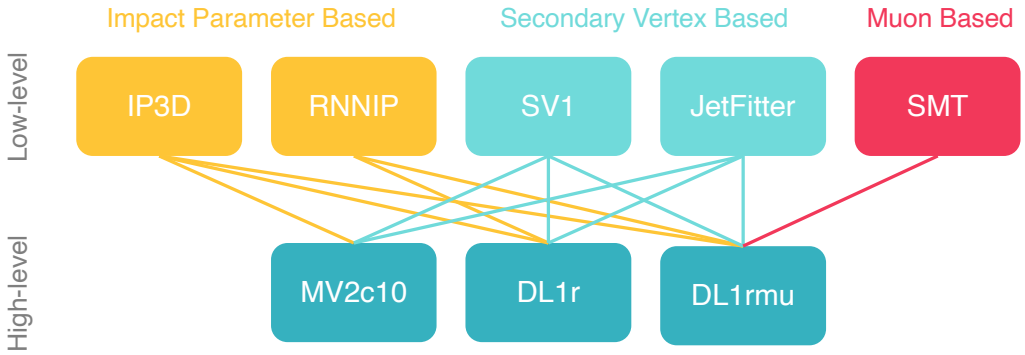

Figure 3.15: Combination of high and low-level b-taggers

3.8.1 Vertexing-based algorithms

Vertexing-based algorithms rely on the fact that when the b-hadron decays, it produces a secondary (and sometimes a tertiary) vertex along its flight path. Secondary vertexing algorithms aim to reconstruct this secondary vertex, and then, using the information about the tracks coming from the vertex, decide on whether the jet originated from a b, c, or light jet.

SV1

SV1 is a secondary vertexing-based algorithm to reconstruct the b-hadron decay. In SV1, all two-track vertices within a jet are considered possible secondary vertex candidates. Vertices that are consistent with material interactions or K_s,Λ, and π decays are removed. The number of two-track vertices is a discriminating variable, as b-jets typically have a longer decay chain than light jets. All tracks from the 2-track vertices are also combined to form an inclusive secondary vertex. Tracks are iteratively removed from the secondary vertex until a goodness of fit threshold is reached. After that, the displacement of this vertex is used to calculate the displacement significance ($L_{3D}/\sigma_{L_{3D}}$). The energy and mass of the tracks in the inclusive vertex and the ratio of the energy in the secondary vertex relative to the sum of all tracks in the jet are also calculated. The ΔR between the jet axis and the secondary vertex location is also calculated. These nine discriminating variables, some of which are shown in Figure 3.16, can be combined to produce a likelihood directly or can be used for training a high-level tagger [83].

JetFitter

JetFitter is a secondary and tertiary vertex-based algorithm to separately reconstruct the B and D hadron decays. It relies on the initial assumption that the B and D hadron decays lie on the jet axis and that the associated tracks will therefore intersect with the jet axis. Jet fitter uses a Kalman

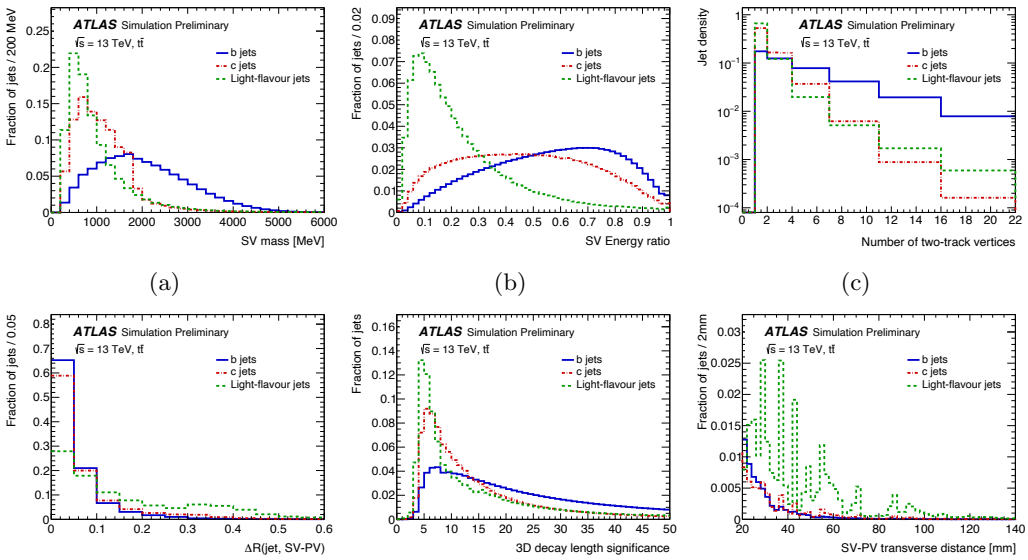

Figure 3.16: SV1 secondary vertex output distributions [83].

filter to iteratively update the position of the primary, secondary and tertiary vertices in the decay chain based on the tracks that intersect with the jet axis. Tracks that are close to each other are iteratively merged until one or two vertices have been reconstructed, corresponding to the B and D decays. The output variables include information about the secondary and tertiary vertices, such as the significance in (x,y,z), the fraction of charged jet energy in each vertex, the vertex masses, and $\Delta R\, p_{\mathrm{T}}$ between the jet and the sum of all track p_{T} in a vertex. These can then be directly combined into a likelihood or used for training a high-level tagger [84].

3.8.2 Impact parameter-based algorithms

Impact parameter-based algorithms search for tracks with significant transverse (d_0) and longitudinal (z_0) impact parameters and are inconsistent with coming from the primary vertex. The impact parameter significance is calculated by dividing the impact parameter by its estimated uncertainty, e.g. d_0/σ_{d_0}, and is illustrated in Figure 3.17. The sign of the impact parameter is positive if the point of closest approach to the primary vertex is in front of the primary vertex with respect to the jet direction. b-jets are more likely to have positive impact parameters, as seen in Figure 3.17. In contrast, light jets decay so quickly that the difference in impact parameters due to the decay distance is not measurable.

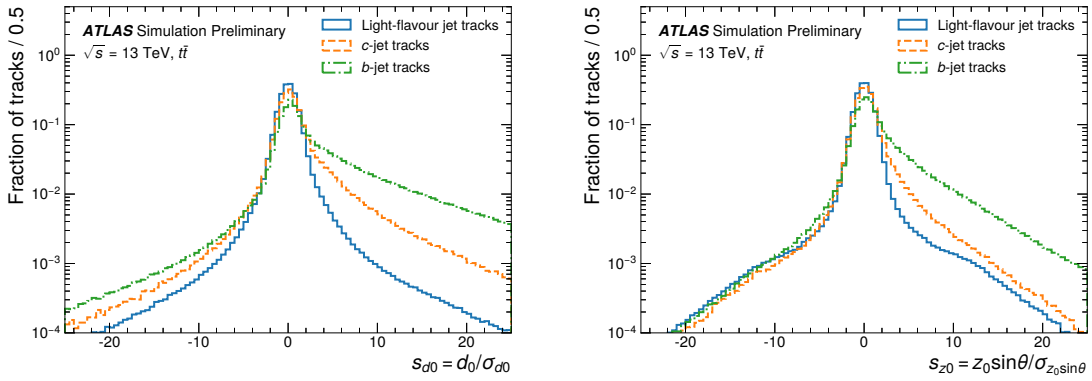

(a) (b)

Figure 3.17: d_0 and z_0 impact parameter significances for light, c and b jets. Figure is reproduced from [85]. The long, non-Gaussian tails are due to decays of Λs and K_ss, photon conversions, and interactions in the detector material [81].

IP3D

IP3D is a Log-Likelihood-Ratio-based algorithm that is based on a two-dimensional probability of each track belonging to a b or c-jet. The probabilities are built from template fits to the s_{d_0} and s_{z_0} impact parameter significances constructed in simulation as shown in Figure 3.18.

$$\text{LLR} = \sum_{n}^{\#\text{ tracks}} \log\left(\frac{p_b, n}{p_l, n}\right)$$

IP3D outputs predicted probabilities for the jet flavour, p_u,p_c,p_b, the number of tracks used to produce the likelihood, and the likelihood itself. As seen in Figure 3.19 IP3D has better performance than the secondary vertex-based taggers in the high b-tag efficiency region.

RNNIP

Similar to IP3D, RNNIP uses the impact parameter significance of the tracks to calculate b-tagging scores for each jet. RNNIP is based on a recurrent neural network (RNN) which allows it to fully exploit correlations between the impact parameters in each jet. In addition to the impact parameter significances, RNNIP uses the track categories, relative p_{T} carried by each track in the jet, and distance of the track from the jet axis as inputs which carry additional information not used by IP3D [86]. RNNIP outputs p_u, p_c, p_b for each jet which can then be combined into a final high-level discriminant such as DL1r.

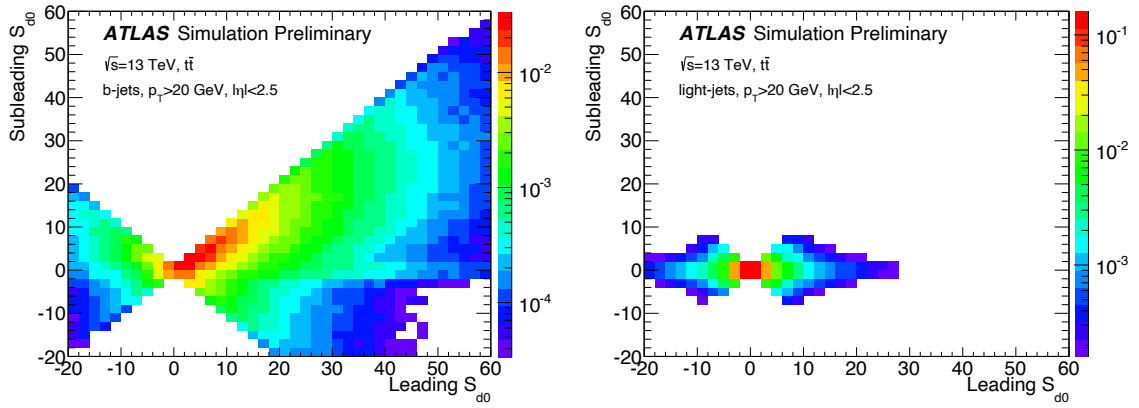

(a) (b)

Figure 3.18: The distribution of the d_0 significance for the leading d_0 significance track and subleading d_0 significance track in b-jets (left) and light jets (right). Figure is reproduced from [86].

Soft Muon Tagger

Seen as about 13% of b-hadron decays include a muon in their final state, the soft-muon-tagger, aims to tag these jets by looking for muons associated with a jet within a $\Delta R < 0.4$. Muons are required to have a minimum p_{T} of 5 GeV, $d_0 < 4$mm, and to be within $|\eta| < 2.5$. The soft muon tagger outputs the angular distance between the muon and jet, the p_{T} d_0 and z_0 impact parameters of the muon, the relative p_{T} of the muon to the jet p_{T}, the charge over momentum ratio (q/p) for the muon, and the ratio of q/p from the muon track in the inner detector relative to the track in the muon spectrometer. Other variables include the difference between the momentum measured in the spectrometer and the inner detector divided by the energy loss in the calorimeter, and the significance of the angular difference $\Delta\phi$ between pairs of adjacent hits along the track. These outputs can then be combined with a high-level tagger for additional discrimination power [87].

3.8.3 Putting it all together; MV2 and DL1r

Each of the algorithms described in the previous sections takes a slightly different, complementary approach to b-tagging. Therefore their outputs are combined with a final high-level b-tagging algorithm. These take the outputs of the individual low-level b-taggers as inputs to produce predictions for p_u, p_c, and p_b, which then can be combined into a single final discriminating variable D.

$$D(f_c) = \log \frac{p_b}{f_c \cdot p_c + (1 - f_c) \cdot p_u}$$

Here, f_c corresponds to the c-jet fraction. This fraction allows one to weigh the importance of the different jet flavours to improve the performance on either b vs c jets or b vs light jets, without

a dedicated retraining. MV2C10 is a BDT-based algorithm, whereas DL1 and DL1r are deep neural network-based algorithms. DL1r and DL1 are essentially the same, but DL1r includes RNNIP inputs and DL1 does not. Figures 3.19, 3.20, 3.21 compare the performance of the different tagging algorithms and inputs discussed in this chapter. As DL1r has the best performance of the three algorithms as shown in Figure 3.21 it was used as the baseline tagger in the HH searches presented in subsequent chapters. Across the HH analyses, the 77% b-tagging working point was used. The misidentification rate is 1/130 for light-flavor jets and 1/4.9 for charm jets [81].

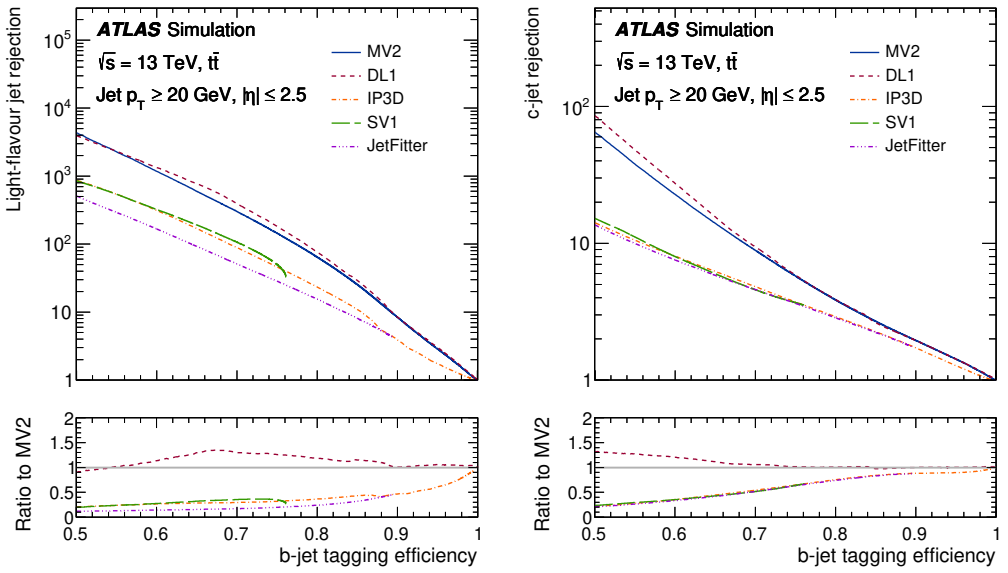

(a) (b)

Figure 3.19: Light-flavour and c-jet rejection as a function of b-jet efficiency for IP3D and SV1. Figures reproduced from [81]

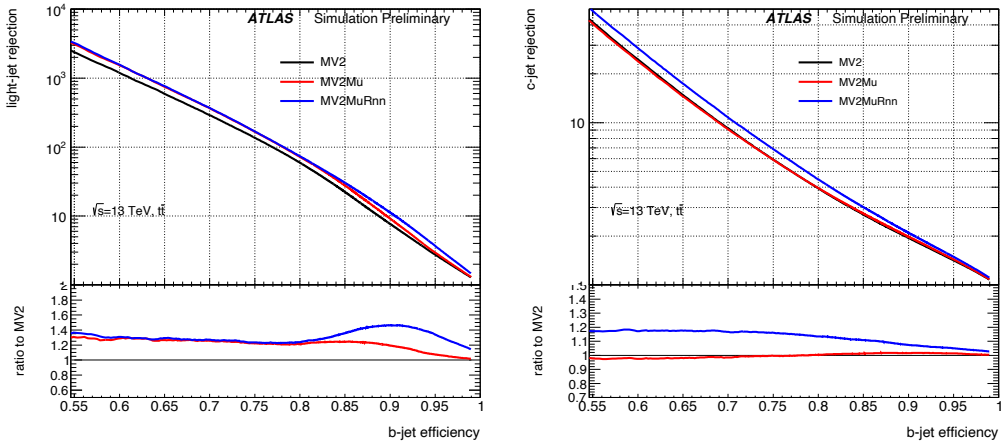

(a) (b)

Figure 3.20: Light-flavour and c-jet rejection as a function of b-jet efficiency for MV2, MV2Mu (includes Soft Muon Tagger inputs), MV2MuRnn (includes Soft Muon Tagger and RNN inputs). Figures reproduced from [88]

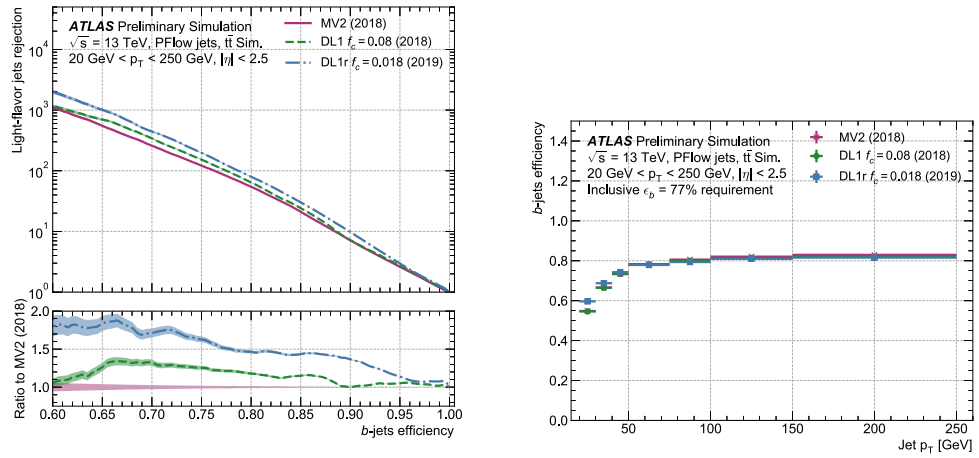

(a) (b)

Figure 3.21: Light-flavour and c-jet rejection as a function of b-jet efficiency and efficiency as a function of p_{T} for the 77% efficiency working point for the MV2, DL1 and DL1r b-taggers [89]

3.9 Tau leptons

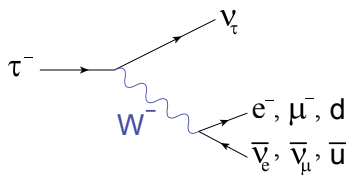

Figure 3.22: Feynman diagram of a τ lepton decay

Tau leptons are important signatures for the $HH \rightarrow b\bar{b}\tau^+\tau^-$ analysis. Tau leptons can decay leptonically or hadronically as illustrated in Figure 3.22 with hadronic decays corresponding to a branching fraction of $\sim 65\%$ [90]. Leptonically decaying tau leptons are identified by the presence of a lepton+$E_{\mathrm{T}}^{\mathrm{miss}}$ in the final state. Hadronically decaying tau leptons are identified in a very similar way to b-jets as they also have a characteristically long lifetime. Hadronically decaying taus typically have a track multiplicity of 1 or 3 tracks in the inner detector due to the presence of charged pions in the final state. To identify taus $R = 0.4$ jets are selected and then topoclusters and tracks associated with the jet are fed into a recurrent neural network [91]. Tau leptons passing the tight selection working point used in the $b\bar{b}\tau^+\tau^-$ analysis have a signal efficiency of 60% with a background rejection of 70 for one-pronged tau leptons and a signal efficiency of 45% with a background rejection of 700 for three-pronged tau leptons [92].

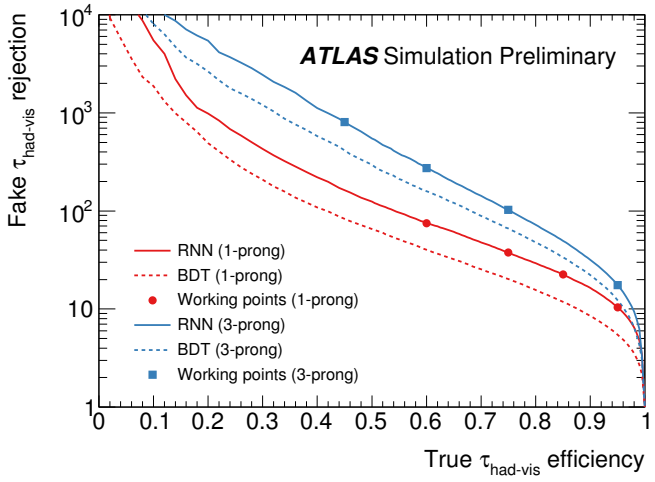

Figure 3.23: ROC curves for tau lepton identification. The markers indicate the four defined working points Tight, Medium, Loose, and Very Loose, with increasing signal selection efficiencies. Figure reproduced from [92].

Chapter 4

B-jet Energy Corrections

4.1 Motivation

This chapter describes a deep neural network-based regression for calibrating the transverse momentum reconstruction of b-jets. Within the standard jet energy calibration algorithms described in Section 3.6, the global sequential calibration step aims to correct the differences between quark and gluon-initiated jets [56]. However, no efforts are made to correct for differences between jets initiated by light vs. heavy flavoured quarks. These jets have distinct differences, which can be accounted for by a dedicated additional calibration. Jets originating from heavy flavoured quarks have a higher fraction of leptons in their final state as their decay is mediated by W bosons, which decay to leptons ($W \to \ell\nu$) 33% of the time [80]. This affects the jet energy reconstruction as neutrinos escape the detector without depositing energy in the calorimeter. In addition, the energy of the muons produced through W-decays are not included in jet reconstruction. This means that a significant fraction of the b-jet energy can go undetected, and as a result, on average b-jets are reconstructed to be slightly lower in momentum than other jets, as shown in Figure 4.3. Finally, because of their higher mass, b-jets tend to spread wider in the $\eta - \phi$ plane [93].

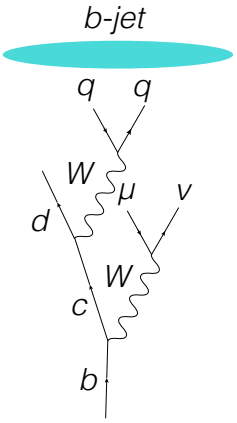

Figure 4.1

b-jet corrections aim to improve the calibration of b-jets by adjusting the momentum to reflect these differences. In other words, find a function f that adjusts the p_T of a jet to p'_T given a b-jet's properties θ:

$$p'_T = f(p_T|\theta_{\text{b-jet}})$$

b-jet corrections are particularly advantageous in searches where a Higgs decays to a bottom quark pair, such as the $H \to b\bar{b}$ decay in $HH \to b\bar{b}\gamma\gamma$, $b\bar{b}\tau^+\tau^-$ and $b\bar{b}b\bar{b}$. The impact of the miscalibrated

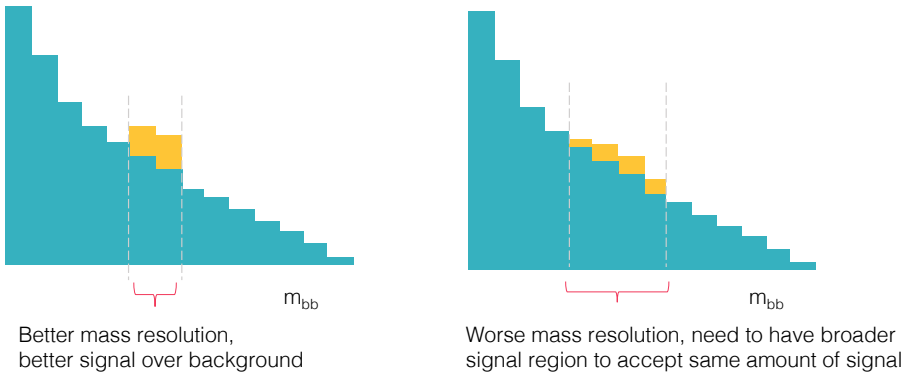

Figure 4.2: A cartoon illustrating the impact that a broader m_{bb} resolution has on analysis.

b-jets is a wider Higgs mass peak with a lower invariant mass m_{bb} than if the jets were perfectly calibrated. As a result, selections that use the $b\bar{b}$ invariant mass will accept more background for the same signal efficiency as illustrated in Figure 4.2.

4.2 Previous approaches

A variety of approaches to this problem have previously been taken on ATLAS, CMS, and CDF and will be discussed. The first proposed use for b-jet corrections via multivariate technique was used in VH(bb) Higgs searches on CDF [94]. Since then, b-jet corrections have been employed by CMS and ATLAS with applications in VH(bb),$t\bar{t}H$, and $b\bar{b}\gamma\gamma$. This section will review the prior literature on b-jet corrections:

The simplest method for b-jet corrections is the Muon-in-jet+PtReco correction developed by ATLAS, which consists of two step; the muon in jet correction and the PtReco correction. The Muon-in-jet correction adds the 4 momentum of any $p_T \geq 5$ GeV muon found within $\Delta R \leq 0.4$ of a b-tagged jet back into the jet. Next the PtReco correction is applied. This correction first derives the mean jet response (α) in bins of p_{T} in a $t\bar{t}$ sample. Then each b-tagged jet in the signal sample is corrected by $1/\alpha(p_T)$ to improve the jet energy scale. Truth vs other jets. This technique has successfully been used in the evidence and observation of VH(bb), where it was shown to improve the di-jet invariant mass by up to 18% [95], [96].

More sophisticated multivariate methods for b-jets corrections have also been used, e.g. on CDF, where a neural network trained on nine input variables was used for b-jet corrections in VH(bb) searches. CMS later extended this method by including additional input variables [97] and by simultaneously estimating the b-jet energy and resolution [93].

On ATLAS, multivariate techniques have also been studied for b-jet corrections. In particular, a BDT with 30 input variables was developed for use in VH(bb) searches [98]. However, to date, only

the Muon-in-jet+PtReco correction has been used in any published ATLAS analyses.

4.3 Datasets

In this chapter, results will be shown with a dataset generated with ATLAS Full Monte Carlo simulation. For training, b-jets from a $t\bar{t}$ dataset was used to provide high statistics across a range of b-jet momenta. The $t\bar{t}$ dataset was generated with PYTHIA 8 with the A14 tune. In addition to the $t\bar{t}$ sample, a resonant $HH \to b\bar{b}b\bar{b}$ Randall Sundrum Graviton (G^*_{KK}) sample was used for performance evaluation. The G^*_{KK} sample was generated with Madgraph Pythia8 EvtGen at A14NNPDF23LO at $m_X = 400$ GeV.

To create the datasets, jets were selected starting from Anti-k_t $R = 0.4$ particle flow jets. Selected jets had a $p_{\mathrm{T}} \geq 20$ GeV and were within the inner detector between $|\eta| \leq 2.5$. To select jets coming from b-hadron decays, the truth particle record in the Monte Carlo simulation is used. Jets were selected if a truth b-hadron was within a ΔR of 0.4 of the reconstructed jet, had a $p_{\mathrm{T}} \geq 5$ GeV, and where the parent particle was either a W, Z, t, or H.

As the reconstructed jets do not include the energies of the muons and neutrino in them, truth jets were used to set the target p_T for the regression. Truth jets are clustered from "stable" truth particles, defined as particles with a $c\tau > 10$mm and incorporate the momenta from all semi-leptonic decay products produced by hadrons [99]. The truth jets are clustered with Anti-k_t $R = 0.4$ and are required to be matched to the reconstructed jet within $\Delta R < 0.3$. Distributions of the reconstructed vs. truth p_{T} are shown in Figure 4.3.

After selections, 2,084,545 b-jets were available in the $t\bar{t}$ dataset. The dataset was split into training, validation, and test sets with fractions of 70%, 20%, & 10% respectively. Evaluation was performed on the $t\bar{t}$ validation and test sets and a resonant $HH \to b\bar{b}b\bar{b}$ Randall Sundrum Graviton (G^*_{KK}) sample with 624,584 b-jets. This G^*_{KK} dataset was used to evaluate the impact of the b-jet corrections on the Higgs invariant mass in a p_{T} range close to what was expected in SM HH production.

Dataset	Number of Jets
$t\bar{t}$	2,084,545
G^*_{KK} HH $m_X = 400$ GeV	624,584

Table 4.1: Number of jets in the available datasets after selection

4.4 Muons in b-jets

The effect of the semi-leptonic b-jet decays on the jet response is visible in Figures 4.5. Jets without a muon within at $\Delta R < 0.4$ are well calibrated with a jet response close to one. However, jets with

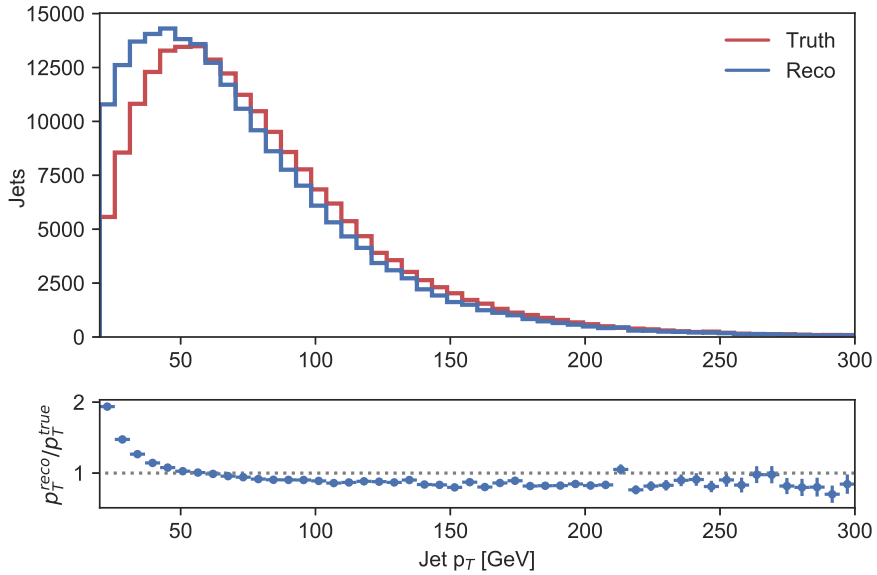

Figure 4.3: Reconstructed and truth jet p_{T} distributions in the $t\bar{t}$ dataset. The true jet p_{T} distribution is shifted upwards relative to the reconstructed jet p_{T} distribution.

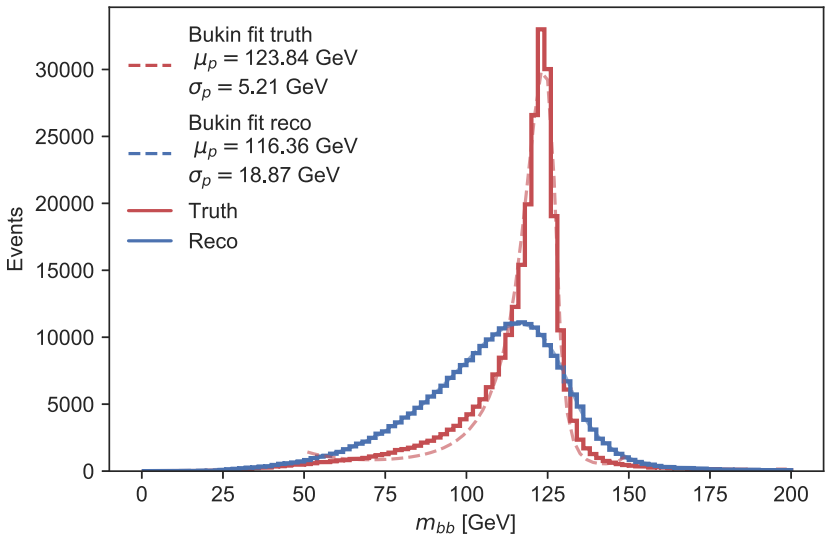

Figure 4.4: Truth vs reconstructed m_{bb} distribution for the Higgs decays from the G^*_{KK} $HH \rightarrow b\bar{b}b\bar{b}$ dataset.

a muon within their jet cone have a median jet response that is below one, due to the energy of the muon and neutrino not being included in the jet calibrations. The effect of the semi-leptonic decays on the $m_{b\bar{b}}$ resolution is visible in Figure 4.6 where the resolution is degraded for b-jet pairs with at least one muon in them. Table 4.2 shows that about 13% of b-jets have a muon within their jet cone.

Figure 4.5, Figure 4.6, Table 4.2

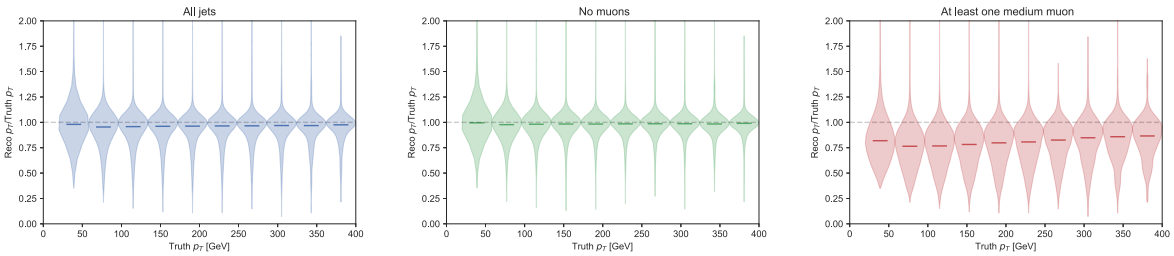

(a) (b) (c)

Figure 4.5: Jet response distributions for (a) All b-jets, (b) Jets with no muon within a ΔR of 0.4, and (c) Jets with at least one muon within a ΔR of 0.4. An average response < 1 is visible across the range of p_{T} bins with the exception of the lowest bin, where the response trends upwards.

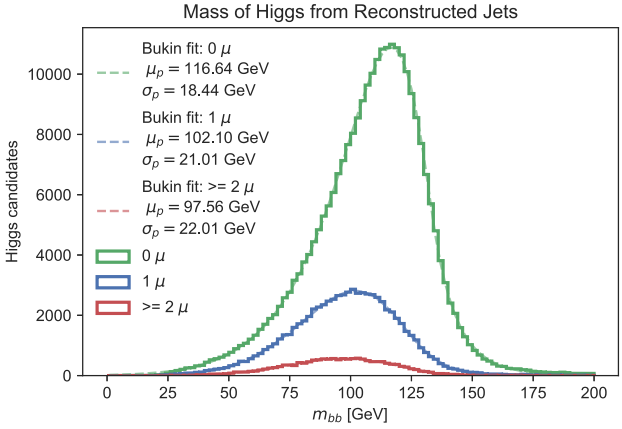

Figure 4.6: Illustration of the effect of muons in jets on the Higgs invariant mass resolution in the $m_X = 400$ GeV G^*_{KK} dataset

4.5 Input variables

Several types of input variables were studied for the regression. The variables considered were chosen based on whether they could be related to the real momentum of the b-jet. For example,

Number of muons	Fraction of Jets
All	100.0%
0 muons	83.7%
1 muon	13.4%
≥ 2 muons	2.9%

Table 4.2: Fraction of jets with muons within $\Delta R < 0.4$ in the G^*_{KK} m_X =400 GeV training dataset

soft lepton variables could indicate the presence of a semi-leptonic decay and carrying energy away from the reconstructed jet. With the advent of machine learning and deep neural networks, many particle physics experiments have seen large improvements in performance in object identification by moving away from carefully curated high-level features and towards training neural networks on large amounts of low-level features which can carry additional information. One of the questions we were trying to study in this project was whether additional, low-level b-tagging information could improve upon prior b-jet corrections such as the Muon-in-jet+PtReco correction. Each set of variables will be described in more detail in the following sections, but they can be summarized as follows:

- Jet-related variables: information on jet calibration
- Soft lepton variables: carry information on whether a semi-leptonic b-hadron decay has occurred and taken energy away from the jet
- DL1 and high-level b-tagging information: level of confidence in a jet being b-jet could lead to a different correction
- SV1 and Jet Fitter vertexing information: can provide information on the jet topology, such as where the secondary and tertiary vertices are located
- IP3D / RNNIP track-based variables: low-level information can provide information on semi-leptonic decays and jet topology

Jet variables

The variables include information on the jet 4-vectors and additional information about the quality of the jet. Several sets of inputs were considered, from the simplest - just considering jet p_{T}, to using the full 4-vector, to sets that included information on the jet quality, including isolation and JVT score (Jet-Related). A final set included lower-level information coming from the tracks and topocluster, such as the jet width, sum of p_{T} of the tracks associated to the jet, etc. All variables used in each set are described in Table 4.3

Variable	Variable Name	Description
p_T	p_T	p_T of jet
$\vec{\text{Jet}}$	p_T	p_T of jet
	η	η of jet
	ϕ	ϕ of jet
	m	Jet mass
Jet-Related	p_T	p_T of jet
	m	Jet mass
	E	Jet energy
	ΔR_{iso}	Distance to next closest jet
	JVT	Jet Vertex Tagger Score [100]
Jet-New	Jet width	$w = \sum_i (\Delta R^i p_T^i)/(\sum p_T^i)$ p_{T}-weighted radial distance of the jet components with respect to the jet axis
	Jet charge	Total charge in jet calculated from tracks
	R_{pT}	Ratio of $\sum p_T(PV)$ for all tracks in primary vertex/ p_T^{jet}
	TrackSumPt	$\sum p_T$ of all tracks in jet
	TrackSumMass	Invariant mass of all tracks in jet
	N90Constituents	Number of topoclusters responsible for 90% of the total jet energy
	EMFrac	Fraction of jet energy deposited in Electromagnetic calorimeter
	HECFrac	Fraction of jet energy deposited in Hadronic EndCap calorimeter
	$\max(p_{T,i})$	p_T of track with highest momentum of all tracks in jet
	ptd	$\sum p_T^2 / \sum p_T$ of all tracks

Table 4.3: Input variables from jets.

Variable	Variable Name	Description
$\vec{\mu}$	p_T	p_T of leading medium muon
	η	η of leading medium muon
	ϕ	ϕ of leading medium muon
	E	E of leading medium muon
All muons	p_T	p_T of up to 3 muons
	η	η of up to 3 muons
	ϕ	ϕ of up to 3 muons
	E	E of up to 3 muons
	isMedium	Boolean for whether muons pass medium ID requirement
	isTight	Boolean for whether muons pass tight ID requirement
All electrons	p_T	p_T of up to 2 medium ID electrons
	η	η of up to 2 medium ID electrons
	ϕ	ϕ of up to 2 medium ID electrons
	E	E of up to 2 medium ID electrons

Table 4.4: Input variables related to muon and electrons. No isolation is applied to the muons or electrons.

Soft lepton variables

These variables provide information on the presence of semi-leptonic decays within the b-jet. Leptons found within a ΔR of 0.4 of the jet were included in the studies, and studied in three separate sets. One set included the 4-vector of the only highest p_{T} muon. The next set included the 4-vectors and quality scores for up to three leading muons. Finally, a set with up to two leading electrons was studied. These sets are detailed in Table 4.4 and their impact is studied in Section 4.9.5. Variables from the Soft Muon Tagger described in Section 3.8 were also studied. The Soft Muon Tagger provides additional information related to the impact parameters of the muon, the muon quality, and the relationship between the muon and the jet and as outlined in Table 4.5

Impact parameter based b-tagging information

RNNIP and IP3D are b-tagging algorithms based on impact parameters of the tracks associated with a jet and are described in Section 3.8.2. For RNNIP, p_b and p_τ were available. For IP3D, p_u,p_c and p_b were available.

Secondary Vertexing Based Variables

Outputs from to the SV1 and JetFitter algorithm discussed in Section 3.8.1 were considered and are shown in Table 4.7 and 4.8 respectively. These were considered as they include information on the distance to the secondary vertex, and in the case of JetFitter, the presence of tertiary vertices. Note that while some variables look the same (e.g. the number of two track vertices), SV1

Variable	Variable Name	Description
SMT	$\Delta R(j, \mu)$	Angular distance between jet and muon
	d_0^μ	Transverse impact parameter of muon
	z_0^μ	Longitudinal impact parameter of muon
	$p_T^j\ p_T^\mu)$	Ratio of jet momentum to muon momentum
	q/p	muon charge to mass ratio
	$(q/p)_{\mathrm{ID}}/(q/p_{\mathrm{MS}})$	from the muon track in the inner detector relative to the track in the muon spectrometer
	$(p_{\mathrm{ID}} - p_{\mathrm{MS}})/E_{\mathrm{calo}}$	Difference between the momentum measured in the spectrometer and the inner detector divided by the energy loss in the calorimeter
	$\sum_i \Delta\phi_i/(\sigma_{\Delta\phi_i})$	Significance of the angular difference $\Delta\phi$ between pairs of adjacent hits along the track

Table 4.5: Input variables available from Soft Muon Tagger

Variable	Variable Name	Description
RNNIP	p_b	Predicted probability for jet coming from a b
	p_τ	Predicted probability for jet coming from a τ lepton
IP3D	p_b	Predicted probability for jet coming from a b
	p_c	Predicted probability for jet coming from a c
	p_u	Predicted probability for jet coming from a u, d, s or gluon
	N_{track}	Number of tracks used in IP3D score calculation
	LLR	Log likelihood ratio built as described in Section 4.9.4

Table 4.6: Variables available from the IP3D and RNNIP taggers

Variable	Variable Name	Description
SV1	$N_{2t}(SV)$	Number of two track vertex candidates
	N_{vertex}	Number of tracks in the secondary vertex
	$m(SV)$	Mass of the tracks at the secondary vertex
	$f_E(SV)$	Fraction of the charged jet energy in the secondary vertex
	L_{xy}	Transverse distance between the primary and secondary vertices
	L_{3D}	Distance between the primary and secondary vertices (x, y, z)
	S_{3D}	L_{3D} significance, distance divided by its uncertainty
	Normdist	L_{3D} normalized by number of silicon layers traversed
	$\Delta R(\text{jet}, SV)$	ΔR between the jet axis and vector sum of all tracks from displaced vertices
	LLR	Log likelihood ratio built from $m(SV), f_E(SV), N_{2t}$, and $\Delta R(\text{jet}, SV)$

Table 4.7: Variables available from the SV1 tagger

and JetFitter use different track quality requirements for their inputs and therefore carry slightly different information. For this reason, variables may appear duplicated.

High-Level *b*-tagging scores

The b-tagging scores for a variety of high-level taggers were considered as inputs to the correction as shown in Table 4.9. The concept behind including these variables is that a jet with a higher b-tagging score is more likely a *b*-jet, and therefore it could potentially receive a different correction relative to a jet where the b-tagging score was lower.

4.6 Preprocessing

Most neural networks are designed for variables that are normally distributed about 0 with unit standard variation. Scaling is performed to transform our data to similar ranges. One of the challenges with many particle physics datasets is their long tails, so instead of translating by the mean and scaling by standard deviation, the median, and interquartile ranges were used for scaling with the sklearn RobustScaler. Non-linear transformations were also experimented with, but did not show large improvements in performance.

Another challenge is that missing variables are often set to a value like -999, -99, or -1. This causes a large spike at that number. There is no great way to handle missing numbers in a dense (non-variable length network). A masking layer was used within a particle flow network that can handle variable length inputs for this purpose.

Variable	Variable Name	Description
Jet Fitter	JetFitter p_b	Jet Fitter predicted probability for jet coming from a b
	JetFitter p_c	Jet Fitter predicted probability for jet coming from a c
	JetFitter p_u	Jet Fitter predicted probability for jet coming from a u, d, s or gluon
	JetFitter LLR	Jet Fitter log-likelihood ratio
	m	Invariant mass of tracks from displaced vertices
	$m_{\text{uncorrected}}$	Invariant mass of tracks from displaced vertices
	f_E	Fraction of charged jet energy in displaced vertices
	$\Delta R_{\text{FlightDir}}$	ΔR between jet axis and $\sum \vec{p}$ of all tracks
	$\Delta\eta_{\text{FlightDir}}$	$\Delta\eta$ between jet axis and $\sum \vec{p}$ of all tracks
	$\Delta\phi_{\text{FlightDir}}$	$\Delta\phi$ between jet axis and $\sum \vec{p}$ of all tracks
	ϕ	Jet ϕ
	θ	Jet θ
	σ_θ	Uncertainty on jet θ
	σ_ϕ	Uncertainty on jet ϕ
	$n_{trkAtVx}$	Average number of tracks at displaced vertices
	n_{vtx}	Number of reconstructed displaced vertices
	L_{3D}	Average distance between PV and displaced vertices
	σ_{3d}	Uncertainty on average distance between PV and displaced vertices
	n_{1t}	Number of one track vertex candidates
	n_{2t}	Number of two track vertex candidates
	VTXsize	
	MaxTrkRapidity	Maximum track rapidity from tracks associated with either of the displaced vertices
	AvgTrkRapidity	Average track rapidity from tracks associated with either of the displaced vertices
	MinTrkRapidity	Minimum track rapidity from tracks associated with either of the displaced vertices
	$n_{trk,vtx\ 1,2}$	Number of tracks associated with the secondary and tertiary vertices
	$m_{vtx\ 1,2}$	Mass of tracks associated with the secondary and tertiary vertices
	$E_{vtx\ 1,2}$	Energy of tracks associated with the secondary and tertiary vertices
	$f_{E,vtx\ 1,2}$	Fraction of charged jet energy from tracks associated with the secondary and tertiary vertices
	$L_{3D,vtx\ 1,2}$	3D distance from the primary vertex to the secondary and tertiary vertices
	$L_{xy,vtx\ 1,2}$	Transverse distance from the primary vertex to the secondary and tertiary vertices
	MaxTrkRapidity$_{vtx\ 1,2}$	Maximum track rapidity from tracks associated with the secondary and tertiary vertices respectively
	AvgTrkRapidity$_{vtx\ 1,2}$	Average track rapidity from tracks associated with the secondary and tertiary vertices respectively
	MinTrkRapidity$_{vtx\ 1,2}$	Minimum track rapidity from tracks associated with the secondary and tertiary vertices respectively

Table 4.8: Input variables available from JetFitter

Variable	Variable Name	Description
DL1	DL1 p_b	DL1 predicted probability for jet coming from a b
	DL1 p_c	DL1 predicted probability for jet coming from a c
	DL1 p_u	DL1 predicted probability for jet coming from a u, d, s or gluon
	DL1r p_b	DL1r (with RNNIP inputs) Predicted probability for jet coming from a b
	DL1r p_c	DL1r (with RNNIP inputs) Predicted probability for jet coming from a c
	DL1r p_u	DL1r (with RNNIP inputs) Predicted probability for jet coming from a u, d, s or gluon
MV2	MV2C10	MV2 predicted probability for jet coming from a b, $f_c = 10\%$
	MV2C10mu	MV2 (with SMT inputs) predicted probability for jet coming from a b, $f_c = 10\%$
	MV2C10r	MV2 (with RNNIP inputs) predicted probability for jet coming from a b, $f_c = 10\%$
	MV2C100	MV2 predicted probability for jet coming from a b with $f_c = 100\%$

Table 4.9: Input variables related to high level taggers

4.7 NN architecture and hyper-parameter optimization

A random grid search was used for initial hyper-parameter optimization, followed by by-hand fine-tuning. Hyper-parameters that were optimized included the learning rate (ranging between 0.001 and 0.00001), the minibatch size (ranging between 32-248), the network architecture (Particle Flow Network, or fully connected dense network), and the number of nodes per layer. The benefit of a particle flow network is that the ordering of the does not matter. For the best performing network on the $t\bar{t}$ validation set, the network architecture is illustrated in Figure 4.7. The learning rate was 0.001, and the minibatch size was 256. The model consisted of a dense network for the jet inputs with (100,100,100,100) nodes per layer, PFN layers with (100,10) nodes per layer. These were then concatenated and merged into a final dense network with (100,100,100,1) nodes per layer. The model has 152,751 trainable parameters.

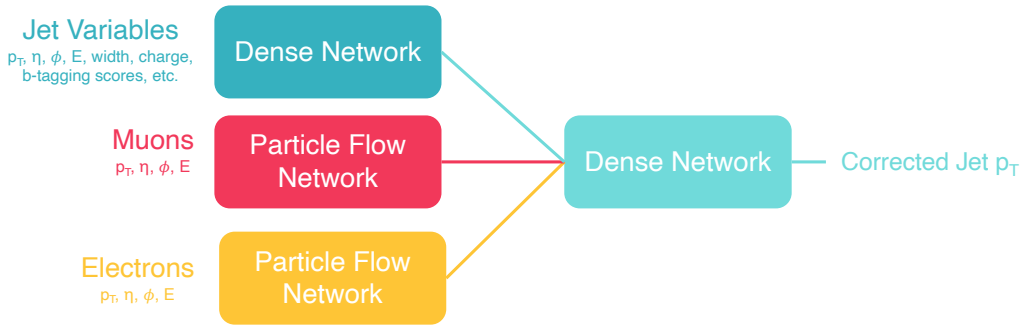

Figure 4.7: Example NN architecture

4.8 Performance metrics

A number of different metrics were considered when developing the regression. The first was the loss on the training and validation sets. These losses were monitored during training, and early stopping was applied on the validation loss to prevent overfitting on the training set. The loss functions evaluated included the Mean Squared Error (MSE), Mean Absolute Error (MAE), Mean Absolute Percentage Error (MAPE) and the logcosh error. The logcosh loss function was the loss that was selected as it was the least sensitive to long tails in the input distributions.

4.8.1 Loss functions

Mean Squared Error

$$L_{\text{MSE}} = \frac{\sum_{i=1}^{n}(y_i - \hat{y}_i)^2}{n}$$

A drawback of this loss function is that it corrects more strongly for large outliers.

Mean Absolute Error

$$L_{\text{MAE}} = \frac{\sum_{i=1}^{n}|y_i - \hat{y}_i|}{n}$$

The MAE loss is less sensitive to large outliers. However, the MAE loss has a gradient that is the same even for large loss values, making it less stable than MSE.

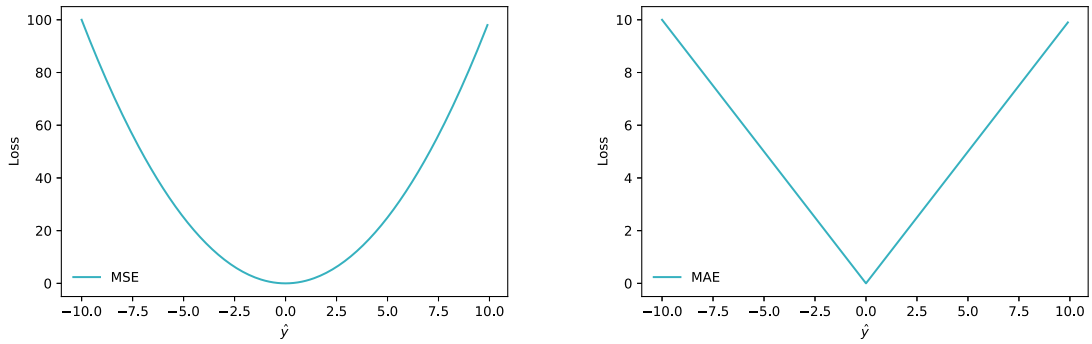

(a) (b)

Figure 4.8: MSE and MAE loss functions

Huber Loss

The Huber loss tries to combine the robustness of the MAE loss with the sensitivity of the MSE loss.

$$L_\delta = \begin{cases} \frac{\sum_{i=1}^{n}(y_i - \hat{y}_i)^2}{2n} & \text{if } |y - \hat{y}| \leq \delta \\ \frac{\sum_{i=1}^{n}\delta|y_i - \hat{y}_i|}{n} - \frac{1}{2}n\delta^2 & \text{if } |y - \hat{y}| > \delta \end{cases}$$

This provides a nice combination of being less sensitive to outliers and having a gradient that is small when the predictions are close to correct. A drawback of Huber loss is that the parameter δ also has to be tuned to the dataset. Figure 4.9a shows the Huber loss function for a variety of δ's.

Logcosh Error

$$L_{\text{logcosh}} = \sum_{i=1}^{n} \log(\cosh(y_i - \hat{y}_i))$$

As shown in Figure 4.9b the logcosh function is similar to the Huber loss, but has the benefit of not having an additional δ hyper-parameter to tune.

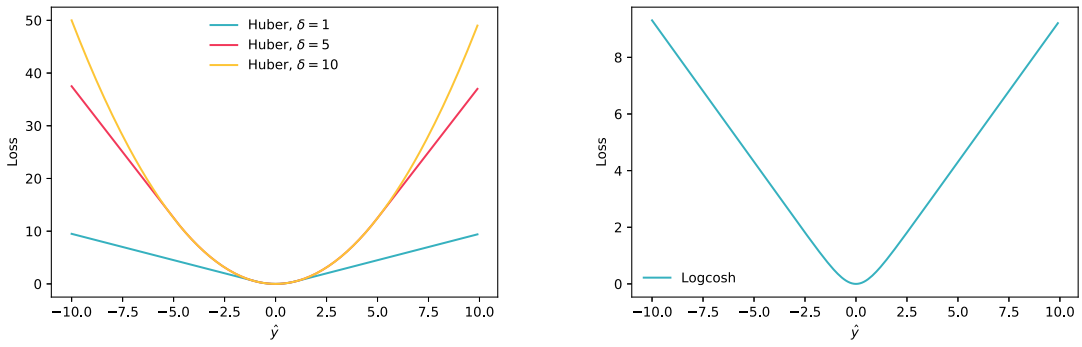

(a) (b)

Figure 4.9: Huber and Logcosh loss functions

4.8.2 Early stopping

Early stopping prevents overfitting on the training dataset, by evaluating the loss of the validation dataset after every epoch and saving the model with the lowest validation loss.

Jet response in validation sample

One of the metrics used to evaluate the regression is the jet response. E.g, the distribution of the reconstructed p_{T} relative to the truth p_{T}. $\frac{p_T^{\text{reco}}}{p_T^{\text{true}}}$. This distribution should be centered about 1, with as narrow width as possible. It can also be evaluated in bins of p_T^{true} for added granularity. Because the jet response distribution typically has long tails, it is preferable to look at the distributions' median

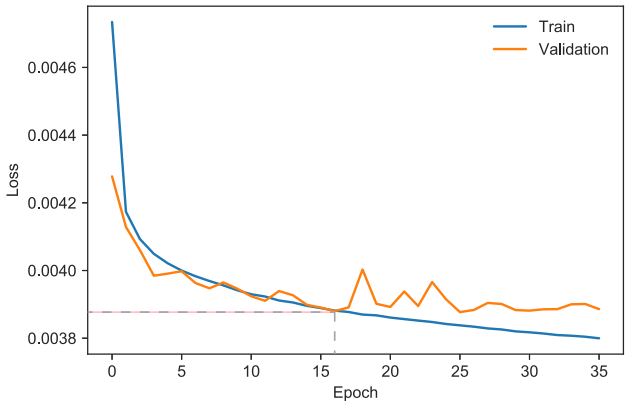

Figure 4.10: Training curve, the grey dashed lines show where the model is saved.

and the interquartile ranges instead of the average and standard deviation. Figure 4.5 demonstrates the jet response binned in truth jet p_{T} for b-jets with and without an associated muon.

m_{bb} resolution in HH samples

The relative improvement in the peak position (μ) and the width (σ) of the m_{bb} distribution is of primary importance in most Higgs searches. This is because most searches are fighting a smoothly falling background. To improve the signal over background ratio, a narrow peak closer to the Higgs mass, as illustrated in Figure 4.2. A Bukin function [101] was used to fit the two b-jet invariant mass distribution. The function is a six-parameter function that convolves a Gaussian core with asymmetric exponential tails.

The function is defined as follows:

$$f(x) = A_p \exp\left[\frac{\xi\sqrt{\xi^2+1}(x-x_i)\sqrt{2\ln 2}}{\sigma_p(\sqrt{\xi^2+1}-\xi)^2\ln(\sqrt{\xi^2+1}+\xi)} + \rho\left(\frac{x-x_i}{x_p-x_i}\right)^2 - \ln 2\right]$$

Where x_1 and x_2 are defined as:

$$x_{1,2} = x_p + \sigma_p\sqrt{2\ln 2}\left(\frac{\xi}{\sqrt{\xi+1}} \mp 1\right)$$

and $\rho = \rho_1$ and $x_i = x_1$ for $x < x_1$ and $\rho = \rho_2$ and $x_i = x_2$ for $x \geq x_2$

The parameters x_p, and σ_p are the position and width of the Gaussian core. A_p corresponds to the amplitude of the peak. ρ_1 and ρ_2 are the parameters defining the shape of the left and right tails and ξ is the asymmetry parameter. Figure 4.3 shows an example of a Bukin fit to the m_{bb} distribution.

In an attempt to compare models with a single number as a metric, the relative m_{bb} resolution is also calculated:

$$m_{bb} \text{ resolution} = \frac{\sigma}{\mu}$$

Although the impact of the different regressions on the invariant mass resolution is a very intuitive metric, one of the challenges with using this metric is that it is evaluated on a different dataset than used in training. Due to this issue, as well as the lower statistics available in the G^*_{KK} dataset, and the fact that this metric is based on a chi-squared fit, there is also significantly more variation in results with different neural network trainings compared to the validation loss. This is demonstrated within 4.11 where the validation loss is compared to the $m_{b\bar{b}}$ resolution.

An additional complication is that μ and σ are not perfectly correlated, leading to some models performing better in σ and some performing better in μ. This is illustrated in Figure 4.12. For this reason, when comparing the impact of certain input variable selections as done in Section 4.9.4, we average across multiple (10) trainings at a time.

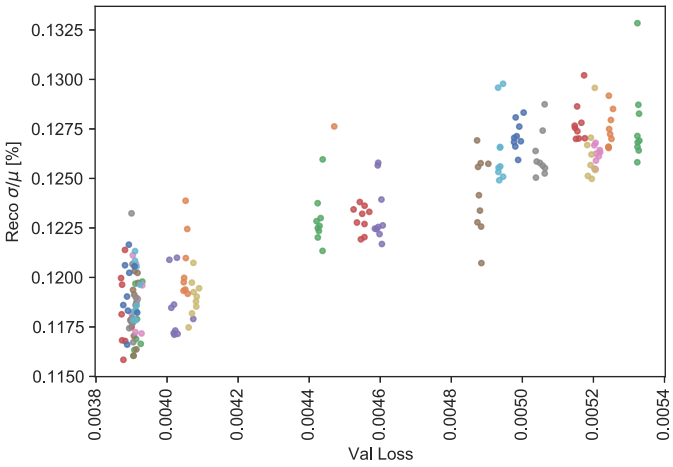

Figure 4.11: Loss on the $t\bar{t}$ validation set compared with m_{bb} resolution on the G^*_{KK} $m_X = 400$ GeV dataset. While a general trend of a lower validation loss correlating with a better (lower $m_{b\bar{b}}$ resolution) is clearly visible, there is more variation on the y-axis than the x-axis.

4.9 Results

The following section will detail the results on the $t\bar{t}$ and G^*_{KK} $HH \to b\bar{b}b\bar{b}$ datasets. It will also examine the importance of various input variables and discuss attempts to prune them. Finally results on the datasets used in the $b\bar{b}\gamma\gamma$ analysis will be presented.

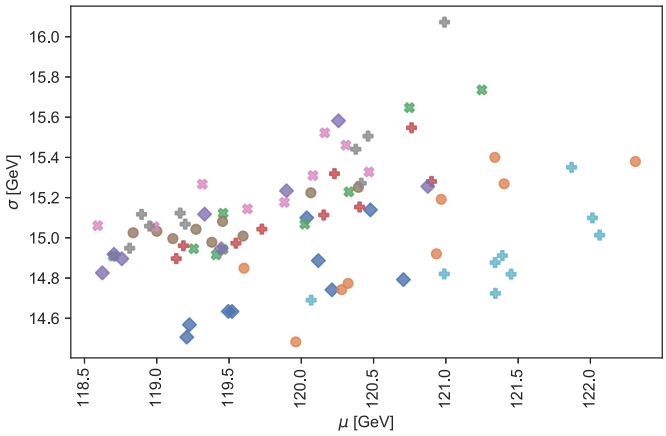

Figure 4.12: m_{bb} μ vs σ on the G^*_{KK} $m_X = 400$ GeV dataset. There is a high amount of variance between NNs trained with different sets of input variables. A trade-off between the μ and σ is visible. NNs that perform better in μ tend to do slightly worse in σ and vice-versa

4.9.1 Performance on $t\bar{t}$ validation set

The primary metric used to evaluate the performance of a neural network architecture and its inputs was the validation loss in the $t\bar{t}$ dataset. Figure 4.13 illustrates the reconstructed b-jet p_{T} distributions before and after the regression. The overall distribution in the validation set has been corrected to more accurately match the true p_{T}. The 2D jet response distribution is shown in Figure 4.14. Here we can see that, in general, the width of the response distribution has been reduced. Figure 4.15 shows the same data, but with the median and interquartile ranges displayed. In general, the response is shifted upwards to be more centered about 1 and is narrower in width. One interesting feature is that after the regression, the jet response is slightly over-corrected at low p_{T} and slightly under-corrected at high p_{T}. This is due to a tendency to correct towards the mean p_{T} of the input distribution. Some potential avenues for improving this include training on a sample that is flat in p_{T} and therefore has higher statistics in the tails of the distribution, or using a technique called generalized numerical inversion [102]. However, as we will see in the next section, the benefit of using a b-jet correction outweighs this pitfall.

4.9.2 Performance on HH dataset

Performance was also checked in the G^*_{KK} dataset. As shown in Figure 4.16 the overall jet p_{T} distribution has been shifted upwards and more closely follows the shape of the truth jet p_{T} distribution. The performance relative to the default reconstruction and the Muon-in-jet+PtReco correction is shown in Figure 4.17. The improvement in the m_{bb} resolution, shown in Figure 4.24, with respect to reconstructed resolution is 27.3%. The improvement with respect to Muon-in-jet+PtReco correction

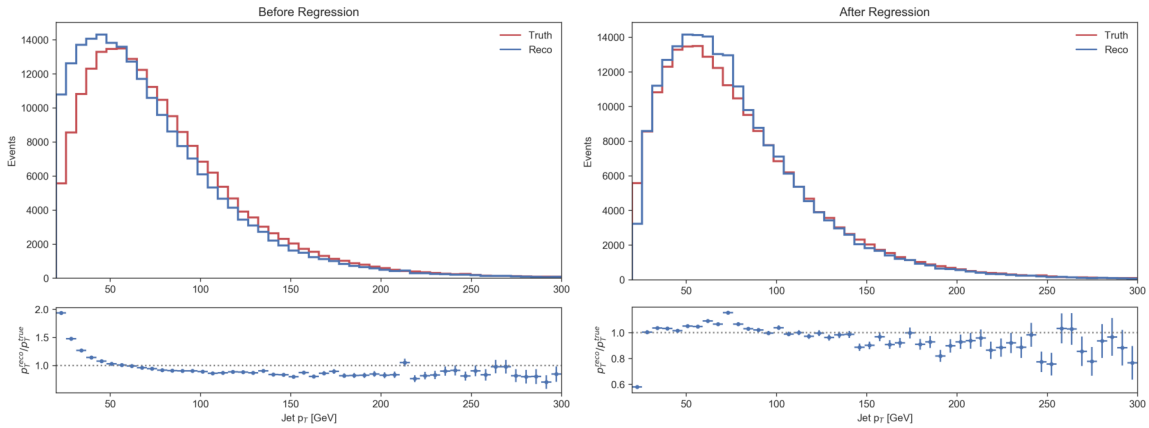

(a) (b)

Figure 4.13: p_T distributions before and after regression on the $t\bar{t}$ sample

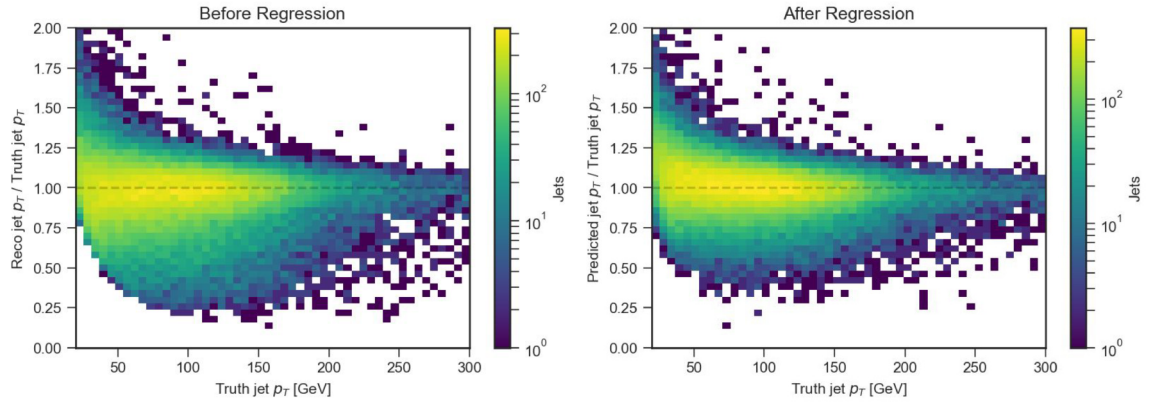

(a) (b)

Figure 4.14: Jet response distributions before and after regression on the $t\bar{t}$ sample

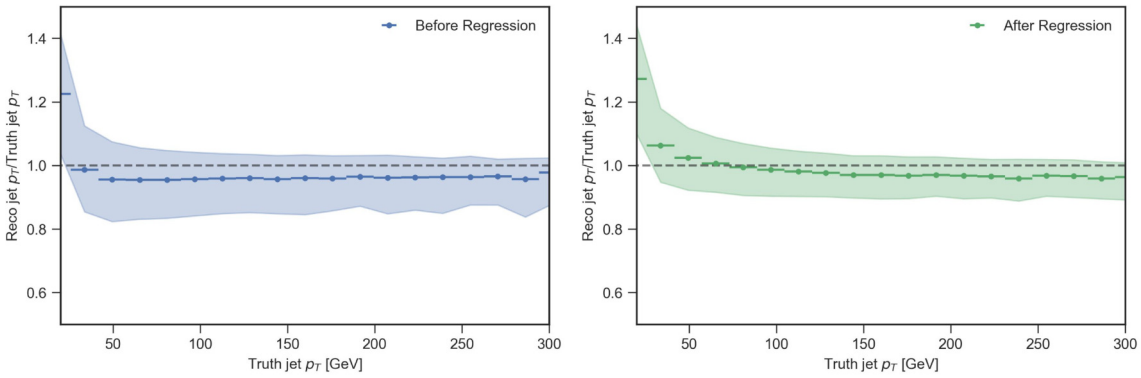

(a) (b)

Figure 4.15: Median and interquartile range of jet response in bins of p_T before and after regression

is 8.5%. This illustrates that the additional variables studied carried additional information used by the regression. A discussion of which input variables had the most impact on the performance is in Section 4.9.4.

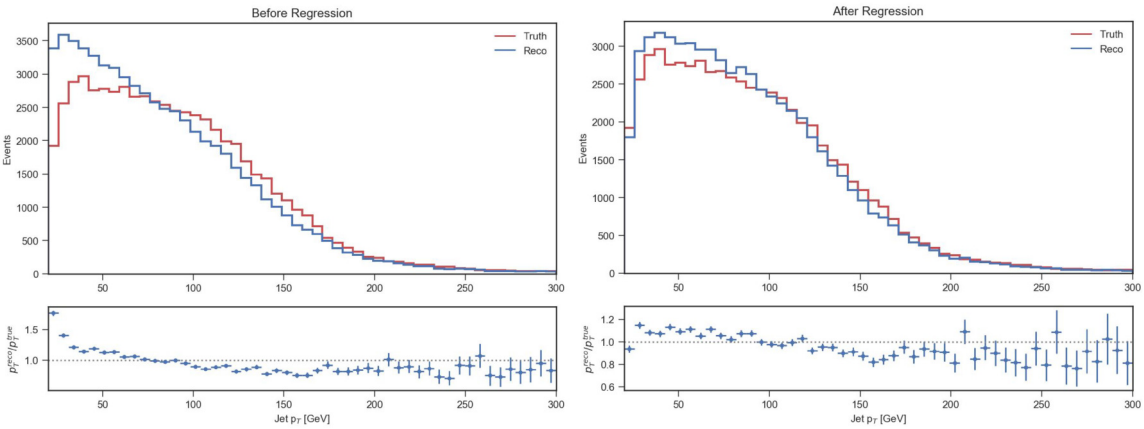

(a) (b)

Figure 4.16: p_T distributions before regression on the G^*_{KK} sample

4.9.3 Background sculpting checks

A concern with any jet calibration is that although it may improve the resolution of a signal peak, it might also be sculpting the background. The b-jet corrections were trained on a jet-by-jet basis to counteract any sculpting over the background. However, we also performed a background sculpting check to test if any background sculpting was present. Here, jets from the $t\bar{t}$ dataset were randomly picked in pairs. If background sculpting was present, we expected a bump in the m_{bb} distribution

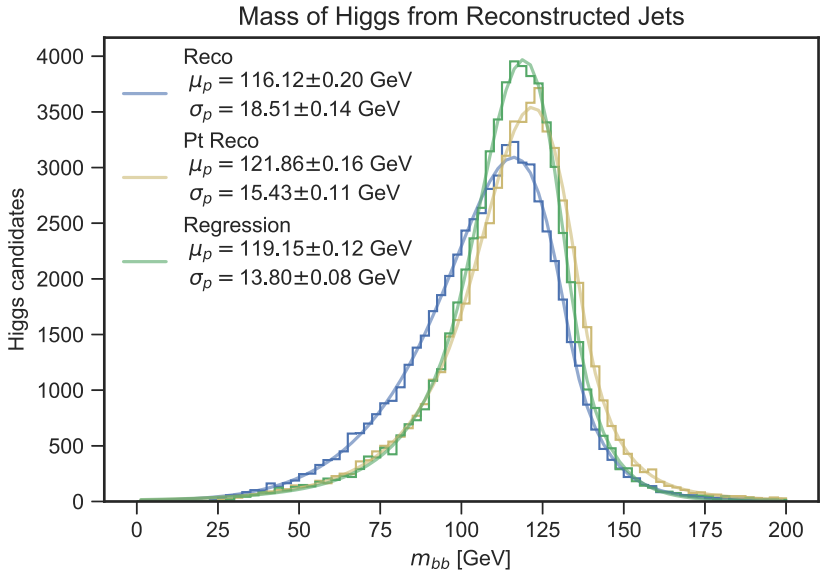

Figure 4.17: Performance of the network with best validation loss and 120 inputs. The relative improvement in the $m_{b\bar{b}}$ resolution in the G^*_{KK} dataset over no correction (Reco) is 27.3%, and over the Muon-in-jet+PtReco correction is 8.5%.

around the Higgs mass. As seen in Figure 4.18, no bump is present.

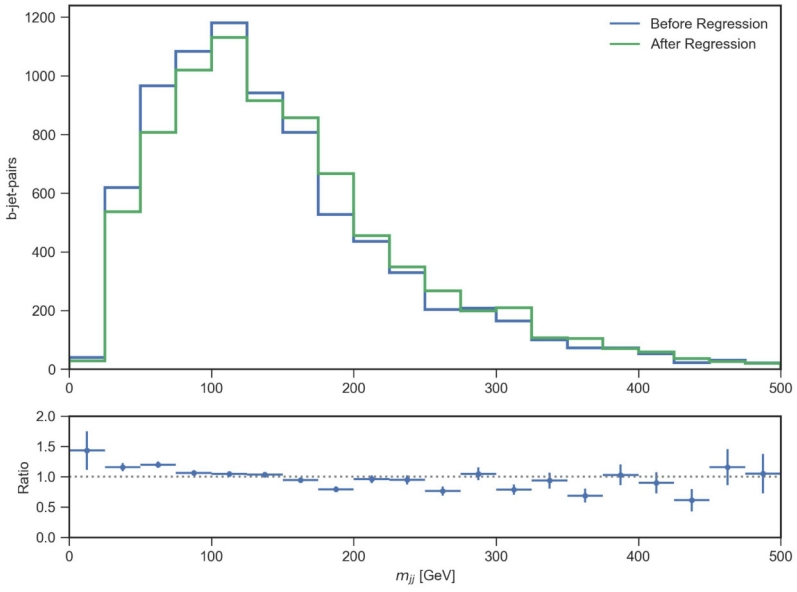

Figure 4.18: Background sculpting check with jet pairs randomly selected from the $t\bar{t}$ dataset.

4.9.4 Impact of different sets of variables

Given the regression's 8.5% improvement relative to the Muon-in-jet+PtReco correction, we were interested in which of the input variables resulted in the increased performance. Many studies were made to check the impact of individual sets of variables. First, variables were ablated individually. However, as many of the input variables were highly correlated, removing any of these variables individually did not produce a significant impact on the performance, see Figure 4.19 for an example of the Pearson correlation coefficient between the JetFitter variables. To simplify the problem, we then grouped inputs by their input type, as shown in the tables in Section 4.5. We then added the groups of inputs into the Baseline regression (using just the jet and leading muon 4-momentum) and checked the change in performance. In Figure 4.20, we can see that the Jet-New and Jet Fitter variables provided the biggest gains in performance relative to only the jet and muon 4-vectors, but adding any set of variables improved the power of the regression on the validation loss.

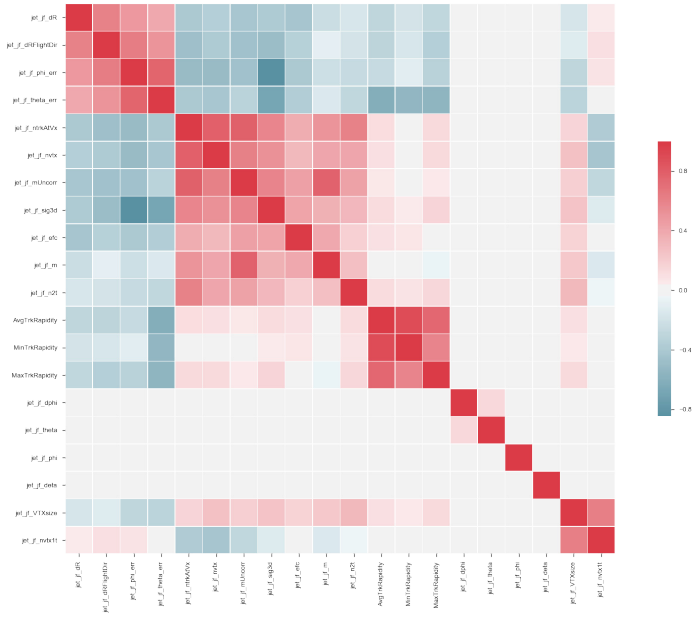

Figure 4.19: Pearson correlation co-efficient of different Jet Fitter variables

Next, we looked at combinations of different input groups as shown in Figure 4.21. Here the general trend is that adding more low-level variables appeared to improve the performance of the regression. This is generally, but not perfectly reflected when comparing the improvements in $m_{b\bar{b}}$ resolution shown in Figure 4.22.

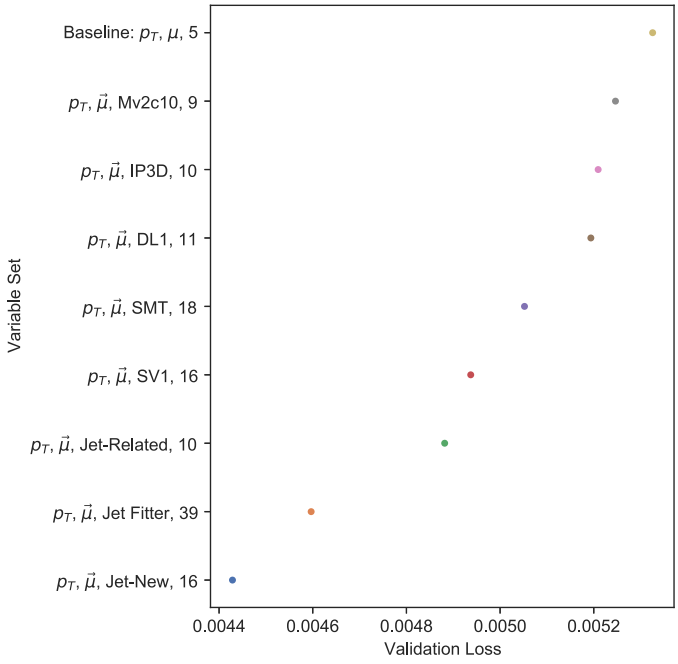

Figure 4.20: Mean validation loss on the $t\bar{t}$ dataset with individual sets of input variables, trained 10 times per set of inputs

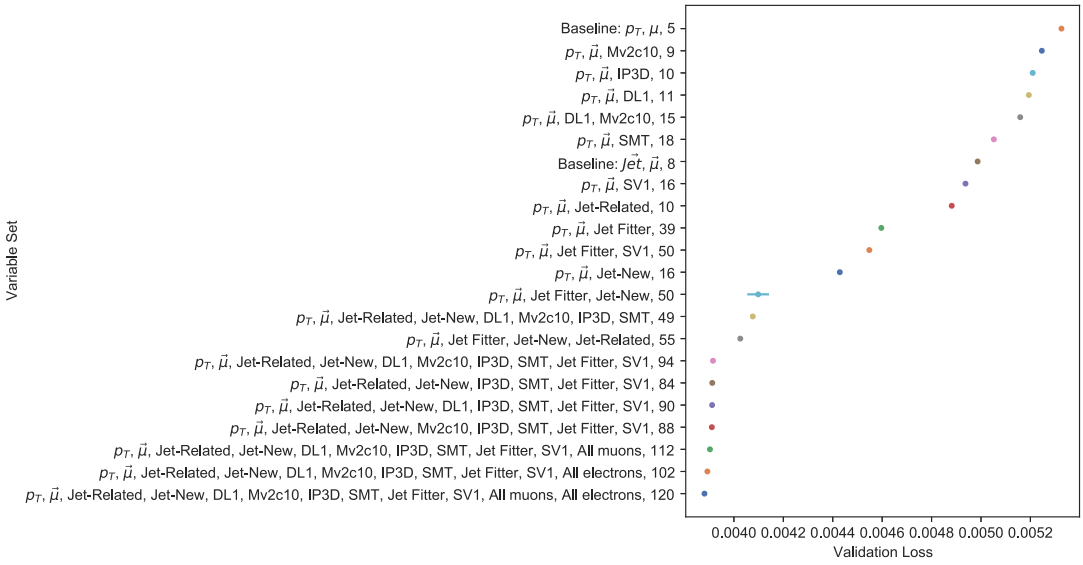

Figure 4.21: Mean validation loss on the $t\bar{t}$ dataset with different sets of variables, trained 10 times per set of inputs

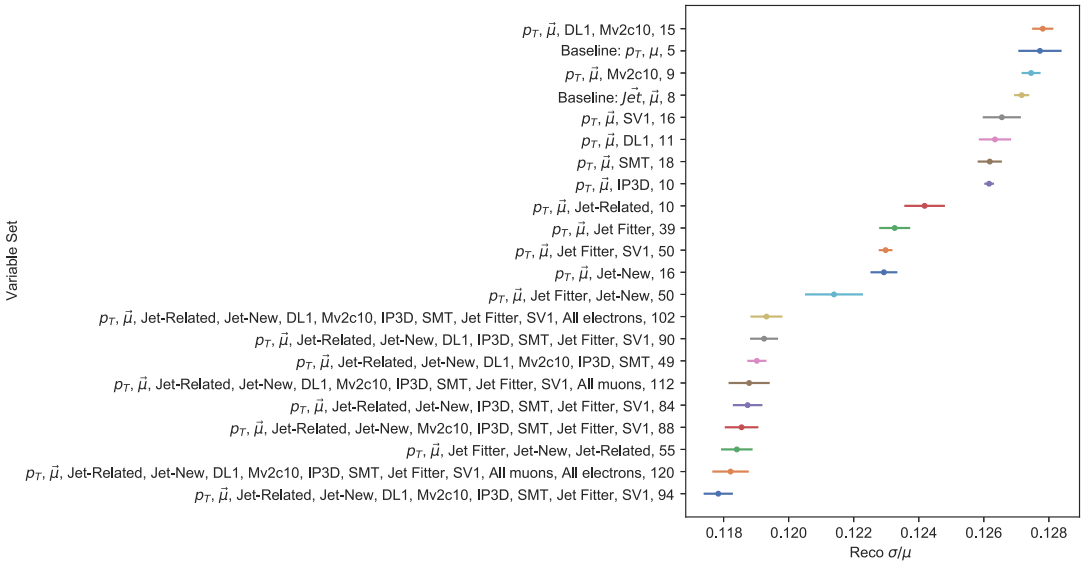

Figure 4.22: Mean resolution improvement on the G^*_{KK} sample with m_X =400 GeV with different sets of variables, trained 10 times per set of inputs

4.9.5 Impact of adding additional leptons

One of the variations we tried was including additional leptons as part of a particle flow network (PFN). Here up to two medium electrons and up to three muons were added as a particle flow branch, in addition to the leading muon included by default. In Figure 4.23, we can see that adding each set of leptons individually improved the validation loss. Adding both leptons at the same time improved the validation loss even more.

4.9.6 Pruning and comparison with the Muon-in-jet+PtReco correction

With ablation and correlation studies we were able to reduce the set of input variables to by more 50% with a marginal loss in performance. This is shown in under "Pruned, 55" in Figure 4.24. The input variables used, included the p_{T} of the jet, the Jet-New and Jet-Related variables described in Table 4.3, the 4 vectors of the 3 leading muons, and the JetFitter variables.

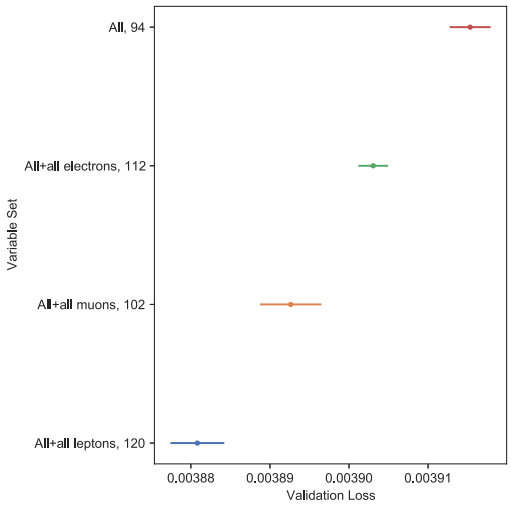

Figure 4.23: Study of adding electrons, muons and both as NN inputs

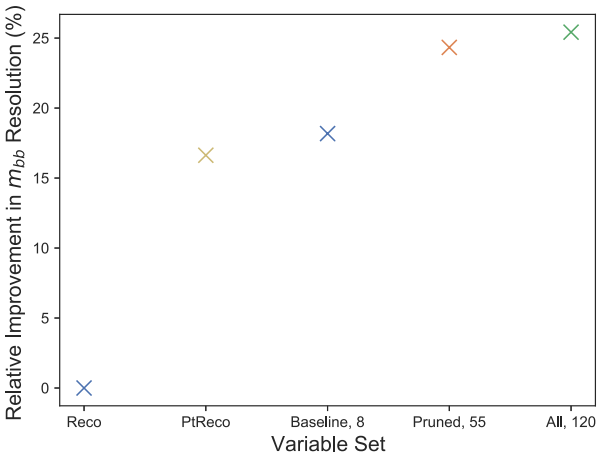

Figure 4.24: Relative resolution improvement with final sets of variables on the G^*_{KK} $m_X = 400$ GeV test dataset

4.10 Discussion

In this chapter, we showed the motivation for jet-by-jet b-jet corrections. We showed the input variables examined and neural network architectures explored. We showed that it is possible to improve the b-jet calibrations and thereby improve the $m_{b\bar{b}}$ resolution by 27% by adding in both the muon 4-vector(s) and various lower-level b-tagging variables. Eventually, this technique could be applied to HH searches to increase signal sensitivity. Additional efforts will be required to

apply these results within an analysis as many of the low-level variables used in this regression are unavailable at the analysis level. In the future, a dedicated regression could be applied within the ATLAS common jet calibrations framework or integrated with the flavour tagging algorithms. Directions for future development could include continuing to distill the input variables to see which have the greatest impact, and training on an extended p_{T} (e.g. one that includes $Z' \to t\bar{t}$) Monte Carlo samples to allow for better calibrations at high p_{T}.

Chapter 5

Search for HH Decaying to $b\bar{b}\gamma\gamma$

5.1 Overview

The $HH \to b\bar{b}\gamma\gamma$ search looks for HH production in ATLAS, where one Higgs decays to two b-jets and the other Higgs decays to two photons. This HH search channel has a very low branching ratio of 0.26%, but the diphoton signature has an excellent trigger efficiency, mass resolution, and low background rates. This leads to $b\bar{b}\gamma\gamma$ channel being one of the most sensitive HH final states for measuring the Higgs self-coupling and HH production cross-section.

The analysis described in this chapter corresponds to our published result performed on the full Run 2 data set of 139 fb^{-1} at 13 TeV [103]. The analysis selects events with two b-jets and two photons in the final state. As the diphoton invariant mass resolution is so excellent, the signal extraction is performed via an unbinned maximum likelihood fit on $m_{\gamma\gamma}$ spectrum. The main processes with similar signatures to $HH \to b\bar{b}\gamma\gamma$ at the LHC include the $\gamma\gamma$+jets, which is a large, smoothly falling continuum background and single Higgs processes, such as ggF, $t\bar{t}H$, and ZH. Like HH production, these single Higgs processes peak right at the Higgs mass in $m_{\gamma\gamma}$. The analysis uses a multivariate approach to separate the HH signal from the background processes, with categories specifically designed to target both SM and BSM values of the Higgs self-coupling, κ_λ. Although no evidence for HH production was found, this analysis has set some of the strongest worldwide limits on SM HH production and constraints on κ_λ from any individual HH channel to date.

5.2 Data and simulated events

This analysis uses pp collision data collected by the ATLAS experiment from 2015 to 2018 with proton beams colliding at a center-of-mass energy of $\sqrt{s} = 13$ TeV. After data quality requirements [104], the full data set represents an integrated luminosity of 139.0 ± 2.4 fb^{-1} [105, 106]. The mean number of inelastic pp interactions per bunch crossing is 34.2 [107].

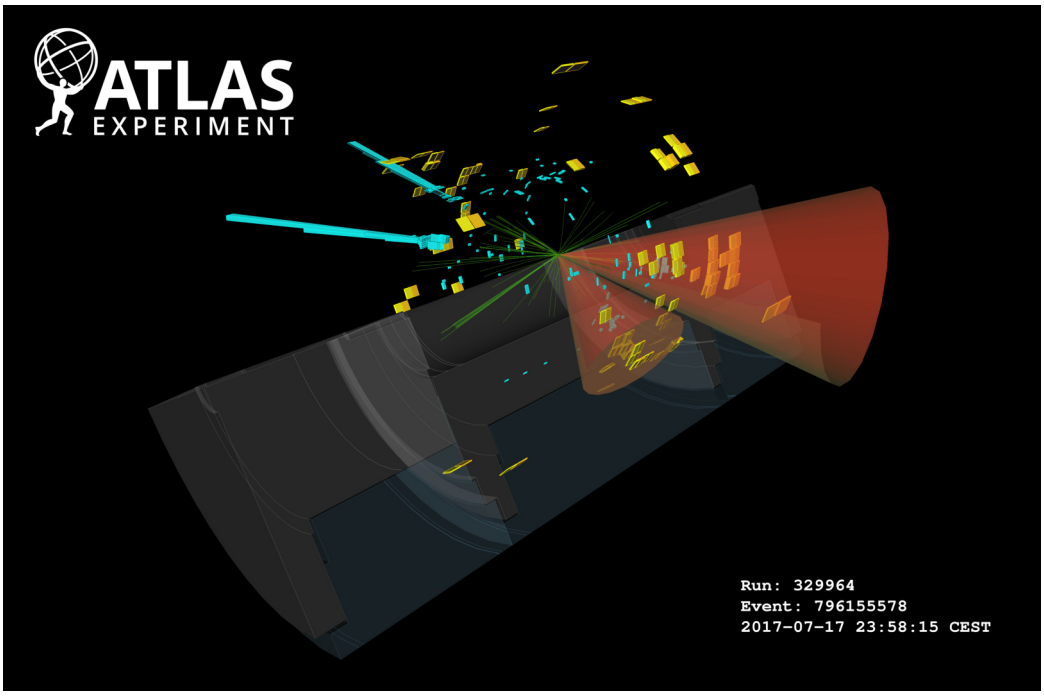

Figure 5.1: An event display showing a candidate $HH \to b\bar{b}\gamma\gamma$ event in the ATLAS detector. The two identified photons are shown in cyan, and the two b-jets are displayed as red cones.

Monte Carlo (MC) simulations are used to model the HH signal and the single Higgs, and diphoton background processes. The reducible backgrounds from final states with jets wrongly identified as photons (γ–jet and dijet backgrounds) are estimated using a data-driven technique described in Section 5.2.4. Section 5.5 provides a visual comparison of the data with simulation.

Different pileup conditions from additional interactions and neighboring bunch crossings were simulated by overlaying the hard-scattering event with inelastic pp events generated by Pythia 8.186 using the NNPDF2.3lo PDF set and the A3 tune [108]. Differences between the simulated and observed distributions of the number of interactions per bunch crossing are corrected by applying pileup scale factors to simulated events. A full simulation of the ATLAS detector [109] based on Geant4 [110] was used to reproduce the detector response to single Higgs boson processes. The continuum background and signal samples were processed by AtlFastII [111], a fast simulation of the ATLAS detector response.

5.2.1 ggF and VBF HH signal simulation

Events from ggF HH production were generated at next-to-leading-order accuracy in QCD with finite top-quark mass in both the real and virtual corrections (NLO FT) [40], using the Powheg Box v2 [112]

generator in the finite top-quark mass approximation [113, 114] with the PDF4LHC15 parton distribution function (PDF) set [115]. The PYTHIA 8.244 generator was used for parton showering, hadronization, and underlying-event simulation. HERWIG 7.1.6 was used as an alternative generator to calculate the theory uncertainty from parton shower variations. Samples were generated for $\kappa_\lambda = 1$ and 10.

For VBF HH production, MADGRAPH5_AMC@NLO 2.6.0 [116] was used to generate events at LO [116, 117]. The NNPDF3.0NLO PDF set [118] was used in the matrix element, interfaced to PYTHIA 8.244.

5.2.2 Single Higgs background simulation

Production of single Higgs bosons via ggF, VBF, WH, ZH ($qq \to ZH$ and $gg \to ZH$), $t\bar{t}H$, tH (tHq and tHW), and bbH was modeled using the same set of MC samples as described in Ref. [119]. For single Higgs boson production, as well as HH production, a Higgs boson mass of 125.09 GeV was assumed [35]. The analysis assumes a branching ratio of 0.227% for the Higgs boson decay into two photons and a branching ratio of 58.2% for the Higgs boson decay into two b-quarks [120, 121]. The inclusive cross-sections of these processes are normalized to the most precise available theoretical values [120]. Though the single Higgs branching fractions and cross-sections are affected by κ_λ through electroweak corrections, they are not parameterized by κ_λ throughout this chapter. A study was done parameterizing the single Higgs backgrounds by κ_λ according to the following prescription [122], but it was found to vary the likelihood scan measurements by less than 4%.

5.2.3 Diphoton background simulation

The $\gamma\gamma$+jets process was simulated with the SHERPA 2.2.4 [123] generator as listed in Table 5.1. QCD NLO-accurate matrix elements for up to one parton, and LO-accurate matrix elements for up to three partons, were calculated with the Comix [124] and OPENLOOPS [125, 126, 127] libraries. These were calculated in the five-flavour scheme including b-quarks in the massless approximation and merged with the SHERPA parton shower [128] using the MEPS@NLO prescription [129, 130] with a dynamic merging cut [131] of 10 GeV. Within the parton shower, b-quarks were then treated as being massive. Finally, events from $t\bar{t}\gamma\gamma$ processes were produced with MADGRAPH5_AMC@NLO in the four-flavour scheme [116].

5.2.4 Data-driven estimate of background processes

Although the $\gamma\gamma$+jets process is simulated in Monte Carlo, γ–jet, and dijet events, where either one or two jets are misidentified as photons, can also contribute to the total background. The fractional contribution of each component can be estimated using a data-driven approach described in Ref. [132]. This approach is based on the photon identification and isolation distributions from

genuine and misidentified photons. After the analysis selection, described in Section 5.4, $(85 \pm 3)\%$ of sideband events are genuine diphoton events, with the remaining $(15 \pm 4)\%$ consisting of γ–jet events and a negligible number of dijet events.

Table 5.1: Summary of nominal Higgs boson pair signal samples and single Higgs boson background samples, split by production mode, and continuum background samples. The generator used in the simulation, the PDF set, and set of tuned parameters (tune) are also provided.

Process	Generator	PDF set	Showering	Tune
ggF HH	Powheg Box v2 +FT [112] [113, 114]	PDFLHC [115]	Pythia 8.2 [133]	A14 [134]
VBF HH	MadGraph5_aMC@NLO [116]	NNPDF3.0nlo [135]	Pythia 8.2	A14
ggF H	NNLOPS [136, 137, 138] [139, 140]	PDFLHC	Pythia 8.2	AZNLO [141]
VBF H	Powheg Box v2 [142, 143, 144, 145, 112, 146, 137, 147, 148]	PDFLHC	Pythia 8.2	AZNLO
WH	Powheg Box v2	PDFLHC	Pythia 8.2	AZNLO
$qq \to ZH$	Powheg Box v2	PDFLHC	Pythia 8.2	AZNLO
$gg \to ZH$	Powheg Box v2	PDFLHC	Pythia 8.2	AZNLO
$t\bar{t}H$	Powheg Box v2 [149, 143, 144, 145, 148]	NNPDF3.0nlo	Pythia 8.2	A14
bbH	Powheg Box v2	NNPDF3.0nlo	Pythia 8.2	A14
tHq	MadGraph5_aMC@NLO	NNPDF3.0nlo	Pythia 8.2	A14
tHW	MadGraph5_aMC@NLO	NNPDF3.0nlo	Pythia 8.2	A14
$\gamma\gamma$+jets	Sherpa 2.2.4 [123]	NNPDF3.0nnlo	Sherpa 2.2.4	–
$t\bar{t}\gamma\gamma$	MadGraph5_aMC@NLO	NNPDF2.3lo	Pythia 8.2	–

5.3 κ_λ reweighting scheme

As Monte Carlo simulations that include the ATLAS detector response and full event reconstruction are computationally expensive to generate, reweighting schemes are used to morph existing HH simulations to the expected kinematic distributions for a range of κ_λ values. This is important because the shape of the HH kinematic distributions change significantly as a function of κ_λ. Reweighting allows us to accurately estimate our sensitivity to κ_λ for a reasonable computational cost.

5.3.1 ggF

For ggF HH production, a reweighting method based on the HH invariant mass m_{HH} is used to provide predictions on the cross-section at different κ_λ values without having to regenerate a lot of computationally expensive Monte Carlo. The reweighting method derives the scale factors as a function of κ_λ in bins of m_{HH} by performing a linear combination of samples generated at different κ_λ values [150]. It is based on the fact that the differential cross-section can be expressed in terms of m_{HH}:

$$\frac{d\sigma(\kappa_\lambda)}{dm_{HH}} = |A(\kappa_\lambda)|^2 = |\kappa_\lambda M_\triangle(m_{HH}) + M_\square(m_{HH})|^2 \tag{5.1}$$

Which can be re-written as:

$$\frac{d\sigma(\kappa_\lambda)}{dm_{HH}} = \kappa_\lambda^2 a_1(m_{HH}) + \kappa_\lambda a_2(m_{HH}) + a_3(m_{HH}) \tag{5.2}$$

Where a_1, a_2, and a_3 only depend on m_{HH} and a_i are solved for using $\kappa_\lambda = 0$, 1, and 20 samples as a basis. Histograms of the truth m_{HH} distributions in 10 GeV bins for the $\kappa_\lambda = 0$, 1, and 20 samples are generated. Then in each m_{HH} bin, Equation 5.3, is used to derive the ratio between the SM ($\kappa_\lambda = 1$) and the desired κ_λ value. The ratio is applied as an event-by-event weight that relies on per-event m_{HH} and the desired κ_λ value.

$$\frac{d\sigma(\kappa_\lambda)}{dm_{HH}} = \frac{19\kappa_\lambda^2 - 399\kappa_\lambda + 380}{380}|A(\kappa_\lambda = 0)|^2 + \frac{-20\kappa_\lambda^2 + 400\kappa_\lambda}{380}|A(\kappa_\lambda = 1)|^2 + \frac{\kappa_\lambda^2 - \kappa_\lambda}{380}|A(\kappa_\lambda = 20)|^2 \tag{5.3}$$

For each κ_λ value, the inclusive cross-section is normalized to NLO FTApprox cross-section from Ref. [151]. This method was validated by comparing the event yields and the distributions of the relevant Higgs boson kinematic variables, including $m_{\gamma\gamma}$, of a sample generated with $\kappa_\lambda = 10$ to a sample generated with $\kappa_\lambda = 1$ and reweighted to $\kappa_\lambda = 10$. Good agreement is obtained in all categories. Based on the maximum differences of signal yields observed in this validation process, a systematic uncertainty in the range of 3%–4% is associated with the reweighting procedure.

5.3.2 VBF

As discussed in 1.9, the full cross-section for the VBF to HH process involves three diagrams:

$$\sigma(\kappa_{2V}, \kappa_\lambda, \kappa_V) = |A|^2 = |\kappa_V \kappa_\lambda M_s + \kappa_V^2 M_t + \kappa_{2V} M_x|^2 \tag{5.4}$$

Expanding the absolute square of the amplitude A yields six terms:

$$\sigma = \kappa_V^2 \kappa_\lambda^2 a_1 + \kappa_V^4 a_2 + \kappa_{2V}^2 a_3 + \kappa_V^3 \kappa_\lambda a_4 + \kappa_V \kappa_\lambda \kappa_{2V} a_5 + \kappa_V^2 \kappa_{2V} a_6 \tag{5.5}$$

In the case where κ_V and κ_{2V} are held fixed at their SM values, the above equation reduces down to:

$$\sigma = \kappa_\lambda^2 a_1 + \kappa_\lambda a_2 + a_3 \tag{5.6}$$

This means that three different Monte Carlo samples can be combined to model the signal at any point in κ_{2V}, κ_λ, κ_V space. Unlike ggF, HH production that can be parameterized with m_{HH} with truth-level Monte Carlo, no single variable has been found for VBF HH production that successfully parameterizes the reweighting procedure. VBF HH production is a more complex process, so instead, events are fully simulated with ATLAS reconstruction and then combined. The default basis uses $\kappa_\lambda = (1,2,10)$ to generate any κ_λ point, where the combination equation takes the

form:

$$\begin{aligned}\sigma(\kappa_{2V},\kappa_\lambda,\kappa_V) = \\ &\left(\frac{\kappa_\lambda^2}{9}-\frac{4\kappa_\lambda}{3}+\frac{20}{9}\right)\times\sigma(1,1,1)\\ &+\left(-\frac{\kappa_\lambda^2}{8}+\frac{11\kappa_\lambda}{8}-\frac{5}{4}\right)\times\sigma(1,2,1)\\ &+\left(\frac{\kappa_\lambda^2}{72}-\frac{\kappa_\lambda}{24}+\frac{1}{36}\right)\times\sigma(1,10,1)\end{aligned} \tag{5.7}$$

Three more bases of κ_λ samples are used to derive the uncertainties on the VBF linear combination: κ_λ = (0,1,10), (0,1,2), (0,2,10). Since samples were generated at LO for four values of the coupling modifier, $\kappa_\lambda = 0, 1, 2$ and 10, the N3LO-to-LO cross-section ratio at the SM value is calculated and this factor is applied to the VBF HH cross-section.

5.4 Event selection

Events must pass several stages of selection before being considered in the signal region of this analysis: trigger, preselection, and boosted decision tree (BDT) selection. Each stage is designed to select the $HH \to b\bar{b}\gamma\gamma$ signal and reject background processes with increasing levels of precision. The trigger level selection is a coarse selection and is required to select the LHC data for storage. The trigger selection is primarily limited by the bandwidth capabilities of the LHC. The preselection stage imposes a set of requirements to select events with two photons and two b-jets in the final state, as we expect to see from the HH signal. Finally, the BDT selection stage uses multivariate methods trained to discriminate the HH signal from the main background processes to further separate signal from background.

Trigger

Events are selected using a diphoton trigger, which was originally designed for $H \to \gamma\gamma$ searches [152]. This trigger requires two reconstructed photon candidates with minimum transverse energies of 35 GeV for the highest transverse energy photon and 25 GeV for the second highest transverse energy photon. The trigger efficiency as a function of sub-leading photon E_T is shown in Figure 5.2. The triggers used in 2015 and 2016 required both photons to satisfy the "Loose" photon identification criteria. In 2017–2018, the Medium criteria was adopted to cope with the increased pp interaction rate [69]. The average trigger efficiency for $HH \to b\bar{b}\gamma\gamma$ signal events is 80% as shown in Figure 5.4.

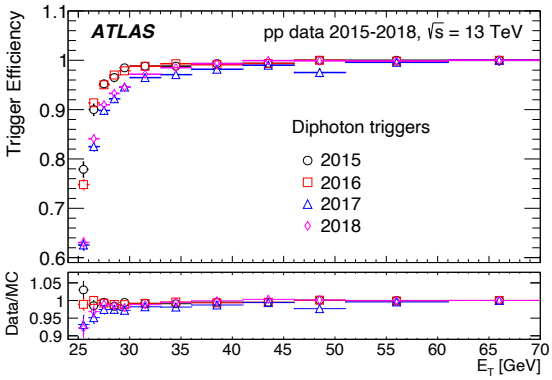

Figure 5.2: Diphoton trigger efficiency as a function of offline reconstructed photon E_T coming from radiative Z decays [153]

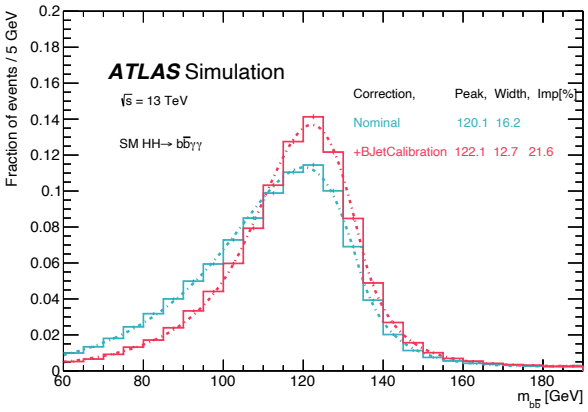

Figure 5.3: Improvement to the m_{bb} resolution due to the Muon-in-Jet+PtReco correction on the SM HH signal

Preselection

After passing the trigger selections, the following additional requirements are made to select for HH signal events:

- At least two photons satisfy the "Tight" identification and "Loose" isolation criteria described in Section 3.3. This requirement is made to select for $H \to \gamma\gamma$ decays where two photons are in the final state. The photon quality requirements improve the chances of the photons being real photons, not jets or electrons faking photons.
- The diphoton invariant mass, built with the two leading photons, satisfies $105 < m_{\gamma\gamma} < 160$ GeV. This window includes the Higgs mass of 125 GeV, while also allowing for sideband data for the background estimation.

- The leading photon p_{T} is larger than 35% of the mass of the diphoton system, $p_{T\gamma,1}/m_{\gamma\gamma} > 0.35$ and the sub-leading photon p_{T} is larger than 25% of the mass of the diphoton system, $p_{T\gamma,2}/m_{\gamma\gamma} > 0.25$. In a $H \to \gamma\gamma$ decay, most of the energy will pass to the two photons. This requirement helps reject background events where the photons might not both be coming from the decay of a heavy particle like the Higgs.

- Exactly two R=0.4 b-tagged jets passing the 77% b-tagging working point are present. This requirement selects for $H \to b\bar{b}$decays. By requiring no more than two b-jets, it also allows for the $b\bar{b}\gamma\gamma$ analysis to be orthogonal to the $HH \to b\bar{b}b\bar{b}$ channel. The misidentification rate at the 77% b-tagging working point is 1/130 for light-flavor jets and 1/4.9 for charm jets [81].

- No isolated electrons or muons are present. This requirement helps reject backgrounds such as ($t\bar{t}H$, ZH or WH) where leptons could occur in the final state. It also ensures that the $b\bar{b}\gamma\gamma$ search is orthogonal to other HH searches that include leptons in the final state, such as $b\bar{b}\tau^+\tau^-$ or $b\bar{b}WW^*$.

- Fewer than six central ($|\eta| < 2.5$) jets are present. This helps reject $t\bar{t}H$ events where the top quarks decay hadronically.

After preselection, the b-jet energy is corrected using the Muon-in-jet+PtReco correction described in Section 4.2. As seen in Figure 5.3 the correction improves the m_{bb} resolution by 21.6%.

The efficiency of the preselection for the SM ggF+VBF HH simulated samples is 12.6%. Figure 5.4 shows the effect of the major preselection cuts on both signal and background. Although much of the signal is discarded, a much larger fraction of the background is removed.

BDT selection

After preselection, a BDT is used to further reject background and target SM HH production as well as BSM HH production - where κ_λ deviates significantly from 1. Events are divided into two regions based on $m^*_{b\bar{b}\gamma\gamma}$, the modified invariant mass of the diphoton and di-b-jet system shown in Figure 5.5. $m^*_{b\bar{b}\gamma\gamma}$, is defined as:

$$m^*_{b\bar{b}\gamma\gamma} = m_{b\bar{b}\gamma\gamma} - m_{b\bar{b}} + \ 125\text{GeV} - m_{\gamma\gamma} + 125\ \text{GeV}$$

Where 125 GeV is the Higgs mass and $m_{b\bar{b}}$ is the invariant mass of the two b-jets. Relative to $m_{b\bar{b}\gamma\gamma}$, $m^*_{b\bar{b}\gamma\gamma}$ improves the four-object mass resolution due to detector resolution effects canceling out.

A high mass region, with $m^*_{b\bar{b}\gamma\gamma} > 350$ GeV, targets the SM HH signal ($\kappa_\lambda = 1$), while a low mass region, with $m^*_{b\bar{b}\gamma\gamma} < 350$ GeV, is used to remain sensitive to BSM HH signals. The ggF and VBF distributions for $m^*_{b\bar{b}\gamma\gamma}$ for various values of κ_λ can be seen in Figure 5.6. From the Figure, we can see that SM-like HH signals with κ_λ =1 have a distribution that peaks higher in $m^*_{b\bar{b}\gamma\gamma}$ relative to BSM-like signals.

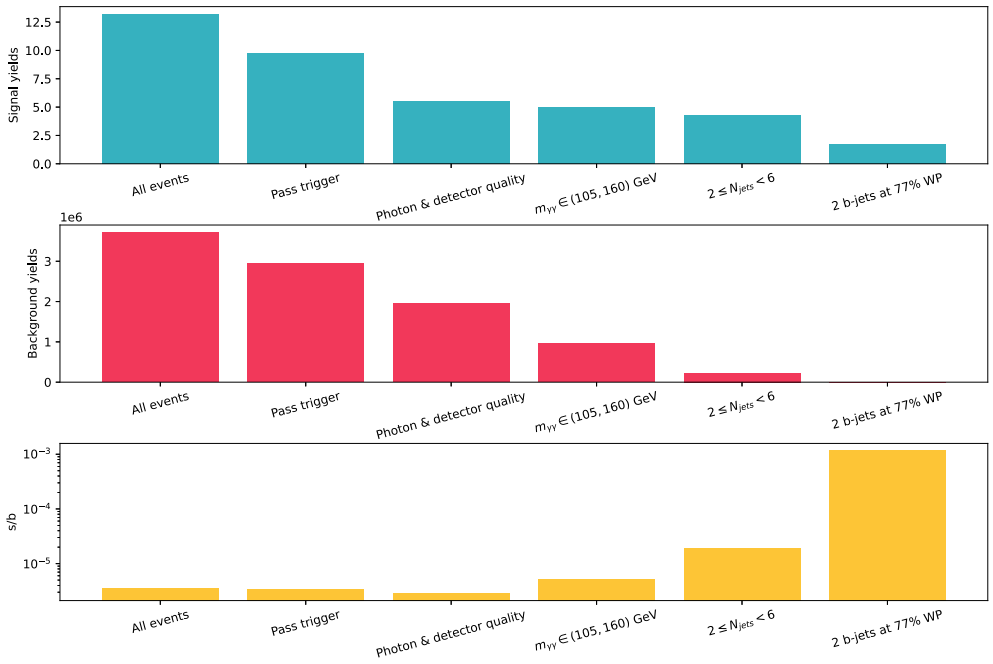

Figure 5.4: Effect of the different preselection stages on the expected number of signal (ggF and VBF HH) and background (single Higgs and $\gamma\gamma$) events and their ratio passing selection.

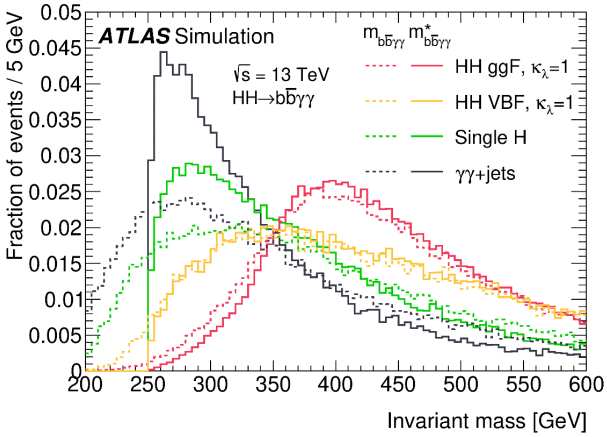

Figure 5.5: Reconstructed four-body mass for ggF and VBF HH signal samples, single Higgs backgrounds and the $\gamma\gamma$+jets background.

In each mass region, a dedicated BDT is trained using XGBoost [154] to discriminate between the HH signal and a weighted combination of $\gamma\gamma$, $t\bar{t}H$, ggH, and ZH simulated backgrounds. In the high mass region, the SM HH sample is used as signal, while in the low mass region, the $\kappa_\lambda = 10$

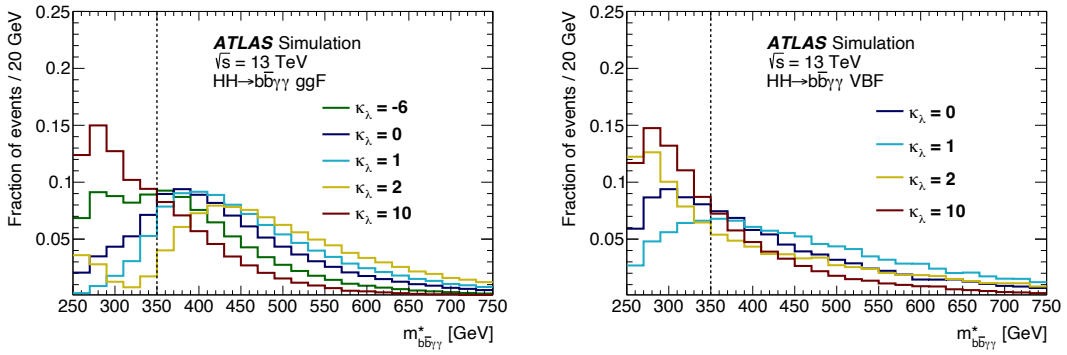

(a) ggF HH production mode (b) VBF HH production mode

Figure 5.6: The $m^*_{b\bar{b}\gamma\gamma}$ distributions after the preselection for (a) ggF HH and (b) VBF HH signals for several κ_λ values. $m^*_{b\bar{b}\gamma\gamma} = 350$ GeV is chosen as the boundary between categories targeting the SM and BSM κ_λ signals.

sample is used for training. Figure 5.7 provides an overview of the overall BDT categorization strategy.

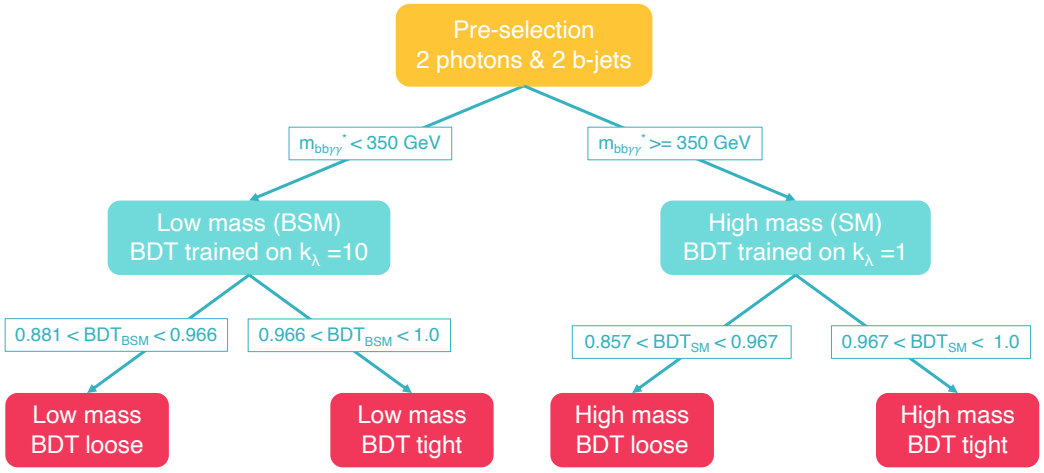

Figure 5.7: A flowchart describing the $b\bar{b}\gamma\gamma$ categorization strategy

The BDT combines several input variables that exploit the different kinematic properties of the signal and background events, as well as the b-tagging information, summarized in Table 5.2. Identical variable sets are used for high mass and low mass categories. The kinematic properties of the reconstructed photons, such as the leading and subleading photon's angular information, and the transverse momentum of the diphoton system divided by its invariant mass, are combined with jet-based information. Particular care was taken to ensure that the BDT event selection does not lead to biases in the $m_{\gamma\gamma}$ background distribution. Variables which are strongly correlated with the

diphoton invariant mass are avoided in the training in order to prevent the BDT event selection from biasing the $m_{\gamma\gamma}$ background distribution. The transverse momenta of the photons are divided by $m_{\gamma\gamma}$ before being used as BDT input variables. A check for potential biases in the $m_{\gamma\gamma}$ background distribution is described in Section 5.6.2. The "single topness" variable (χ_{Wt}) is also used as a BDT input and is designed to provide discrimination power against $t\bar{t}H$. It is defined as:

$$\chi_{Wt} = \min \sqrt{\left(\frac{m_{j_1 j_2} - m_W}{m_W}\right)^2 + \left(\frac{m_{j_1 j_2 j_3} - m_t}{m_t}\right)^2}, \tag{5.8}$$

where the minimum is taken over all combinations of three jets in the event, $m_W = 80$ GeV, and $m_t = 173$ GeV.

Table 5.2: Variables used as inputs to the BDT. All vectors in the event are rotated so that the leading photon ϕ is equal to zero, while their relative azimuthal angular differences are kept unchanged.

Variable	Definition
Photon-related kinematic variables	
$p_{\mathrm{T}}/m_{\gamma\gamma}$	Transverse momentum of each of the two photons divided by the diphoton invariant mass $m_{\gamma\gamma}$
η and ϕ	Pseudorapidity and azimuthal angle of the leading and subleading photon
Jet-related kinematic variables	
b-tag status	Tightest fixed b-tag working point (60%, 70%, or 77%) that the jet passes
p_{T}, η and ϕ	Transverse momentum, pseudorapidity and azimuthal angle of the two jets with the highest b-tagging score
$p_{\mathrm{T}}^{b\bar{b}}$, $\eta_{b\bar{b}}$ and $\phi_{b\bar{b}}$	Transverse momentum, pseudorapidity and azimuthal angle of the b-tagged jets system
$m_{b\bar{b}}$	Invariant mass of the two jets with the highest b-tagging score
H_{T}	Scalar sum of the p_{T} of the jets in the event
Single topness	For the definition, see Eq. (5.8)
Missing transverse momentum variables	
$E_{\mathrm{T}}^{\mathrm{miss}}$ and ϕ^{miss}	Missing transverse momentum and its azimuthal angle

Among the input variables in Table 5.2, $m_{b\bar{b}}$ and H_{T}, the scalar sum of the p_{T} of the jets in the event, show the highest discriminating power against the $\gamma\gamma$+jets continuum background. Distributions for these two input variables are shown in Figure 5.8.

The BDT score distributions in the low mass and high mass regions are shown in Figure 5.9 for all events passing the preselection. In each mass region, two categories based on the BDT score are

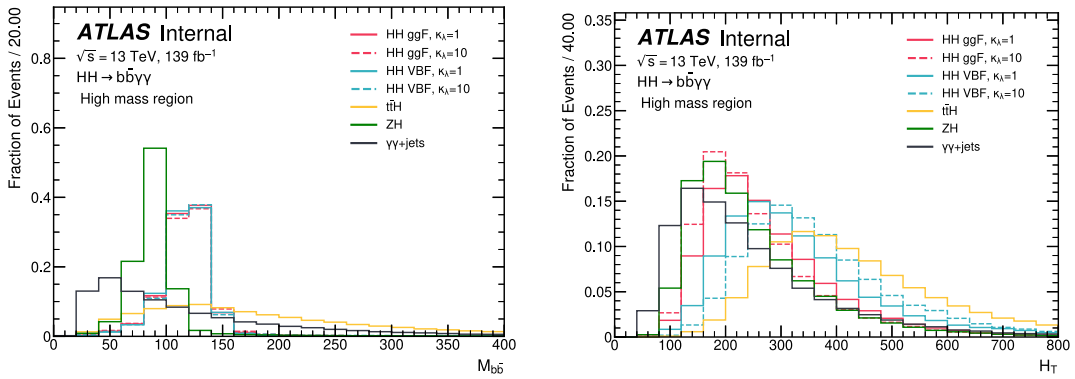

(a) (b)

Figure 5.8: High mass category distributions for (a) m_{bb} (b) H_{T}. The two BDT input variables with the most discrimination power.

defined. The boundaries of the categories are chosen by maximizing the combined number-counting significance [155]. The number-counting significance per category is an approximation of the final expected significance and is defined as:

$$Z_c \approx= \sqrt{2((s_c + b_c)\ln(1 + s_c/b_c) - s_c)}$$

Where s are the number of signal events and b are the expected number of background events in the signal region $120 < m_{\gamma\gamma} < 130$ GeV of each category. The combined significance adds the number counting significances across categories in quadrature. In the case of the four categories this is:

$$Z = \sqrt{Z_1^2 + Z_2^2 + Z_3^2 + Z_4^2}$$

The resulting four categories are required to have at least nine continuum background events in the data sideband region, defined as the range $105 < m_{\gamma\gamma} < 160$ GeV, excluding $120 < m_{\gamma\gamma} < 130$ GeV. This guarantees that the final selection on the data sideband retains enough events to perform a fit to the distribution of the diphoton invariant mass, $m_{\gamma\gamma}$.

The purity and expected significance of the four resulting BDT categories in the $120 < m_{\gamma\gamma} < 130$ GeV signal region are shown in Figure 5.10. The high mass BDT tight category has the highest fraction of SM HH relative to the irreducible single Higgs backgrounds, and the highest overall expected significance for SM HH signal. In the high mass categories, ZH $t\bar{t}H$ and ggF single Higgs production modes all contribute roughly equally to the backgrounds. In the low mass categories, $t\bar{t}H$ has a higher fraction of the signal yields than the other single Higgs backgrounds.

The low mass categories do not individually have a high sensitivity to SM HH, but, as shown in Figure 5.11 they provide additional acceptance for BSM values of κ_λ. This is due to the m_{HH}

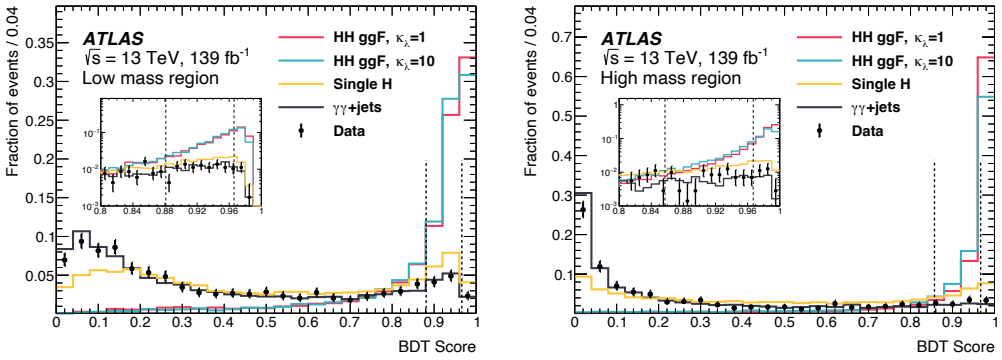

(a) Low mass region (b) High mass region

Figure 5.9: The BDT distribution of the HH ggF signal for two different values of k_λ and the main backgrounds in the (a) low mass region and (b) high mass region. Distributions are normalized to unit area. The dashed lines denote the category boundaries. Events with a BDT score below 0.881 in the low mass region or below 0.857 in the high mass region are discarded.

distribution being peaked at low m_{HH} values for κ_λ values far from the SM. In Figure 5.11, we can also see that the high mass BDT categories have the highest acceptance around κ_λ =1 and shoulders that drop off quickly far from the Standard Model. This comes from a combination of the BDT being trained to target κ_λ =1, but also due to the maximum interference of the triangle and box diagrams leading to a hard m_{HH} spectrum. The asymmetry in the shoulders comes from the m_{HH} spectrum being harder for negative BSM values of κ_λ than positive ones.

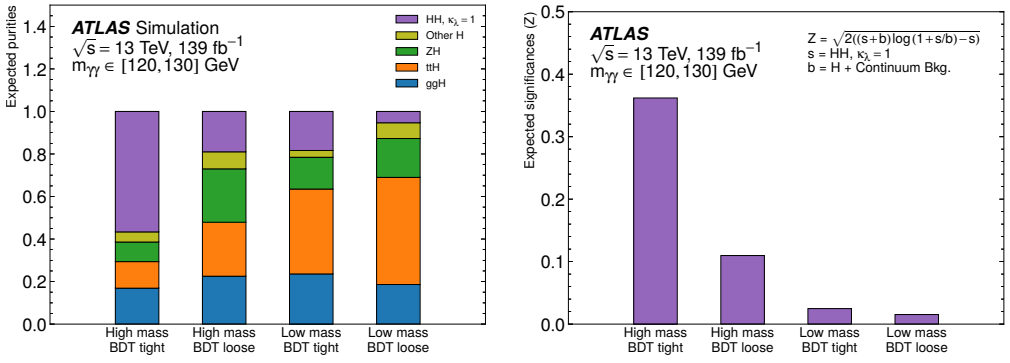

(a) (b)

Figure 5.10: (a) The relative amount (purity) of expected events from SM HH and single Higgs boson production processes for each of the four BDT categories (b) The expected number counting significance in each of the four categories.

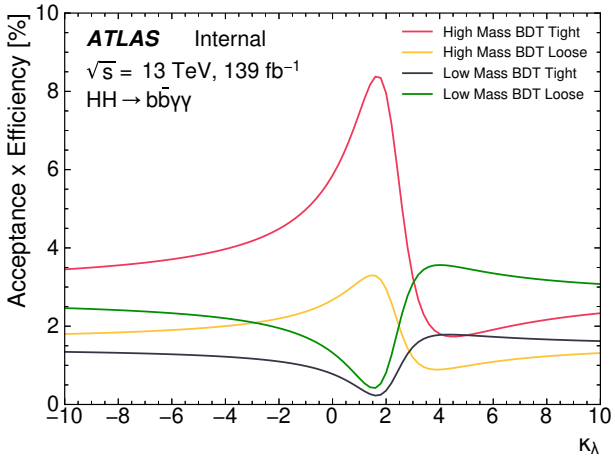

Figure 5.11: Acceptance x Efficiency on the HH signal for the 4 different $b\bar{b}\gamma\gamma$ categories. The two SM BDT categories peak close to the SM value of 1, where the m_{HH} distribution peaks at higher invariant masses. The two BSM categories are inversely shaped and have a minimum close to the SM.

5.5 Comparison of data with predictions

Figure 5.12 shows the level of agreement between data and the background prediction for the $m_{\gamma\gamma}$ distribution after the preselection. The smoothly falling continuum background consists primarily of $\gamma\gamma$, γ–jet, and dijet events. The continuum background is scaled by the $\gamma\gamma$, γ–jet, and dijet fractions and normalized to the data sideband. The $\gamma\gamma$+jets continuum background is further divided according to the flavours of the two jets ($b\bar{b}$ or other jets). This decomposition is taken from the proportions predicted by the SHERPA event generator, as described in Section 5.2, and it is shown for illustration. On top of the continuum background, the single Higgs backgrounds produce a noticeable peak at the Higgs mass of 125 GeV. The HH signal also peaks at the Higgs mass, but is barely visible on top of the backgrounds.

Figure 5.13 shows the $m_{\gamma\gamma}$ distributions for each BDT category. Across all categories, a consistent agreement with data is observed. After BDT selection, the overall statistics are drastically reduced relative to Figure 5.12, with many $m_{\gamma\gamma}$ bins having no data events at all. Due to the low statistics in the signal regions, the Monte Carlo histograms shown in these figures are not directly used to perform a fit to the data. Instead, an unbinned likelihood fit is performed using parameterized functional forms describing the signal and background processes. This approach does not rely on a strict agreement between data and Monte Carlo.

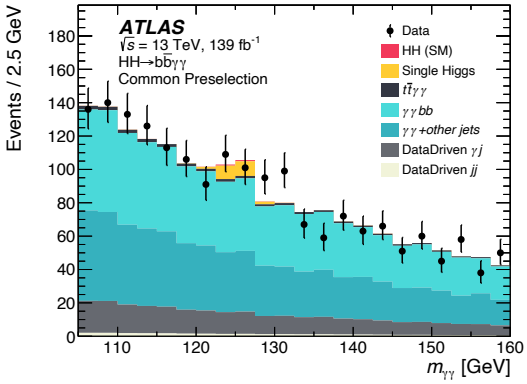

Figure 5.12: Distributions of $m_{\gamma\gamma}$ for events passing the preselection criteria. The data-derived fractions of nonresonant $\gamma\gamma$, γ–jet or jet–γ, and dijet background are applied and the total background is normalized to the data sideband.

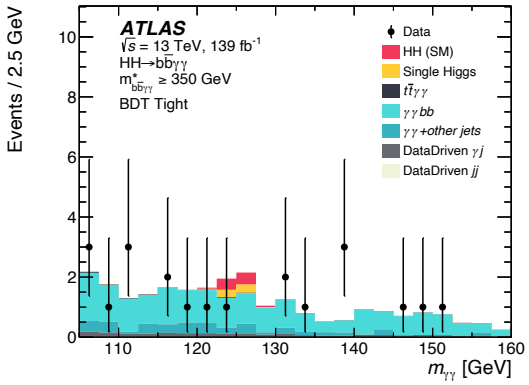

(a) High mass BDT tight selection

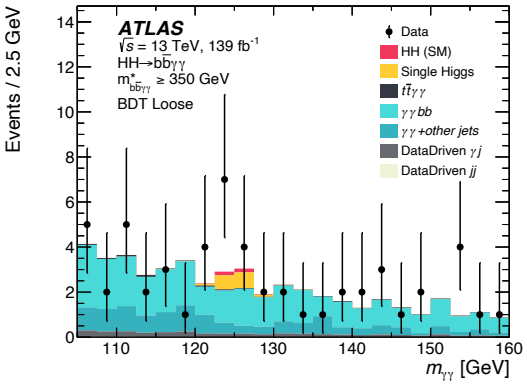

(b) High mass BDT loose selection

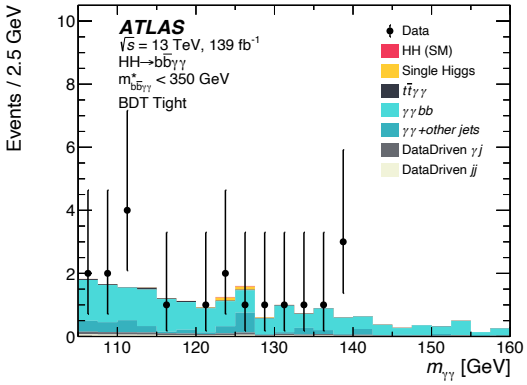

(c) Low mass BDT tight selection

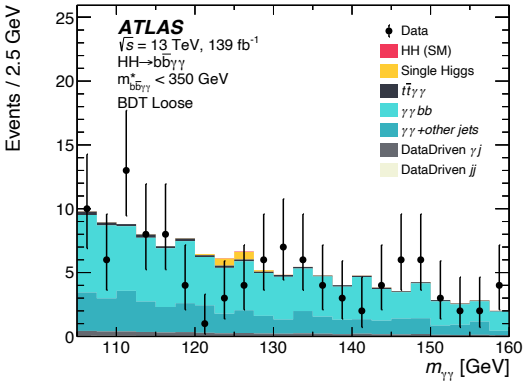

(d) Low mass BDT loose selection

Figure 5.13: Distributions of $m_{\gamma\gamma}$ in all signal categories

5.6 Signal and background parameterization

As this analysis uses an unbinned maximum likelihood fit to the diphoton invariant mass spectrum for its statistical analysis, functional forms must be derived to describe the shape of the expected $m_{\gamma\gamma}$ distributions. The shape of these functions is derived on Monte Carlo simulation. For the HH signal and single Higgs backgrounds, the parameters of the shape are derived in simulation. The overall strength of the HH signal is derived during the likelihood fit to data, and the normalization of the single Higgs backgrounds are fixed to the SM. The diphoton backgrounds are more challenging to model accurately in simulation. Therefore although the functional form is derived in simulation, all of the shape parameters are allowed to float freely during the likelihood fit.

5.6.1 $H \to \gamma\gamma$ parameterization

For the HH signal and single Higgs boson background distributions, the parameterized forms are determined through fits to simulated samples and the expected normalizations are obtained from their theoretical cross-sections multiplied by the product of the acceptance times efficiency from the simulation. The $m_{\gamma\gamma}$ distributions for both the HH signal and single Higgs backgrounds are expected to produce a resonant peak at the Higgs mass. The diphoton invariant mass distribution shapes are modeled with a double-sided crystal ball (DCSB) function [72, 156], which is characterized by a Gaussian core and asymmetric power-law tails. This function is used throughout $H \to \gamma\gamma$ analyses as it allows the modeling of event distributions in which non-Gaussian tails can arise from experimental effects, such as photon energy mismeasurements.

The double-sided crystal ball function is defined as:

$$f_{\mathrm{DCSB}}(m_{\gamma\gamma}) = N_c \times \begin{cases} e^{-t^2/2} & \alpha_{\mathrm{low}} < t < \alpha_{\mathrm{high}} \\ e^{-\alpha_{\mathrm{low}}^2/2} \cdot (1 - n_{\mathrm{low}} - t \cdot \alpha_{\mathrm{low}} \cdot n_{\mathrm{low}})^{-n_{\mathrm{low}}} & t < -\alpha_{\mathrm{low}} \\ e^{-\alpha_{\mathrm{high}}^2/2} \cdot (1 - n_{\mathrm{high}} + t \cdot \alpha_{\mathrm{high}} \cdot n_{\mathrm{high}})^{-n_{\mathrm{high}}} & t > -\alpha_{\mathrm{high}} \end{cases} \tag{5.9}$$

Where $t = (m_{\gamma\gamma} - \mu_{\mathrm{DSCB}})/\sigma_{\mathrm{DSCB}}$, and μ_{CB}, $\sigma_{\mathrm{CB},c}$ are the peak position and the width of the Gaussian core of the function, N_c normalizes the distribution, and α_{low}, α_{high}, n_{low} and n_{high} describe the tails.

The shape parameters are determined by fitting the diphoton mass distribution in simulation for each category. The width of the fit function is largely insensitive to the specific signal processes considered in the analysis, with maximum variations of approximately 10%. The parameterized form of $m_{\gamma\gamma}$ is obtained from the simulation of the ggF and VBF HH processes with $\kappa_\lambda = 1$, described in Section 5.2. No significant dependence of the functional form on κ_λ was found. Table 5.3 shows the mean and width of the double-sided Crystal Ball fit to the $m_{\gamma\gamma}$ distribution for simulated Higgs boson pair events. The fits for each category are shown in Figure 5.14. The chosen functional forms

are found to model both the single Higgs and HH events well.

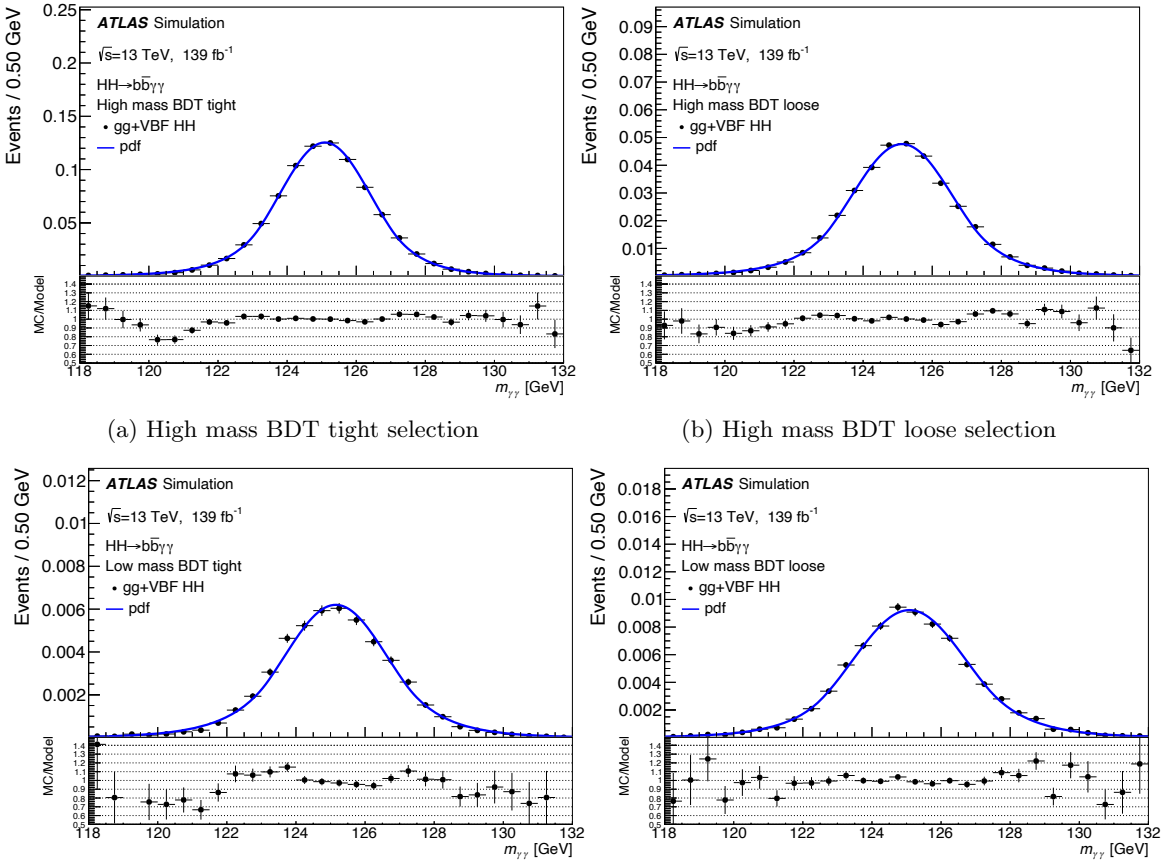

(a) High mass BDT tight selection

(b) High mass BDT loose selection

(c) Low mass BDT tight selection

(d) Low mass BDT loose selection

Figure 5.14: Diphoton invariant mass distributions of the ggF and VBF HH processes with κ_λ=1 for the (a) high mass BDT tight, (b) high mass BDT loose, (c) low mass BDT tight, and (d) low mass BDT loose categories. The fit to the distributions by a double-sided Crystal Ball function is superimposed.

Table 5.3: The mean and width of the double-sided Crystal Ball function and the corresponding statistical uncertainty as obtained from the fit to the $m_{\gamma\gamma}$ distribution for simulated ggF and VBF HH events.

Category	μ_{DSCB} [GeV]	σ_{DSCB} [GeV]
High mass BDT tight	125.09 ± 0.01	1.33 ± 0.01
High mass BDT loose	125.13 ± 0.01	1.47 ± 0.02
Low mass BDT tight	125.15 ± 0.05	1.50 ± 0.06
Low mass BDT loose	125.08 ± 0.03	1.64 ± 0.03

5.6.2 Background parameterization

The smoothly falling continuum diphoton background is modeled using an exponential function. Because this is a challenging background to model accurately, the shape of the function is derived from simulation, but the parameters of the function are left to vary in the final fit to data.

The decision to use an exponential function was made after evaluating several alternatives, such as the Bernstein polynomial, Novosibirsk function, and an exponential+polynomial function. Each function was evaluated on the $\gamma\gamma$+jets Monte Carlo template, normalized to the data sidebands where $m_{\gamma\gamma}$ is between 105–120 and 130–160 GeV. The functions were evaluated to reduce the potential bias they might introduce to the background estimate. For example, a function with many degrees of freedom could absorb a potential signal, on the other hand, a function with too few degrees of freedom could poorly model the background and create an artificial signal. This potential bias is known as the "spurious signal" as it represents signal that is not actually present [72, 157]. The spurious signal is illustrated in Figure 5.15.

The spurious signal is calculated from the signal event yield extracted from a signal-plus-background fit to the background-only diphoton invariant mass distribution. The number of fitted signal events is computed for Higgs boson masses in intervals of 1 GeV from 121 GeV to 129 GeV. The bias is taken as the largest number of fitted spurious signal events in this 8 GeV mass window, N_{sp}.

Of the different analytic functions that were tested, the one with the smallest number of parameters was chosen from the functions that passed either of the following criteria:

- $|\text{Max}(N_{\text{sp}}/\sigma_{\text{bkg}})| < 20\%$
- $|\text{Max}((N_{\text{sp}} - 2\Delta_{\text{MC}})/N_{\text{ref}})| < 10\%$

Where σ_{bkg} is the statistical uncertainty on the data, and Δ_{MC} is the statistical uncertainty on the Monte Carlo background template, and N_{ref} is the expected number of signal yields from the HH signal. The second condition is used to account for local statistical fluctuations in the background template due to low MC statistics. For an example see Figure 5.15. In each category, the exponential function was found to be the best choice as it had the smallest number of degrees of freedom and resulted in a consistently small bias. The exponential function is defined as:

$$f_{\text{bkg,c}}^{\text{nonres}}(m_{\gamma\gamma}) = e^{-a \cdot m_{\gamma\gamma}}$$

The bias was found to be at most 39% of the expected error on the fitted signal yield originating from the data statistics as shown in Table 5.4. The difference in shape between the simulated events and the exponential form measured in the data sidebands was found to have a negligible impact on the spurious signal.

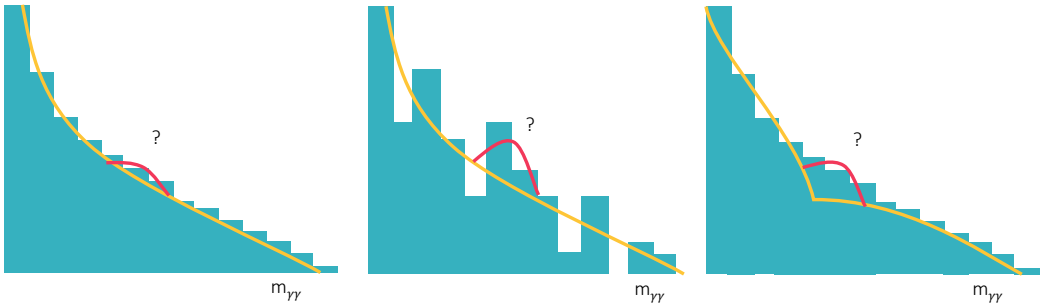

Figure 5.15: Illustration of spurious signal (a) and how it can be exacerbated by (b) poor Monte Carlo statistics and (c) poor background modelling

Table 5.4: Spurious signal result for the exponential pdf for the various ggF HH categories. In each category, the spurious signal (N_{sp}) and its ratio to the expected statistical error from data ($Z_{\text{sp}} = N_{\text{sp}}/\sigma_{\text{bkg}}$)) are shown.

Category	N_{sp}	Z_{sp}
High mass BDT tight	0.69	0.39
High mass BDT loose	0.99	0.38
Low mass BDT tight	0.59	0.38
Low mass BDT loose	1.09	0.27

5.7 Statistical interpretation

The results of this analysis are obtained from a simultaneous maximum-likelihood fit of the diphoton invariant mass distribution across all analysis categories. To perform this fit, a likelihood is first constructed to describe the expected distribution of signal and background in data. The likelihood is parameterized as a function of the signal strength, μ, and a set of nuisance parameters, θ. This likelihood can then be profiled to find the best-fit μ and θ, which maximize the likelihood. A test statistic based on the log-likelihood ratio, the ratio between a conditional likelihood, where the signal strength μ is varied, and the maximum likelihood can then be constructed. This test statistic can be used to interpret the data for statistical hypothesis testing, such as determining the significance of a observed result, or putting upper limits on the possible signal strengths. This section will discuss each of these steps in the context of the $b\bar{b}\gamma\gamma$ analysis in more detail.

Likelihood

The likelihood function is constructed as the product of Poisson probability distributions in each category, c. The likelihood function is defined as:

$$\mathcal{L} = \prod_{c} \left(\text{Pois}(n_c | N_c(\theta)) \cdot \prod_{i=1}^{n_c} f_c(m^i_{\gamma\gamma}, \theta) \cdot G(\theta) \right), \tag{5.10}$$

Where for each event i in a category c, n_c is the observed number of events, N_c is the expected number of events, f_c is the value of the probability density function (pdf), θ are nuisance parameters, and $G(\theta)$ is a set of constraints on the nuisance parameters. The nuisance parameters represent uncertain aspects of the model, such as the background shape parameterization and systematics uncertainties which are described in Section 5.8.

The expected number of events per category N_c, defined in Eq. (5.11), is the sum of the expected yields from HH production processes(N_{HH}), single Higgs boson production which is a resonant background ($N^{\text{res}}_{\text{bkg}}$), the nonresonant background (N^{nonres}), as well as the spurious-signal uncertainty ($N_{\text{SS,c}}$):

$$N_c(\theta) = \mu \cdot N_{HH,\text{c}}(\theta^{\text{yield}}_{HH}) + N^{\text{res}}_{\text{bkg,c}}(\theta^{\text{yield}}_{\text{res}}) + N^{\text{nonres}}_{\text{bkg,c}} + N_{\text{SS,c}} \cdot \theta^{\text{SS,c}} \tag{5.11}$$

Here μ is the signal strength, $\theta^{\text{SS,c}}$ represent the nuisance parameters associated with the background function bias, and θ^{yield} represent the nuisance parameters affecting the event yield. Nuisance parameters can be correlated across the different signal and background components, and categories.

The signal strength μ corresponds to the ratio between the number of observed HH signal events and the predicted number of events from the Standard Model:

$$\mu = \frac{N_{HH,\text{fitted}}}{N_{HH,\text{ predicted, SM}}}$$

A signal strength of $\mu = 1$ corresponds to the SM prediction, and a signal strength of $\mu = 0$ corresponds to the background-only hypothesis. If systematic uncertainties on the HH cross-sections are not applied, μ corresponds to the ratio between the observed and predicted HH cross-sections.

The probability density function f_c, shown in Eq. (5.12), represents the shape information of each process in each category. This is the sum of the double-sided Crystal Ball functions modeling the HH production processes, single Higgs boson production, the analytic function modeling the nonresonant background, and the spurious signal. It is normalized by N_c, the expected number of events per category:

$$\begin{aligned} f_c(m_{\gamma\gamma}, \theta) = [&\mu \cdot N_{HH,\text{c}}(\theta^{\text{yield}}_{HH}) \cdot f_{HH,\text{c}}(m_{\gamma\gamma}, \theta^{\text{shape}}_{HH}) + N^{\text{res}}_{\text{bkg,c}}(\theta^{\text{yield}}_{\text{res}}) \cdot f^{\text{res}}_{\text{bkg,c}}(m_{\gamma\gamma}, \theta^{\text{shape}}_{\text{res}}) \\ &+ N_{\text{SS,c}} \cdot \theta^{\text{SS,c}}_{HH} \cdot f_{HH,\text{c}}(m_{\gamma\gamma}, \theta^{\text{shape}}_{HH}) + N^{\text{nonres}}_{\text{bkg,c}} \cdot f^{\text{nonres}}_{\text{bkg,c}}(m_{\gamma\gamma}, \theta^{\text{shape}}_{\text{nonres}})]/N_c(\theta^{\text{yield}}_{\text{nonres}}), \end{aligned} \tag{5.12}$$

Here θ^{shape} represents the nuisance parameters related to the shape variations of the functional forms. When a nuisance parameter is related to shape and yield variations at the same time, the two effects are correlated. The nominal yields of the resonant background processes are initially set

to values from simulation.

Profile likelihood ratio test

The likelihood ratio test can be used to estimate the goodness of fit for two different statistical models by comparing the ratios of their likelihoods. We are specifically interested in determining the best fit value for our parameter of interest, the signal strength μ. The two models we will compare are the maximum likelihood estimate $\mathcal{L}(\hat{\mu}, \hat{\theta})$, and the conditional maximum likelihood estimate, $\mathcal{L}(\hat{\hat{\theta}}(\mu))$. In the maximum likelihood estimate, the signal strength and nuisance parameters are profiled to find values of μ and θ that unconditionally maximize the overall likelihood function. These parameters are known as $\hat{\mu}$ and $\hat{\theta}$. The conditional maximum likelihood estimate holds μ fixed, and profiles θ to find the values that maximize the likelihood function at that value of μ. The profile likelihood ratio can then be written as [155]:

$$\lambda(\mu) = -2 \ln \frac{\mathcal{L}(\mu, \hat{\hat{\theta}}(\mu))}{\mathcal{L}(\hat{\mu}, \hat{\theta})} \,, \tag{5.13}$$

This ratio can then be assessed for different values of μ to interpret the best-fit signal strength and confidence intervals. A ratio of 1 will indicate good agreement between the maximum likelihood estimate and the conditional maximum likelihood estimate for a particular value of μ. For numerical stability reasons, often the negative log-likelihood ratio $-\ln(\mathcal{L}(\mu, \hat{\hat{\theta}}(\mu)))$ is profiled instead of the likelihood ratio as shown in Figure 5.16.

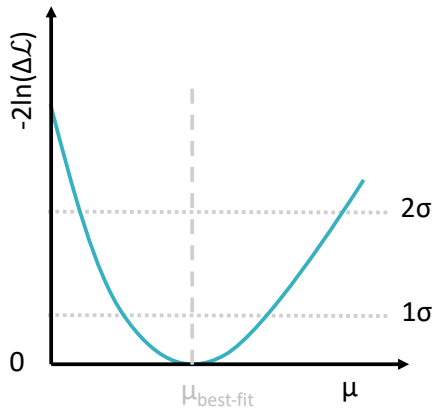

Figure 5.16: Illustration of negative log-likelihood ratio profiled in μ

For the κ_λ likelihood scans described in Section 5.9, the same likelihood-ratio method is used, but κ_λ is profiled instead of μ. During these scans, μ is set to 1, meaning that this profile describes the log-likelihood ratio under the Standard Model hypothesis.

Test statistic

To use the likelihood ratio test for hypothesis testing, the profile-likelihood-ratio-based test statistic $\tilde{q}_\mu$ is used, as defined in Eq. (5.14). This test statistic can be used to determine the p-values for a given hypothesis. The $\tilde{q}_\mu$ test statistic makes the assumption that the signal strength μ is greater than 0 [155].

$$\tilde{q}_\mu = \begin{cases} -2\ln\frac{\lambda(\mu,\hat{\hat{\theta}}(\mu))}{\lambda(0,\hat{\hat{\theta}}(0))} & \hat{\mu} < 0, \\ -2\ln\frac{\lambda(\mu,\hat{\hat{\theta}}(\mu))}{\lambda(\hat{\mu},\hat{\theta}(\mu))} & 0 \leq \hat{\mu} \leq \mu, \\ 0 & \hat{\mu} > \mu. \end{cases} \tag{5.14}$$

p-values

Now that the test statistic has been defined, we can finally get to the matter of hypothesis testing. Hypothesis testing in particle physics can be used to either calculate the significance of a result or to set limits on the signal strength. The p-value, p, sits at the heart of these two goals and is defined as the probability of obtaining test results at least as extreme as the observed result. A larger p-value indicates that the observed result is more consistent with the hypothesis, and a small p-value indicates that the observed result is less consistent with the hypothesis. This is illustrated in Figure 5.17, where the distribution, $f(t|\alpha)$, represents a Poisson probability distribution hypothesis with α expected events. t_{obs} events are observed, and the p-value represents the fractional area of the distribution allowing for $t > t_{\text{obs}}$.

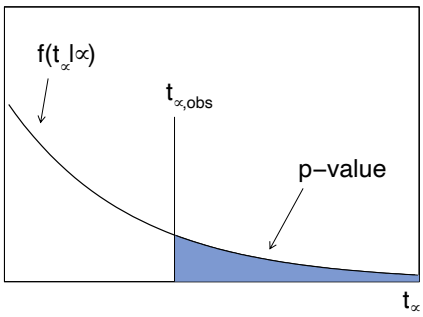

Figure 5.17: The p-value corresponds to the area under the probability distribution where $t > t_{\text{obs}}$. Reproduced from [155].

Formally, the p-value for the q_μ test statistic is:

$$p_\mu = \int_{q_{\text{obs}}}^{\infty} f(q_\mu|\mu)dq_\mu$$

This p-value can not usually be calculated analytically as the test-statistic distribution is often

very complex. While pseudo-experiments can be used to sample the probabilities used to define the likelihood, this is a very computationally expensive procedure. Instead, the asymptotic approximation [155] is usually used for the test-statistic distribution:

$$\tilde{q}_\mu = \begin{cases} \mu^2/\sigma^2 - 2\mu\hat{\mu}/\sigma^2 & \hat{\mu} < 0, \\ (\mu - \hat{\mu})^2/\sigma^2 & 0 \leq \hat{\mu} \leq \mu, \\ 0 & \hat{\mu} > \mu. \end{cases} \tag{5.15}$$

This approximation allows us to analytically determine the CDF:

$$F(\tilde{q}_\mu|\mu') = \begin{cases} \Phi(\sqrt{\tilde{q}_\mu}) & 0 < \tilde{q}_\mu < \mu^2/\sigma^2, \\ \Phi(\frac{\tilde{q}_\mu + (\mu^2 - 2\mu\mu')/\sigma^2}{2\mu/\sigma}) & \tilde{q}_\mu > \mu^2/\sigma^2 \end{cases} \tag{5.16}$$

Where Φ^{-1} is the inverse cumulative distribution function of the standard Gaussian. This CDF can then be used to calculate the expected p-values for the observed data under a given hypothesis. The accuracy of the asymptotic approximation in this analysis was checked with pseudo-experiment studies and the results were found to agree with the pseudo-experiments to within 8%.

CLs method for limit setting

The p-values can be use to set upper limits on HH production using the $\mathrm{CL_S}$ method [158]. In other words, this method asks the question of what the maximum possible signal strength μ that can be excluded within a certain confidence interval is. This method compares the ratios of the p-values in the signal+background hypothesis to that of the background-only hypothesis as illustrated in Figure 5.18. In searches, where signal is not yet observable, such as all of the HH searches described in this chapter and Chapter 7 at the time of writing this thesis the 95% CLs test is employed to set limits on the HH signal strength. The 95% CLs exclusion intervals are defined by:

$$CL_s = \frac{p_{s+b}}{p_b} < 0.05$$

Where p_{s+b} is the p-value for the signal + background hypothesis, i.e. where HH production occurs with signal strength $\mu = 1$:

$$p_{s+b} = \int_{q_{\mathrm{obs}}}^{\infty} f(q_\mu|1) dq_\mu$$

And p_b is the p-value for background only hypothesis, where no HH production is expected:

$$p_b = \int_{q_{\mathrm{obs}}}^{\infty} f(q_\mu|0) dq_\mu$$

Where f is the pdf of the test-statistic distribution.

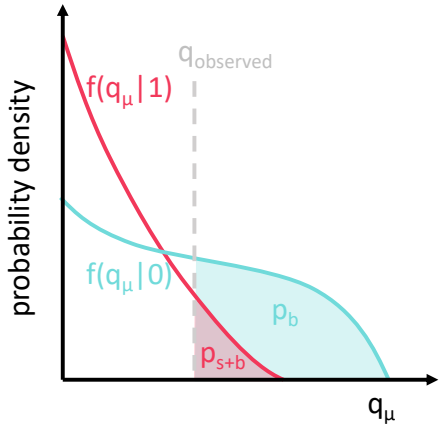

Figure 5.18: Illustration of CLs method

Significance

In cases where the observed data deviates strongly from the background-only hypothesis, we can set a significance for this result. The particle physics community defines 3σ and 5σ benchmarks for observing "evidence of" or "observation of" a new process as described in Table 5.5. The significance, Z, of a p-value is defined as:

$$Z = \Phi^{-1}(1-p)$$

Where Φ^{-1} is the inverse cumulative distribution function of the standard Gaussian. As illustrated in Figure 5.19 we can correspondingly write:

$$p = \int_{n\sigma}^{\infty} \frac{1}{2\pi} e^{-z^2/2} = 1 - \frac{1}{2}\text{erf}(\frac{n}{\sqrt{2}})$$

Currently, none of the HH searches observe a statistically significant deviation from the background-only hypothesis, but as we look forward to the HL-LHC in Chapter 8, we expect to move from search mode to measurement mode and the statistical significance will become relevant.

Table 5.5: Table comparing significances with their p-values for common use cases:

Use	Z	p
Evidence for a new particle/process relative to background only hypothesis	3	$< 1.35 \times 10^{-3}$
Observation of a new particle/process relative to background only hypothesis	5	$< 2.87 \times 10^{-7}$

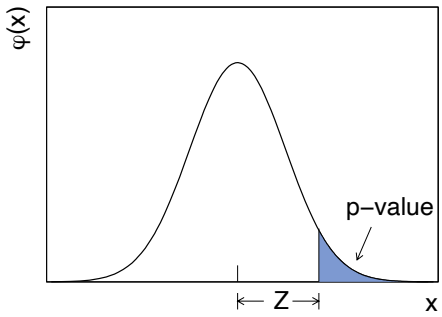

Figure 5.19: Illustration of relationship between significance and p-values, the p-value corresponds to the area under the unit Gaussian. The significance, Z corresponds to the distance between the mean and the lower bound on the integral. Reproduced from [155].

5.8 Systematic uncertainties

The sensitivity of the analysis is currently limited by the statistical precision. The assessment of the systematic uncertainties is described below and their impact on the results is discussed in Section 5.9.4.

5.8.1 Experimental uncertainties

- *Luminosity:* The uncertainty in the integrated luminosity of the full Run 2 data set is 1.7% [106], obtained using the LUCID-2 detector [105] for the primary luminosity measurements.

- *Spurious signal:* The continuum background processes of the analysis are estimated from data and are subject to uncertainties related to the potential bias arising from the chosen background model, as described in Section 5.6.2. The background functional form bias is assessed as an additional uncertainty in the total number of signal events in each category.

- *Photon energy scale and resolution:* These uncertainties come from the measurement and calibration of the photon energies and are obtained from Ref. [69]. They depend on both the energy of the photon and which part of the calorimeter the photon was identified in. As the photon can traverse different amounts of material and different portions of the calorimeter have different responses and segmentation.

- *Photons identification and isolation:* The systematic uncertainties from the photon identification and isolation efficiencies are estimated by are evaluated by varying the correction factors for photon selection efficiencies in simulation by the corresponding uncertainties and affect the diphoton selection efficiency. [69].

- *Trigger efficiency:* The efficiency of the diphoton trigger used to select events is evaluated in simulation and data using a bootstrap method and radiative Z decays [153]. The difference between data and MC is taken as a systematic uncertainty. In the diphoton invariant mass range of $105 < m_{\gamma\gamma} < 160$ GeV, the trigger efficiency uncertainty affects the acceptance by 1% in each category.

- *Vertex selection efficiency:* The uncertainty in the vertex selection efficiency is assessed by comparing the efficiency of finding photon-pointing vertices in $Z \to e^+e^-$ events in data with that in simulation [159]. The resulting uncertainty is found to have a negligible effect on the signal selection efficiency.

- *Jet energy scale and resolution:* The jet energy scale and resolution uncertainties [56] affect the $m_{b\bar{b}}$ distribution, while flavour-tagging uncertainties affect the acceptance of the analysis categories. The experimental uncertainties in jet energy scale and resolution are propagated to the $E_{\mathrm{T}}^{\mathrm{miss}}$ calculation. In addition, the uncertainties in the scale and resolution of the $E_{\mathrm{T}}^{\mathrm{miss}}$ soft term are evaluated by using the method described in Ref. [160].

- *Flavour tagging:* The flavour-tagging uncertainties for b- and c-jets are estimated in $t\bar{t}$ events [81, 161], while the misidentification uncertainty of light-flavour jets is determined using dijet events [162]. Additional uncertainties from the b-jet momentum correction accounting for the presence of muons and neutrinos are found to be negligible.

5.8.2 Theory uncertainties

- *QCD scale:* For single Higgs boson and SM HH production, the effects of theoretical scale uncertainties due to missing higher-order corrections on the production rates are estimated by varying the factorization and renormalization scales up and down from their nominal values by a factor of two, recalculating the cross-section in each case, and taking the largest deviation from the nominal cross-section as the uncertainty. These range between +4.8% and -8.5% for the entire κ_λ range of -10 to 10.

- *PDF+α_s:* The uncertainties in the cross-sections, including effects of PDF+α_{s} uncertainties are 3% and taken from Refs. [36, 120].

- *Higgs branching ratios:* The uncertainties in the $H \to \gamma\gamma$ and $H \to b\bar{b}$ branching fractions are on the order of 2.9 and 1.7% and are taken from Refs. [36, 120].

- *Higgs mass:* The uncertainty in the value of the Higgs boson mass of 0.2% is applied [35].

- *Top mass:* The uncertainties in SM HH ggF production arising from the choice of renormalization scheme and scale of the top-quark mass and their combination with those from

factorization and renormalization scale variations are based on Ref. [22] and taken to be ± 2.6%.

- *Higgs + Heavy flavour:* A 100% uncertainty is assigned to the single Higgs boson ggF and VBF production modes and to Higgs boson production in association with a W boson. This is motivated by studies of heavy-flavour production in association with top-quark pairs [163, 164] and of W boson production in association with b-jets [165]. No additional heavy-flavour uncertainty is assigned to the single Higgs boson $t\bar{t}H$ and ZH production modes, where the dominant heavy-flavour production is already accounted for in the LO process.

- *Parton shower:* For all samples, the uncertainty related to the choice of parton showering model is evaluated by comparing the predictions of the nominal MC samples and alternative samples using a different parton showering model as shown in Figure 5.20.

- κ_λ *reweighting:* In addition, for the HH production processes, a systematic uncertainty is assigned to the κ_λ reweighting. These are evaluated per category based on the difference between that sample yield and reweighted yields at κ_λ =10 and are on the order of 5%.

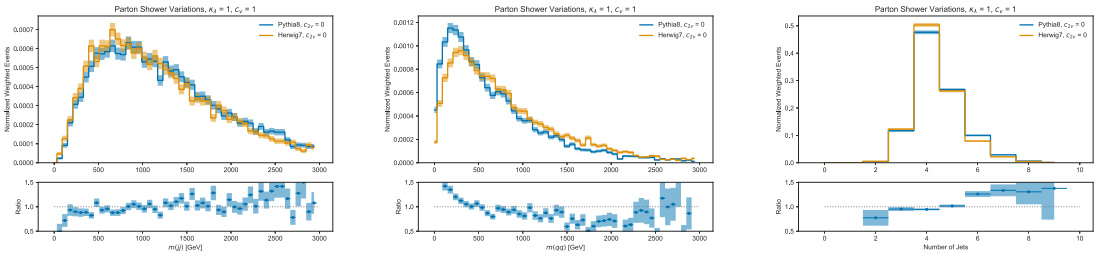

(a) (b) (c)

Figure 5.20: Example of the effect of parton shower variations on VBF HH signal distributions for $m_{b\bar{b}}$, $m(qq)$ (VBF jets), and N_{jets}

5.9 Results

Figure 5.21 shows the continuum background, continuum+single Higgs background, and signal+background fits to the data after unblinding. The parameters of the continuum background are fit to the data in the sideband regions, and the single Higgs backgrounds are determined from simulation. Each of the categories has a very low total event count in the entire signal and sideband region, showing the statistical limitations of this analysis. Negative fluctuations in the signal+background fit are observed in all four categories, with the fluctuation in the high mass BDT tight category being the most notably affected. The impact of these negative fluctuations is that the observed limits of the

signal strength are slightly better than expected. Negative fluctuations in the signal strength are to be expected at an equal rate as positive fluctuations.

Table 5.6 summarizes the per category expected and observed yields in the signal region. No significant excess over the SM background expectations was found, and instead, under-fluctuations are observed in most categories. The expected yields are dominated by the continuum background.

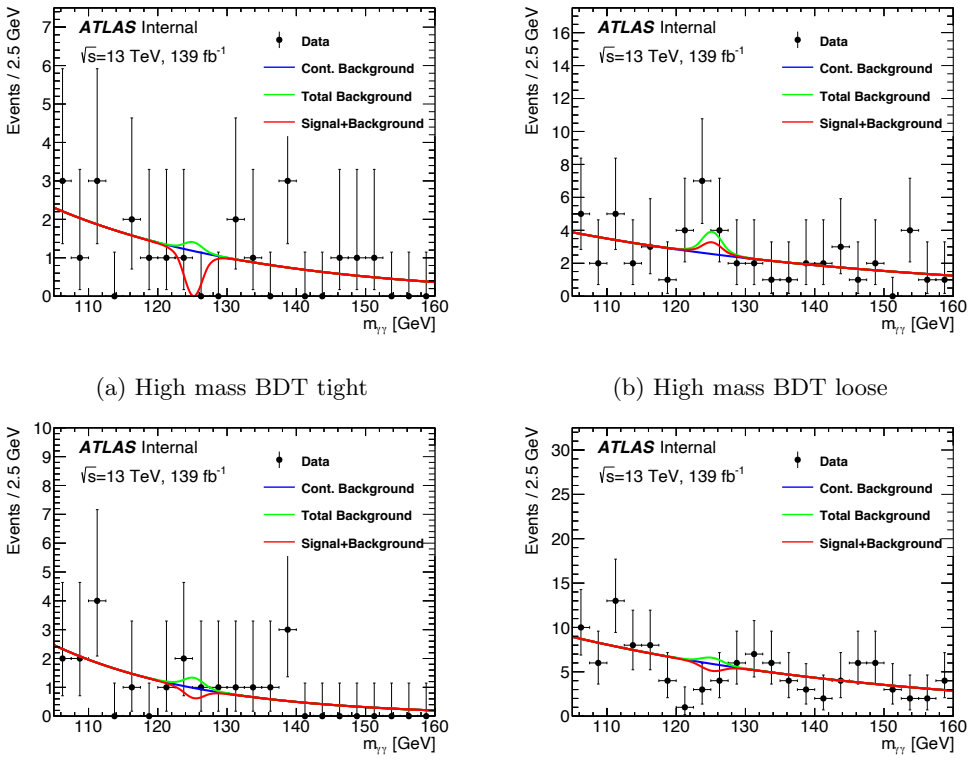

(a) High mass BDT tight

(b) High mass BDT loose

(c) Low mass BDT tight

(d) Low mass BDT loose

Figure 5.21: Data are compared with the signal+background fit: (a) high mass BDT tight, (b) high mass BDT loose, (c) low mass BDT tight, and (d) low mass BDT loose. Both the continuum background and the background from single Higgs boson production are considered. The data points in the Figure are the same as shown in Figure 5.13.

Table 5.6: The number of data events observed in the $120 < m_{\gamma\gamma} < 130$ GeV window, the number of HH signal events expected for $\kappa_\lambda = 1$ and for $\kappa_\lambda = 10$, and events expected for single Higgs boson production (estimated using MC simulation), as well as for the continuum background. For the single Higgs boson, "Rest" includes the following production modes: VBF, WH, tHq, and tHW. The values are obtained from a fit of the Asimov data set [155] generated under the SM signal-plus-background hypothesis, $\kappa_\lambda = 1$. The continuum background component of the Asimov data set is obtained from the fit of the data sideband. The uncertainties in the HH and single Higgs boson yields include the systematic uncertainties discussed in Section 5.8. The uncertainty on the continuum background is given by the sum in quadrature of the statistical uncertainty from the fit to the data and the spurious-signal uncertainty.

	High mass BDT tight	High mass BDT loose	Low mass BDT tight	Low mass BDT loose
Continuum background	$4.9^{+1.1}_{-1.3}$	$9.5^{+1.5}_{-1.7}$	$3.7^{+0.9}_{-1.1}$	$24.9^{+2.3}_{-2.5}$
Single Higgs boson background	$0.67^{+0.29}_{-0.13}$	$1.6^{+0.6}_{-0.2}$	$0.23^{+0.09}_{-0.03}$	$1.40^{+0.33}_{-0.16}$
ggF+bbH	$0.26^{+0.28}_{-0.16}$	$0.4^{+0.5}_{-0.2}$	$0.07^{+0.08}_{-0.04}$	$0.27^{+0.27}_{-0.16}$
$t\bar{t}H$	$0.19^{+0.03}_{-0.03}$	$0.49^{+0.09}_{-0.07}$	$0.107^{+0.022}_{-0.017}$	$0.75^{+0.13}_{-0.11}$
ZH	$0.142^{+0.035}_{-0.025}$	$0.48^{+0.09}_{-0.07}$	$0.040^{+0.020}_{-0.014}$	$0.27^{+0.06}_{-0.04}$
Rest	$0.074^{+0.032}_{-0.014}$	$0.16^{+0.07}_{-0.03}$	$0.012^{+0.008}_{-0.004}$	$0.111^{+0.030}_{-0.012}$
SM $HH(\kappa_\lambda = 1)$ signal	$0.87^{+0.10}_{-0.18}$	$0.37^{+0.04}_{-0.07}$	$0.049^{+0.006}_{-0.010}$	$0.078^{+0.008}_{-0.015}$
ggF	$0.86^{+0.10}_{-0.18}$	$0.35^{+0.04}_{-0.07}$	$0.046^{+0.006}_{-0.010}$	$0.072^{+0.008}_{-0.015}$
VBF	$(12.6^{+1.3}_{-1.2}) \cdot 10^{-3}$	$(16.1^{+1.4}_{-1.2}) \cdot 10^{-3}$	$(3.2^{+0.4}_{-0.4}) \cdot 10^{-3}$	$(6.9^{+0.5}_{-0.6}) \cdot 10^{-3}$
Alternative $HH(\kappa_\lambda = 10)$ signal	$6.5^{+1.0}_{-0.8}$	$3.6^{+0.6}_{-0.4}$	$4.5^{+0.7}_{-0.6}$	$8.5^{+1.3}_{-1.0}$
Data	2	17	5	14

5.9.1 Limits on Standard Model HH production

Using the CLs method, an observed (expected) upper limit at 95% CL on the signal strength of 4.2 (5.7) times the SM prediction is obtained. Ignoring the theoretical uncertainties on the HH cross-section, the analysis sets an observed (expected) 95% CL upper limit on the HH production cross-section at 130 fb (180 fb). This is about a 1σ under-fluctuation relative to the expected limits. A check of the results that quantifies the upper limits by using pseudo-experiments, is performed and the increase of the limit value relative to the asymptotic approximation is found to be less than 8% for both the observed and expected upper limits.

5.9.2 κ_λ cross-section scan

Upper limits on the HH production cross-section are also computed as a function of κ_λ, as shown in Figure 5.22. For this purpose, single Higgs boson production cross-sections and Higgs boson decay branching ratios are assumed to have SM values, and the coupling strength between the Higgs boson

and other particles are also set to their SM values [119]. The theory uncertainties related to the signal cross-section are not included.

The expected constraints on κ_λ at 95% CL, as obtained with a background hypothesis excluding $pp \to HH$ production, are $[-2.4, 7.7]$, whereas the observed constraints are $[-1.5, 6.7]$ at 95% CL. As it increases the overall expected cross-sections, the inclusion of the VBF HH production mode tightens the constraints by about 5% relative to an alternative fit considering only the ggF production mode.

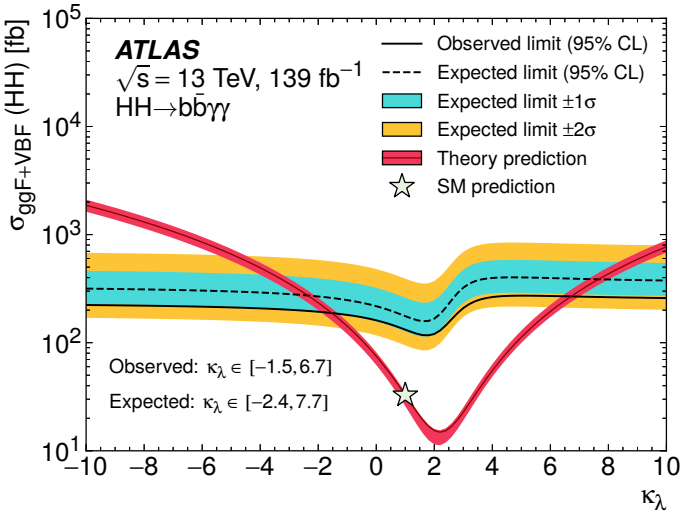

Figure 5.22: Observed and expected limits at 95% CL on the cross-section of Higgs boson pair production as a function of the Higgs boson self-coupling modifier $\kappa_\lambda = \lambda_{HHH}/\lambda_{HHH}^{\mathrm{SM}}$. The expected constraints on κ_λ are obtained with a background hypothesis excluding $pp \to HH$ production. The $\pm 1\sigma$ and $\pm 2\sigma$ variations about the expected limit due to statistical and systematic uncertainties are also shown. The theory prediction curve represents the scenario where all parameters and couplings are set to their SM values except for κ_λ. The uncertainty band on the theory prediction curve shows the cross-section uncertainty.

5.9.3 κ_λ likelihood scan

An alternative statistical analysis uses a negative log-likelihood scan to determine the best-fit value of κ_λ and its uncertainty under the assumption that SM HH production exists. The coupling strengths of the Higgs boson to fermions and gauge bosons are set to their SM values. The values of the negative log-likelihood ratio, $-2\ln\lambda(\mu)$, as a function of κ_λ are shown in Figure 5.23. The Asimov data set [155] is generated under the SM signal-plus-background hypothesis, $\kappa_\lambda = 1$. All systematic uncertainties, including those of the theoretical prediction of the HH production cross-section, are included. The best-fit value corresponds to $\kappa_\lambda = 2.8^{+2.0}_{-2.2}$ $(^{+3.8}_{-4.3})$ for the 1σ (2σ) confidence

interval. The expected value corresponds to $\kappa_\lambda = 1.0^{+5.5}_{-2.4}$ $(^{+7.3}_{-4.2})$ for the 1σ (2σ) confidence interval. The second minimum in the expected likelihood scan curve corresponds to a similar fitted signal yield with respect to the κ_λ point at the first minimum, which is a consequence of a higher cross-section, but lower acceptance and worse signal-to-background separation. The m_{HH} distribution has a different shape at each of the two minima, as shown in Figure 5.6.

5.9.4 Impact of systematic uncertainties

The dominant systematic uncertainties are listed in Table 5.7. The main uncertainties are related to the choice of functional form for the continuum background (spurious signal), to the parton showering model, and to the photon energy resolution. This analysis is currently statistically limited, with the statistical uncertainty on the SM limit being on the order of 200%. The systematic uncertainties combined have an impact of 30%.

Table 5.7: Breakdown of the dominant systematic uncertainties. The impact of the uncertainties corresponds to the relative variation of the expected upper limit on the cross-section when re-evaluating the profile likelihood ratio after fixing the nuisance parameter in question to its best-fit value, while all remaining nuisance parameters remain free to float. The impact is shown in %. Only systematic uncertainties with an impact of at least 0.2% are shown. Uncertainties of the "Norm. + Shape" type affect both the normalization and the parameters of the functional form. The rest of the uncertainties affect only the yields.

Source	Type	Relative impact of the systematic uncertainties [%]
Experimental		
Photon energy resolution	Norm. + Shape	0.4
Jet energy scale and resolution	Normalization	< 0.2
Flavour tagging	Normalization	< 0.2
Theoretical		
Factorization and renormalization scale	Normalization	0.3
Parton showering model	Norm. + Shape	0.6
Heavy-flavour content	Normalization	0.3
$\mathcal{B}(H \to \gamma\gamma, b\bar{b})$	Normalization	0.2
Spurious signal	Normalization	3.0

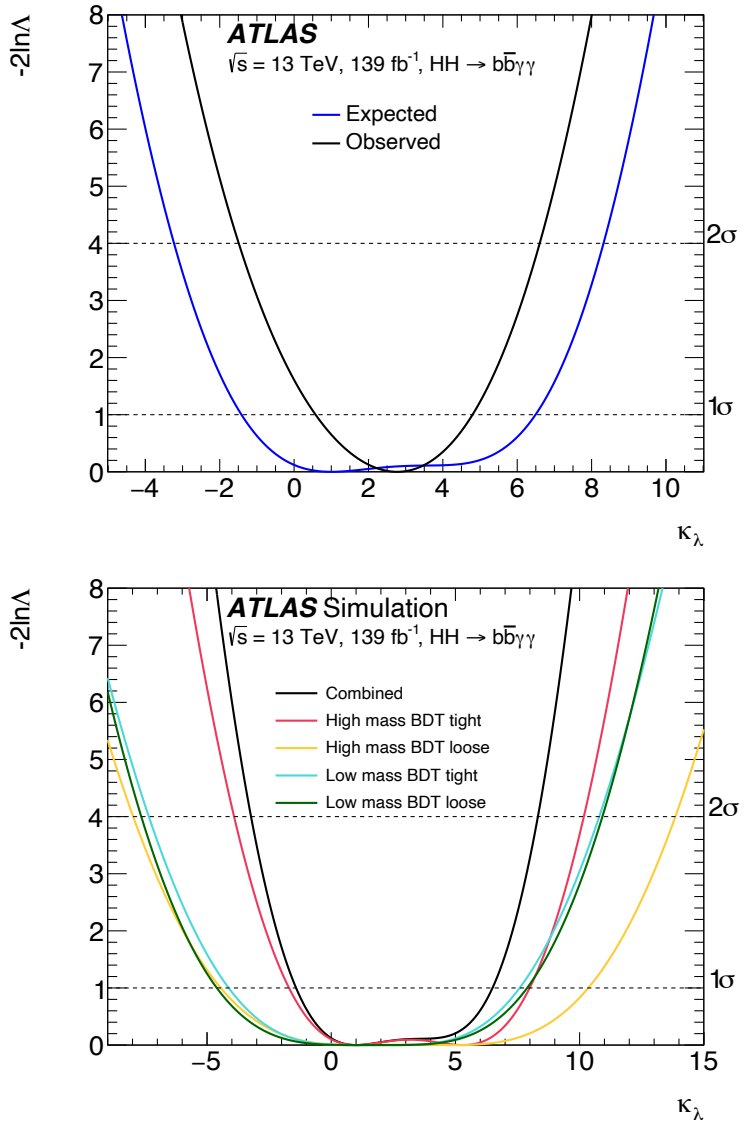

Figure 5.23: Values of the negative log-profile-likelihood ratio ($-2\ln\lambda$) as a function of κ_λ evaluated for (a) the combination of all the categories and (b) each category individually. The coupling of the Higgs boson to fermions and gauge bosons is set to SM values in the profile likelihood calculation. The expected result corresponds to an Asimov data set [155] generated under the SM signal-plus-background hypothesis, $\kappa_\lambda = 1$. All systematic uncertainties, including the theoretical uncertainties in the HH production cross-section, are included. The intersections of the solid curves and the horizontal dashed lines indicate the 1σ and 2σ confidence-level intervals.

5.10 Comparison with Early Run 2 Results and CMS

Relative to the previous $b\bar{b}\gamma\gamma$ search in Early Run 2 with 36fb^{-1}, this analysis used a data set that is about four times larger. The previous search recorded observed (expected) limits on the SM cross-section of 12.9 (21) and observed limits on κ_λ of -8.1-13.1 [166]. The results improve upon the previous ATLAS limits on the $HH \to b\bar{b}\gamma\gamma$ production cross-section by a factor of five, and the allowed κ_λ range shrinks by about a factor of two. Some of the major analysis improvements relative to the previous search include the categorization based on $m^*_{b\bar{b}\gamma\gamma}$ and the use of boosted decision trees instead of a cut-based event selection. Other improvements come from improved object definitions. For example, the b-tagging working point was moved from 70% in Early Run 2 to 77% for this analysis due to moving from the MV210 b-tagging algorithm to DL1r without a large increase in backgrounds. The use of the Muon-in-jet+PtReco b-jet correction also improved the analysis sensitivity by about 10%.

The analysis presented in this chapter also sets limits that are stronger than an Early Run 2 combination of the $b\bar{b}b\bar{b}$, $b\bar{b}\tau^+\tau^-$, $b\bar{b}\gamma\gamma$, $b\bar{b}WW^*$, $WWWW$ and $WW\gamma\gamma$ channels with up to 36 fb^{-1} of 13 TeV data. The observed (expected) limits in the Early Run 2 combination were 6.9(10)xSM, and constraints on κ_λ were $-5.0 < \kappa_\lambda < 12.0$ at 95% CL [167].

The CMS Collaboration also recently set observed (expected) upper limits of 7.7 (5.2) times the SM prediction at 95% CL on enhancements of Higgs boson pair production in the $b\bar{b}\gamma\gamma$ final state with 137 fb^{-1} of 13 TeV data [168]. Although ATLAS saw a downward fluctuation in the observed data, and CMS saw an upwards fluctuation, the expected limits of 5.7 (ATLAS) and 5.2 (CMS) times the standard model signal strength are very similar. The CMS 95% CL constraints on κ_λ were observed (expected) to be between $-3.3 < \kappa_\lambda < 8.5$ ($-2.5 < \kappa_\lambda < 8.2$). For comparison, the expected constraints on κ_λ from ATLAS are $-2.4 < \kappa_\lambda < 7.7$, which are very close to those from CMS.

The CMS results are competitive with the ATLAS results despite very different analysis strategies. At the trigger level, CMS uses lower diphoton trigger thresholds than ATLAS, which could allow for increased sensitivity low values of m_{HH} and therefore BSM values of κ_λ. The CMS diphoton trigger thresholds are 30 and 22 GeV for the leading and subleading photons, relative to 35 and 25 GeV on ATLAS. The diphoton mass resolution in ATLAS and CMS is about the same at 3 GeV. CMS uses two sets of b-jet corrections, the first uses a DNN to perform a jet-by-jet correction on the b-jet p_{T}, the second uses an event-by-event BDT to exploit the kinematic properties of the $b\bar{b}\gamma\gamma$ system. After corrections, the CMS b-jet resolution is about 25 GeV, and on ATLAS it is also 25 GeV.

One of the main differences between the ATLAS and CMS analysis strategies include that CMS uses a 2-dimensional fit in ($m_{b\bar{b}}$,$m_{\gamma\gamma}$) for their signal extraction. This was also considered on ATLAS, but did not appear to yield any significant advantage relative to our strategy of 1-dimensional fit on $m_{\gamma\gamma}$, with $m_{b\bar{b}}$ used as an input to the BDT. Compared to ATLAS, CMS uses many more

analysis categories, with fourteen different analysis categories instead of 4. Similar to ATLAS, these categories are also based on $m^*_{b\bar{b}\gamma\gamma}$. Contrary to ATLAS, CMS uses two VBF targeted categories and one $t\bar{t}H$ category, where ATLAS has neither. The $t\bar{t}H$ category is particularly interesting is it can be used to constrain the single Higgs backgrounds and simultaneously probe both κ_λ and k_t as shown in Figure 5.24. On ATLAS, these confidence intervals are probed during the combination of HH results with single Higgs results.

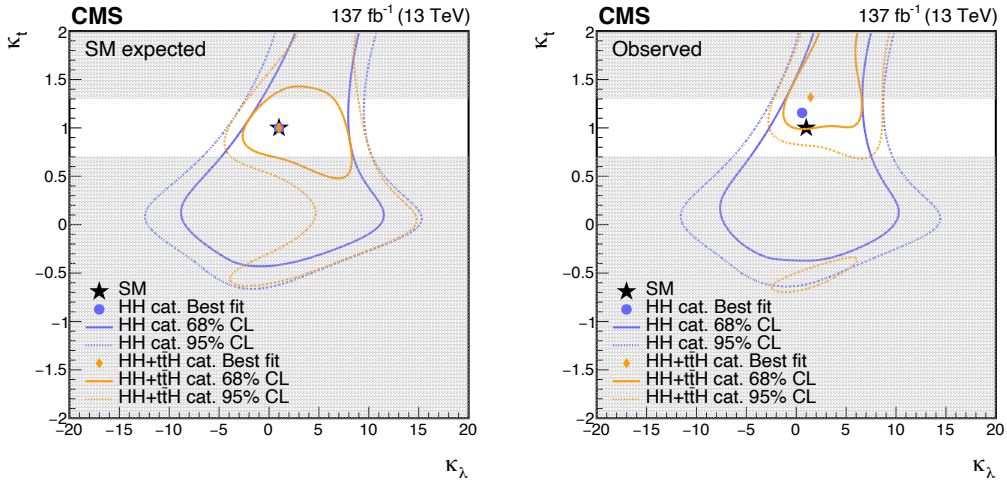

Figure 5.24: CMS Negative log-likelihood contours of κ_λ and k_t. (a) evaluated with an Asimov dataset assuming the SM hypothesis and (b) in the observed data. The regions of the 2D scan where the parameterization of k_t for κ_λ is not reliable are shown in the grey band

5.11 Conclusions

Searches for Higgs boson pair production are performed in the $b\bar{b}\gamma\gamma$ final state using 139 fb^{-1} of 13 TeV pp collision data collected with the ATLAS detector at the LHC. No significant excess above the Standard Model background expectation is observed. A 95% CL upper limit of 130 fb is set on the $pp \to HH$ production cross-section, where the expected limit is 180 fb. The observed (expected) limit corresponds to 4.2 (5.7) times the cross-section predicted by the Standard Model. Constraints on the Higgs boson self-coupling are also derived, and limits of $-1.5 < \kappa_\lambda < 6.7$ are obtained, where $-2.4 < \kappa_\lambda < 7.7$ is expected. The expected constraints on the HH production cross-section and on κ_λ are obtained with a background hypothesis excluding $pp \to HH$ production. Relative to the Early Run 2 results with 36fb^{-1} these results represent a factor of five improvement on the upper limits of the SM HH production cross-section and shrink the constraints on the κ_λ range by a factor of two. Future analysis improvements and the outlook for Run 3 will be discussed in Chapter 6, and Chapter 8 will discuss detailed prospects for the HL-LHC.

Chapter 6

$HH \to b\bar{b}\gamma\gamma$ Outlook for Run 3

Run 3 started in early 2022 and marked the start of a new period of data-taking at the LHC. Run 3 will operate at 13.7 TeV and will have similar beam conditions and instantaneous luminosity to Run 2. Run 3 is expected to take data for the same amount of time as Run 2, doubling the overall statistics. This will bring the total integrated luminosity across Run 2 and 3 to 300fb^{-1}. Between Run 2 and 3, the major detector upgrade in ATLAS was the installation of the New Small Wheel detectors, two muon spectrometers in the forward regions of the detector [169]. The impact of the new small wheels is likely to be small in the main HH search channels, $b\bar{b}\gamma\gamma$, $b\bar{b}\tau^+\tau^-$, and $b\bar{b}b\bar{b}$ as forward muons are not a major factor in the final state. The major search channels are likely to continue to be statistically limited throughout Run 3, so it is possible to estimate the improvements to the analysis by scaling the luminosity by $\mathcal{L}_{\text{Run 3}}/\mathcal{L}_{\text{Run 2}} = 300/139 = 2.16$. This estimate has been done to produce expected limits in Run 3 in Figure 6.1, ignoring any changes to cross-sections and systematic uncertainties. Through luminosity scaling alone, the limits from the three analysis channels are expected to be in the range of 2.7-5.3 times the Standard Model cross-section.

Luminosity scaling can be a pessimistic predictor of the potential sensitivity improvements, because it ignores the improvements that are made in the physics object identification, calibration, and individual analysis strategies that are often made over the course of data taking. For example, Figure 6.1 also shows the expected Full Run 2 results predicted from scaling the Early Run 2 results by the final Full Run 2 integrated luminosity. The final Full Run 2 results in all three channels improved substantially over those predicted by luminosity scaling, with $b\bar{b}\gamma\gamma$ and $b\bar{b}\tau^+\tau^-$ channels both improving the 95% CL limits more than a factor of two over predictions. Improved b-tagging and τ-identification techniques have allowed the analysis channels to improve signal acceptance. For example, all analysis moved from a 70% signal efficiency b-tagging working point in Early Run 2 to a 77% signal efficiency b-tagging working point without a considerably worse mistag rate on light jets. In addition, the widespread adoption of multivariate techniques such as neural networks and boosted decision trees, and careful categorization allowed the Full Run 2 analyses to improve signal

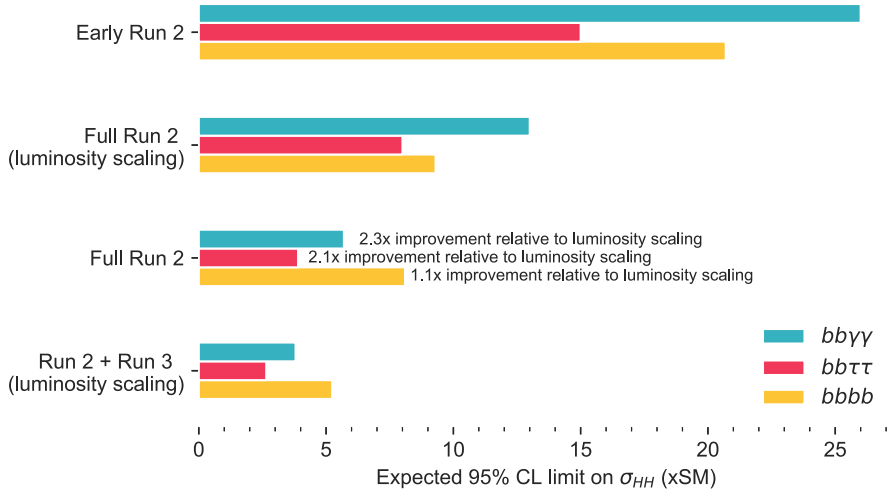

Figure 6.1: Improvements of the 95% CL upper limits on the HH cross-section between the Early Run 2 analysis (26-31fb^{-1}) and the Full Run 2 analyses (126-139fb^{-1})

extraction. Section 6.1 will discuss some ideas for improving the $b\bar{b}\gamma\gamma$ analysis sensitivity during Run 3.

6.1 Potential $b\bar{b}\gamma\gamma$ Analysis Improvements

In addition to doubling the total integrated luminosity in Run 3, increased sensitivity of the $b\bar{b}\gamma\gamma$ analysis is likely to come from improved physics object performance, and analysis strategies. This section lists a few of the many ideas being explored to improve the $b\bar{b}\gamma\gamma$ sensitivity during Run 3. Where appropriate, the expected improvements to the sensitivity are estimated using the Asimov number counting significance, defined in Equation 5.4 with the expected signal and background yields taken from Table 5.6.

6.1.1 Graph neural networks for improved b-jet identification

Improved b-jet identification algorithms can allow for increasing the signal efficiency by increasing the b-tagging working point without affecting background rejection. Recently a b-tagging algorithm that uses graph neural networks (GNNs) for object identification has been proposed [170]. This algorithm differs from the ones described in Section 3.8 in that it directly uses the particle tracks as inputs without the need for intermediate low-level algorithms. At the 77% WP DL1r has a light-jet mistag rate of 1/130, the same light-jet mistag rate with the GNN can be achieved at an 82% b-tagging efficiency. In $b\bar{b}\gamma\gamma$ any improvement in b-tagging affects the signal yields 2x as there are

two b-jets in the final state, so the signal efficiency could improve by up to 10%. An increase of 10% in the signal yields would improve the $b\bar{b}\gamma\gamma$ analysis sensitivity by about 10%.

6.1.2 Regression for improved b-jet calibrations

The regression described in Chapter 4 corrects the b-jet energies on a jet-by-jet basis, and as shown in Figure 4.17, has the potential to improve the $m_{b\bar{b}}$ resolution by 8.5% relative to the Muon-in-jet+PtReco correction that is currently being used in the $b\bar{b}\gamma\gamma$ analysis. Improving the $m_{b\bar{b}}$ resolution by incorporating the regression could help reduce the continuum backgrounds by 8.5%, which would likely increase the analysis sensitivity by about 4%.

6.1.3 Kinematic fit for improved b-jet calibrations

In addition to jet-by-jet b-jet corrections, as done with the regression and Muon-in-jet+PtReco corrections, it is also possible to perform an event-by-event b-jet correction, known as the kinematic likelihood fit. This correction uses the fact that HH production does not include any real missing transverse momentum to balance the kinematics of the $b\bar{b}$ and $\gamma\gamma$ pair as illustrated in 6.2. The benefit is that the excellent 2-3% resolution of the $H \to \gamma\gamma$ system can be used to correct the less accurately measured $H \to b\bar{b}$ system, which has a mass resolution of 15%. Such a kinematic likelihood fit has successfully been used in VH($b\bar{b}$) where is was shown to improve the $m_{b\bar{b}}$ resolution by an addition 25% over the Muon-in-jet+PtReco correction[172, 173]. Initial studies of the kinematic fit in the $b\bar{b}\gamma\gamma$ analysis have shown that the fit could lead to an additional improvement of 10% improvement in the $m_{b\bar{b}}$ resolution on top of the Muon-in-jet+PtReco corrections[171]. Assuming no background sculpting, this improvement could translate to an improvement in the $b\bar{b}\gamma\gamma$ analysis sensitivity of up to 5%.

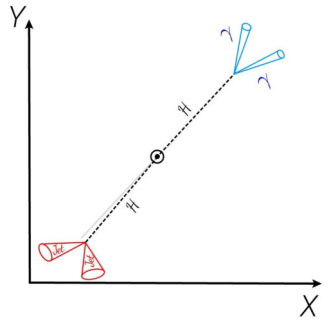

Figure 6.2: An illustration of the kinematic fit [171]

6.1.4 Multiclass MVA outputs for constraining single Higgs backgrounds

Another idea for improving the Run 3 $b\bar{b}\gamma\gamma$ analysis involves the use of multiclass BDT or NN outputs to separate the different classes of signals instead of binary classification. Figure 6.3 shows the results of a neural network trained to separate between the $b\bar{b}\gamma\gamma$ HH signal, single Higgs backgrounds, and $\gamma\gamma$ backgrounds. Reasonable separation power is achieved, with the most confusion occurring between the single Higgs and $\gamma\gamma$ backgrounds. A benefit of this approach is that it could potentially be used to constrain the single Higgs backgrounds in data at the same time as performing the $m_{\gamma\gamma}$ fit. In addition, a $t\bar{t}H$ category, for example, could be used to simultaneously provide sensitivity

to the k_t Higgs coupling, allowing for an interpretation of the results that does not assume k_t =1. However, using a multiclass MVA adds additional complexity to the categorization strategies and therefore requires careful optimization.

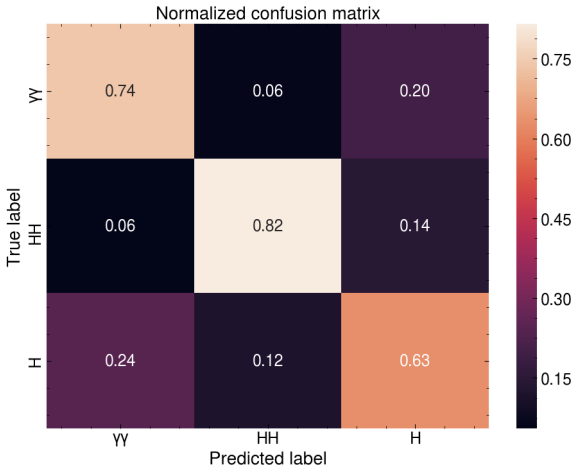

Figure 6.3: Multiclass NN predictions on the $b\bar{b}\gamma\gamma$ validation set

6.1.5 Parameterized neural networks for increased κ_λ sensitivity

Another idea for improving the signal extraction for the $b\bar{b}\gamma\gamma$ analysis in Run 3 and beyond is using a parameterized neural network to increase the sensitivity to κ_λ. The concept behind a parameterized neural network is that instead of training multiple individual networks to target specific values of a parameter, such as a particle mass, or coupling, a single neural network can be trained where the parameter of interest is used as an input variable [174]. The neural network then can learn to interpolate between parameter values, and will learn to make different predictions allowing for better signal to background discrimination depending on the value of the input parameter [174]. Figure 6.4 illustrates how the current approach and a parameterized approach would differ for the $b\bar{b}\gamma\gamma$ analysis.

Parameterized neural networks have recently successfully been used in resonant searches such as $H \to aa \to \gamma\gamma\gamma\gamma$ [175] $HH \to b\bar{b}\tau^+\tau^-$ [176]. Here the neural network was parameterized as a function of the resonant particle mass m_a or m_X, and the neural networks were shown to be able to smoothly interpolate between different resonance masses and provide strong signal to background discrimination. However, this idea has not been explored in the context of a non-resonant search where the parameter is a coupling such as κ_λ rather than a resonant particle mass. Many of the BDT input variable distributions have a rich dependence on κ_λ, shown for some example input variables in Figure 6.5, so parameterized neural networks could potentially improve the κ_λ sensitivity.

For this study, a small neural network with (100, 10, 10, 10) nodes per layer was trained with

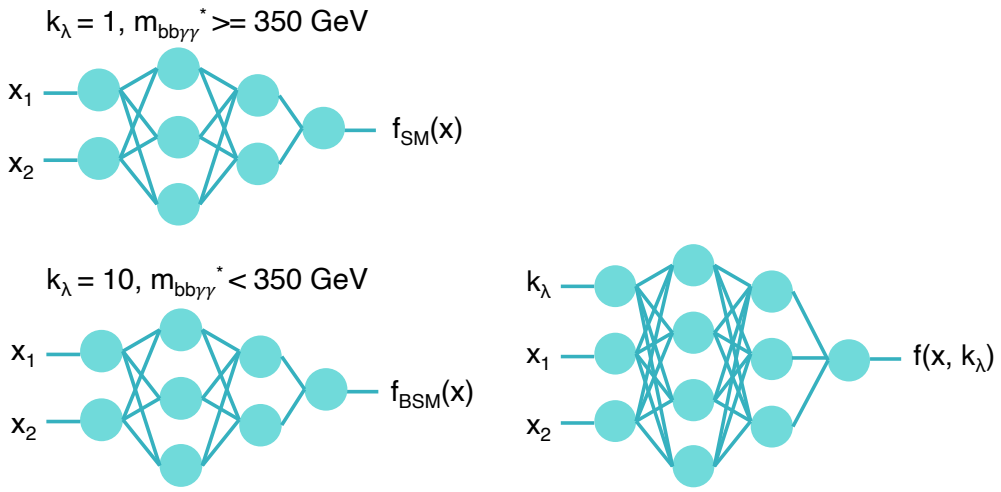

(a) (b)

Figure 6.4: (a) Current approach to the analysis, two neural networks are trained separately with $\kappa_\lambda = 1$ and $\kappa_\lambda = 10$ signal samples (b) Parameterized neural network. The neural network is trained with samples across a variety of κ_λ values and uses κ_λ is an input. The NN output changes as a function of κ_λ.

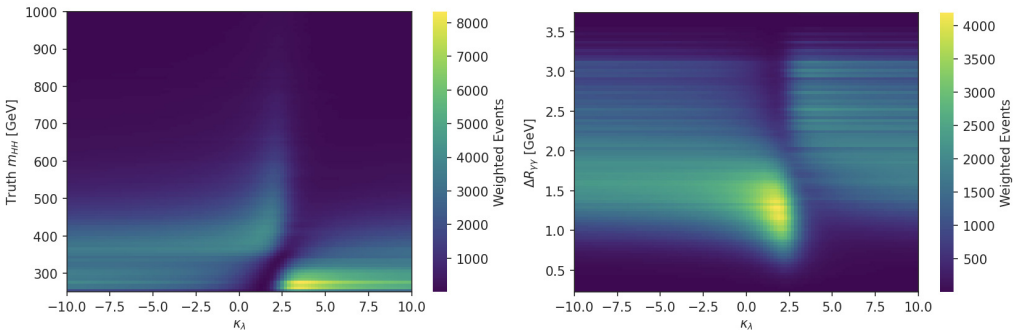

(a) (b)

Figure 6.5: 2D profiles of (a) m_{HH} and (b) $\Delta R_{\gamma\gamma}$ as a function of κ_λ, normalized in bins of κ_λ illustrating how the BDT input distributions change as a function of κ_λ. The PNN can make use of the full shape of these distributions.

signal samples generated with $\kappa_\lambda = 1$ and 10, with the $\kappa_\lambda = 1$ sample also reweighted to $\kappa_\lambda = 0$, 2, and 5.6. Three categories were generated by maximizing the Asimov significance for the SM signal and requiring 11 events in the data sideband for each category. The results were derived through an unbinned maximum likelihood fit in $m_{\gamma\gamma}$ as in Chapter 5, but using only statistical uncertainties. The 95% CL limit on the signal strength was found to be 5.61×SM, and κ_λ was constrained to the interval of [-2.16, 7.40] at 95% CL. The SM limits are 0.2% weaker than the limits derived with

the version of the analysis described in Chapter 5, where previous statistics only results on the signal strength were 5.60×SM. A large improvement in the expected constraints on κ_λ was observed relative to the previous statistics-only results that constrained κ_λ between [-2.42, 7.68].

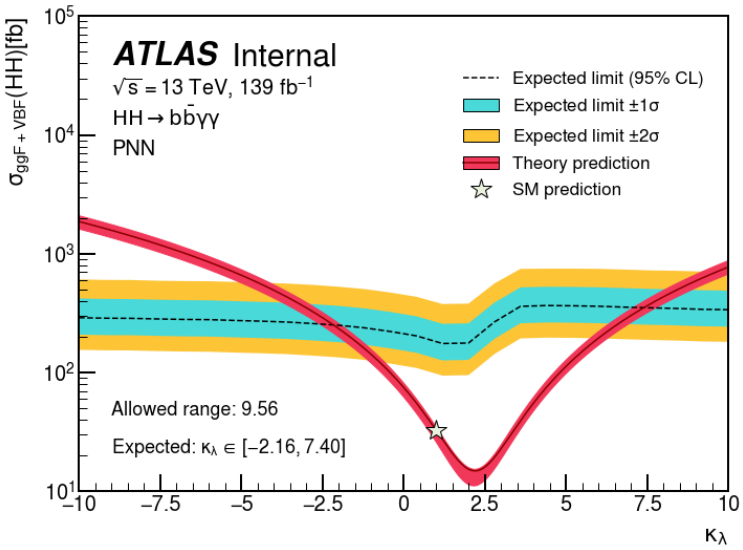

Figure 6.6: Expected cross-section limits obtained with PNN evaluated on the interval of $-10.0 < \kappa_\lambda < 10.0$ in increments of 0.4. κ_λ is expected to be constrained to [-2.16,7.40] at 95% CL, which is an improvement relative to the expected constraints on κ_λ between [-2.42, 7.68] with the $b\bar{b}\gamma\gamma$ analysis strategy presented in Chapter 5.

6.2 Discussion

This chapter explored the prospects of the $b\bar{b}\gamma\gamma$ analysis during Run 3 and explored a couple of ways in which the analysis sensitivity could be improved in the future. As the $b\bar{b}\gamma\gamma$ analysis is currently statistically limited, the greatest increases in analysis sensitivity to the HH cross-section will come from increased data, and methods that improve object identification and calibration and thereby allow for increasing the signal acceptance while maintaining background rejection rates. Creative analysis strategies such as using a multiclass MVA, or a parameterized neural network could further improve sensitivity to specific couplings in the future.

Chapter 7

Combination of Searches for HH Production

This chapter combines the results of the $b\bar{b}\gamma\gamma$ analysis presented in Chapter 5 with the results from the two other most sensitive HH analysis channels: $b\bar{b}\tau^+\tau^-$ [176] and $b\bar{b}b\bar{b}$ [103]. Combining these three orthogonal final states allows us to capitalize on the strengths of each channel, and achieve stronger constraints on SM HH production the Higgs self-coupling. In this chapter, we will first introduce the $b\bar{b}b\bar{b}$ and $b\bar{b}\tau^+\tau^-$ analysis channels and compare the analysis strategies between the three different channels. We will then introduce the statistical framework for the combination in Section 7.4, and discuss the statistical orthogonality tests in Section 7.3. Finally, we will discuss the combined results in Section 7.5 as presented in Ref. [177, 30].

7.1 Overview of analysis channels used in the combination

7.1.1 $HH \to b\bar{b}b\bar{b}$

$HH \to b\bar{b}b\bar{b}$ has the largest branching ratio (∼34%) among all HH decay channels due to the fact that $H \to b\bar{b}$ is the dominant Higgs decay channel [178]. However, as this is a fully hadronic final state, out of the three most sensitive decay channels, it also has largest background rates. These backgrounds predominantly come from QCD multi-jet production (90%) and $t\bar{t}$ production (10%). Other backgrounds, such as single Higgs production and electroweak diboson production, are negligible in comparison [103]. The QCD multi-jet and $t\bar{t}$ backgrounds both suffer from poor modelling at high p_{T} and high b-jet multiplicities, so, unlike $b\bar{b}\tau^+\tau^-$ and $b\bar{b}\gamma\gamma$, $b\bar{b}b\bar{b}$ uses an entirely data-driven background estimate.

The $b\bar{b}b\bar{b}$ channel uses the Run 2 dataset taken from 2016 to 2018 with a total integrated luminosity of 126 fb^{-1}. This is a smaller integrated luminosity than the 139fb^{-1}used by $b\bar{b}\gamma\gamma$ and $b\bar{b}\tau^+\tau^-$

because the 2015 dataset and parts of the 2016 dataset were not used due to inefficiencies with the b-jet trigger. Events must pass either the "2b1j" or "2b2j" trigger selections which both require two b-tagged jets with an E_{T} of 35 GeV. To have a low enough trigger rate, the "2b1j" trigger requires 1 jet with a minimum E_{T} of 100 GeV, and the "2b2j" trigger requires 2 additional jets with a minimum E_{T} of 35 GeV. These trigger selections have a total energy sum of 170 GeV (2×35+100) and 150 GeV(4×35) respectively. This total energy is much higher than the $b\bar{b}\gamma\gamma$ channel, which triggers on only two photons with energies of 35 and 25 GeV, so 60 GeV total energy. This difference in these total energy thresholds at the trigger level plays a key role in understanding the differences in sensitivity to κ_λ between $b\bar{b}b\bar{b}$ and the two other channels. When the self-coupling is far from the SM value of 1, the m_{HH} distribution peaks at low HH invariant masses. Because $HH \to b\bar{b}b\bar{b}$ is able to trigger less efficiently on the low m_{HH} events, this means that it is less sensitive to κ_λ. In contrast, κ_{2V}, the coupling between two Higgs bosons and two vector bosons, which can be probed through VBF HH production, has a spectrum that becomes much harder at BSM values of the coupling. As it is no longer constrained by the trigger thresholds in the high mass region, $HH \to b\bar{b}b\bar{b}$ sets the leading constraints on the κ_{2V} coupling [30].

Events selected in the $b\bar{b}b\bar{b}$ analysis must contain at least 4 central (η <2.5), b-tagged jets with $p_{\mathrm{T}} > 40$ GeV, where the four highest jets are used to reconstruct the HH decays. Additional background rejection and separation of the events into ggF and VBF channels is done by applying some additional conditions to the event kinematics, such as through cuts on the jet rapidities, the number of jets, and jet pair invariant masses described in further detail in Ref. [103]. The acceptance×efficiency is defined as:

$$Acceptance \times Efficiency = \frac{Yield}{\sigma_{HH} \times BR \times \mathcal{L}_{\mathrm{int}}} \tag{7.1}$$

The acceptance is shown for both the ggF and VBF selection in Figure 7.1. As expected, the VBF selection has a much lower acceptance than ggF, proportional to the small size of the VBF cross-section.

For defining the signal region (SR), the discriminant variable X_{HH} is used and expressed as:

$$X_{HH} = \sqrt{\left(\frac{m_{H1} - 124\ \mathrm{GeV}}{0.1\ m_{H1}}\right)^2 + \left(\frac{m_{H2} - 117\ \mathrm{GeV}}{0.1\ m_{H2}}\right)^2}. \tag{7.2}$$

It defines a contour in the (m_{H_1}, m_{H_2}) signal mass plane adapted to the simulated HH distribution and is shown in Figure 7.2. The background estimation strategy also uses this mass plane to reweight events from an alternative phase space with two b-tagged jets to the control regions which partially surround the signal region on the mass plane. The dominant uncertainties in this analysis come from the uncertainties coming from the data-driven background estimate.

The discriminant variable used by the analysis for the signal extraction is the invariant mass of

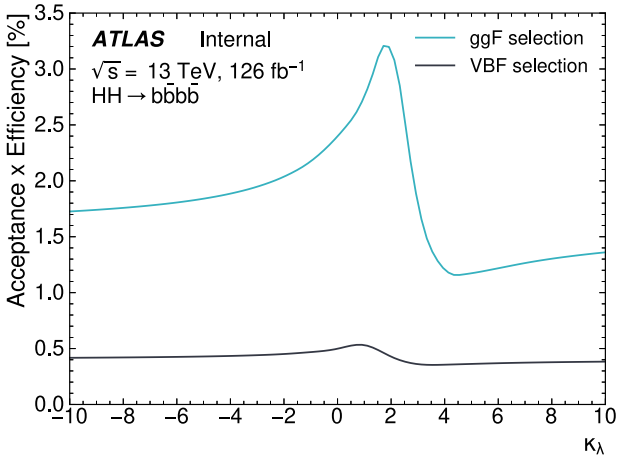

Figure 7.1: Acceptance×efficiency for each of the ggF and VBF $b\bar{b}b\bar{b}$ categories on the combined ggF and VBF HH signals

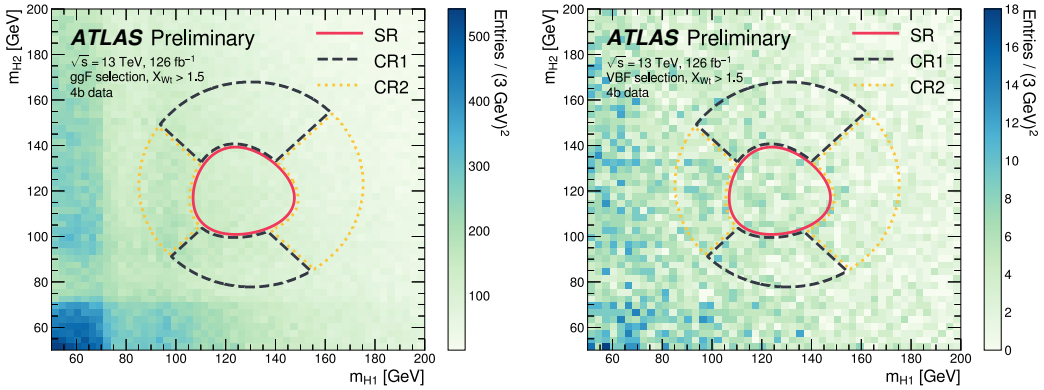

(a) ggF 4b data

(b) VBF 4b data

Figure 7.2: The mass planes of the reconstructed Higgs bosons candidates for the a ggF and b VBF signal selections in data[179].

the HH system (m_{HH}). Additional categories are generated by binning in the year of data-taking, X_{HH} and $|\Delta\eta_{HH}|$ as shown in Figure 7.3. This contrasts with $b\bar{b}\gamma\gamma$ where the signal extraction is performed in $m_{\gamma\gamma}$. As seen in Figure 7.3, the m_{HH} spectrum for the HH signal does not have a resonant peak in m_{HH} and is instead characterized through a small excess across many m_{HH} categories and bins.

The observed (expected) limit on SM non-resonant HH production cross-section via the ggF and VBF processes is 165 fb (241 fb), and the observed (expected) upper limit on signal strength is determined to be 5.4 (8.1) at 95% CL. The observed (expected) constraints on the Higgs boson

trilinear coupling modifier, κ_λ, are determined to be [-3.9, 11.1] ([-4.6, 10.8]) at 95% CL.

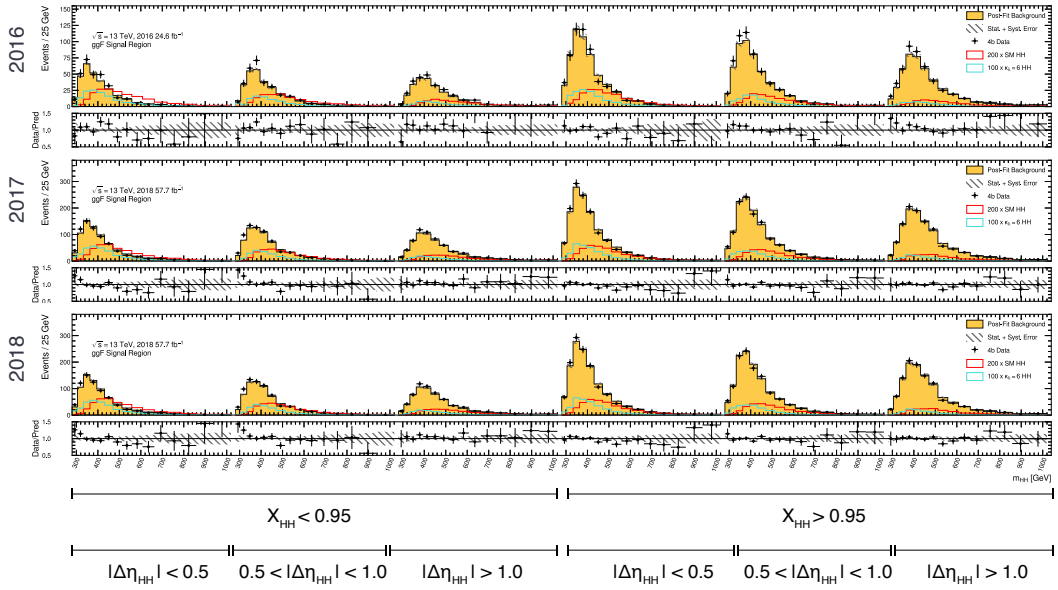

Figure 7.3: Signal extraction strategy in $HH \to b\bar{b}b\bar{b}$. Image adapted from Ref. [179].

7.1.2 $HH \to b\bar{b}\tau^+\tau^-$

The $HH \to b\bar{b}\tau^+\tau^-$ decay channel has an HH branching fraction of 7.3%. While smaller than that of $b\bar{b}b\bar{b}$, it is much larger than $b\bar{b}\gamma\gamma$. Tau leptons, however, can decay hadronically or leptonically as described in Section 3.9, increasing the complexity of this analysis. The τ leptons provide excellent QCD multi-jet background rejection. As such, $b\bar{b}\tau^+\tau^-$ lives in a comfortable middle ground, balancing a higher branching ratio with a relatively clean final state.

The $b\bar{b}\tau^+\tau^-$ search [176] selects two τ leptons and exactly two b-tagged jets. As τ leptons can decay leptonically or hadronically, the $b\bar{b}\tau^+\tau^-$ decay channel has different signal regions targeting semi-leptonic ($\tau_{\text{lep}}\tau_{\text{had}}$) and fully-hadronic ($\tau_{\text{had}}\tau_{\text{had}}$) di-$\tau$ final states. Semi-leptonic di-τ decays occur 45.6% of the time, and fully-hadronic di-τ decays occur 42% of the time [80]. In the $b\bar{b}\tau_{\text{lep}}\tau_{\text{had}}$ channel, events are required to have exactly one electron or muon, and one reconstructed hadronic τ lepton with opposite charge. In the $b\bar{b}\tau_{\text{had}}\tau_{\text{had}}$ channel, events are required to have exactly two reconstructed hadronic τ leptons with opposite charges. The $b\bar{b}\tau_{\text{lep}}\tau_{\text{had}}$ channel relies on two triggers, the Single Lepton Trigger (SLT) and the Lepton+Tau Trigger (LTT). The SLT requires an electron or muon to be reconstructed with a minimum E_{T} of 20-26 GeV. The LTT trigger has a lower threshold on the electron or muon of 14 or 17 GeV, but additionally requires a reconstructed hadronic $\tau_{\text{had-vis}}$ with a minimum p_{T} of 25 GeV. These trigger thresholds are very low compared to $b\bar{b}\gamma\gamma$ and make

the $b\bar{b}\tau_{\text{lep}}\tau_{\text{had}}$ channel especially sensitive to κ_λ. The $b\bar{b}\tau_{\text{had}}\tau_{\text{had}}$ channel triggers on single and di-$\tau_{\text{had-vis}}$triggers. The single $\tau_{\text{had-vis}}$trigger has a minimum $\tau_{\text{had-vis}}$reconstructed p_{T} between 80-160 GeV depending on the data-taking period. The di-$\tau_{\text{had-vis}}$trigger requires a minimum p_{T} of 35 and 25 GeV for the leading and subleading τs, which is similar in overall energy as $b\bar{b}\gamma\gamma$. The Acceptance×Efficiency for each channel is shown in Figure 7.4.

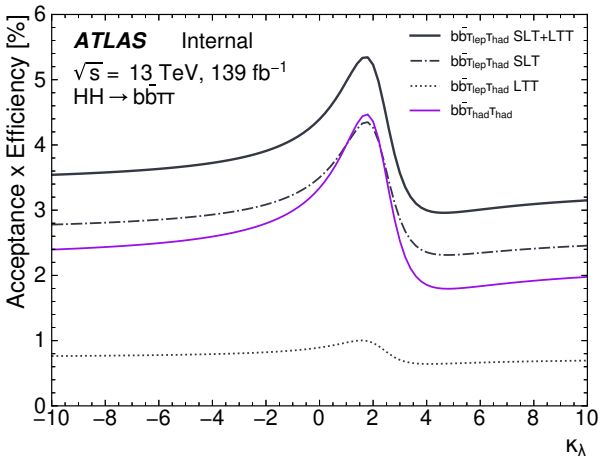

Figure 7.4: Acceptance×Efficiency for each of the $b\bar{b}\tau^+\tau^-$ categories

An electron and muon veto is applied in the $b\bar{b}\tau_{\text{had}}\tau_{\text{had}}$ channel for orthogonality with the $b\bar{b}\tau_{\text{lep}}\tau_{\text{had}}$ channel. In both the $b\bar{b}\tau_{\text{lep}}\tau_{\text{had}}$ and $b\bar{b}\tau_{\text{had}}\tau_{\text{had}}$ channels, the two b-jets are selected using the `DL1r` tagger at the 77% efficiency working point. The dominant backgrounds come from $t\bar{t}$, Z + heavy flavor (Z+HF), multi-jet, single top-quark, and single Higgs boson production. The normalization of the $t\bar{t}$ and Z+HF backgrounds are constrained with data in dedicated control regions. The contributions from misidentified τ leptons originating from quark- and gluon-initiated jets are estimated using data-driven methods for the $t\bar{t}$ and multi-jet backgrounds. This data-driven background estimation is the largest source of uncertainty in the $b\bar{b}\tau^+\tau^-$ analysis. A deep neural network is used in the $b\bar{b}\tau_{\text{lep}}\tau_{\text{had}}$ analysis and a BDT is used in the $b\bar{b}\tau_{\text{had}}\tau_{\text{had}}$ analysis and trained on Monte Carlo to differentiate between signal and background. Unlike in $b\bar{b}\gamma\gamma$ where SM and BSM samples are used, only the SM $HH \to b\bar{b}\tau^+\tau^-$ sample is used for training. The final statistical results are obtained through a fit of the BDT and DNN outputs in the $b\bar{b}\tau_{\text{had}}\tau_{\text{had}}$ and $b\bar{b}\tau_{\text{lep}}\tau_{\text{had}}$ signal regions shown in Figure 7.5.

The observed (expected) limit on SM non-resonant HH production cross-section via the ggF and VBF processes is 165 fb (241 fb), and the observed (expected) upper limit on signal strength is determined to be 4.7 (3.9) at 95% CL. The observed (expected) constraints on the Higgs boson trilinear coupling modifier, κ_λ, are determined to be [-2.4, 9.34] ([-2.0, 9.1]) at 95% CL.

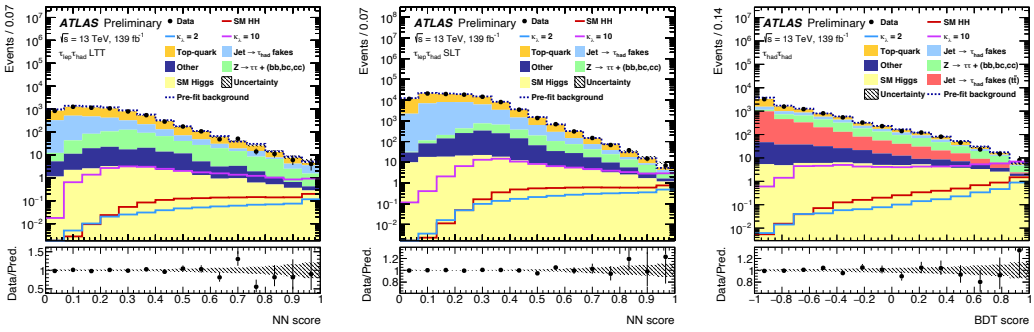

(a) $b\bar{b}\tau_{\text{lep}}\tau_{\text{had}}$ LTT (b) $b\bar{b}\tau_{\text{lep}}\tau_{\text{had}}$ SLT (c) $b\bar{b}\tau_{\text{had}}\tau_{\text{had}}$

Figure 7.5: MVA scores of the non-resonant $b\bar{b}\tau^+\tau^-$ analysis used for the signal extraction: a the NN score in the $b\bar{b}\tau_{\text{lep}}\tau_{\text{had}}$ signal region using the lepton-plus-τ_{had}triggers (LTT), b NN score in the $b\bar{b}\tau_{\text{lep}}\tau_{\text{had}}$ region using the single-lepton triggers (SLT), and c BDT score used in the $b\bar{b}\tau_{\text{had}}\tau_{\text{had}}$ signal region [176].

7.2 Comparison of the $b\bar{b}b\bar{b}$, $b\bar{b}\tau^+\tau^-$ and $b\bar{b}\gamma\gamma$ channels

While the overall branching ratios in the primary HH decay channels vary between 0.26-34%, due to the combination of backgrounds and signatures in each channel, the overall acceptances vary in similarly large magnitudes. $b\bar{b}\gamma\gamma$, the channel with the lowest branching ratio, has the highest acceptance, whereas $b\bar{b}b\bar{b}$, the channel with the highest branching ratio has the lowest overall acceptance. These are shown as a function of κ_λ in Figure 7.6. Across all channels, acceptance peaks at κ_λ values close to the κ_λ =2.2 when the m_{HH} distribution is the hardest (see Figure 6.5) and decreases at high and low values of κ_λ where the m_{HH} spectrum softens. This loss in acceptance at low m_{HH} is in part due to the triggers which have minimum p_{T} requirements on the objects. The triggers are summarized in Table 7.1. It can be noted that both $b\bar{b}\gamma\gamma$ and $b\bar{b}\tau^+\tau^-$, the two channels with the highest sensitivity to κ_λ have triggers with lower overall transverse momenta in their final states than $b\bar{b}b\bar{b}$.

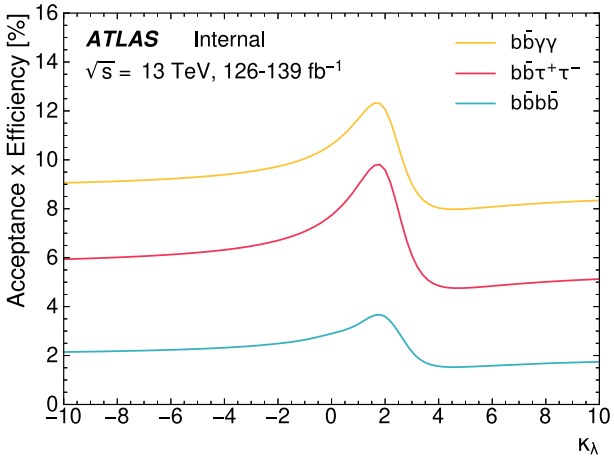

Figure 7.6: Acceptance×efficiency as a function of κ_λ for the $b\bar{b}\gamma\gamma$, $b\bar{b}\tau^+\tau^-$ and $b\bar{b}b\bar{b}$ searches. Both ggF and VBF HH signals are included.

Table 7.1: Comparison of the main characteristics of the three HH decay channels considered in this combination

	$b\bar{b}\gamma\gamma$	$b\bar{b}\tau^+\tau^-$	$b\bar{b}b\bar{b}$
Branching ratio	0.026%	7.3%	33.9%
$\mathcal{L}_{\text{int}}[\text{fb}^{-1}]$	139	139	126
Discriminant	$m_{\gamma\gamma}$	MVA outputs	m_{HH}
Main backgrounds	$\gamma\gamma$ + single Higgs	$t\bar{t}$ & Z+heavy flavour	QCD (data-driven)
Main uncertainty	Spurious signal	Data-driven background estimate	Data-driven background estimate
Trigger	E_T, γ_1 >35 GeV + E_T, γ_2 >25 GeV	$e\|\mu : E_T$ >20-26 GeV or $e\|\mu : E_T$ >14-17 GeV $+\tau_{\text{had}} : p_T > 25$ GeV or $\tau_{\text{had}} : p_T > 80-160$ GeV or $\tau_{\text{had1}} : p_T > 35$ $+\tau_{\text{had2}} : p_T > 25$ GeV	$2b : E_T$ >35 GeV $+1j : E_T > 100$ GeV or $2b : E_T$ >35 GeV + $2j : E_T$ >35 GeV

7.3 Statistical orthogonality tests

All of the HH search channels are designed to be statistically orthogonal. This allows for a straightforward combination of the individual likelihoods when creating the join likelihood discussed in

Section 7.4. All three channels use the same 77% working point from the `DL1r` tagger for selecting $b-$jets. For orthogonality $HH \to b\bar{b}b\bar{b}$ requires exactly 4 b-jets in its signal region, whereas $HH \to b\bar{b}\tau^+\tau^-$ and $HH \to b\bar{b}\gamma\gamma$ require exactly two. To ensure orthogonality between $b\bar{b}\gamma\gamma$ and $b\bar{b}\tau^+\tau^-$, $b\bar{b}\gamma\gamma$ implements a lepton veto, rejecting any events that have a lepton in them, as τ decays always contain at least one lepton. To check that the selections are indeed implemented correctly, an orthogonality check is performed by running the selections for each analysis over the same datasets and Monte Carlo simulations and checking for any overlaps in the selections. Figure 7.7 shows that no overlapping selections were found in data between each of the analysis categories.

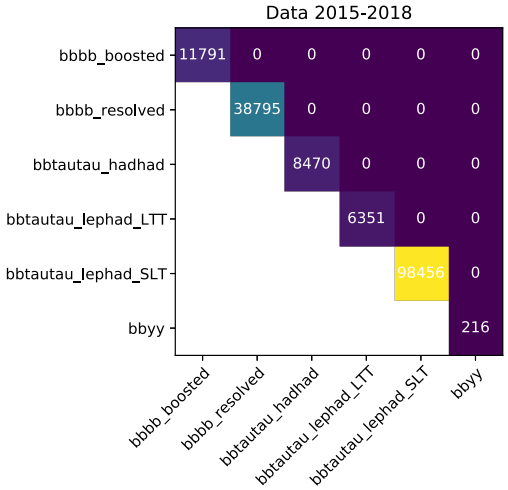

Figure 7.7: Overlap studies results on data. No overlapping events are seen in any of the categories.

7.4 Statistical framework for combination

The combination of various channels is realized by constructing a joint likelihood function that takes into account data, models, and correlated (when applicable) systematic uncertainties from all channels. Nuisance parameters that apply to all analyses are correlated, e.g. those related to the Higgs branching fractions, PDF and QCD scale uncertainties, luminosity, and detector-related and combined performance uncertainties (jet energy scale, flavour tagging uncertainties). The log-likelihood ratio and test statistic $\tilde{q_\mu}$ follow the same definitions as described in Section 5.7. In the workspaces, $b\bar{b}\gamma\gamma$ assumes the SM prediction of the cross-section at $m_H = 125.09$ GeV while $b\bar{b}\tau^+\tau^-$ uses $m_H = 125$ GeV. In this combination analysis, the $b\bar{b}\gamma\gamma$ signal is rescaled to the prediction at $m_H = 125$ GeV to be consistent with $b\bar{b}\tau^+\tau^-$ and $b\bar{b}b\bar{b}$. This brings a slight difference ($\sim 0.1\%$) in the yield of the $b\bar{b}\gamma\gamma$ signal, which has a negligible impact on the final results.

7.5 Results

7.5.1 Limits on Standard Model HH production

The double-Higgs boson analyses in the $b\bar{b}b\bar{b}$, $b\bar{b}\tau^+\tau^-$ and $b\bar{b}\gamma\gamma$ decay channels are combined in order to place constraints on the production cross-section and the Higgs boson's self-coupling. First, the value of the signal strength μ_{HH}, defined as the ratio of the double-Higgs production cross-section, including only the ggF HH and VBF HH processes, to its SM prediction of 32.7 fb is determined. To produce this result, the ratio of the ggF HH to VBF HH production cross-sections and the relative kinematic distributions are assumed to be as predicted by the SM, and the other minor production modes are neglected.

This combination yields an observed 95% CL upper limit on μ_{HH} of 2.4, with an expected upper limit of 2.9 in the absence of HH production. The limits on the signal strength obtained from the individual channels and their combination are shown in Figure 7.8. The best-fit value obtained from the fit to the data is $\mu_{HH} = -0.7 \pm 1.3$, which is compatible with the SM prediction of unity, with a p-value of 0.2.

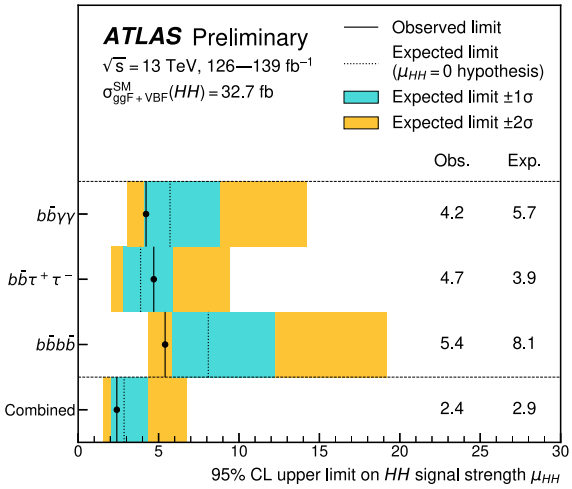

Figure 7.8: Observed and expected 95% CL upper limits on the signal strength for double-Higgs production from the $b\bar{b}b\bar{b}$, $b\bar{b}\tau^+\tau^-$ and $b\bar{b}\gamma\gamma$ decay channels, and their statistical combination. The value $m_H = 125.09$ GeV is assumed when deriving the predicted SM cross-section. The expected limit and the corresponding error bands are derived assuming the absence of the HH process and with all nuisance parameters profiled to the observed data.

From the same combination, a 95% CL upper limit on $\sigma(pp \to HH)$ of 73 fb (where only ggF HH and VBF HH processes are considered), compared with an expected limit of 85 fb assuming no HH production. When deriving the cross-section limits, the theoretical uncertainties of the predicted cross-sections are not included.

7.5.2 κ_λ cross-section scan

The cross-section limit as a function of the coupling modifier is shown in Figure 7.9 and described in Table 7.2. The signal acceptance of the HH analyses has a strong dependence on the value of κ_λ shown in Figure 7.6, determining the shapes of the exclusion limit curve. The $b\bar{b}\gamma\gamma$ channel has excellent limits on κ_λ in part due to the excellent acceptance at low m_{HH} and the analysis strategy, which targets both SM and BSM values of κ_λ. $b\bar{b}\tau^+\tau^-$ also has excellent limits on κ_λ despite only targeting SM HH signals. The $b\bar{b}b\bar{b}$ channel's cross-section limits at large values of κ_λ are not as strong as the other two channels, but close to κ_λ =2.2, where the m_{HH} spectrum is the hardest, its expected limits are just as strong as those from $b\bar{b}\gamma\gamma$.

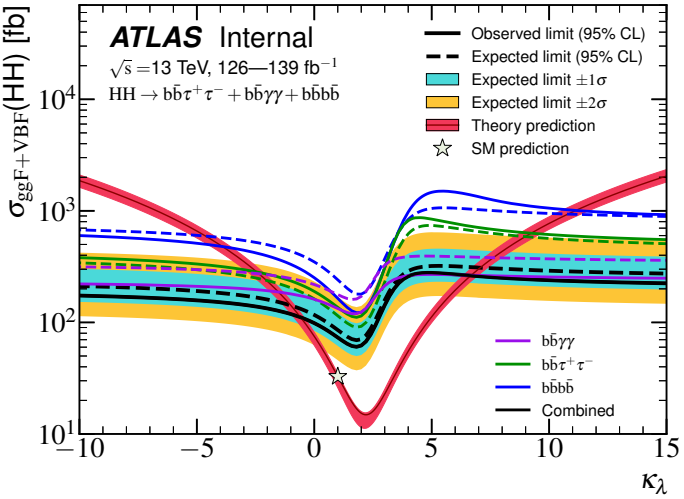

Figure 7.9: Observed and expected 95% confidence level upper limits on the non-resonant HH production cross-section as a function of κ_λ in the $b\bar{b}\gamma\gamma$, $b\bar{b}\tau^+\tau^-$ and $b\bar{b}b\bar{b}$ searches, and their statistical combination. The expected limits assume no HH production. The theory prediction curve represents the scenario where all parameters and couplings are set to their SM values except for κ_λ.

Table 7.2: Observed and expected 95% confidence level allowed ranges for κ_λ, for the $b\bar{b}\gamma\gamma$, $b\bar{b}\tau^+\tau^-$, and $b\bar{b}b\bar{b}$ searches, and their statistical combination. The expected limits assume no HH production.

	κ_λ Observed	κ_λ Expected
$b\bar{b}\gamma\gamma$	$[-1.53, 6.66]$	$[-2.34, 7.62]$
$b\bar{b}\tau^+\tau^-$	$[-2.42, 9.34]$	$[-1.98, 9.08]$
$b\bar{b}b\bar{b}$	$[-3.81, 11.32]$	$[-4.52, 10.99]$
Combined	$[-0.58, 6.65]$	$[-0.97, 7.08]$

7.5.3 κ_λ likelihood scan

Constraints on the coupling modifiers are obtained by using the values of the test statistic as a function of κ_λ in the asymptotic approximation and including the theoretical uncertainty of the cross-section predictions. The κ_λ parameterisation of NLO EW corrections in the Higgs boson decay and self-energy, as well as in single-Higgs backgrounds, is included when deriving these results, although its impact on the constraints is negligible. With these assumptions, the observed (expected) constraints at 95% CL are $-0.6 < \kappa_\lambda < 6.6$ ($-2.1 < \kappa_\lambda < 7.8$). The expected constraint is derived using the SM assumption.

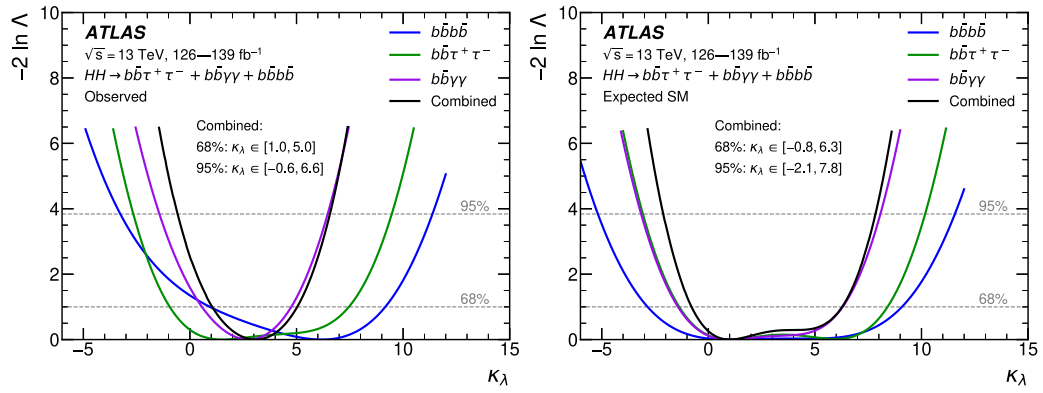

(a) (b)

Figure 7.10: Observed (a) and expected (b) value of the test statistic (-2 ln λ), as a function of the κ_λ parameter for the $HH \to b\bar{b}\gamma\gamma$ (violet), $HH \to b\bar{b}\tau^+\tau^-$ (green), $HH \to b\bar{b}b\bar{b}$ (blue) analyses and for the double-Higgs combination (black). All other coupling modifiers are fixed to their SM value.

Table 7.3: Expected and observed best fit values and 95% CL intervals of κ_λ for the $b\bar{b}\gamma\gamma$, $b\bar{b}\tau^+\tau^-$ and $b\bar{b}b\bar{b}$ searches, and their statistical combination.

Channel	Observed Value	Observed 95% CL	Expected 95% CL
$b\bar{b}\gamma\gamma$	$2.8^{+2.0}_{-2.2}$	$[-3.2, 8.1]$	$[-1.4, 6.5]$
$b\bar{b}\tau^+\tau^-$	$1.5^{+5.9}_{-2.5}$	$[-3.1, 10.2]$	$[-2.7, 9.5]$
$b\bar{b}b\bar{b}$	$6.2^{+3.0}_{-5.2}$	$[-5.2, 11.6]$	$[-3.3, 11.4]$
Combined	$3.1^{+1.9}_{-2.0}$	$[-2.1, 7.8]$	$[-0.6, 6.6]$

7.6 Comparison with Early Run 2 results and CMS

The previous combination of searches for HH pair production was performed using up to 36.1 fb^{-1} ATLAS data [167]. It includes six channels: $b\bar{b}b\bar{b}$, $b\bar{b}WW^*$, $b\bar{b}\tau^+\tau^-$, $W^+W^-W^+W^-$, $b\bar{b}\gamma\gamma$ and $W^+W^-\gamma\gamma$. The combination results were presented in terms of limits set on the HH production cross-section, σ_{HH}, for the SM $\kappa_\lambda = 1$ case and as a function of κ_λ. For the non-resonant search, the combined observed (expected) limit at 95% confidence level was 6.9 (10) times the predicted Standard Model cross-section. The observed (expected) κ_λ limit was $-5.0 < \kappa_\lambda < 12.0$ ($-5.8 < \kappa_\lambda < 12.0$). The combination presented in this chapter only combines three channels, instead of six, and achieves constraints on SM HH production that are almost 3x as strong. These gains are mostly due to improved object identification strategies and the adoption of multivariate techniques.

The CMS Collaboration also published a combination of HH searches using its full Run 2 dataset, up to 138 fb^{-1} of data [180]. The CMS combination includes the $b\bar{b}$ ZZ, Multilepton, $b\bar{b}\gamma\gamma$, $b\bar{b}\tau^+\tau^-$, and $b\bar{b}b\bar{b}$ channels. The CMS combined observed (expected) upper limit on non-resonant HH production at 95% CL is 3.4 (2.5) times the predicted Standard Model cross-section, and the observed allowed range of the self-coupling modifier κ_λ is $-1.24 \leq \kappa_\lambda \leq 6.49$ shown in Figure 7.11. A comparison of the expected results from the three leading channels, $b\bar{b}\gamma\gamma$, $b\bar{b}\tau^+\tau^-$, and $b\bar{b}b\bar{b}$ for both ATLAS and CMS is shown in Figure 7.12.

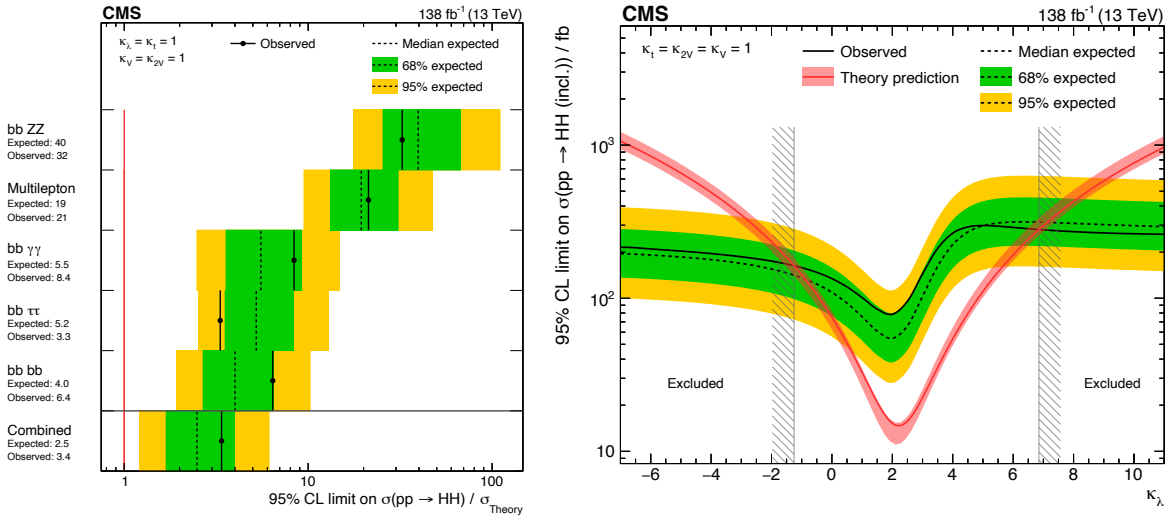

(a) (b)

Figure 7.11: CMS Run 2 combined HH results (a) SM limits on the HH cross-section (b) the 95% CL constraints on κ_λ [180]

One of the differences in the combined results relative to ATLAS is that in CMS, the $b\bar{b}b\bar{b}$ results have the best overall expected SM sensitivity. This is in part due to the use of a boosted $b\bar{b}b\bar{b}$ channel that is combined with the resolved $b\bar{b}b\bar{b}$ channel. In the boosted channel, the four b-jets from the two

Higgs decays merge and form two large radius jets. The boosted channel sets observed (expected) limits of 9.9 (5.1) times the SM cross-section [181], and the resolved channel sets limits of 3.9 (7.8) times the SM cross-section [182]. ATLAS only has a resolved $b\bar{b}b\bar{b}$ search, but its expected limits of 8.1 times the SM cross-section are comparable with the CMS resolved channel expected limits of 7.8 times the SM cross-section. Given the demonstrated high sensitivity of the boosted channel in CMS, ATLAS is considering a boosted $b\bar{b}b\bar{b}$ analysis in the future.

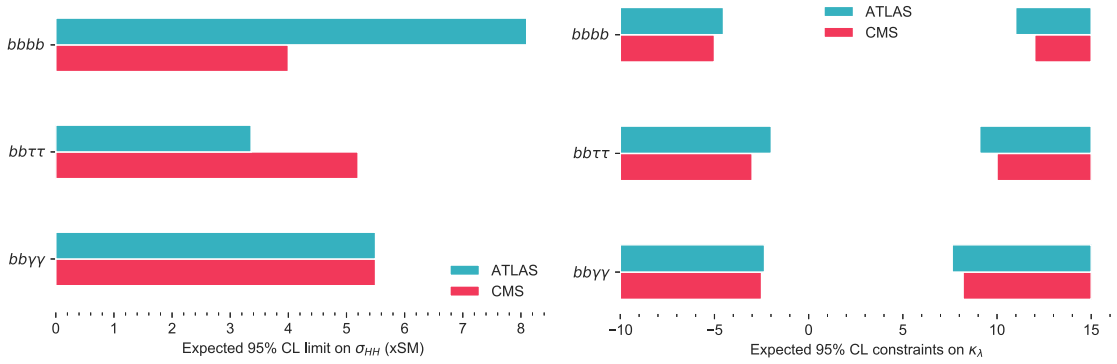

(a) (b)

Figure 7.12: Comparison of ATLAS and CMS results for $b\bar{b}b\bar{b}$, $b\bar{b}\tau^+\tau^-$, and $b\bar{b}\gamma\gamma$ (a) SM expected limits on the HH cross-section (b) the expected 95% CL constraints on κ_λ

7.7 Discussion

This chapter presented the results of the Run 2 combination of $b\bar{b}b\bar{b}$, $b\bar{b}\tau^+\tau^-$, and $b\bar{b}\gamma\gamma$ channels. The observed (expected) upper limits on μ_{HH} were 2.4 (2.9) at 95% CL. Observed (expected) constraints on κ_λ from the 95% CLs cross-section limits were placed for κ_λ between $[-0.58, 6.65]$ ($[-0.97, 7.08]$). A likelihood scan under the SM HH hypothesis was also performed, and sets observed (expected) constraints on κ_λ at 95% CL are $-0.6 < \kappa_\lambda < 6.6$ ($-2.1 < \kappa_\lambda < 7.8$). In the future, additional channels such as $bbWW$, $bbZZ$, $WWWW$, and $WW\gamma\gamma$ will likely be combined for additional sensitivity to HH production.

Although not discussed in detail in this chapter, recently a combination of the $b\bar{b}b\bar{b}$, $b\bar{b}\tau^+\tau^-$ and $b\bar{b}\gamma\gamma$ channels with single Higgs processes from the $\gamma\gamma$, ZZ, WW, $\tau\tau$, and $b\bar{b}$ final states was performed [30]. This combination benefits from both the single Higgs sensitivity to κ_λ and also has the power to vary other couplings such as k_t, κ_b, κ_V, and κ_τ simultaneously. The results of this combined κ_λ likelihood scan are shown in Figure 7.13. The results from this combined likelihood scan under the SM HH hypothesis sets observed (expected) constraints on κ_λ at 95% CL are $-1.4 < \kappa_\lambda < 6.1$ ($-2.2 < \kappa_\lambda < 7.7$)While HH channels have the best sensitivity to κ_λ, the

combined results allow for a more generic interpretation.

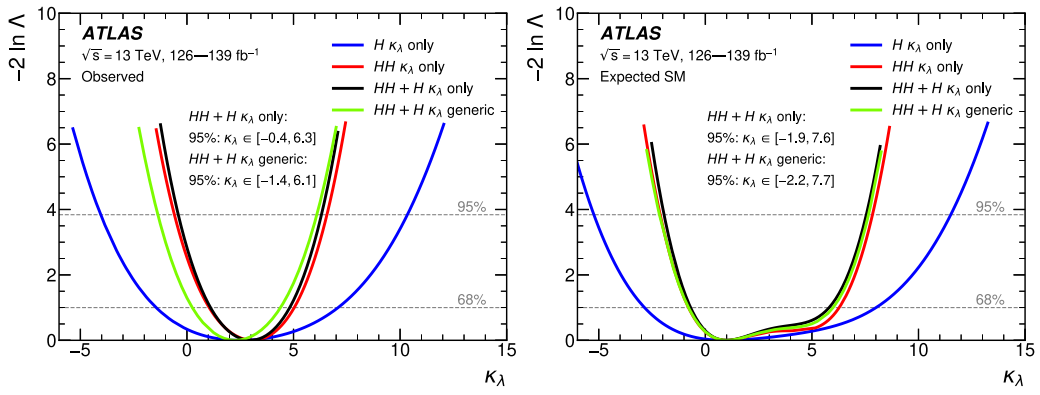

(a) (b)

Figure 7.13: Observed (a) and expected (b) value of the test statistic ($-2\ln\Lambda$), as a function of the κ_λ parameter for the single-Higgs (blue) and HH analyses (red), and their combination (black) derived from the combined single-Higgs and double-Higgs analyses with all other coupling modifiers fixed to unity. The combined result for the generic model (free floating κ_t, κ_b, κ_V and κ_τ) is also superimposed (green curve). The observed best fit value of κ_λ is slightly shifted for the generic model result relative to the other models due to its correlation with κ_b, κ_t, and κ_τ parameters, whose best fit values are slightly below, but compatible with, unity.

Chapter 8

HH Prospects at the HL-LHC

8.1 The HL-LHC Upgrade

The High Luminosity LHC (HL-LHC) project plans to upgrade the LHC accelerators to increase the peak luminosity of pp collisions by a factor of five with respect to Run 2 of the LHC, and ultimately to deliver 3000–4000 fb^{-1} of integrated luminosity at $\sqrt{s} = 14\,\text{TeV}$ [21]. This upgrade is scheduled for the mid-2020's after the conclusion of the Run 3 data-taking period. The HL-LHC is expected to begin operation in the late 2020's as shown in Figure 8.1. The HL-LHC upgrade will consist of an upgrade to both the accelerator, as well as the LHC detectors. On the accelerator front, the focusing magnets and beam optics at the ATLAS and CMS collision points will be upgraded to allow for the increase in luminosity. New collimators will be installed to improve the beam quality. The accelerators within the LHC injector chain will also undergo improvements. Within ATLAS, data acquisition and trigger systems will be upgraded to cope with the increased rate of the HL-LHC, but the largest upgrade will come from the installation of a brand new all-silicon Inner Tracker (the ITk) which will be discussed in Chapter 9. This increased luminosity will allow for the measurement of rare processes like HH production. This chapter explores the expected physics reach for HH searches and measurements of the Higgs self-coupling at the HL-LHC as presented in Ref. [183, 184].

Figure 8.1: Expected timeline of Run 2, Run 3, and the HL-LHC along with the total number of HH and single Higgs bosons expected to be recorded by the end of each data-taking period.

8.2 Motivation

Previous ATLAS HL-LHC projections of the $b\bar{b}b\bar{b}$, $b\bar{b}\tau^+\tau^-$ and $b\bar{b}\gamma\gamma$ final states and their statistical combination were performed using extrapolations of the early Run 2 measurements with $24.3\,\text{fb}^{-1}$ of data for $b\bar{b}b\bar{b}$ and $36.1\,\text{fb}^{-1}$ of data for $b\bar{b}\tau^+\tau^-$, both at $\sqrt{s} = 13\,\text{TeV}$. A dedicated analysis using truth information from simulated samples, smeared to emulate the expected ATLAS detector response at the HL-LHC, was developed to estimate prospects for $b\bar{b}\gamma\gamma$ [185]. Including systematic uncertainties, the combined expected significance for the observation of the SM HH production was found to be $3.0\,\sigma$, and the signal strength relative to the SM expectation was expected to be measured with an accuracy of 40%. The Higgs boson trilinear self-coupling modifier ($\kappa_\lambda \equiv \lambda_{HHH}/\lambda^{\text{SM}}_{HHH}$) was expected to be constrained to $0.25 \leq \kappa_\lambda \leq 1.9$ at $1\,\sigma$ confidence level, and $-0.4 \leq \kappa_\lambda \leq 7.3$ at $2\,\sigma$ confidence level.

Since the Early Run 2 projections, all three analysis channels have been updated substantially, as described in Chapter 6. To incorporate these advances in analysis strategy, this chapter presents an updated combination of the HL-LHC projection studies of the $b\bar{b}\gamma\gamma$, $b\bar{b}\tau^+\tau^-$ and $b\bar{b}b\bar{b}$ final states [183, 184] assessed through extrapolation of the latest available analyses based on the full Run 2 dataset with an integrated luminosity of $139\,\text{fb}^{-1}$ at $\sqrt{s} = 13\,\text{TeV}$. The object reconstruction and identification efficiencies are assumed to be identical between the projections and the considered Run 2 analyses with consideration of the detector upgrades [186]. Other aspects, including different triggers, the increased pile-up level, and improved analysis strategies could affect the projections, but they are not considered.

8.3 Extrapolation procedure

The $HH \to b\bar{b}\gamma\gamma$, $b\bar{b}\tau^+\tau^-$ and $b\bar{b}b\bar{b}$ search channels are projected [183, 184] to the HL-LHC following the procedures below. The projections are combined using the same extended statistical framework based on the profile likelihood ratio [155] described in Section 7.4.

First, all signal and background distributions are scaled by a multiplicative factor, which is the ratio between the target integrated luminosity of $3000\,\text{fb}^{-1}$ at the HL-LHC to the integrated luminosity of $139\,\text{fb}^{-1}$ in Run 2.

Next, the change of cross-sections, due to the higher center-of-mass energy of $\sqrt{s} = 14$ TeV at the HL-LHC, is accounted for with additional scaling factors summarized in Table 8.1 and illustrated in Figure 8.2. The cross-sections of the HH signal and single Higgs boson backgrounds are all scaled following the recommendations [187] from the LHC Higgs Working Group. The remaining backgrounds are scaled by a factor of 1.18 to account for the expected increase in gluon-luminosity at the HL-LHC. In the Run 2 $b\bar{b}\tau^+\tau^-$ analysis, the normalization of simulated Z+HF and $t\bar{t}$ backgrounds are determined from data. This results in an additional multiplicative factor of 1.37 for the Z+HF background, while the $t\bar{t}$ normalization does not change as the multiplicative factor is consistent

with unity. The combined results are obtained assuming a Higgs boson mass of $m_H = 125.00\,\text{GeV}$. In the $b\bar{b}\gamma\gamma$ channel projection, the mass of the Higgs boson is shifted from the Run 2 analysis value of 125.09 GeV to 125.00 GeV. The change in the mass assumption has a negligible impact on the final sensitivity.

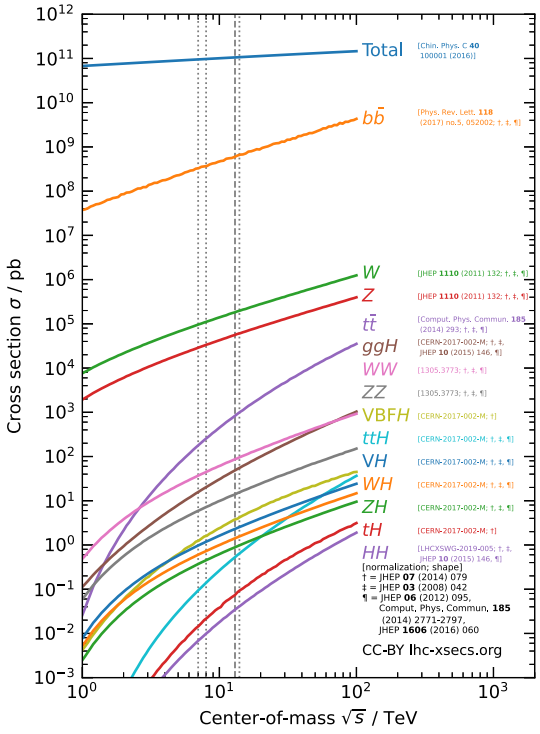

Figure 8.2: Expected changes to overall cross-sections as a function of increased center-of-mass energy. The dotted lines correspond to 7, 8 and 14 GeV, and the dashed line corresponds to 13 TeV. Image from [188].

The projected results in individual analyses are obtained by considering different scenarios of systematic uncertainties. In the baseline scenario, the systematic uncertainties are adjusted following the latest recommendations for HL-LHC projections [189]. The expected uncertainty on the integrated luminosity ($\mathcal{L}$) of the full HL-LHC dataset is 1%, while the Run 2 uncertainty is 1.7 %. This improvement is expected to come from detector upgrades to the luminosity and beam conditions motoring systems. Theoretical systematic uncertainties are reduced by a factor of two relative to those used in the Run 2 analyses, under the assumption of continued theory advances, moving towards higher order QCD and EW corrections, and more accurate estimates of the parton density functions. The statistical components of the experimental uncertainties are scaled according to the increase of the integrated luminosity by $1/\sqrt{\mathcal{L}}$ until the intrinsic detector limitations are reached. The intrinsic detector limitations are projected with the expected performance of the detector upgrades, e.g. ITk,

Table 8.1: Scale factors applied to the HH signal and background processes in the Run 2 $b\bar{b}b\bar{b}$, $b\bar{b}\tau^+\tau^-$ and $b\bar{b}\gamma\gamma$ analyses to account for the change in cross-sections due to the increase of centre-of-mass energy from $\sqrt{s} = 13\,\text{TeV}$ to $\sqrt{s} = 14\,\text{TeV}$ at the HL-LHC.

Process	Scale factor
Signals	
ggF HH	1.18
VBF HH	1.19
Backgrounds	
ggF H	1.13
VBF H	1.13
WH	1.10
ZH	1.12
$t\bar{t}H$	1.21
Others	1.18

taken into account. The Monte Carlo statistical uncertainties are neglected, as done in the previous projection studies [185]. The detector-limited components are either kept the same or scaled, taking into account detector and performance upgrades. In the $b\bar{b}\gamma\gamma$ channel, the uncertainty on the measured value of the Higgs boson mass is reduced from 240 MeV [35] to 20 MeV [187]. The spurious signal uncertainty from the Run 2 analysis is removed, assuming that background modeling strategies will improve sufficiently at the HL-LHC [185]. In the $b\bar{b}b\bar{b}$ analysis, the primary experimental uncertainties come from the data-driven background estimate. The bootstrap uncertainty quantifies the impact of varying initial conditions and the limited size of training samples used in the background estimate and is expected to be reduced by a factor of 2 due to increased training sample size. The shape uncertainty quantifies the impact of the arbitrary choice in deciding to derive the background estimate in one control region with respect to the other and is expected to remain the same due to no change in analysis strategy. Across all Run 2 HH analyses [190, 176], a reweighting procedure (described in Section 5.3) of the simulated ggF and VBF HH samples is performed to create discriminant distributions for a set of κ_λ values, and a non-closure uncertainty is accounted for this procedure. In their HL-LHC projections, the non-closure uncertainty is removed, assuming that computing power will be sufficient to generate signal samples for all relevant κ_λ values. The systematic uncertainties are modified using scale factors that multiply the magnitudes of the nominal Run 2 systematic uncertainties. These scale factors are summarized in Table 8.2.

As in the Run 2 HH combination discussed in Chapter 7, the likelihood functions from each channel are multiplied to produce a combined likelihood function. The various searches can then be simultaneously fit to the data to constrain the parameters of interest. All signal regions considered in the combined fit are orthogonal due to different selection criteria, or they have a negligible number

of overlapping events. The extrapolated systematic uncertainties are correlated between the $b\bar{b}\gamma\gamma$, $b\bar{b}\tau^+\tau^-$, and $b\bar{b}b\bar{b}$ search channels following the same strategies as in Ref. [177].

Table 8.2: Summary of HL-LHC scale factors for relevant systematic uncertainties according to the recommendations of the ATLAS conventions for HL-LHC projections [189]. A "*" indicates that the uncertainty is considered by the corresponding analysis.

Source	**Scale factor**	$\boldsymbol{b\bar{b}\gamma\gamma}$	$\boldsymbol{b\bar{b}\tau^+\tau^-}$	$\boldsymbol{b\bar{b}b\bar{b}}$
Experimental Uncertainties				
Luminosity	0.6	*	*	
b-jet tagging efficiency	0.5	*	*	*
c-jet tagging efficiency	0.5	*	*	*
Light-jet tagging efficiency	1.0	*	*	*
Jet energy scale and resolution, E_T^{miss}	1.0	*	*	*
κ_λ reweighting	0.0	*	*	*
Photon efficiency (ID, trigger, isolation efficiency)	0.8	*		
Photon energy scale and resolution	1.0	*		
Spurious signal	0.0	*		
Value of m_H	0.08	*		
τ_{had} efficiency (statistical)	0.0		*	
τ_{had} efficiency (systematic)	1.0		*	
τ_{had} energy scale	1.0		*	
Fake-τ_{had} estimation	1.0		*	
MC statistical uncertainties	0.0		*	
Background bootstrap uncertainty×0.5			*	
Background shape uncertainty	1.0			*
Theoretical Uncertainties	0.5	*	*	*

To provide an envelope for interpreting the results, three additional uncertainty scenarios are considered beyond the baseline configuration described above in the text. The results, presented in Section 8.4, are obtained considering the following four scenarios:

- No systematic uncertainties.
- Baseline: systematic uncertainties are scaled as in Table 8.2.
- Theoretical uncertainties halved: theoretical systematic uncertainties are scaled as in Table 8.2, while experimental systematic uncertainties are assumed to keep their Run 2 values.
- Run 2 systematic uncertainties: both the theoretical and experimental systematic uncertainties are assumed to keep their Run 2 values.

8.4 Results

8.4.1 Limits on Standard Model HH production

The expected HH signal significance and precision on the measured signal strength in the SM hypothesis are summarized in Table 8.3, assuming different uncertainty scenarios. In the baseline scenario, a significance of $3.4\,\sigma$is expected to be reached when combining the $b\bar{b}\gamma\gamma$, $b\bar{b}\tau^+\tau^-$, and $b\bar{b}b\bar{b}$ decay channels. The signal strength relative to the SM prediction is expected to be measured with an accuracy of $^{+34}_{-31}$%. Without systematic uncertainties, the expected significance is $4.9\,\sigma$, and the SM signal strength is expected to be probed with a relative error of ± 23%. Under the 'Theoretical uncertainties halved' and 'Run 2 systematic uncertainties' scenarios, the expected significance decreases to $2.1\,\sigma$ and $1.9\,\sigma$, respectively. In these two uncertainty configurations, the SM signal strength is expected to be measured with an accuracy larger than 50%.

Table 8.3: Projected significance and signal strength precision of the SM HH signal combining the $b\bar{b}\gamma\gamma$, $b\bar{b}\tau^+\tau^-$ and $b\bar{b}b\bar{b}$ channels at $3000\,\text{fb}^{-1}$ and $\sqrt{s} = 14\,\text{TeV}$ for the four uncertainty scenarios. The significances for individual $b\bar{b}\gamma\gamma$, $b\bar{b}\tau^+\tau^-$, and $b\bar{b}b\bar{b}$ channels are also summarized.

	Significance [σ]				Combined signal
Uncertainty scenario	$b\bar{b}\gamma\gamma$	$b\bar{b}\tau^+\tau^-$	$b\bar{b}b\bar{b}$	Combination	strength precision [%]
No syst. unc.	2.3	4.0	1.8	4.9	$-23/+23$
Baseline	2.2	2.8	0.99	3.4	$-31/+34$
Theoretical unc. halved	1.1	1.7	0.65	2.1	$-49/+51$
Run 2 syst. unc.	1.1	1.5	0.65	1.9	$-57/+68$

In the $b\bar{b}\gamma\gamma$ channel, one of the main limiting factors to the sensitivity arises from the spurious signal systematic uncertainty associated with the choice of the functional form used for modeling the continuum background. The baseline scenario assumes that the $b\bar{b}\gamma\gamma$ spurious signal systematic uncertainty will be 0 at the HL-LHC thanks to improved background modeling strategies. The effect of different levels of spurious signal uncertainty on the baseline scenario was studied in the $b\bar{b}\gamma\gamma$ projections [183]. In the most pessimistic projection, where this uncertainty at the HL-LHC is scaled as the continuum background, and it is 25 times the current Run 2 value, the combined significance of the baseline scenario is reduced by 10 %. If the spurious signal uncertainty is less than 4 times the current Run 2 value, which is the level suggested by studies of background template-enhancing techniques, the combined significance is reduced by less than 1 %.

In the $b\bar{b}\tau^+\tau^-$ channel, one of the main limiting factors to the sensitivity arises from the statistical uncertainty associated with the Monte Carlo simulated samples [184]. This uncertainty is included in the 'Theoretical uncertainties halved' and 'Run 2 systematic uncertainties' scenarios, but not in the

'Baseline' scenarios. If this statistical uncertainty is neglected in the 'Run 2 systematic uncertainties' scenario, the combined significance for that scenario improves from $1.7\,\sigma$ to $2.3\,\sigma$.

In the $b\bar{b}b\bar{b}$ channel, the main limiting factors to the sensitivity come from the data-driven background estimate. This uncertainty is included in all scenarios except for the 'Statistics only' scenario. In the optimistic case where the bootstrap and shape uncertainties are scaled by 0.2 and 0.2, instead of 0.5 and 1.0 the combined significance for the 'Baseline' scenario improves from $0.6\,\sigma$ to $1.4\,\sigma$.

In the baseline scenario, the dominant source of uncertainty affecting the combined results is the 100 % theoretical uncertainty on the ggF, VBF, and W-associated single Higgs boson production modes due to the imperfect modeling of additional heavy-flavour jet radiation in these processes [163, 191, 165]. The second largest uncertainty comes from the theoretical uncertainty on the HH cross-section.

The expected significance is also estimated in cases where the Higgs boson self-coupling may be different from the SM prediction of $\kappa_\lambda = 1$. For each κ_λ value, the HH significance scales with the HH cross-section and the product of the analysis acceptance times efficiency [177]. Figure 8.3 shows the HH significance as a function of κ_λ for all four uncertainty scenarios. The significance is estimated on Asimov datasets produced assuming the signal plus background hypothesis, where the signal is generated with a κ_λ value under test. In the baseline scenario, evidence for the HH production ($3\,\sigma$) is expected at the HL-LHC if $\kappa_\lambda < 1.2$ or $\kappa_\lambda > 4.8$, while observation ($5\,\sigma$) is expected if $\kappa_\lambda < 0.0$ or $\kappa_\lambda > 5.8$.

To further characterize the analysis sensitivity, the projected 95% confidence level (CL) limits on the SM HH signal strength have been evaluated for the various systematic uncertainty scenarios assuming the absence of Higgs boson pair production. They are shown in Figure 8.4, and summarized for $b\bar{b}\gamma\gamma$, $b\bar{b}\tau^+\tau^-$, $b\bar{b}b\bar{b}$, and their combination in Table 8.4. The SM HH production is expected to be excluded at more than 99 % CL in the 'No systematic uncertainty' and 'Baseline' scenarios, and at 96.5 % CL in the 'Theory uncertainty halved' scenario. In the 'Run 2 systematic uncertainties' scenario, the 95% CL upper limit on the HH signal strength is set at 1.1.

Figure 8.5 presents the significance and the 95% CL limit on the SM HH signal strength as a function of the integrated luminosity from $1000\,\text{fb}^{-1}$ to $3000\,\text{fb}^{-1}$ at $\sqrt{s} = 14\,\text{TeV}$ at the HL-LHC assuming the four uncertainty scenarios. The 'Run 2 systematic uncertainties' and the 'Theory uncertainty halved' results do not show a large dependence on the increased integrated luminosity, meaning that such scenarios are already expected to be dominated by the effect of systematic uncertainties at $1000\,\text{fb}^{-1}$. In contrast, results in the 'No systematic uncertainties' and the 'Baseline' scenarios improve more substantially with increasing integrated luminosity.

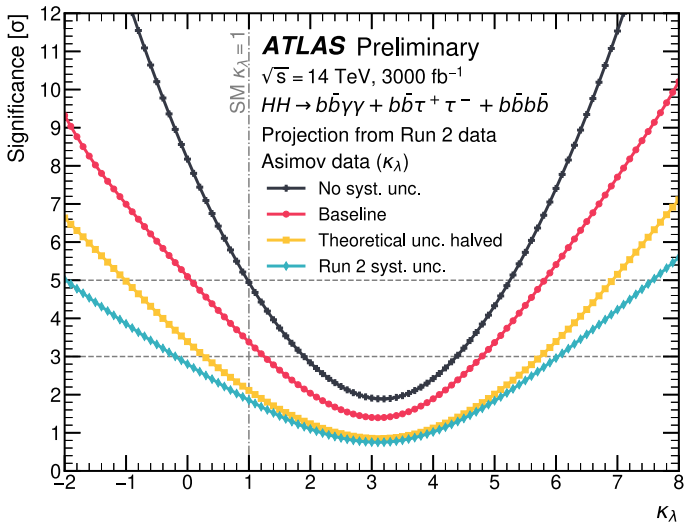

Figure 8.3: Projected HH significance for different κ_λ hypotheses at $\sqrt{s} = 14\,\text{TeV}$, $3000\,\text{fb}^{-1}$ at the HL-LHC assuming the four different uncertainty scenarios described in the text. The significance is estimated on Asimov datasets produced under the signal plus background hypothesis, where the signal is generated with the κ_λ value under test. Dashed horizontal lines correspond to $3\,\sigma$ and $5\,\sigma$. The dashed vertical line indicates the SM hypothesis of $\kappa_\lambda = 1$.

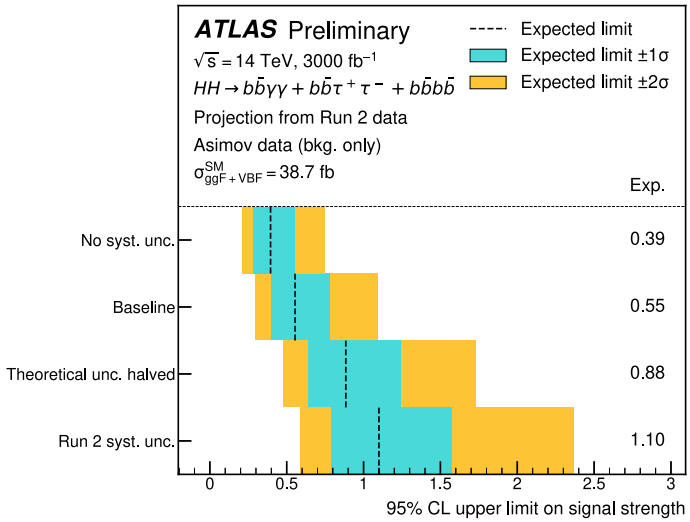

Figure 8.4: Projected 95 % CL upper limits on the expected signal strength for SM HH production when considering an integrated luminosity of $3000\,\text{fb}^{-1}$ at $\sqrt{s} = 14\,\text{TeV}$ for different uncertainty scenarios. The limits are derived assuming no HH production.

Table 8.4: Projected 95 % CL upper limits on the signal strength for SM HH production combining the $b\bar{b}\gamma\gamma$, $b\bar{b}\tau^+\tau^-$ and $b\bar{b}b\bar{b}$ channels when considering an integrated luminosity of 3000 fb^{-1} at $\sqrt{s} = 14$ TeV for different uncertainty scenarios. The upper limits for $b\bar{b}\gamma\gamma$, $b\bar{b}\tau^+\tau^-$, and $b\bar{b}b\bar{b}$ are also included. The limits assume no HH production.

	Signal strength 95% CL upper limit			
Uncertainty scenario	$b\bar{b}\gamma\gamma$	$b\bar{b}\tau^+\tau^-$	$b\bar{b}b\bar{b}$	Combination
No syst. unc.	0.86	0.49	1.1	0.39
Baseline	0.93	0.71	2.0	0.55
Theoretical unc. halved	1.7	1.1	3.1	0.88
Run 2 syst. unc.	1.9	1.4	3.4	1.1

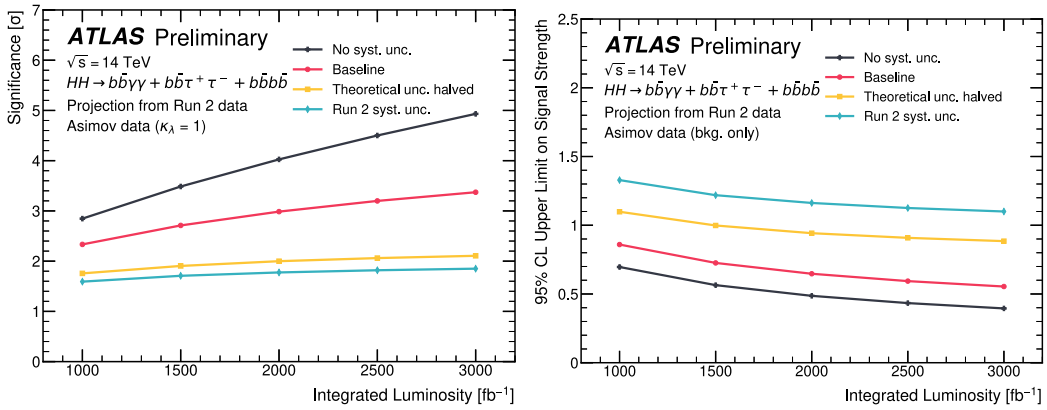

(a) Significance

(b) 95% upper limit

Figure 8.5: Significance (a) and 95 % CL upper limits (b) on the expected signal strength for SM HH production projected to 1000–3000 fb^{-1} at $\sqrt{s} = 14$ TeV at the HL-LHC assuming the four different uncertainty scenarios described in the text. The significance is evaluated using a signal plus background Asimov dataset generated under the SM hypothesis. The upper limits are derived using background-only Asimov data, where no HH production is assumed.

8.4.2 κ_λ likelihood scan

The κ_λ confidence intervals derived from a likelihood-ratio scan are presented. Several maximum likelihood fits are conducted using an Asimov dataset constructed under the SM hypothesis of $\kappa_\lambda = 1$. Values of the negative log-profile-likelihood ratio as a function of κ_λ for all four uncertainty scenarios are shown in Figure 8.6. The corresponding $1\,\sigma$ and $2\,\sigma$ confidence intervals are summarized in Table 8.5. In the baseline uncertainty scenario, the allowed $1\,\sigma$ ($2\,\sigma$) confidence interval for κ_λ is expected to be $[0.5, 1.6]$ ($[0.0, 2.5]$). With no systematic uncertainties, they are further reduced to $[0.7, 1.4]$ ($[0.3, 1.9]$). Figure 8.8 presents the individual contributions from the $b\bar{b}\gamma\gamma$, $b\bar{b}\tau^+\tau^-$ and $b\bar{b}b\bar{b}$ channels to the combined results assuming the various uncertainty scenarios.

It is worth noting that the $b\bar{b}\gamma\gamma$ and $b\bar{b}b\bar{b}$ likelihood scans does not exhibit the double minimum feature that occurs in the $b\bar{b}\tau^+\tau^-$ analysis. This stems from the fact that the search for $HH \to b\bar{b}\gamma\gamma$ has different categories based on $m^*_{b\bar{b}\gamma\gamma}$ and can therefore distinguish ambiguous κ_λ values that are characterized by similar yields, but different HH mass distributions. $b\bar{b}b\bar{b}$ extracts the signal based on m_{HH}. In $b\bar{b}\gamma\gamma$, the high mass, SM-like categories have strong sensitivity to the $\kappa_\lambda = 1$ sample, but are also unable to reject events near $\kappa_\lambda = 5$ [183]. The low mass, BSM-like categories are less sensitive to signal when κ_λ is close to 1, and more sensitive to signal where κ_λ is far from 1. Combining the sensitivities of the two categories breaks the degeneracy that would have occurred if the $b\bar{b}\gamma\gamma$ analysis had only used a single inclusive mass region.

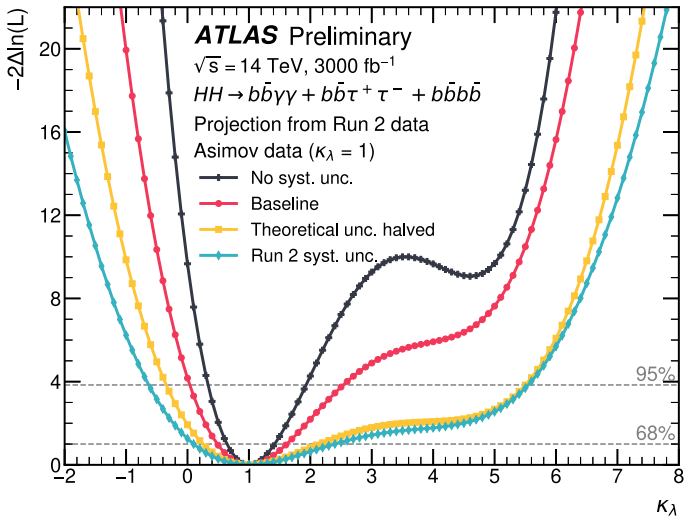

Figure 8.6: Negative log-profile-likelihood ratio as a function of κ_λ evaluated on an Asimov dataset constructed under the SM hypothesis of $\kappa_\lambda = 1$, projected to $3000\,\text{fb}^{-1}$ and $\sqrt{s} = 14\,\text{TeV}$, assuming the four uncertainty scenarios described in the text. Dashed horizontal lines correspond to $1\,\sigma$ and $2\,\sigma$ confidence intervals.

Table 8.5: Projected confidence intervals for κ_λ evaluated on an Asimov dataset constructed under the SM hypothesis of $\kappa_\lambda = 1$, combining the $b\bar{b}\gamma\gamma$, $b\bar{b}\tau^+\tau^-$ and $b\bar{b}b\bar{b}$ channels at $3000\,\text{fb}^{-1}$ and $\sqrt{s} = 14\,\text{TeV}$, assuming the four uncertainty scenarios.

Uncertainty scenario	κ_λ 68% CI	κ_λ 95% CI
No syst. unc.	$[0.7, 1.4]$	$[0.3, 1.9]$
Baseline	$[0.5, 1.6]$	$[0.0, 2.5]$
Theoretical unc. halved	$[0.3, 2.2]$	$[-0.3, 5.5]$
Run 2 syst. unc.	$[0.1, 2.4]$	$[-0.6, 5.6]$

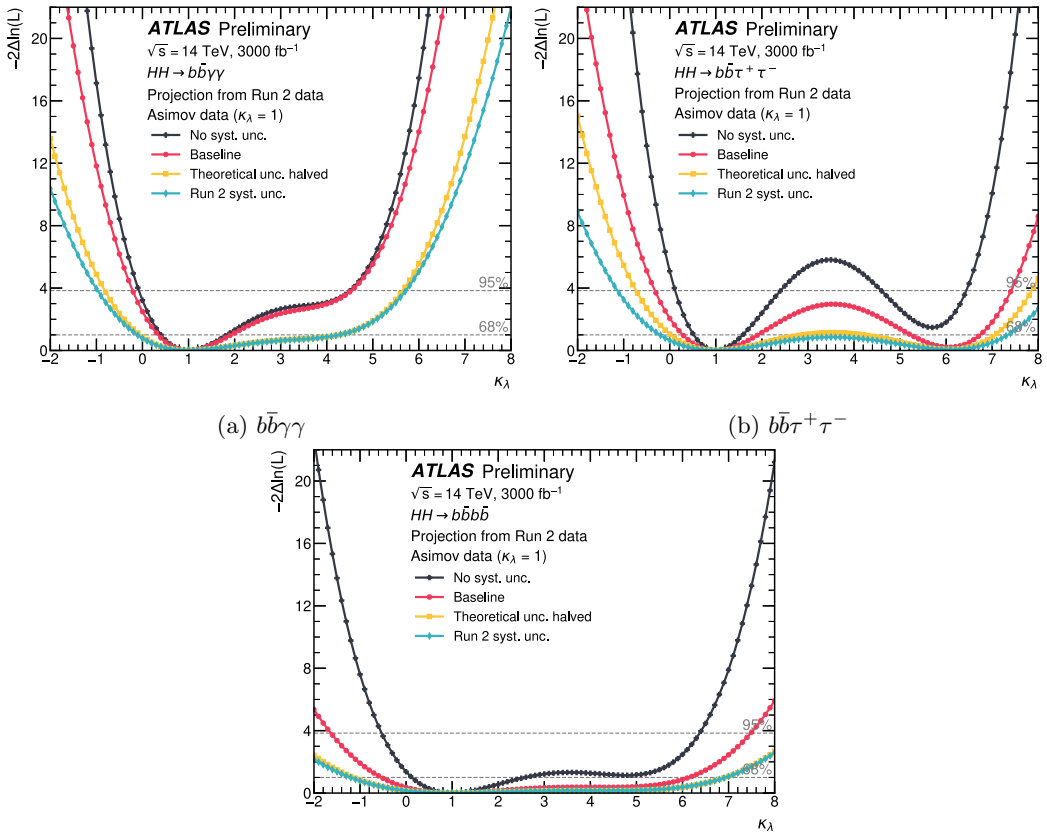

(a) $b\bar{b}\gamma\gamma$ (b) $b\bar{b}\tau^+\tau^-$

(c) $b\bar{b}b\bar{b}$

Figure 8.7: Significance (a) and 95 % CL upper limits (b) on the expected signal strength for SM HH production projected to 1000–3000 fb^{-1} at $\sqrt{s} = 14$ TeV at the HL-LHC under the four different uncertainty scenarios described in the text.

8.4.3 κ_λ cross-section scan

The projected 95% CL upper limits on the HH cross-section as a function of κ_λ assuming no HH production are shown in Figure 8.9 for the baseline uncertainty scenario. The constraints on κ_λ are derived from the intersection of the projection with the κ_λ-dependent theoretical prediction of the HH production cross-section at $\sqrt{s} = 14$ TeV [23]. In the baseline scenario, the projected 95 % CL interval on κ_λ is found to be $[2.0, 4.1]$. The κ_λ values outside of this interval are expected to be excluded at 95 % CL by the HL-LHC using 3000 fb^{-1} data at $\sqrt{s} = 14$ TeV. In particular, the SM hypothesis $\kappa_\lambda = 1$ is excluded. The κ_λ constraint intervals derived from the cross-section limit scan for the four uncertainty scenarios are summarized in Table 8.6.

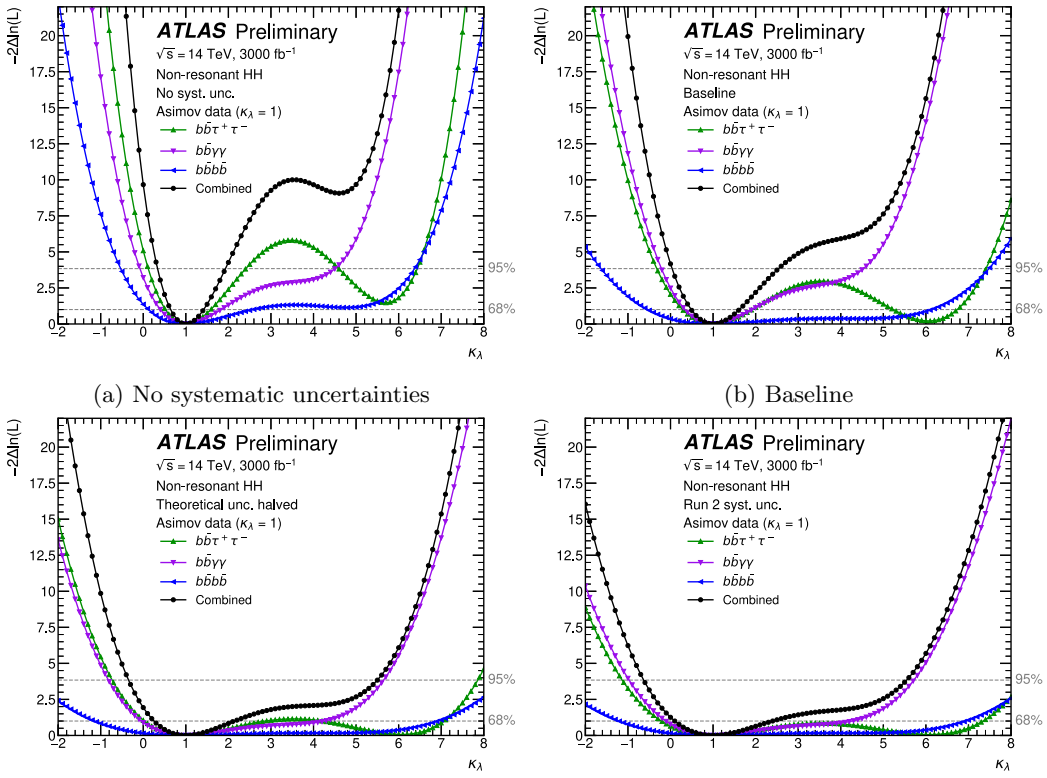

(a) No systematic uncertainties

(b) Baseline

(c) Theoretical uncertainties halved

(d) Run 2 systematic uncertainties

Figure 8.8: Negative log-profile-likelihood ratio as a function of κ_λ evaluated on an Asimov dataset constructed under the SM hypothesis of $\kappa_\lambda = 1$, for $b\bar{b}b\bar{b}$, $b\bar{b}\tau^+\tau^-$, $b\bar{b}\gamma\gamma$ projections and their combination assuming the four different uncertainty scenarios described in the text. Dashed horizontal lines correspond to $1\,\sigma$ and $2\,\sigma$ confidence intervals.

Table 8.6: Projected 95 % CL limits on κ_λ for different uncertainty scenarios when considering an integrated luminosity of $3000\,\text{fb}^{-1}$ at $\sqrt{s} = 14\,\text{TeV}$. The limits are obtained from cross-section scans comparing different κ_λ signal hypotheses to the background-only hypothesis.

	95 % CL limits on κ_λ from cross-section scan			
Uncertainty scenario	$b\bar{b}\gamma\gamma$	$b\bar{b}\tau^+\tau^-$	$b\bar{b}b\bar{b}$	Combination
No syst. unc.	$[1.2, 4.2]$	$[2.4, 4.5]$	$[0.8, 5.6]$	$[3.0, 3.3]$
Baseline	$[1.1, 4.3]$	$[1.7, 5.4]$	$[-0.6, 6.8]$	$[2.1, 4.0]$
Theoretical unc. halved	$[0.1, 5.2]$	$[0.9, 6.2]$	$[-1.7, 7.9]$	$[1.3, 4.9]$
Run 2 syst. unc.	$[0.1, 5.3]$	$[0.6, 6.5]$	$[-1.8, 7.9]$	$[1.0, 5.0]$

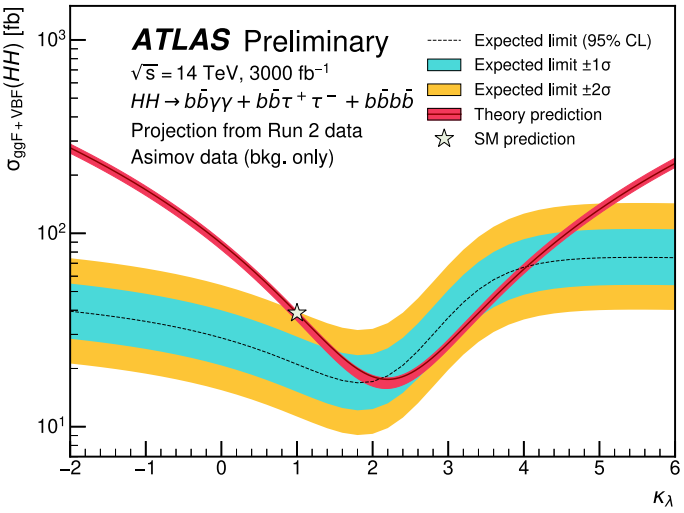

Figure 8.9: Expected 95 % CL limits on the HH cross-section for different κ_λ hypotheses at $\sqrt{s} = 14\,\text{TeV}$, $3000\,\text{fb}^{-1}$ at the HL-LHC with the baseline uncertainty scenario. The expected cross-section limits assume a complete absence of HH production. The theory prediction curve represents the situation where all parameters and couplings are set to their SM values except for κ_λ.

8.5 Discussion

A combination of the HL-LHC projection studies of the Higgs boson pair production in the $b\bar{b}\gamma\gamma$, $b\bar{b}\tau^+\tau^-$, and $b\bar{b}b\bar{b}$ final states is presented based on extrapolations of the full Run 2 analyses. The projected significance for the SM HH signal is $3.4\,\sigma(4.9\,\sigma)$, assuming the baseline (no systematic uncertainties) scenario. The signal strength relative to the SM prediction is expected to be measured with an accuracy of $^{+34}_{-31}\%$ ($\pm 23\%$). The $1\,\sigma$ confidence interval on κ_λ is constrained to $[0.7, 1.4]$ in the baseline scenario or $[0.5, 1.6]$ without systematic uncertainties.

Considering the different uncertainty scenarios, the main limitations to the HH sensitivity are the theoretical uncertainties on the HH cross-section and on the additional heavy-flavour jet radiation in ggF, VBF, and WH production modes of the single Higgs boson, the uncertainties associated with the data-driven background estimate in the $b\bar{b}b\bar{b}$ channel, the limited size of simulated event samples in the projection study of the $b\bar{b}\tau^+\tau^-$ channel, and the background modeling uncertainty in the $b\bar{b}\gamma\gamma$ channel.

Chapter 9

The Inner Tracker Upgrade

9.1 Overview

One of the major detector upgrades for HL-LHC is the ATLAS Inner Tracker upgrade [192]. During this upgrade, the ATLAS pixel detector, strip detector, and Transition Radiation Tracker will be removed and replaced with an all-silicon Inner Tracker (ITk). The ITk upgrade is necessary to handle the harsher environment at the HL-LHC, which will increase both the radiation dose and the total occupancy of the inner detector due to pile-up. The luminosity will increase from $1 \times 10^{34}\text{cm}^{-2}\text{s}^{-1}$ during Run 2 up to $7 \times 10^{34}\text{cm}^{-2}\text{s}^{-1}$ at the HL-LHC. In addition, the total integrated luminosity will increase due to the longer running time going from 300fb^{-1} at the end of Run 3 to an expected 4000fb^{-1} at the end of the HL-LHC program [192]. The total radiation dose around the interaction region will increase by a factor of 20 relative to conditions at the end of Run 2, up to 1×10^{16} 1 MeV neutron equivalent dose/cm^2 ($\text{n}_{\text{eq}}/\text{cm}^2$) [193]. Due to the large dose, the first inner layer of the ITk will use a new type of pixel sensor that is better suited for the high radiation environment, and the entire inner system will be replaced after 2000fb^{-1} of data has been collected. The average amount of pile-up will quadruple, from 50 during Run 2 to 200 at the HL-LHC, greatly increasing the combinatorial complexity of tracking and vertexing in such a dense environment. Despite these challenges, the ITk is designed to improve or maintain the overall tracking performance of the ATLAS detector. This will be achieved by increasing the granularity of the inner tracker and reducing the material budget.

The ITk will consist of 5 layers of pixel detectors and 4 layers of strip detectors. The pixel system will provide a coverage of up to $|\eta| < 4$, and the strip detectors will extend to $|\eta| < 2.7$. The layout is shown in Figure 9.1, and a more detailed view can be seen in Figure 9.4. The granularity of the inner detector will be increased by reducing the size of the pixel pitch and increasing the total number of readout channels. The pixel detector will consist of 13m^2 of active silicon and pixels with a 50×50 μm pitch resulting in 5 billion readout channels. The strip detector will have 160m^2 with

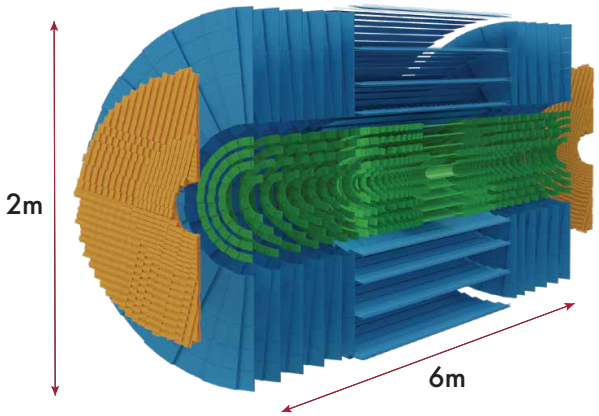

Figure 9.1: A rendering of the ITk pixels (green), strips (blue), and the High Granularity Timing Detector (yellow) [60]

strips of 69-85μm pitch, resulting in about 50 million readout channels [194]. There are about 60 times the number of pixel channels and 10 times the number of strip channels with respect to the current ATLAS inner system [193].

The material budget will be reduced by using thinner modules, an improved layout with inclined planes, and serial powering. This will mitigate effects such as multiple scattering that can degrade track parameter resolutions. The pixel sensors will be 100-150μm thick compared with 200-250μm in the current pixel detector. Inclined planes in the outer barrel portion of the ITk, shown in Figure 9.4, will allow for better coverage with less material. The serial powering scheme that will be brought in for the ITk allows the pixel modules to be operated along power chains of up to 14 modules at a time. As much of the material budget in both the Run 2 inner detector and ITk comes from pixel cabling and services, this powering scheme dramatically reduces the overall material effects. Figure 9.2 shows the material budget for the Run 2 inner detector compared with the anticipated ITk material budget. The maximum number of radiation lengths in the ITk corresponds to about half of those in the Run 2 inner detector.

Figure 9.3 shows some of the expected performance metrics for the ITk. We can see that despite the increased pile-up, the vertex reconstruction efficiency is expected to be much better than in the Run 2 ATLAS detector. Also, in Figure 9.3 we can see the expected b-tagging performance is expected to stay on par with Run 2, despite the larger amount of pile-up. This is particularly important for the HH analyses, which often use final states involving b-jets from the $H \to b\bar{b}$ decay channel.

To build a detector of such complexity and scale, detailed quality control must be performed across all subsystems. This chapter will focus on quality control methods developed for the pixel detector subsystems. First, we will describe the general operation of a pixel module - the basic unit

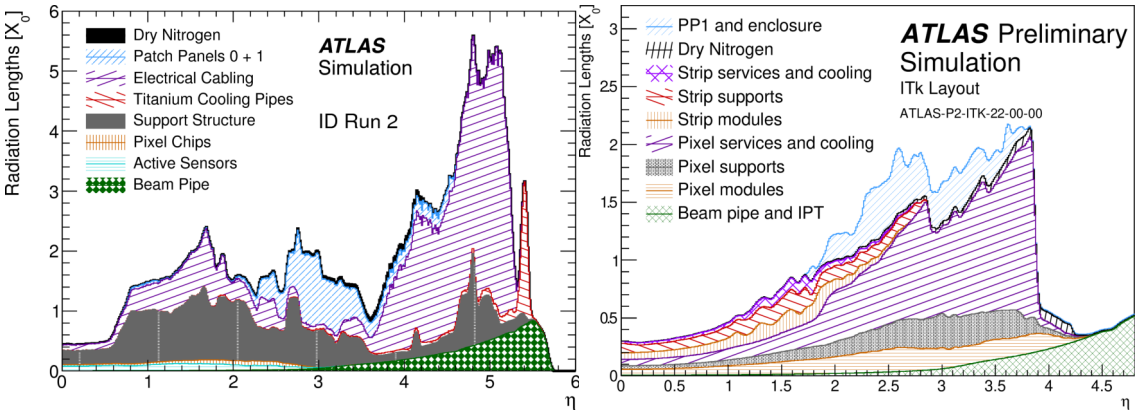

(a) (b)

Figure 9.2: Material budget of (a) the current ATLAS inner detector and (b) the ITk. Note that the scale on both images is not the same. [194]

of a pixel detector - then we will discuss the readout electronics, and finally, we will discuss some common tests performed to check the operation of the module. These tests were performed in the context of two different demonstrator programs for the ITk that will be discussed in the next section.

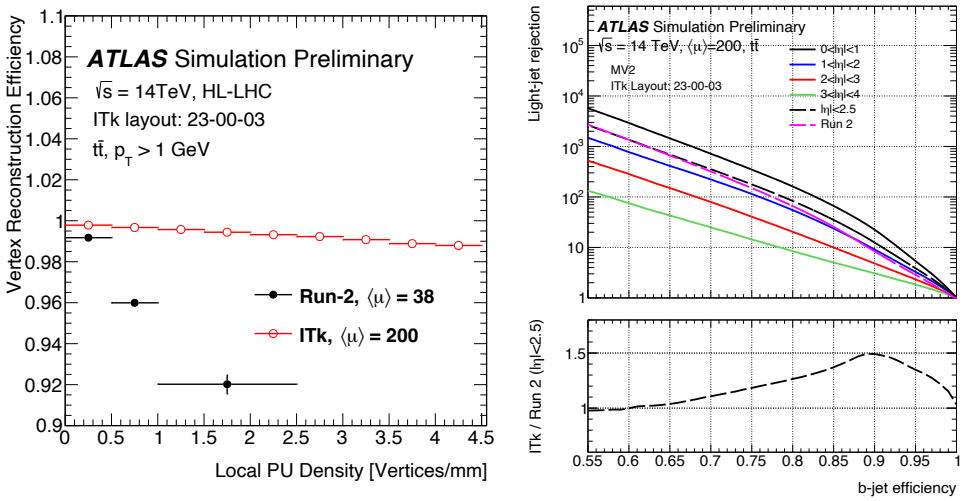

(a) (b)

Figure 9.3: Some expected performance metrics of the ITk. (a) Expected vertex reconstruction efficiency, and (b) expected b-tagging performance for the MV2 b-tagging algorithm [186]

9.2 Pixel demonstrator geometries

This thesis work was related to two different pixel detector demonstrator programs for the ITk, one at CERN and the other at SLAC National Accelerator Laboratory. Assembly and integration for the ITk pixels will happen at both locations. CERN will be responsible for the outer barrel system (the three outermost layers in red in Figure 9.4 excluding the end caps), and SLAC will be responsible for the inner system (the two innermost red layers in red in Figure 9.4). The idea behind the demonstrators is to build prototype versions of the pixel subsystems. This helps develop local expertise in building the detectors, and allows for the development and testing of construction and quality control methods. The demonstrators can also be used for system-level tests such as thermal testing, interlock testing, and readout testing to ensure that all the different parts can be integrated and function properly together.

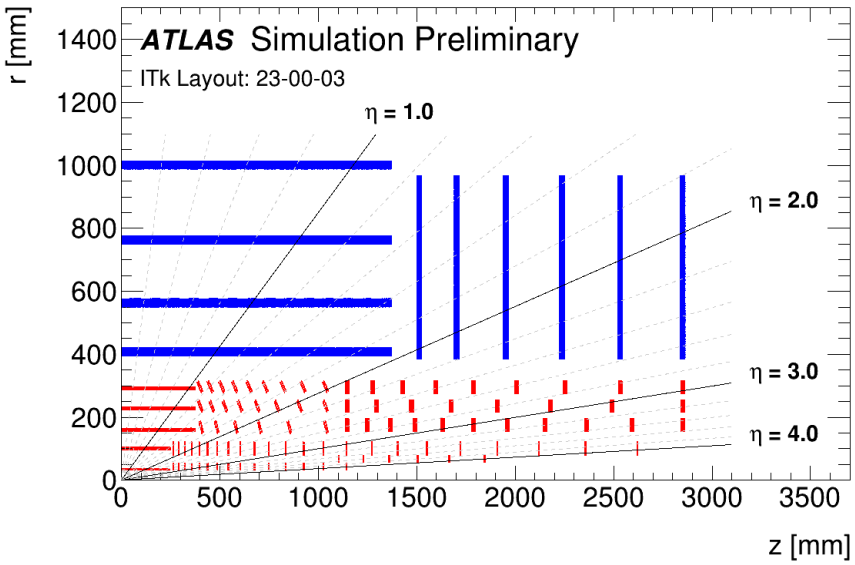

Figure 9.4: Layout of one quadrant of the ITk. The pixel subsystem is shown in red and the strip subsystem is shown in red. Only the active material is shown. [186]

An example of the CERN outer barrel demonstrator is shown in Figure 9.5. While the entire outer barrel system consists of many layers of staves arranged in a cylindrical pattern, the demonstrator consists of a single stave. In addition, as the final pixel sensor and readout chips were still undergoing development at the time of this work, the outer barrel demonstrator relied on readout chips and sensors left over from the ATLAS Inner B-layer (IBL). These modules will be referred to as FE-I4 modules, corresponding to the name of their readout chip. The modules come in two flavours: quad modules with four readout chips per sensor and dual modules with two readout chips per sensor. These modules are glued to carbon fiber support structures.

(a) (b)

Figure 9.5: A CAD illustration of the (a) outer barrel system and (b) the FE-I4 outer barrel demonstrator at CERN. The pixel modules are shown in green, non-instrumented heater modules are shown in blue.

SLAC is responsible for assembling and integrating the pixel inner system. An example of a ring-based demonstrator from SLAC is shown in Figure 9.6. This demonstrator uses modules with RD53A readout chips arranged in triplet (three chips per module) and quad module configurations attached to the carbon fiber coupled ring.

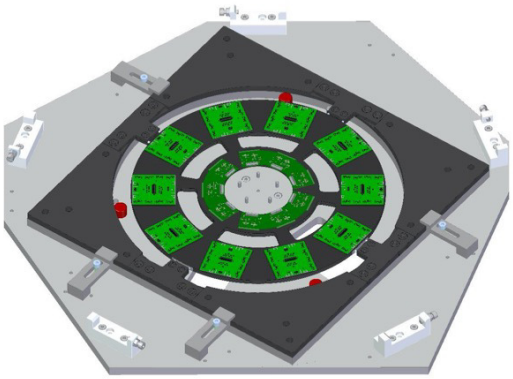

Figure 9.6: A CAD illustration of a coupled ring demonstrator at SLAC. Triplet pixel modules are shown in dark green while quad modules are bright green.

9.3 Pixel module overview

A pixel module, illustrated in Figure 9.7 is the basic unit for the pixel detector. A pixel module consists of a sensor, a readout chip, and a flexible printed-circuit-board (PCB), called a module flex. The sensor is the active element of the detector and produces a signal when a charged particle passes through it. The exact way the signal is produced will be described in Section 9.4.2. The sensor is bump-bonded to the readout chip via indium or tin solder bumps. The readout chip takes in the signals from each sensor, discriminates if there is a hit from a charged particle, and converts the data into a digital signal to be sent to upstream processing, as will be described in Section 9.4.3. The readout chip is wirebonded to the module flex, which carries the data to the data acquisition systems and performs module monitoring and slow controls. The wirebonds between the readout chip and the readout chip are sometimes covered in epoxy for mechanical protection. In addition, a spray-on parylene coating can be used to avoid high-voltage discharges between the high-voltage module biasing lines and ground.

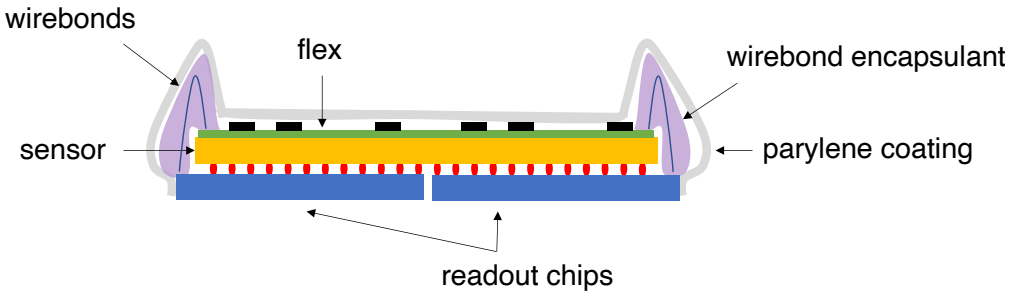

Figure 9.7: Pixel module sandwich layout. The sensor sits between the readout chips and the module flex.

In this chapter, multiple sensor types and readout chips will be discussed. The sensors to be used for the ITk are shown in Table 9.1. The same readout chip can be used for different sensor types, provided they have the same form factor. The two readout chips that will be discussed in this chapter are the FE-I4 modules that were used for the IBL, and the RD53A modules, which were used to test three different readout technologies for both the ATLAS and CMS inner tracker upgrades. The three different technologies use different circuitry for shaping and discriminating signals from the sensors and are known as the synchronous, linear, and differential front-ends as shown in Figure 9.8 [195]. The ITkPixV1 readout chip is a prototype chip that uses the differential front-end across its channels. A comparison of all three readout chips is shown in Table 9.2. In addition to multiple vendors for sensor production, multiple flip-chipping facilities for bump-bonding the sensor to the readout chip exist, and different vendors were considered through a market survey process. As many different flavours of the pixel module assemblies exist, but the general testing procedure is similar, they will be described interchangeably throughout this chapter.

Table 9.1: Pixel sensor options [192]

	3D sensor	Planar sensor
Location	Innermost layer (L0)	Layers 1-4
Radiation tolerance	up to 1.31×10^{16} 1 MeV n_{eq}/cm^2	up to 3.8×10^{15} 1 MeV n_{eq}/cm^2
Pixel size [μm]	25×100 or 50×50	50×50
Thickness [μm]	100-150	100-150
Replaced at 2000fb^{-1}	Yes	No
Semiconductor type	n-type rods in p-type substrate	n-type implants in p-type substrate

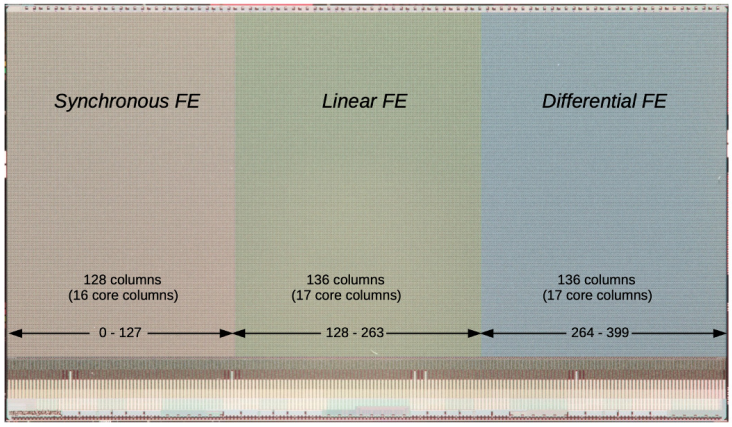

Figure 9.8: RD53A Layout [195]. ATLAS has chosen to go with the differential front-end for the ITkPixV1 chip.

Table 9.2: Pixel readout chips [196]

	FE-I4	RD53A	ITkPixV1
Feature size [nm]	130	65	65
Chip size[mm]	20.2×18.8	20×11.6	20×20
Pixel size [μm]	50×250	50×50	50×50
Columns×rows	80×336	400×192	400×384
Data bandwidth	160 MBs	4×1.28 GBs	4×1.28 GBs

9.4 Pixel module testing

A set of tests are performed to check that the module is of reasonable quality for use in the demonstrator or eventually ITk production. These tests are essential at the scale of the ATLAS ITk as we want to ensure the modules that go into the detector are of sufficiently high quality. In addition, any systematic problem during production could lead to delays in construction. Often these tests, or a subset of them, are done at multiple stages during module assembly. Testing the modules between assembly steps allows for quality control and tracking of systematic problems during production.

Some common tests performed on pixel modules:

- Mass measurements to check that no extra material is being added
- Metrology to test for module flatness and alignment
- Optical inspection to check for any visible problems in wirebonding or alignment of the module
- Sacrificial wirebond pull tests to check the quality of the wire bonds
- IV Curve for sensor testing
- Electrical tests for characterizing the readout chip:

  Digital scan

  Analog scan

  Time over threshold scan

  Threshold scan

  Tuning
- Source scan or disconnected bump bond scan to test the entire module
- Thermal cycling tests to check for thermal stresses and delamination between sensors and readout chips

These tests are often performed both at room temperature and cold - close to the operational temperature of the module. Cooling systems using Peltier coolers, cold boxes, fans, or CO2 cooling are used to keep the module at the desired temperature and to avoid thermal run-away as the module heats up. Room temperature testing is often faster than testing cold and can be used to check for any initial problems with the module. Cold testing simulates the -40^{o}C operating temperature in the ITk - required to keep the leakage current low even after radiation damage [192]. As the silicon in the sensors has temperature-dependent properties, testing at two temperatures allows for the characterization of the sensor. Different parts of the module also have different coefficients of thermal expansion (CTE). Testing at the different temperatures allows one to determine if there are any problems with CTE mismatch. The most common module tests will be described in this chapter. For more detailed information on each of the tests, please refer to Ref. [197] and [192].

9.4.1 Optical inspections

Optical inspections are performed by eye or using a microscope. Problems with missing, bent, incorrectly connected, and spurious wirebonds can often be spotted via an optical inspection. An example of a pixel module and a microscope image showing with extra wirebonds is shown in Figure 9.9.

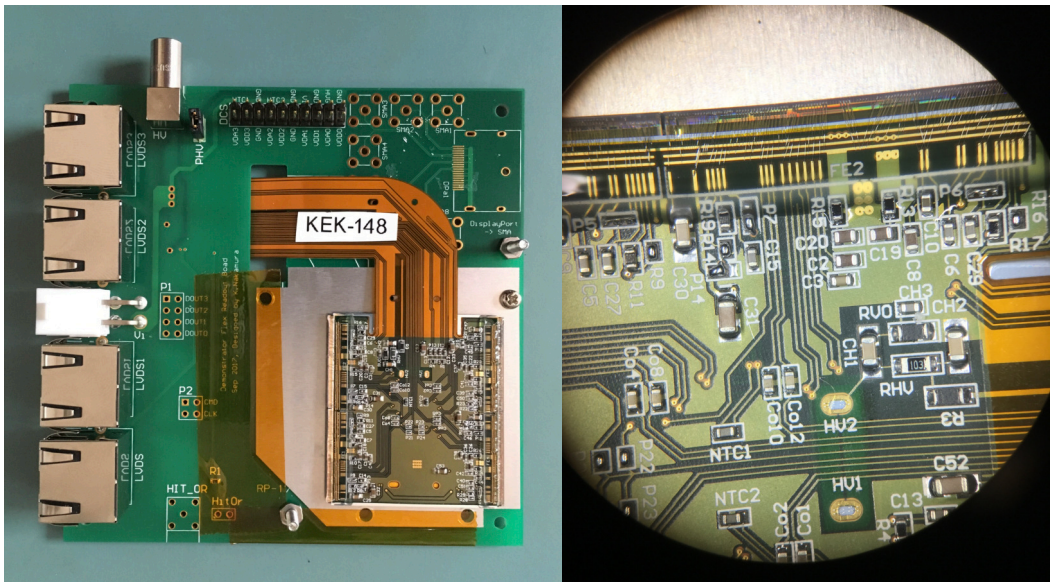

(a) (b)

Figure 9.9: (a) An FE-I4 pixel module on its carrier board and (b) a visual inspection revealing spurious wirebonds around the HV2 via and C31

9.4.2 Pixel sensor operation and IV curves

The pixel sensors to be used in the ITk include both planar and 3D sensors, as described earlier in Table 9.1. The general principle of operation for both types of sensors is the same and is based on the operation of a p-n junction. A schematic of a pixel sensor is shown in Figure 9.10.

A p-n junction is created between n-type and p-type materials. N-type materials are semiconductors doped with additional electron donor atoms, p-type materials have dopants with one less valence electron leaving a "hole". The p-n junction can either be achieved by interfacing p and n-type materials with each other, either by implanting p-type dopants into an n-type material, or n-type dopants into a p-type material. For silicon, p-type dopants include gallium, aluminum, indium, and boron. N-type dopants for silicon include phosphorous and arsenic [198].

Within the p-n junction the excess electrons from the donor atoms from the n-type material will drift to fill the holes in the p-type material. Because the atoms within the material have stayed

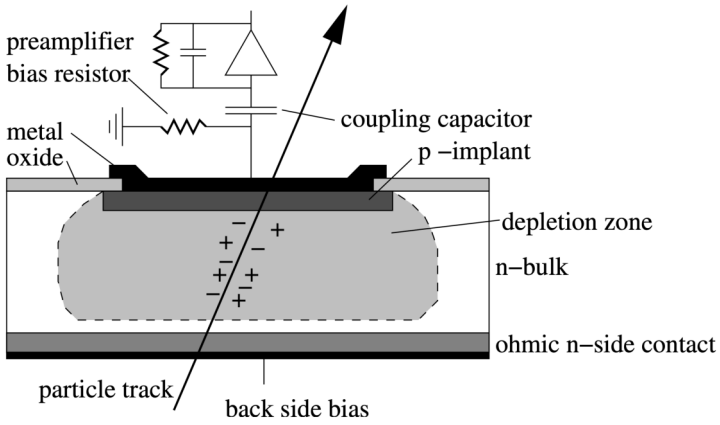

Figure 9.10: Schematic of a pixel sensor. Figure reproduced from Ref. [198]

stationary, a small electric field is also created. The strength of this electric field eventually stops the diffusion process of electrons filling the holes. This process creates a small depletion zone, which is a region where there are no free charge carriers and therefore also high resistivity. To increase the size of the depletion zone, silicon pixel sensors are often operated in "reverse bias" mode. Here the p-type material is connected to a negative voltage, and the n-type material is connected to a positive voltage. This reverse bias effectively cancels out the initial field created by the movement of the electrons, and causes even more electrons to drift, increasing the size of the depletion zone [198].

When a charged particle passes through the depletion zone of the silicon, electron-hole pairs are created, which drift in the applied electric field. For silicon, an average energy of 3.6 eV is required to create one electron-hole pair. This is 3 times larger than the silicon band-gap of 1.12 eV. The difference is due to the creation of phonons that dissipate energy as heat [198]. The movement of the electron-hole pairs induces a current on the readout electrode. The number of electron-hole pairs created increases with the width of the depletion zone, creating a stronger signal when the depletion zone is larger. For 150 μm of silicon, a minimum ionizing particle will create about 10,000 electron-hole pairs [198].

The width of the depletion zone can be described by:

$$W \approx \sqrt{\frac{2\epsilon_0 \epsilon_{\mathrm{Si}}}{eN_D} V}$$

Where ϵ_0 is the permittivity of free-space, ϵ_{Si} is the permittivity of silicon, e the unit of charge, N_D is the dopant concentration, and V is the bias voltage across the sensor. Notably, the width of the depletion zone has a square root dependence on the bias voltage. If the bias voltage is increased to very high values, electrical breakdown can occur, and then the sensor can no longer maintain its reverse bias.

While a larger depletion zone allows for a more sensitive pixel detector, it also results in a higher leakage current. The leakage current depends on a few factors, the primary factor being the thermal generation of e-h pairs within the depletion zone [198]. Therefore the leakage current, J_{vol} is also directly proportional to the width of the depletion zone.

$$J_{\text{vol}} \approx -e\frac{n_i}{\tau_g}W \approx -e\frac{n_i}{\tau_g}\sqrt{\frac{2\epsilon_0\epsilon_{\text{Si}}}{eN_D}V}$$

Where τ_g is carrier lifetime, n_i is intrinsic carrier lifetime. Irradiated sensors will often have defects in the lattice structure of the silicon, which results in a shorter carrier lifetime and correspondingly higher leakage currents. A higher operating temperature will also change the carrier lifetimes and result in higher leakage currents for higher temperatures [198]. The sensors can be characterized by applying different bias voltages to the sensors and recording the observed leakage current. Figure 9.11 shows the ideal shape of the IV curve, and Figure 9.12 shows some example IV curves for planar modules from the CERN outer barrel demonstrator program. The modules were not brought to their breakdown voltage while testing, and several different types of sensors were tested, but the square root dependence on the bias voltage can be observed. The breakdown voltage for the tested modules is expected to be $>$ 130 V or 170 V, depending on whether the tested sensors were 100 or 150 μm thick [197].

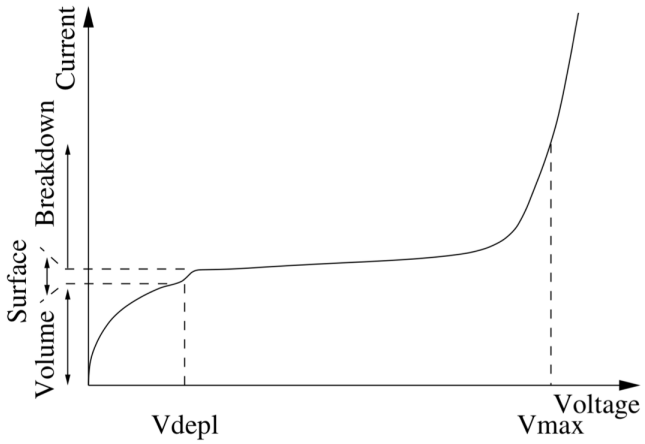

Figure 9.11: IV Curve [198]

9.4.3 Pixel sensor readout and readout chip testing

According to the Shockley-Ramo theorem, the induced current on the readout electrodes is:

$$i = q\vec{E} \cdot \vec{v}$$

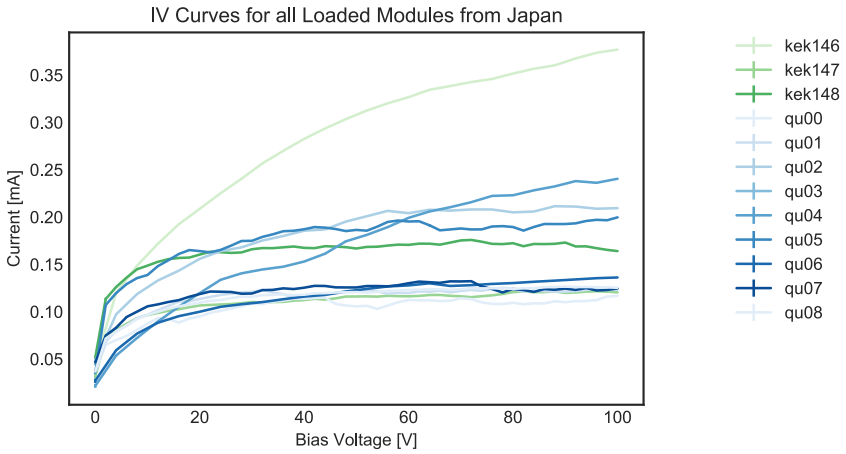

Figure 9.12: Measured IV Curves for a number of FE-I4 modules. Different sensor types are shown, but the leakage currents all display the expected $\sqrt{V}$ dependence on voltage. During testing,the sensors are not brought to their breakdown voltage.

Where q is the charge of the particle, v is the particle's velocity, and E is the electric field inside the semiconductor. As a result higher electric fields also result in a larger induced current [198]. The readout chip takes in the induced current and processes it to see if a signal exceeds a threshold. Each channel has an analog portion of the readout circuitry which shapes the induced signal and discriminates whether it has exceeded a set threshold, and a digital portion which measures the pulse-width and digitizes the result. The result is passed to a buffer shared between columns of pixels until they are read out. Digital and analog charge injection circuitry allows for tests of the analog and digital portions of the readout chip without a sensor attached. A schematic for the FE-I4 readout circuitry is shown in Figure 9.13.

Digital scan

The digital scan tests the digital portion of the readout system. Hits are repeatedly enabled within the digital readout portion and then read out. Pixels that have faulty digital readout circuitry will not have a 100% success rate and can be masked. As this is a simple test, it can also help determine if the readout chain is set up correctly. Problems with the readout system can show up as streaks of faulty pixels along the columns of the scans indicating problems with the readout timing, amplification, or noise. Figure 9.14 shows an example digital scan.

Analog scan

The analog scan tests the analog portion of the readout system, including the amplification and shaping circuits. Charge is injected through a charge injection circuit at the beginning of the

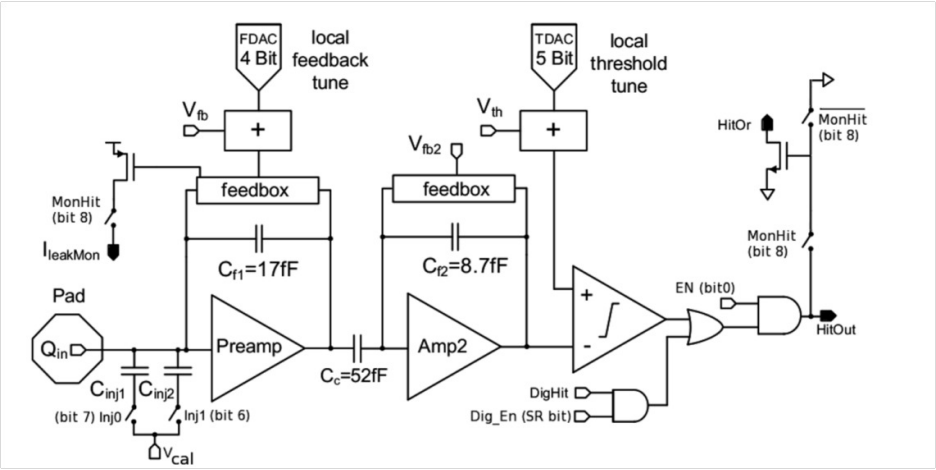

Figure 9.13: FE-I4 readout per pixel circuitry. The sensor is connected to the pad on the left. The analog charge injection circuitry is on the bottom right. The analog charge integration and pulse shaping circuitry comes from the two amplifiers. A comparator on the right compares to a set threshold. The digital charge injection circuitry is on the bottom right. EN allows for masking of the pixel if it is faulty.

amplification and shaping portion of the readout circuit. In an analog scan, the injected amount of charge is much higher than the threshold voltage, ensuring that a hit will be read out if everything is working as expected. Once again, the charge is injected a pre-set number of times and the number of hits is recorded. Figure 9.14 shows an example of an analog scan. Some pixels in this scan are noisy, corresponding to a greater number of hits than injected, and some are quiet or dead, corresponding to less than 100% or 0% success.

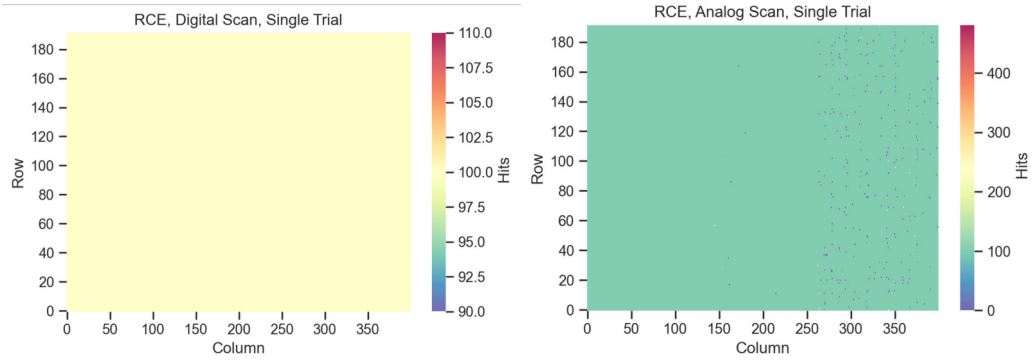

(a) (b)

Figure 9.14: Examples of (a) a digital scan on the RD53A front-end (b) an analog scan on the RD53A front-end. In the analog scan, there is some noise on the linear and differential front-ends seen in the 2nd and 3rd thirds of the module.

Time over threshold scan

The time over threshold (ToT) for an input pulse corresponds to the pulse height from the sensor and is approximately proportional to the ionization charge in the sensor. This time over threshold is measured in clock cycles using the LHC clock frequency of 25 ns. The ToT can have a non-linear response to the amount of charge detected, and therefore a look-up table is used to calibrate the charge to ToT ratio [199]. Variations in the ToT when signals of different pulse heights cross the threshold are known as timewalk. To associate a hit with a particular bunch crossing, the timewalk needs to be smaller than the time interval between bunch crossings. For certain applications, such as the identification of a particle species or detection of long-lived particles, the ToT of a hit in the pixel module can be used to perform a dE/dx measurement within the tracking detector [200]. However, in the ATLAS pixel detector, most particles are minimally ionizing, therefore the goal is to have a ToT response that is as uniform as possible. A time over threshold scan can be used to characterize this response.

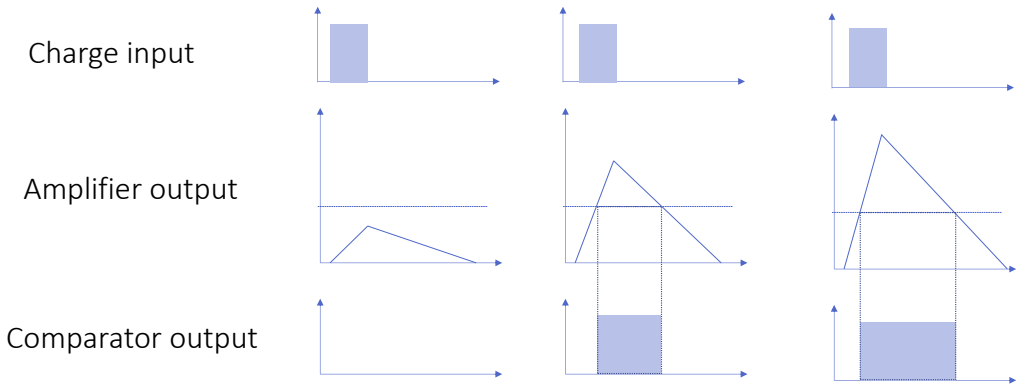

Figure 9.15: Time over threshold scan illustration. For the same charge inputs, different pixels may have a different response.

A time over threshold scan injects a set amount of charge into the analog portion of readout circuitry and checks how much time each pixel records the signal as being over threshold. As the readout circuitry for each pixel can have slight variations, the ToT will be slightly different for each pixel. Figure 9.15 shows an illustration of a ToT scan for different pixels where each pixel has a different response to the same amount of injected charge, and therefore a different ToT. A dedicated tuning program can be performed to make the per-pixel response as uniform as possible. Figure 9.16 shows an example of a ToT scan on an RD53A module where each front-end was tuned to have a mean ToT of 7 clock cycles. Variation of the ToT between the front-ends is an effect of the different shaping and amplification systems, and the front-end and pixel-specific tunings.

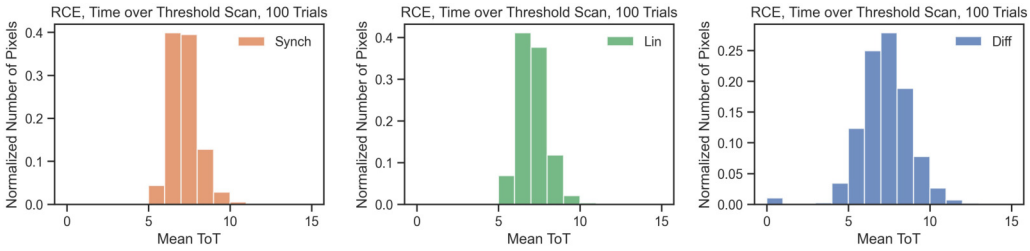

Figure 9.16: Time over threshold scan results for the different RD53A front-ends

Threshold scan

The front-end chips discriminate between signals that are below threshold and ones that are not. Ideally, a perfect chip will always produce a hit for a signal above the threshold. However, in the real world, the discriminators are sensitive to noise and the same injected charge will not always lead to the same output. In a threshold scan, the input charge is continuously varied, and the output is recorded. Repeated many times, this allows us to generate a probability distribution, known as an S-curve, of when a particular pixel fires for a given number of input charges. This distribution can be fit using an error function:

$$f(x) = \frac{A}{2}\frac{\text{erf}(x-\mu)}{\sqrt{2}\sigma} + \frac{A}{2}$$

Where A is the amplitude of the curve, μ describes the amount of charge injected that results in a hit being recorded 50% of the time. σ describes the width of the S-curve. An ideal curve would have a very small width, σ, indicating a very stable performance as a function of injected charge. Figure 9.17a shows an example S-curve for a single pixel from an FE-I4 module tuned to have a threshold at 25. Figure 9.17b shows the S-curves for an RD53A module. The light band that has a μ of 110 comes from one of the three front-end chips being incorrectly tuned.

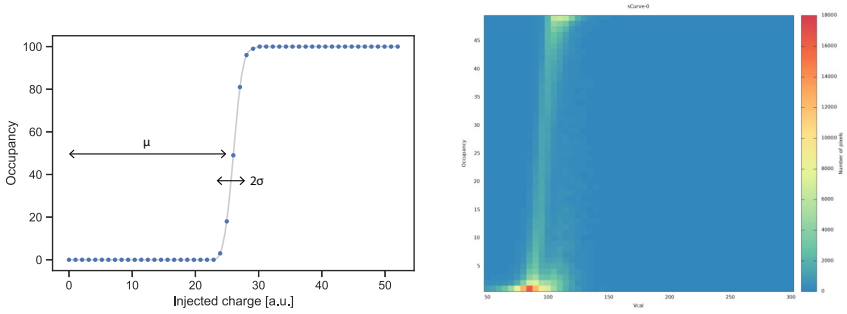

(a) (b)

Figure 9.17: Example s-curves for (a) single pixel on an FE-I4 module (b) all pixels in an RD53A module

Threshold tuning

Global and local registers can be set to achieve a desired per-pixel response for a given input charge distribution. This can be achieved by varying the thresholds for a given pixel, as illustrated in Figure 9.18. For example, in Figure 9.13 the local registers for the FE-I4 modules can be seen at the top under the FDAC and TDAC inputs. Tuning maps carrying information about the optimal tunings for each module can be saved for every sensor to achieve the desired per-pixel response. The tuning will depend on the operating conditions, such as the temperature and desired pixel responses. Figure 9.19 shows an example of an FE-I4 module tuned to have a response of 2750e. It is important to repeat the tunings after significant radiation damage, as radiation damage can change the overall pixel responses.

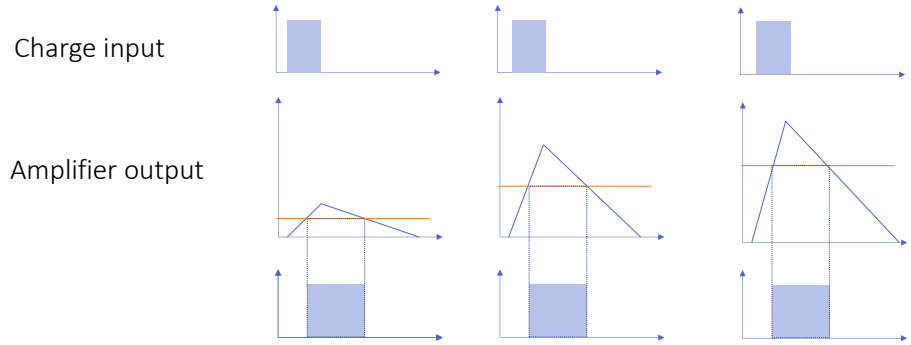

Figure 9.18: Threshold tuning illustration. As the analog circuitry in each amplifier can has slight variations in response to a set charge injection, global and local registers can adjust the thresholds such that the response is the same for all pixels.

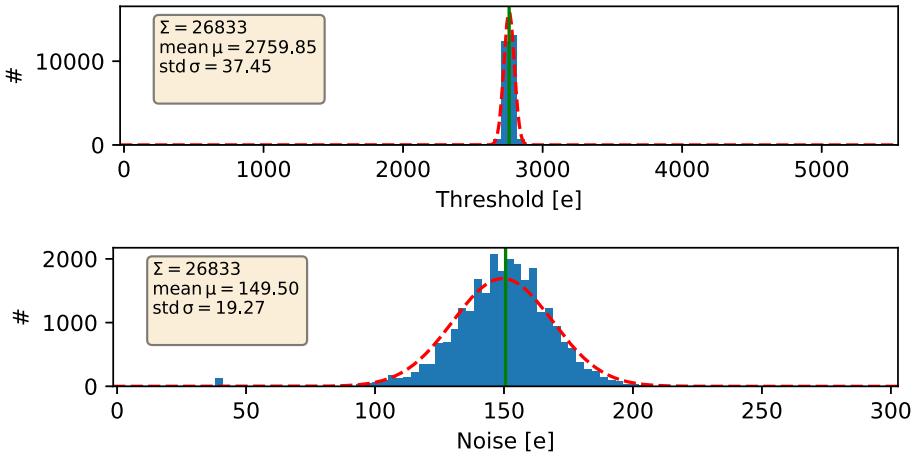

Figure 9.19: Results of an example threshold scan after tuning an FE-I4 module for a mean response of 2750e.

9.4.4 Source scans

Until now, we have talked about scans that test individual components of the pixel modules. Source scans allow one to test the entire pixel module, including the sensor, readout chip, and readout chain. For these scans, a radioactive source is placed a controlled distance away from the module and the module. The module then collects data in a self-triggering mode for a few minutes. The CERN demonstrator program used a 30 MBq, ^{90}Sr source. This source undergoes nuclear beta decay with a decay energy of 0.546 MeV, which is distributed between the electron, anti-neutrino, and Yttrium isotope ^{90}Y. Yttrium also beta decays with a decay energy of 2.28 MeV and then becomes stable ^{90}Zr. Thus this is a good source of relatively low-energy electrons. In Figure 9.21, we can see the result of such a source scan. Darker areas indicate where fewer hits were triggered due to the surface mount components on top of the module. The lighter regions which split the module into quarters indicate the boundaries of the 4 different readout chips. This particular module qualifies as having <1% non-functional pixels which is the yield being targeted within the ITk program [197].

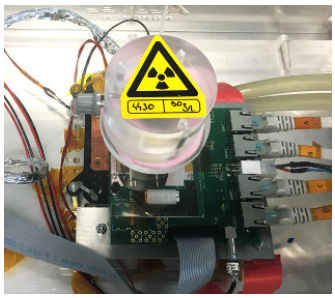

Figure 9.20: Source scan set-up

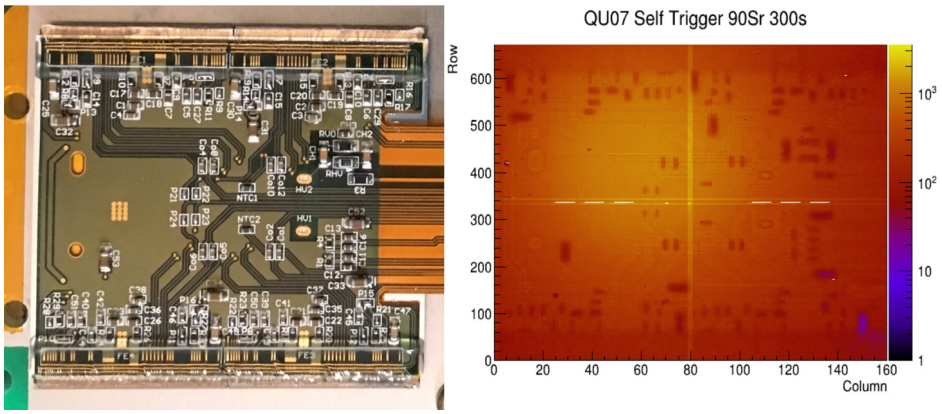

(a) (b)

Figure 9.21: (a) a close-up of the FE-I4 module with the module flex on top (b) the results of a source scan where the surface mounted components are visible

9.5 Discussion

The results from the tests described in this chapter can be used to determine the best procedures for module assembly, transportation, and loading onto the support structures. Part of the work in this thesis involved developing scripts, documentation, and specifications for tracking the results of these tests in a database to aggregate them. Storing the results at each step of module production allows one to check for any systematic problems from certain vendors or assembly sites. Eventually, the results stored in the database can also be used to decide which pixel modules should be placed where in the detector.

In addition, the qualified and characterized pixel modules can be used in the demonstrators to perform system-level tests. These tests ensure that all of the detector components can be integrated together and function as a whole. For example, Figure 9.22 shows the results of a system-level source scan of the CERN-based outer barrel demonstrator using pixel modules tested as a part of this thesis. These system-level studies are important for testing the loading procedures, speed, and reliability of the readout systems, cooling, serial powering, and interlock systems. In the future, additional demonstrators and testing using the next-generation ITkPixV1 will allow us to produce more accurate and reliable prototypes, which will inform the construction of the ITk itself. The expertise gained from performing the system-level tests with the demonstrator will eventually allow for testing of the ITk pixel subsystems before installing them in the ATLAS detector cavern.

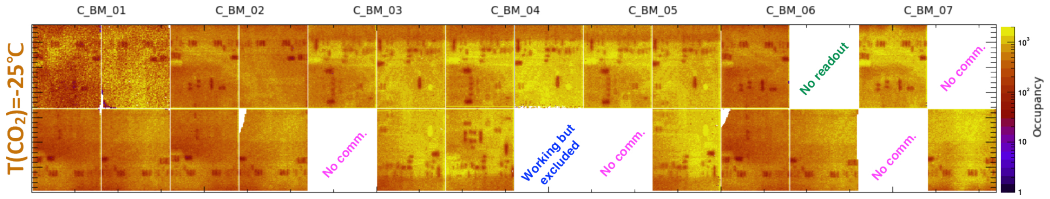

Figure 9.22: Example of a system-level source scan for the CERN-based outer barrel demonstrator [194]

Chapter 10

Conclusions

A decade after the Higgs discovery, we are still learning new things about the Higgs boson. This thesis has gotten us closer to answering the question of whether HH production occurs. But for now, the answers lie in the future. HH production holds important clues for us to understand the Higgs self-coupling and the nature of electroweak symmetry breaking.

This thesis explored HH production in the $b\bar{b}\gamma\gamma$ channel using the Full Run 2 dataset of 139 fb^{-1} at 13 TeV. As no significant excess above the Standard Model background expectation was observed, limits on the SM HH signal strength were set, corresponding to limits at 4.2 times the SM. The Higgs boson self-coupling κ_λ was also constrained between $-1.5 < \kappa_\lambda < 6.7$. Relative to the Early Run 2 results with 36fb^{-1}, these results improve the upper limits of the SM HH production cross-section by a factor of 5 and shrink the constraints on κ_λ by a factor of two.

In addition, the results from the $b\bar{b}\gamma\gamma$ channel were combined with results from the $b\bar{b}b\bar{b}$ and $b\bar{b}\tau^+\tau^-$ channels. The combined observed upper limits on μ_{HH} were 2.4 at 95% CL. Constraints on κ_λ from the 95% CLs cross-section limits were placed at for κ_λ between $[-2.1, 7.8]$. These represent the strongest worldwide limits on SM HH production to date.

There is a long road ahead before we can expect to claim evidence for HH production with ATLAS. The High Luminosity LHC upgrade will be required to accumulate enough data for sensitivity to HH production. As part of the HL-LHC, the ATLAS inner detector will be replaced with a new all-silicon inner detector. The projected significance for the SM HH signal combining the $b\bar{b}\gamma\gamma$, $b\bar{b}\tau^+\tau^-$, and $b\bar{b}b\bar{b}$ channels with 4000fb^{-1} of data from the HL-LHC is $3.4\,\sigma$. The signal strength relative to the SM prediction is expected to be measured with an accuracy of $^{+34}_{-31}$%. We can also expect to constrain κ_λ to $[0.7, 1.4]$ at $1\,\sigma$ confidence.

If we are lucky, we may see a deviation from the expected SM signal in the future, which would point us to new physics and open up a whole new range of possibilities. In either case, whether the HH production is Standard Model-like or not, furthering our understanding of the universe by measuring it at its most fundamental scales is an achievement in itself.

Bibliography

[1] ATLAS Collaboration. "Observation of a new particle in the search for the Standard Model Higgs boson with the ATLAS detector at the LHC". In: *Phys. Lett. B* 716 (2012), p. 1. DOI: 10.1016/j.physletb.2012.08.020. arXiv: 1207.7214 [hep-ex].

[2] CMS Collaboration. "Observation of a new boson at a mass of 125 GeV with the CMS experiment at the LHC". In: *Phys. Lett. B* 716 (2012), p. 30. DOI: 10.1016/j.physletb.2012.08.021. arXiv: 1207.7235 [hep-ex].

[3] ATLAS Collaboration. "Study of the spin and parity of the Higgs boson in diboson decays with the ATLAS detector". In: *Eur. Phys. J. C* 75 (2015), p. 476. DOI: 10.1140/epjc/s10052-015-3685-1. arXiv: 1506.05669 [hep-ex]. Erratum: Eur. Phys. J. C **76** (2016) 152.

[4] CMS Collaboration. "Constraints on the spin-parity and anomalous HVV couplings of the Higgs boson in proton collisions at 7 and 8 TeV". In: *Phys. Rev. D* 92 (2015), p. 012004. DOI: 10.1103/PhysRevD.92.012004. arXiv: 1411.3441 [hep-ex].

[5] ATLAS Collaboration. *A combination of measurements of Higgs boson production and decay using up to* $139\,fb^{-1}$ *of proton–proton collision data at* $\sqrt{s} = 13$ *TeV collected with the ATLAS experiment*. ATLAS-CONF-2020-027. 2020. URL: https://cds.cern.ch/record/2725733.

[6] CMS Collaboration. *Combined Higgs boson production and decay measurements with up to 137* fb^{-1} *of proton-proton collision data at* $\sqrt{s} = 13$ *TeV*. CMS-PAS-HIG-19-005. 2020. URL: https://cds.cern.ch/record/2706103.

[7] S. Velasco N. Wolchover and L. Reading-Ikkanda. *A New Map of All the Particles and Forces*. 2020. URL: https://www.quantamagazine.org/a-new-map-of-the-standard-model-of-particle-physics-20201022/.

[8] P A Zyla et al. "Review of Particle Physics, 2020-2021. RPP". In: *PTEP* 2020 (2020), 083C01. 2093 p. DOI: 10.1093/ptep/ptaa104. URL: https://cds.cern.ch/record/2729066.

[9] ATLAS Collaboration. "Measurement of the Higgs boson mass in the $H \to ZZ^* \to 4\ell$ and $H \to \gamma\gamma$ channels with $\sqrt{s} = 13\,\text{TeV}$ pp collisions using the ATLAS detector". In: *Phys. Lett. B* 784 (2018), p. 345. DOI: 10.1016/j.physletb.2018.07.050. arXiv: 1806.00242 [hep-ex].

[10] F. Englert and R. Brout. "Broken Symmetry and the Mass of Gauge Vector Mesons". In: *Phys. Rev. Lett.* 13 (1964), pp. 321–323. DOI: 10.1103/PhysRevLett.13.321.

[11] Peter W. Higgs. "Broken symmetries, massless particles and gauge fields". In: *Phys. Lett.* 12 (1964), pp. 132–133. DOI: 10.1016/0031-9163(64)91136-9.

[12] Peter W. Higgs. "Broken Symmetries and the Masses of Gauge Bosons". In: *Phys. Rev. Lett.* 13 (1964), pp. 508–509. DOI: 10.1103/PhysRevLett.13.508.

[13] G. S. Guralnik, C. R. Hagen, and T. W. B. Kibble. "Global Conservation Laws and Massless Particles". In: *Phys. Rev. Lett.* 13 (1964), p. 585. DOI: 10.1103/PhysRevLett.13.585.

[14] Peter W. Higgs. "Spontaneous Symmetry Breakdown without Massless Bosons". In: *Phys. Rev.* 145 (1966), pp. 1156–1163. DOI: 10.1103/PhysRev.145.1156.

[15] T. W. B. Kibble. "Symmetry Breaking in Non-Abelian Gauge Theories". In: *Phys. Rev.* 155 (1967), pp. 1554–1561. DOI: 10.1103/PhysRev.155.1554.

[16] "A detailed map of Higgs boson interactions by the ATLAS experiment ten years after the discovery". In: *Nature* 607.7917 (2022), pp. 52–59. DOI: 10.1038/s41586-022-04893-w. arXiv: 2207.00092 [hep-ex].

[17] Graham D. Kribs and Adam Martin. "Enhanced di-Higgs production through light colored scalars". In: *Phys. Rev. D* 86 (2012), p. 095023. DOI: 10.1103/PhysRevD.86.095023. arXiv: 1207.4496 [hep-ph].

[18] Andrew Noble and Maxim Perelstein. "Higgs self-coupling as a probe of electroweak phase transition". In: *Phys. Rev. D* 78 (2008), p. 063518. DOI: 10.1103/PhysRevD.78.063518. arXiv: 0711.3018 [hep-ph].

[19] Pankaj Agrawal et al. "Determining the shape of the Higgs potential at future colliders". In: *Phys. Rev. D* 101.7 (2020), p. 075023. DOI: 10.1103/PhysRevD.101.075023. arXiv: 1907.02078 [hep-ph].

[20] David E Morrissey and Michael J Ramsey-Musolf. "Electroweak baryogenesis". In: *New Journal of Physics* 14.12 (Dec. 2012), p. 125003. DOI: 10.1088/1367-2630/14/12/125003. URL: https://doi.org/10.1088%2F1367-2630%2F14%2F12%2F125003.

[21] M. Cepeda et al. "Higgs Physics at the HL-LHC and HE-LHC". In: (2019). arXiv: 1902.00134 [hep-ph].

[22] J. Baglio et al. "$gg \to HH$: Combined uncertainties". In: *Phys. Rev. D* 103.5 (2021), p. 056002. DOI: 10.1103/PhysRevD.103.056002. arXiv: 2008.11626 [hep-ph].

[23] Massimiliano Grazzini et al. "Higgs boson pair production at NNLO with top quark mass effects". In: *JHEP* 05 (2018), p. 059. DOI: 10.1007/JHEP05(2018)059. arXiv: 1803.02463 [hep-ph].

[24] Giuseppe Degrassi et al. "Probing the Higgs self coupling via single Higgs production at the LHC". In: *JHEP* 12 (2016), p. 080. DOI: 10.1007/JHEP12(2016)080. arXiv: 1607.04251 [hep-ph].

[25] Fabio Maltoni et al. "Trilinear Higgs coupling determination via single-Higgs differential measurements at the LHC". In: *Eur. Phys. J. C* 77.12 (2017), p. 887. DOI: 10.1140/epjc/s10052-017-5410-8. arXiv: 1709.08649 [hep-ph].

[26] Stefano Di Vita et al. "A global view on the Higgs self-coupling". In: *JHEP* 09 (2017), p. 069. DOI: 10.1007/JHEP09(2017)069. arXiv: 1704.01953 [hep-ph].

[27] Martin Gorbahn and Ulrich Haisch. "Indirect probes of the trilinear Higgs coupling: $gg \to h$ and $h \to \gamma\gamma$". In: *JHEP* 10 (2016), p. 094. DOI: 10.1007/JHEP10(2016)094. arXiv: 1607.03773 [hep-ph].

[28] Wojciech Bizon et al. "Constraints on the trilinear Higgs coupling from vector boson fusion and associated Higgs production at the LHC". In: *JHEP* 07 (2017), p. 083. DOI: 10.1007/JHEP07(2017)083. arXiv: 1610.05771 [hep-ph].

[29] Matthew McCullough. "An Indirect Model-Dependent Probe of the Higgs Self-Coupling". In: *Phys. Rev. D* 90.1 (2014). [Erratum: Phys. Rev. D **92** (2015) 039903], p. 015001. DOI: 10.1103/PhysRevD.90.015001,10.1103/PhysRevD.92.039903. arXiv: 1312.3322 [hep-ph].

[30] "Constraining the Higgs boson self-coupling from single- and double-Higgs production with the ATLAS detector using pp collisions at $\sqrt{s} = 13$ TeV". In: (Nov. 2022). arXiv: 2211.01216 [hep-ex].

[31] ATLAS Collaboration. *Constraint of the Higgs boson self-coupling from Higgs boson differential production and decay measurements*. ATL-PHYS-PUB-2019-009. 2019. URL: https://cds.cern.ch/record/2667570.

[32] R. Frederix et al. "Higgs pair production at the LHC with NLO and parton-shower effects". In: *Phys. Lett. B* 732 (2014), pp. 142–149. DOI: 10.1016/j.physletb.2014.03.026. arXiv: 1401.7340 [hep-ph].

[33] Luca Di Luzio, Ramona Gröber, and Michael Spannowsky. "Maxi-sizing the trilinear Higgs self-coupling: how large could it be?" In: *Eur. Phys. J. C* 77.11 (2017), p. 788. DOI: 10.1140/epjc/s10052-017-5361-0. arXiv: 1704.02311 [hep-ph].

[34] Graham D. Kribs et al. "Electroweak oblique parameters as a probe of the trilinear Higgs boson self-interaction". In: *Phys. Rev. D* 95.9 (2017), p. 093004. DOI: 10.1103/PhysRevD.95.093004. arXiv: 1702.07678 [hep-ph].

[35] ATLAS and CMS Collaborations. "Combined Measurement of the Higgs Boson Mass in pp Collisions at $\sqrt{s} = 7$ and 8 TeV with the ATLAS and CMS Experiments". In: *Phys. Rev. Lett.* 114 (2015), p. 191803. DOI: 10.1103/PhysRevLett.114.191803. arXiv: 1503.07589 [hep-ex].

[36] J. Alison et al. "Higgs boson potential at colliders: Status and perspectives". In: *Rev. Phys.* 5 (2020). Ed. by Biagio Di Micco et al., p. 100045. DOI: 10.1016/j.revip.2020.100045. arXiv: 1910.00012 [hep-ph].

[37] Ding Yu Shao et al. "Threshold resummation effects in Higgs boson pair production at the LHC". In: *JHEP* 07 (2013), p. 169. DOI: 10.1007/JHEP07(2013)169. arXiv: 1301.1245 [hep-ph].

[38] Daniel de Florian and Javier Mazzitelli. "Higgs pair production at next-to-next-to-leading logarithmic accuracy at the LHC". In: *JHEP* 09 (2015), p. 053. DOI: 10.1007/JHEP09(2015)053. arXiv: 1505.07122 [hep-ph].

[39] S. Dawson, S. Dittmaier, and M. Spira. "Neutral Higgs boson pair production at hadron colliders: QCD corrections". In: *Phys. Rev. D* 58 (1998), p. 115012. DOI: 10.1103/PhysRevD.58.115012. arXiv: hep-ph/9805244 [hep-ph].

[40] S. Borowka et al. "Higgs Boson Pair Production in Gluon Fusion at Next-to-Leading Order with Full Top-Quark Mass Dependence". In: *Phys. Rev. Lett.* 117.1 (2016), p. 012001. DOI: 10.1103/PhysRevLett.117.079901. arXiv: 1604.06447 [hep-ph].

[41] Daniel de Florian and Javier Mazzitelli. "Higgs Boson Pair Production at Next-to-Next-to-Leading Order in QCD". In: *Phys. Rev. Lett.* 111 (2013), p. 201801. DOI: 10.1103/PhysRevLett.111.201801. arXiv: 1309.6594 [hep-ph].

[42] ATLAS Collaboration. *Constraints on the Higgs boson self-coupling from the combination of single-Higgs and double-Higgs production analyses performed with the ATLAS experiment*. ATLAS-CONF-2019-049. 2019. URL: https://cds.cern.ch/record/2693958.

[43] J. Alison et al. "Higgs boson pair production at colliders: status and perspectives". In: *Double Higgs Production at Colliders Batavia, IL, USA, September 4, 2018-9, 2019*. Ed. by B. Di Micco et al. 2019. arXiv: 1910.00012 [hep-ph].

[44] R Scrivens et al. "Overview of the status and developments on primary ion sources at CERN*". In: (2011). URL: https://cds.cern.ch/record/1382102.

[45] Michael Benedikt et al. *LHC Design Report*. CERN Yellow Reports: Monographs. Geneva: CERN, 2004. DOI: 10.5170/CERN-2004-003-V-3. URL: https://cds.cern.ch/record/823808.

[46] Christiane Lefèvre. "The CERN accelerator complex. Complexe des accélérateurs du CERN". 2008. URL: https://cds.cern.ch/record/1260465.

[47] Oliver Sim Brüning et al. *LHC Design Report*. CERN Yellow Reports: Monographs. Geneva: CERN, 2004. DOI: 10.5170/CERN-2004-003-V-1. URL: https://cds.cern.ch/record/782076.

[48] ATLAS Collaboration. *Characterization of Interaction-Point Beam Parameters Using the pp Event-Vertex Distribution Reconstructed in the ATLAS Detector at the LHC*. ATLAS-CONF-2010-027. 2010. URL: https://cds.cern.ch/record/1277659.

[49] ATLAS Collaboration. "Combined measurement of differential and total cross sections in the $H \to \gamma\gamma$ and the $H \to ZZ^* \to 4\ell$ decay channels at $\sqrt{s} = 13\,\text{TeV}$ with the ATLAS detector". In: *Phys. Lett. B* 786 (2018), p. 114. DOI: 10.1016/j.physletb.2018.09.019. arXiv: 1805.10197 [hep-ex].

[50] ATLAS Collaboration. "Public ATLAS Luminosity Results for Run-2 of the LHC". 2018. URL: https://twiki.cern.ch/twiki/bin/view/AtlasPublic/LuminosityPublicResultsRun2.

[51] Joao Pequenao. "Computer generated image of the whole ATLAS detector". 2008. URL: https://cds.cern.ch/record/1095924.

[52] Tracking CP. *ATLAS Track Reconstruction*. 2022. URL: https://atlassoftwaredocs.web.cern.ch/trackingTutorial/idoverview/ (visited on 10/14/2022).

[53] R.L. Gluckstern. "Uncertainties in track momentum and direction, due to multiple scattering and measurement errors". In: *Nuclear Instruments and Methods* 24 (1963), pp. 381–389. ISSN: 0029-554X. DOI: https://doi.org/10.1016/0029-554X(63)90347-1. URL: https://www.sciencedirect.com/science/article/pii/0029554X63903471.

[54] Zbynek Drasal and Werner Riegler. "An extension of the Gluckstern formulae for multiple scattering: Analytic expressions for track parameter resolution using optimum weights". In: *Nucl. Instrum. Meth. A* 910 (2018), pp. 127–132. DOI: 10.1016/j.nima.2018.08.078. arXiv: 1805.12014 [physics.ins-det].

[55] ATLAS Collaboration. "The ATLAS Experiment at the CERN Large Hadron Collider". In: *JINST* 3 (2008), S08003. DOI: 10.1088/1748-0221/3/08/S08003.

[56] ATLAS Collaboration. "Jet energy scale and resolution measured in proton–proton collisions at $\sqrt{s} = 13\,\text{TeV}$ with the ATLAS detector". In: *Eur. Phys. J. C* 81 (2020), p. 689. DOI: 10.1140/epjc/s10052-021-09402-3. arXiv: 2007.02645 [hep-ex].

[57] ATLAS Collaboration. *ATLAS Liquid Argon Calorimeter: Technical Design Report*. ATLAS-TDR-2; CERN-LHCC-96-041. 1996. URL: https://cds.cern.ch/record/331061.

[58] ATLAS Collaboration. *ATLAS Tile Calorimeter: Technical Design Report*. ATLAS-TDR-3; CERN-LHCC-96-042. 1996. URL: https://cds.cern.ch/record/331062.

[59] ATLAS Collaboration. *ATLAS Muon Spectrometer: Technical Design Report*. ATLAS-TDR-10; CERN-LHCC-97-022. CERN, 1997. URL: https://cds.cern.ch/record/331068.

[60] Xiaocong Ai et al. "A Common Tracking Software Project". In: *Comput. Softw. Big Sci.* 6.1 (2022), p. 8. DOI: 10.1007/s41781-021-00078-8. arXiv: 2106.13593 [physics.ins-det].

[61] ATLAS Collaboration. "Muon reconstruction performance of the ATLAS detector in proton–proton collision data at $\sqrt{s} = 13\,\text{TeV}$". In: *Eur. Phys. J. C* 76 (2016), p. 292. DOI: 10.1140/epjc/s10052-016-4120-y. arXiv: 1603.05598 [hep-ex].

[62] ATLAS Collaboration. "Performance of the ATLAS trigger system in 2015". In: *Eur. Phys. J. C* 77 (2017), p. 317. DOI: 10.1140/epjc/s10052-017-4852-3. arXiv: 1611.09661 [hep-ex].

[63] ATLAS Collaboration. "Electron reconstruction and identification in the ATLAS experiment using the 2015 and 2016 LHC proton–proton collision data at $\sqrt{s} = 13\,\text{TeV}$". In: *Eur. Phys. J. C* 79 (2019), p. 639. DOI: 10.1140/epjc/s10052-019-7140-6. arXiv: 1902.04655 [hep-ex].

[64] T Cornelissen et al. *Concepts, Design and Implementation of the ATLAS New Tracking (NEWT)*. Tech. rep. Geneva: CERN, 2007. URL: https://cds.cern.ch/record/1020106.

[65] ATLAS Collaboration. "Performance of the ATLAS track reconstruction algorithms in dense environments in LHC Run 2". In: *Eur. Phys. J. C* 77 (2017), p. 673. DOI: 10.1140/epjc/s10052-017-5225-7. arXiv: 1704.07983 [hep-ex].

[66] Karri Folan Di Petrillo. "Search for long-lived, massive particles in events with a displaced vertex and a displaced muon using $\sqrt{s} = 13$ TeV pp-collisions with the ATLAS detector". Presented 30 Apr 2019. 2019. URL: https://cds.cern.ch/record/2677474.

[67] ATLAS Collaboration. *Early Inner Detector Tracking Performance in the 2015 Data at $\sqrt{s} = 13$ TeV*. ATL-PHYS-PUB-2015-051. 2015. URL: https://cds.cern.ch/record/2110140.

[68] ATLAS Collaboration. "Jet reconstruction and performance using particle flow with the ATLAS Detector". In: *Eur. Phys. J. C* 77 (2017), p. 466. DOI: 10.1140/epjc/s10052-017-5031-2. arXiv: 1703.10485 [hep-ex].

[69] ATLAS Collaboration. "Electron and photon performance measurements with the ATLAS detector using the 2015–2017 LHC proton–proton collision data". In: *JINST* 14 (2019), P12006. DOI: 10.1088/1748-0221/14/12/P12006. arXiv: 1908.00005 [hep-ex].

[70] ATLAS Collaboration. *Vertex Reconstruction Performance of the ATLAS Detector at $\sqrt{s} = 13$ TeV*. ATL-PHYS-PUB-2015-026. 2015. URL: https://cds.cern.ch/record/2037717.

[71] ATLAS Collaboration. "ATLAS event at 13 TeV - First stable beam, 3 June 2015 - run: 266904, evt: 25884805". General Photo. 2015. URL: https://cds.cern.ch/record/2022202.

[72] ATLAS Collaboration. "Measurement of Higgs boson production in the diphoton decay channel in pp collisions at center-of-mass energies of 7 and 8 TeV with the ATLAS detector". In: *Phys. Rev. D* 90 (2014), p. 112015. DOI: 10.1103/PhysRevD.90.112015. arXiv: 1408.7084 [hep-ex].

[73] ATLAS Collaboration. "Muon reconstruction and identification efficiency in ATLAS using the full Run 2 pp collision data set at $\sqrt{s} = 13$ TeV". In: *Eur. Phys. J. C* 81 (2021), p. 578. DOI: 10.1140/epjc/s10052-021-09233-2. arXiv: 2012.00578 [hep-ex].

[74] Matteo Cacciari, Gavin P. Salam, and Gregory Soyez. "The anti-k_t jet clustering algorithm". In: *JHEP* 04 (2008), p. 063. DOI: 10.1088/1126-6708/2008/04/063. arXiv: 0802.1189 [hep-ph].

[75] Matteo Cacciari, Gavin P. Salam, and Gregory Soyez. "FastJet user manual". In: *Eur. Phys. J. C* 72 (2012), p. 1896. DOI: 10.1140/epjc/s10052-012-1896-2. arXiv: 1111.6097 [hep-ph].

[76] ATLAS Collaboration. *Jet 2012 Monte Carlo Event Displays*. Public Results. 2012. URL: https://twiki.cern.ch/twiki/bin/view/AtlasPublic/JetEtmissApprovedBOOST2014EventDisplays.

[77] ATLAS Collaboration. *Tagging and suppression of pileup jets with the ATLAS detector*. ATLAS-CONF-2014-018. 2014. URL: https://cds.cern.ch/record/1700870.

[78] ATLAS Collaboration. "Determination of jet calibration and energy resolution in proton–proton collisions at $\sqrt{s} = 8$ TeV using the ATLAS detector". In: *Eur. Phys. J. C* 80 (2020), p. 1104. DOI: 10.1140/epjc/s10052-020-08477-8. arXiv: 1910.04482 [hep-ex].

[79] Izaak Neutelings. *B tagging jets*. 2022. URL: https://tikz.net/jet_btag/ (visited on 10/14/2022).

[80] R. L. Workman et al. "Review of Particle Physics". In: *PTEP* 2022 (2022), p. 083C01. DOI: 10.1093/ptep/ptac097.

[81] ATLAS Collaboration. "ATLAS b-jet identification performance and efficiency measurement with $t\bar{t}$ events in pp collisions at $\sqrt{s} = 13$ TeV". In: *Eur. Phys. J. C* 79 (2019), p. 970. DOI: 10.1140/epjc/s10052-019-7450-8. arXiv: 1907.05120 [hep-ex].

[82] ATLAS Collaboration. "Performance of b-jet identification in the ATLAS experiment". In: *JINST* 11 (2016), P04008. DOI: 10.1088/1748-0221/11/04/P04008. arXiv: 1512.01094 [hep-ex].

[83] ATLAS Collaboration. *Secondary vertex finding for jet flavour identification with the ATLAS detector*. ATL-PHYS-PUB-2017-011. 2017. URL: https://cds.cern.ch/record/2270366.

[84] ATLAS Collaboration. *Topological b-hadron decay reconstruction and identification of b-jets with the JetFitter package in the ATLAS experiment at the LHC*. ATL-PHYS-PUB-2018-025. 2018. URL: https://cds.cern.ch/record/2645405.

[85] ATLAS Collaboration. *Deep Sets based Neural Networks for Impact Parameter Flavour Tagging in ATLAS*. ATL-PHYS-PUB-2020-014. 2020. URL: https://cds.cern.ch/record/2718948.

[86] ATLAS Collaboration. *Identification of Jets Containing b-Hadrons with Recurrent Neural Networks at the ATLAS Experiment*. ATL-PHYS-PUB-2017-003. 2017. URL: https://cds.cern.ch/record/2255226.

[87] Andrea Sciandra. "Development of a new Soft Muon Tagger for the identification of b-jets in ATLAS". In: *PoS* EPS-HEP2017 (2017). Ed. by Paolo Checchia et al., p. 768. DOI: 10.22323/1.314.0768.

[88] ATLAS Collaboration. *Optimisation and performance studies of the ATLAS b-tagging algorithms for the 2017-18 LHC run*. ATL-PHYS-PUB-2017-013. 2017. URL: https://cds.cern.ch/record/2273281.

[89] ATLAS Collaboration. "Expected performance of the 2019 ATLAS b-taggers". 2019. URL: http://atlas.web.cern.ch/Atlas/GROUPS/PHYSICS/PLOTS/FTAG-2019-005/.

[90] ATLAS Collaboration. "Identification and energy calibration of hadronically decaying tau leptons with the ATLAS experiment in pp collisions at $\sqrt{s} = 8\,\text{TeV}$". In: *Eur. Phys. J. C* 75 (2015), p. 303. DOI: 10.1140/epjc/s10052-015-3500-z. arXiv: 1412.7086 [hep-ex].

[91] ATLAS Collaboration. *Measurement of the tau lepton reconstruction and identification performance in the ATLAS experiment using pp collisions at* $\sqrt{s} = 13$ *TeV*. ATLAS-CONF-2017-029. 2017. URL: https://cds.cern.ch/record/2261772.

[92] ATLAS Collaboration. *Identification of hadronic tau lepton decays using neural networks in the ATLAS experiment*. ATL-PHYS-PUB-2019-033. 2019. URL: https://cds.cern.ch/record/2688062.

[93] "A deep neural network for simultaneous estimation of b quark energy and resolution". In: (2019).

[94] T. Aaltonen et al. "Improved b-jet Energy Correction for $H \to b\bar{b}$ Searches at CDF". In: (July 2011). arXiv: 1107.3026 [hep-ex].

[95] M. Aaboud et al. "Evidence for the $H \to b\bar{b}$ decay with the ATLAS detector". In: *JHEP* 12 (2017), p. 024. DOI: 10.1007/JHEP12(2017)024. arXiv: 1708.03299 [hep-ex].

[96] Morad Aaboud et al. "Observation of $H \to b\bar{b}$ decays and VH production with the ATLAS detector". In: *Phys. Lett. B* 786 (2018), pp. 59–86. DOI: 10.1016/j.physletb.2018.09.013. arXiv: 1808.08238 [hep-ex].

[97] Caterina Vernieri. "Search for resonances decaying to $H(b\bar{b})$ pairs with the CMS experiment at the LHC". PhD thesis. Pisa, Scuola Normale Superiore, Aug. 2014.

[98] Elisabeth Schopf. "Improvement of the Higgs Mass Resolution in the Decay Channel H -> bb in Associated Production with a W Boson at the ATLAS Detector Using Multivariate Regression". MA thesis. Bonn U., 2014.

[99] ATLAS Collaboration. *Proposal for particle-level object and observable definitions for use in physics measurements at the LHC*. ATL-PHYS-PUB-2015-013. 2015. URL: https://cds.cern.ch/record/2022743.

[100] ATLAS Collaboration. "Identification and rejection of pile-up jets at high pseudorapidity with the ATLAS detector". In: *Eur. Phys. J. C* 77 (2017), p. 580. DOI: 10.1140/epjc/s10052-017-5081-5. arXiv: 1705.02211 [hep-ex]. Erratum: in: *Eur. Phys. J. C* 77 (2017), p. 712. DOI: 10.1140/epjc/s10052-017-5245-3.

[101] A. D. Bukin. *Fitting function for asymmetric peaks*. 2007. DOI: 10.48550/ARXIV.0711.4449. URL: https://arxiv.org/abs/0711.4449.

[102] ATLAS Collaboration. *Generalized Numerical Inversion: A Neutral Network Approach to Jet Calibration*. ATL-PHYS-PUB-2018-013. 2018. URL: https://cds.cern.ch/record/2630972.

[103] ATLAS Collaboration. "Search for Higgs boson pair production in the two bottom quarks plus two photons final state in pp collisions at $\sqrt{s} = 13$ TeV with the ATLAS detector". In: (2021). arXiv: 2112.11876 [hep-ex].

[104] ATLAS Collaboration. "ATLAS data quality operations and performance for 2015–2018 data-taking". In: *JINST* 15 (2020), P04003. DOI: 10.1088/1748-0221/15/04/P04003. arXiv: 1911.04632 [physics.ins-det].

[105] G. Avoni et al. "The new LUCID-2 detector for luminosity measurement and monitoring in ATLAS". In: *JINST* 13.07 (2018), P07017. DOI: 10.1088/1748-0221/13/07/P07017.

[106] ATLAS Collaboration. *Luminosity determination in pp collisions at $\sqrt{s} = 13$ TeV using the ATLAS detector at the LHC*. ATLAS-CONF-2019-021. 2019. URL: https://cds.cern.ch/record/2677054.

[107] ATLAS Collaboration. "Emulating the impact of additional proton-proton interactions in the ATLAS simulation by pre-sampling sets of inelastic Monte Carlo events". In: (Feb. 2021). arXiv: 2102.09495 [hep-ex].

[108] ATLAS Collaboration. *The Pythia 8 A3 tune description of ATLAS minimum bias and inelastic measurements incorporating the Donnachie–Landshoff diffractive model*. ATL-PHYS-PUB-2016-017. 2016. URL: https://cds.cern.ch/record/2206965.

[109] ATLAS Collaboration. "The ATLAS Simulation Infrastructure". In: *Eur. Phys. J. C* 70 (2010), p. 823. DOI: 10.1140/epjc/s10052-010-1429-9. arXiv: 1005.4568 [physics.ins-det].

[110] GEANT4 Collaboration, S. Agostinelli, et al. "GEANT4 – a simulation toolkit". In: *Nucl. Instrum. Meth. A* 506 (2003), p. 250. DOI: 10.1016/S0168-9002(03)01368-8.

[111] ATLAS Collaboration. "The simulation principle and performance of the ATLAS fast calorimeter simulation FastCaloSim". In: (2010). ATL-PHYS-PUB-2010-013. URL: http://cdsweb.cern.ch/record/1300517.

[112] Paolo Nason and Carlo Oleari. "NLO Higgs boson production via vector-boson fusion matched with shower in POWHEG". In: *JHEP* 02 (2010), p. 037. DOI: 10.1007/JHEP02(2010)037. arXiv: 0911.5299 [hep-ph].

[113] G. Heinrich et al. "NLO predictions for Higgs boson pair production with full top quark mass dependence matched to parton showers". In: *JHEP* 08 (2017), p. 088. DOI: 10.1007/JHEP08(2017)088. arXiv: 1703.09252 [hep-ph].

[114] G. Heinrich et al. "Probing the trilinear Higgs boson coupling in di-Higgs production at NLO QCD including parton shower effects". In: *JHEP* 06 (2019), p. 066. DOI: 10.1007/JHEP06(2019)066. arXiv: 1903.08137 [hep-ph].

[115] Jon Butterworth et al. "PDF4LHC recommendations for LHC Run II". In: *J. Phys. G* 43 (2016), p. 023001. DOI: 10.1088/0954-3899/43/2/023001. arXiv: 1510.03865 [hep-ph].

[116] J. Alwall et al. "The automated computation of tree-level and next-to-leading order differential cross sections, and their matching to parton shower simulations". In: *JHEP* 07 (2014), p. 079. DOI: 10.1007/JHEP07(2014)079. arXiv: 1405.0301 [hep-ph].

[117] Fady Bishara, Roberto Contino, and Juan Rojo. "Higgs pair production in vector-boson fusion at the LHC and beyond". In: *Eur. Phys. J. C* 77.7 (2017), p. 481. DOI: 10.1140/epjc/s10052-017-5037-9. arXiv: 1611.03860 [hep-ph].

[118] Richard D. Ball et al. "Parton distributions with LHC data". In: *Nucl. Phys.* B 867 (2013), pp. 244–289. DOI: 10.1016/j.nuclphysb.2012.10.003. arXiv: 1207.1303 [hep-ph].

[119] ATLAS Collaboration. "Combined measurements of Higgs boson production and decay using up to 80 fb^{-1} of proton–proton collision data at $\sqrt{s} = 13\,\mathrm{TeV}$ collected with the ATLAS experiment". In: *Phys. Rev. D* 101 (2020), p. 012002. DOI: 10.1103/PhysRevD.101.012002. arXiv: 1909.02845 [hep-ex].

[120] D. de Florian et al. "Handbook of LHC Higgs Cross Sections: 4. Deciphering the Nature of the Higgs Sector". In: (2016). DOI: 10.23731/CYRM-2017-002. arXiv: 1610.07922 [hep-ph].

[121] A. Djouadi, J. Kalinowski, and M. Spira. "HDECAY: A Program for Higgs boson decays in the standard model and its supersymmetric extension". In: *Comput. Phys. Commun.* 108 (1998), pp. 56–74. DOI: 10.1016/S0010-4655(97)00123-9. arXiv: hep-ph/9704448.

[122] J R Andersen et al. "Handbook of LHC Higgs Cross Sections: 3. Higgs Properties". In: (July 2013). Ed. by S Heinemeyer et al. DOI: 10.5170/CERN-2013-004. arXiv: 1307.1347 [hep-ph].

[123] Enrico Bothmann et al. "Event generation with Sherpa 2.2". In: *SciPost Phys.* 7.3 (2019), p. 034. DOI: 10.21468/SciPostPhys.7.3.034. arXiv: 1905.09127 [hep-ph].

[124] Tanju Gleisberg and Stefan Höche. "Comix, a new matrix element generator". In: *JHEP* 12 (2008), p. 039. DOI: 10.1088/1126-6708/2008/12/039. arXiv: 0808.3674 [hep-ph].

[125] Federico Buccioni et al. "OpenLoops 2". In: *Eur. Phys. J. C* 79.10 (2019), p. 866. DOI: 10.1140/epjc/s10052-019-7306-2. arXiv: 1907.13071 [hep-ph].

[126] Fabio Cascioli, Philipp Maierhöfer, and Stefano Pozzorini. "Scattering Amplitudes with Open Loops". In: *Phys. Rev. Lett.* 108 (2012), p. 111601. DOI: 10.1103/PhysRevLett.108.111601. arXiv: 1111.5206 [hep-ph].

[127] Ansgar Denner, Stefan Dittmaier, and Lars Hofer. "COLLIER: A fortran-based complex one-loop library in extended regularizations". In: *Comput. Phys. Commun.* 212 (2017), pp. 220–238. DOI: 10.1016/j.cpc.2016.10.013. arXiv: 1604.06792 [hep-ph].

[128] Steffen Schumann and Frank Krauss. "A parton shower algorithm based on Catani–Seymour dipole factorisation". In: *JHEP* 03 (2008), p. 038. DOI: 10.1088/1126-6708/2008/03/038. arXiv: 0709.1027 [hep-ph].

[129] Stefan Höche et al. "A critical appraisal of NLO+PS matching methods". In: *JHEP* 09 (2012), p. 049. DOI: 10.1007/JHEP09(2012)049. arXiv: 1111.1220 [hep-ph].

[130] Stefan Höche et al. "QCD matrix elements + parton showers. The NLO case". In: *JHEP* 04 (2013), p. 027. DOI: 10.1007/JHEP04(2013)027. arXiv: 1207.5030 [hep-ph].

[131] Frank Siegert. "A practical guide to event generation for prompt photon production with Sherpa". In: *J. Phys. G* 44.4 (2017), p. 044007. DOI: 10.1088/1361-6471/aa5f29. arXiv: 1611.07226 [hep-ph].

[132] ATLAS Collaboration. "Measurement of isolated-photon pair production in pp collisions at $\sqrt{s} = 7\,\text{TeV}$ with the ATLAS detector". In: *JHEP* 01 (2013), p. 086. DOI: 10.1007/JHEP01(2013)086. arXiv: 1211.1913 [hep-ex].

[133] Torbjörn Sjöstrand et al. "An introduction to PYTHIA 8.2". In: *Comput. Phys. Commun.* 191 (2015), p. 159. DOI: 10.1016/j.cpc.2015.01.024. arXiv: 1410.3012 [hep-ph].

[134] ATLAS Collaboration. *ATLAS Pythia 8 tunes to 7 TeV data*. ATL-PHYS-PUB-2014-021. 2014. URL: https://cds.cern.ch/record/1966419.

[135] Richard D. Ball et al. "Parton distributions for the LHC run II". In: *JHEP* 04 (2015), p. 040. DOI: 10.1007/JHEP04(2015)040. arXiv: 1410.8849 [hep-ph].

[136] Keith Hamilton, Paolo Nason, and Giulia Zanderighi. "MINLO: multi-scale improved NLO". In: *JHEP* 10 (2012), p. 155. DOI: 10.1007/JHEP10(2012)155. arXiv: 1206.3572 [hep-ph].

[137] John M. Campbell et al. "NLO Higgs boson production plus one and two jets using the POWHEG BOX, MadGraph4 and MCFM". In: *JHEP* 07 (2012), p. 092. DOI: 10.1007/JHEP07(2012)092. arXiv: 1202.5475 [hep-ph].

[138] Keith Hamilton et al. "Merging H/W/Z + 0 and 1 jet at NLO with no merging scale: a path to parton shower + NNLO matching". In: *JHEP* 05 (2013), p. 082. DOI: 10.1007/JHEP05(2013)082. arXiv: 1212.4504 [hep-ph].

[139] Giuseppe Bozzi et al. "Transverse-momentum resummation and the spectrum of the Higgs boson at the LHC". In: *Nucl. Phys. B* 737 (2006), pp. 73–120. DOI: 10.1016/j.nuclphysb.2005.12.022. arXiv: hep-ph/0508068 [hep-ph].

[140] Daniel de Florian et al. "Transverse-momentum resummation: Higgs boson production at the Tevatron and the LHC". In: *JHEP* 11 (2011), p. 064. DOI: 10.1007/JHEP11(2011)064. arXiv: 1109.2109 [hep-ph].

[141] ATLAS Collaboration. "Measurement of the Z/γ^* boson transverse momentum distribution in pp collisions at $\sqrt{s} = 7$ TeV with the ATLAS detector". In: *JHEP* 09 (2014), p. 145. DOI: 10.1007/JHEP09(2014)145. arXiv: 1406.3660 [hep-ex].

[142] Keith Hamilton et al. "NNLOPS simulation of Higgs boson production". In: *JHEP* 10 (2013), p. 222. DOI: 10.1007/JHEP10(2013)222. arXiv: 1309.0017 [hep-ph].

[143] Paolo Nason. "A new method for combining NLO QCD with shower Monte Carlo algorithms". In: *JHEP* 11 (2004), p. 040. DOI: 10.1088/1126-6708/2004/11/040. arXiv: hep-ph/0409146.

[144] Stefano Frixione, Paolo Nason, and Carlo Oleari. "Matching NLO QCD computations with parton shower simulations: the POWHEG method". In: *JHEP* 11 (2007), p. 070. DOI: 10.1088/1126-6708/2007/11/070. arXiv: 0709.2092 [hep-ph].

[145] Simone Alioli et al. "A general framework for implementing NLO calculations in shower Monte Carlo programs: the POWHEG BOX". In: *JHEP* 06 (2010), p. 043. DOI: 10.1007/JHEP06(2010)043. arXiv: 1002.2581 [hep-ph].

[146] Ken Mimasu, Veronica Sanz, and Ciaran Williams. "Higher order QCD predictions for associated Higgs production with anomalous couplings to gauge bosons". In: *JHEP* 08 (2016), p. 039. DOI: 10.1007/JHEP08(2016)039. arXiv: 1512.02572 [hep-ph].

[147] Gionata Luisoni et al. "$HW^{\pm}$/HZ + 0 and 1 jet at NLO with the POWHEG BOX interfaced to GoSam and their merging within MiNLO". In: *JHEP* 10 (2013), p. 083. DOI: 10.1007/JHEP10(2013)083. arXiv: 1306.2542 [hep-ph].

[148] Heribertus B. Hartanto et al. "Higgs boson production in association with top quarks in the POWHEG BOX". In: *Phys. Rev. D* 91.9 (2015), p. 094003. DOI: 10.1103/PhysRevD.91.094003. arXiv: 1501.04498 [hep-ph].

[149] Stefano Frixione, Paolo Nason, and Giovanni Ridolfi. "A positive-weight next-to-leading-order Monte Carlo for heavy flavour hadroproduction". In: *JHEP* 09 (2007), p. 126. DOI: 10.1088/1126-6708/2007/09/126. arXiv: 0707.3088 [hep-ph].

[150] ATLAS Collaboration. *Validation of signal Monte Carlo event generation in searches for Higgs boson pairs with the ATLAS detector*. ATL-PHYS-PUB-2019-007. 2019. URL: https://cds.cern.ch/record/2665057.

[151] S. Amoroso et al. "Les Houches 2019: Physics at TeV Colliders: Standard Model Working Group Report". In: *11th Les Houches Workshop on Physics at TeV Colliders: PhysTeV Les Houches*. Mar. 2020. arXiv: 2003.01700 [hep-ph].

[152] ATLAS Collaboration. "Performance of electron and photon triggers in ATLAS during LHC Run 2". In: *Eur. Phys. J. C* 80.1 (2020), p. 47. DOI: 10.1140/epjc/s10052-019-7500-2. arXiv: 1909.00761 [hep-ex].

[153] ATLAS Collaboration. "Performance of electron and photon triggers in ATLAS during LHC Run 2". In: *Eur. Phys. J. C* 80 (2020), p. 47. DOI: 10.1140/epjc/s10052-019-7500-2. arXiv: 1909.00761 [hep-ex].

[154] Tianqi Chen and Carlos Guestrin. "XGBoost: A Scalable Tree Boosting System". In: *KDD 16*. (2016), pp. 785–794. DOI: 10.1145/2939672.2939785. arXiv: 1603.02754 [cs.LG].

[155] Glen Cowan et al. "Asymptotic formulae for likelihood-based tests of new physics". In: *Eur. Phys. J. C* 71 (2011). [Erratum: Eur. Phys. J. C **73** (2013) 2501], p. 1554. DOI: 10.1140/epjc/s10052-011-1554-0. arXiv: 1007.1727 [physics.data-an].

[156] M. Oreglia. *A Study of the Reactions $\psi' \to \gamma\gamma\psi$*. 1980. URL: https://www.slac.stanford.edu/cgi-wrap/getdoc/slac-r-236.pdf.

[157] ATLAS Collaboration. *Recommendations for the Modeling of Smooth Backgrounds*. ATL-PHYS-PUB-2020-028. 2020. URL: https://cds.cern.ch/record/2743717.

[158] Alexander L. Read. "Presentation of search results: the CL_s technique". In: *J. Phys. G* 28 (2002), pp. 2693–2704. DOI: 10.1088/0954-3899/28/10/313.

[159] ATLAS Collaboration. "Search for resonances in diphoton events at $\sqrt{s} = 13\,\text{TeV}$ with the ATLAS detector". In: *JHEP* 09 (2016), p. 001. DOI: 10.1007/JHEP09(2016)001. arXiv: 1606.03833 [hep-ex].

[160] ATLAS Collaboration. "Performance of missing transverse momentum reconstruction with the ATLAS detector using proton–proton collisions at $\sqrt{s} = 13\,\text{TeV}$". In: *Eur. Phys. J. C* 78 (2018), p. 903. DOI: 10.1140/epjc/s10052-018-6288-9. arXiv: 1802.08168 [hep-ex].

[161] ATLAS Collaboration. *Measurement of b-tagging efficiency of c-jets in $t\bar{t}$ events using a likelihood approach with the ATLAS detector*. ATLAS-CONF-2018-001. 2018. URL: https://cds.cern.ch/record/2306649.

[162] ATLAS Collaboration. *Calibration of light-flavour b-jet mistagging rates using ATLAS proton–proton collision data at $\sqrt{s} = 13$ TeV*. ATLAS-CONF-2018-006. 2018. URL: https://cds.cern.ch/record/2314418.

[163] ATLAS Collaboration. "Measurements of inclusive and differential fiducial cross-sections of $t\bar{t}$ production with additional heavy-flavour jets in proton–proton collisions at $\sqrt{s} = 13$ TeV with the ATLAS detector". In: *JHEP* 04 (2019), p. 046. DOI: 10.1007/JHEP04(2019)046. arXiv: 1811.12113 [hep-ex].

[164] ATLAS Collaboration. "Study of heavy-flavor quarks produced in association with top quark pairs at $\sqrt{s} = 7$ TeV using the ATLAS detector". In: *Phys. Rev. D* 89 (2014), p. 072012. DOI: 10.1103/PhysRevD.89.072012. arXiv: 1304.6386 [hep-ex].

[165] ATLAS Collaboration. "Measurement of the cross-section for W boson production in association with b-jets in pp collisions at $\sqrt{s} = 7$ TeV with the ATLAS detector". In: *JHEP* 06 (2013), p. 084. DOI: 10.1007/JHEP06(2013)084. arXiv: 1302.2929 [hep-ex].

[166] ATLAS Collaboration. "Search for Higgs boson pair production in the $\gamma\gamma b\bar{b}$ final state with 13 TeV pp collision data collected by the ATLAS experiment". In: *JHEP* 11 (2018), p. 040. DOI: 10.1007/JHEP11(2018)040. arXiv: 1807.04873 [hep-ex].

[167] ATLAS Collaboration. "Combination of searches for Higgs boson pairs in pp collisions at $\sqrt{s} = 13$ TeV with the ATLAS detector". In: *Phys. Lett. B* 800 (2020), p. 135103. DOI: 10.1016/j.physletb.2019.135103. arXiv: 1906.02025 [hep-ex].

[168] CMS Collaboration. "Search for nonresonant Higgs boson pair production in final states with two bottom quarks and two photons in proton–proton collisions at $\sqrt{s} = 13$ TeV". In: *JHEP* 03 (2021), p. 257. DOI: 10.1007/JHEP03(2021)257. arXiv: 2011.12373 [hep-ex].

[169] ATLAS Collaboration. *ATLAS New Small Wheel: Technical Design Report*. ATLAS-TDR-020; CERN-LHCC-2013-006. 2013. URL: https://cds.cern.ch/record/1552862.

[170] *Graph Neural Network Jet Flavour Tagging with the ATLAS Detector*. Tech. rep. Geneva: CERN, 2022. URL: https://cds.cern.ch/record/2811135.

[171] Mohamed Belfkir. "Search for Higgs pair production at LHC collider (CERN): The first measurement for Higgs potential and search for new physics". PhD thesis. Savoy Mont Blanc University, 2021.

[172] ATLAS Collaboration. "Evidence for the $H \to b\bar{b}$ decay with the ATLAS detector". In: *JHEP* 12 (2017), p. 024. DOI: 10.1007/JHEP12(2017)024. arXiv: 1708.03299 [hep-ex].

[173] ATLAS Collaboration. "Observation of $H \to b\bar{b}$ decays and VH production with the ATLAS detector". In: *Phys. Lett. B* 786 (2018), p. 59. DOI: 10.1016/j.physletb.2018.09.013. arXiv: 1808.08238 [hep-ex].

[174] Pierre Baldi et al. "Parameterized neural networks for high-energy physics". In: *Eur. Phys. J. C* 76.5 (2016), p. 235. DOI: 10.1140/epjc/s10052-016-4099-4. arXiv: 1601.07913 [hep-ex].

[175] "Search for the exotic decay of the Higgs boson into two light pseudoscalars with four photons in the final state in proton-proton collisions at $\sqrt{s} = 13$ TeV". In: (Aug. 2022). arXiv: 2208.01469 [hep-ex].

[176] ATLAS Collaboration. *Search for resonant and non-resonant Higgs boson pair production in the $b\bar{b}\tau^+\tau^-$ decay channel using 13 TeV pp collision data from the ATLAS detector*. ATLAS-CONF-2021-030. 2021. URL: https://cds.cern.ch/record/2777236.

[177] *Combination of searches for non-resonant and resonant Higgs boson pair production in the $b\bar{b}\gamma\gamma$, $b\bar{b}\tau^+\tau^-$ and $b\bar{b}b\bar{b}$ decay channels using pp collisions at $\sqrt{s} = 13$ TeV with the ATLAS detector*. Tech. rep. Geneva: CERN, 2021. URL: http://cds.cern.ch/record/2786865.

[178] D. de Florian et al. "Handbook of LHC Higgs Cross Sections: 4. Deciphering the Nature of the Higgs Sector". In: (Oct. 2016). arXiv: 1610.07922 [hep-ph].

[179] *Search for non-resonant pair production of Higgs bosons in the $b\bar{b}b\bar{b}$ final state in pp collisions at $\sqrt{s} = 13$ TeV with the ATLAS detector*. Tech. rep. Geneva: CERN, 2022. URL: https://cds.cern.ch/record/2811390.

[180] "A portrait of the Higgs boson by the CMS experiment ten years after the discovery". In: *Nature* 607.7917 (2022), pp. 60–68. DOI: 10.1038/s41586-022-04892-x. arXiv: 2207.00043 [hep-ex].

[181] *Search for nonresonant pair production of highly energetic Higgs bosons decaying to bottom quarks*. Tech. rep. Geneva: CERN, 2022. arXiv: 2205.06667. URL: https://cds.cern.ch/record/2809466.

[182] *Search for Higgs boson pair production in the four b quark final state*. Tech. rep. Geneva: CERN, 2021. URL: https://cds.cern.ch/record/2771912.

[183] ATLAS Collaboration. *Measurement prospects of Higgs boson pair production in the $b\bar{b}\gamma\gamma$ final state with the ATLAS experiment at the HL-LHC*. ATL-PHYS-PUB-2022-001. 2022. URL: http://cds.cern.ch/record/2799146.

[184] ATLAS Collaboration. *Projected sensitivity of Higgs boson pair production in the $bb\tau\tau$ final state using proton-proton collisions at HL-LHC with the ATLAS detector*. ATL-PHYS-PUB-2021-044. 2021. URL: http://cds.cern.ch/record/2798448.

[185] ATLAS Collaboration. *Measurement prospects of the pair production and self-coupling of the Higgs boson with the ATLAS experiment at the HL-LHC*. ATL-PHYS-PUB-2018-053. 2018. URL: https://cds.cern.ch/record/2652727.

[186] ATLAS Collaboration. *Expected tracking and related performance with the updated ATLAS Inner Tracker layout at the High-Luminosity LHC*. ATL-PHYS-PUB-2021-024. 2021. URL: https://cds.cern.ch/record/2776651.

[187] M. Cepeda et al. "Report from Working Group 2: Higgs Physics at the HL-LHC and HE-LHC". In: *CERN Yellow Rep. Monogr.* 7 (2019). Ed. by Andrea Dainese et al., pp. 221–584. DOI: 10.23731/CYRM-2019-007.221. arXiv: 1902.00134 [hep-ph].

[188] F. Sauerburger. *LHC cross section plot*. 2022. URL: https://lhc-xsecs.org/.

[189] ATLAS Collaboration. *Report on the Physics at the HL-LHC and Perspectives for the HE-LHC*. ATL-PHYS-PUB-2019-006. 2019. URL: https://cds.cern.ch/record/2664870.

[190] Georges Aad et al. "Search for Higgs boson pair production in the two bottom quarks plus two photons final state in pp collisions at $\sqrt{s} = 13$ TeV with the ATLAS detector". In: (Dec. 2021). arXiv: 2112.11876 [hep-ex].

[191] ATLAS Collaboration. "Measurements of fiducial cross-sections for $t\bar{t}$ production with one or two additional b-jets in pp collisions at $\sqrt{s} = 8$ TeV using the ATLAS detector". In: *Eur. Phys. J. C* 76 (2016), p. 11. DOI: 10.1140/epjc/s10052-015-3852-4. arXiv: 1508.06868 [hep-ex].

[192] ATLAS Collaboration. *ATLAS Inner Tracker Pixel Detector: Technical Design Report*. ATLAS-TDR-030; CERN-LHCC-2017-021. 2017. URL: https://cds.cern.ch/record/2285585.

[193] Giovanni Calderini. "The ATLAS ITk detector for High Luminosity LHC upgrade". In: *Nucl. Instrum. Meth. A* 1040 (2022), p. 167048. DOI: 10.1016/j.nima.2022.167048.

[194] Lingxin Meng. "ATLAS ITk Pixel Detector Overview". In: (May 2021). arXiv: 2105.10367.

[195] Maurice Garcia-Sciveres. *The RD53A Integrated Circuit*. Tech. rep. Geneva: CERN, 2017. URL: https://cds.cern.ch/record/2287593.

[196] Eric Buschmann. "The Reaodout System for the ITk Pixel Demonstrator for the ATLAS High-Luminosity Upgrade". PhD thesis. Georg-August-Universisaet Goettingen, 2019.

[197] Lingxin Meng. *RD53A Module Testing Document*. Tech. rep. Geneva: CERN, 2019. URL: https://cds.cern.ch/record/2702738.

[198] L. Rossi et al. *Pixel Detectors: From Fundamentals to Applications*. Particle Acceleration and Detection. Berlin: Springer-Verlag, 2006. ISBN: 978-3-540-28332-4, 978-3-540-28333-1. DOI: 10.1007/3-540-28333-1.

[199] Malte Backhaus. "High bandwidth pixel detector modules for the ATLAS Insertable B-Layer". PhD thesis. Universitaet Bonn, 2014.

[200] ATLAS Collaboration. *dE/dx measurement in the ATLAS Pixel Detector and its use for particle identification*. ATLAS-CONF-2011-016. 2011. URL: https://cds.cern.ch/record/1336519.